UNIVERSITY OF SOUTHAMPTON

Faculty of Engineering and Physical Sciences
School of Electronics and Computer Science
Next Generation Wireless Research Group

Transceivers for Integrated Sensing and Communication

by

Hugo Zakaria Jose Hawkins
BEng in Electrical and Electronic Engineering
ORCiD: 0000-0001-5324-4795

A thesis for the degree of
Doctor of Philosophy

December 2025

University of Southampton

Abstract

Faculty of Engineering and Physical Sciences
School of Electronics and Computer Science

Doctor of Philosophy

Transceivers for Integrated Sensing and Communication

by Hugo Zakaria Jose Hawkins

The motivation of the work described in this Thesis is to investigate different communication waveforms, and characterise their performance when used for both communication and sensing. The need to combine communication and sensing functions in an ever more crowded spectrum has been shown by a review of the relevant published literature, in which it is concluded that this combination will be a critical consideration for the derivation and implementation of future waveforms. The trade-offs between communication and sensing performance have been identified for a range of candidate waveforms, considering applications primarily differentiated by their capability of sensing target velocity.

The work first considers the popular Orthogonal Frequency-Division Multiplexing (OFDM) as a baseline, and the relative performance of IM-OFDM. It is shown that Frequency Domain (FD) Index Modulation (IM) reduces the Time Domain (TD) Peak to Average Power Ratio (PAPR) of the OFDM signal, and increases the transmit power on the activated subcarriers through power redistribution. A novel IM-OFDM Integrated Sensing and Communication (ISAC) solution was conceived, which outperforms OFDM ISAC by collecting multiple sensing observations. The delay caused by the collection of multiple observations has no impact on the sensing performance, as the error floors remain constant when the number of collected observations is varied. For four collected observations, the IM-OFDM(4,3) scheme is shown to outperform OFDM both in terms of sensing and communication, where the parameter 3 represents M_A, the number of activated subcarriers in each group, and the parameter 4 represents M_G, the number of subcarriers in each group.

If a modest sensing and communication performance improvement is deemed sufficient, the IM-OFDM(4,3) configuration may be recommended. If a higher sensing performance is desired at the cost of communication performance erosion, the IM-OFDM(2,1) or IM-OFDM(4,1) schemes may be employed, depending on the target velocity and the required throughput. It has also been shown that the IM-OFDM(4,1)

scheme using Phase Shift Keying (PSK) modulation has a better sensing performance than the other systems. As noted in the complexity analysis, the demodulation complexity is proportional to the number of subcarriers in a group, with IM-OFDM(2,1) having the lowest demodulation complexity amongst the IM-OFDM systems. Increasing the interpolation factor leads to a similar improvement in sensing performance in all systems, albeit at the cost of increased complexity. Increasing the number of subcarriers and the number of symbol slots will also increase the sensing resolution, but would require a substantial system modification.

Then the more recent Orthogonal Time Frequency Space (OTFS) waveform was considered as it is designed to be less affected by the Doppler shift induced by large velocities compared to OFDM. Code Division Multiple Access (CDMA) was employed to provide multi-user communication capabilities, whilst also allowing for monostatic sensing. CDMA was chosen due to its simplicity and its ability to reduce the Delay-Doppler Domain (DD) variability in the transmit signal characteristics relative to OTFS, thereby aiding sensing. This is in contrast to the other multi-user methodologies, such as the newer Sparse Code Multiple Access (SCMA) multi-user method, which increases the DD variability in the transmit signal characteristics.

Three different configurations of Code Division Multiple Access OTFS (CDMA-OTFS) were introduced. The results demonstrate that Zadoff-Chu Delay Code Division Multiple Access OTFS (Dl-CDMA-OTFS) and Delay Doppler Code Division Multiple Access OTFS (DD-CDMA-OTFS) are the configurations that consistently outperform pure OTFS sensing, whilst maintaining a similar communication performance at the same throughput. The added modulation complexity of CDMA-OTFS is similar to other OTFS multi-user methodologies, but the demodulation complexity of CDMA-OTFS is lower. CDMA-OTFS sensing can also consistently outperform OTFS sensing whilst not requiring any additional complexity for target parameter estimation. A correlation-based CDMA-OTFS sensing method was also conceived. In contrast to the data cancellation method, the correlation-based method does not allow CDMA-OTFS sensing to outperform OTFS sensing, actually resulting in an inferior performance. Hence, further work on this method was curtailed in favour of more promising schemes.

Affine Frequency Division Multiplexing (AFDM) may be viewed as a generalised form of OFDM, which can be tuned to exhibit similar characteristics to OTFS, and thus allows AFDM to mitigate the effects of higher Doppler shifts, and to separate propagation paths by their associated delays and Doppler shifts. Hence, AFDM is an attractive alternative to OTFS, especially for ISAC.

Iterative soft-Minimum Mean Square Error (MMSE) equalisation in conjunction with both Recursive Systematic Convolutional (RSC) and RSC-Unity Rate Convolutional (URC) coding has been utilised for AFDM, and this scheme is shown to exhibit a lower

Bit Error Rate (BER) at high Energy per bit over Noise power (E_b/N_0) than its equivalent OTFS counterparts, at lower matrix dimension, at high coding rates, and at low numbers of iterations. This is because AFDM possesses higher degrees of freedom than OTFS, since AFDM is a one-dimensional waveform, whereas OTFS is two-dimensional. When the number of iterations is increased, the BER performance of the AFDM configurations and their equivalent OTFS configurations are shown to be similar. At the communication receiver velocity of 150 m/s, both AFDM and OTFS tend to outperform OFDM, for both coded and uncoded transmission. Given that the RSC BER performance fails to improve beyond two iterations, this solution is recommended for low-complexity transceivers. By contrast, if the extra complexity of the RSC-URC aided transceiver is affordable, an extra E_b/N_0 gain of 1.8 dB may be attained at a BER of 10^{-5} and a code rate of 0.5. The sensing results show that AFDM has a comparable integer index estimation Root Mean Square Error (RMSE) performance to OTFS, with a greater sensing flexibility. Scoring the estimates by decoding the reflected data does not impact the integer index estimation, likely due to the poor resolution of the simulated systems.

Contents

List of Figures

List of Tables

Declaration of Authorship

I declare that this thesis and the work presented in it is my own and has been generated by me as the result of my own original research.

I confirm that:

1. This work was done wholly or mainly while in candidature for a research degree at this University;
2. Where any part of this thesis has previously been submitted for a degree or any other qualification at this University or any other institution, this has been clearly stated;
3. Where I have consulted the published work of others, this is always clearly attributed;
4. Where I have quoted from the work of others, the source is always given. With the exception of such quotations, this thesis is entirely my own work;
5. I have acknowledged all main sources of help;
6. Where the thesis is based on work done by myself jointly with others, I have made clear exactly what was done by others and what I have contributed myself;
7. Parts of this work have been published as:
   [1] H. Hawkins, C. Xu, L. -L. Yang and L. Hanzo, "IM-OFDM ISAC Outperforms OFDM ISAC by Combining Multiple Sensing Observations", in *IEEE Open Journal of Vehicular Technology*, vol. 5, pp. 312-329, 2024, doi: 10.1109/OJVT.2024.3366772.
   [2] ——, "CDMA/OTFS Sensing Outperforms Pure OTFS at the Same Communication Throughput", in *IEEE Open Journal of Vehicular Technology*, vol. 6, pp. 502-519, 2025, doi: 10.1109/OJVT.2025.3532848.
   [3] ——, "Iterative Soft-MMSE detection aided AFDM and OTFS," in *IEEE Open Journal of Vehicular Technology*, vol. 6, pp. 2944-2959, 2025, doi: 10.1109/OJVT.2025.3623883.

Signed:..... Date:.....

Acknowledgements

I would like to thank my supervisors, Prof. Lajos Hanzo, Prof. Lie-Liang Yang and Dr. Chao Xu for their help, guidance, and support. I am grateful that they offered me this opportunity and encouraged me at every step, guiding me on the minutae of communication waveforms and their coding, regardless of the hour. Their knowledge and dedication have been crucial in enabling me to complete this work. They supported the selection of a bluesky study from the start, and have used their extensive experience to guide the choices made, always ensuring I remained positive through all setbacks. I am so appreciative of the immense and unrelenting efforts my supervisors have made, as well as their patience and understanding of my circumstances.

I also thank my parents who continue to support me through my studies.

I acknowledge the use of the Matlab libraries, the ITPP (IT++) libraries, and the existing ITPP code from the Next Generation Wireless Research Group. Special thanks to Dr. Chao Xu for his ITPP signal transmission and reception framework and the Unity Rate Convolutional coding functions, Dr. Jin Wang for the ITPP functions associated with Recursive Systematic Convolutional coding, and Prof. Robert G. Maunder for an ITPP variable library.

I would like to thank Mr. Flavien Roussel from Naïo Technologies for granting permission to use images of their autonomous farming units.

I acknowledge the use of the IRIDIS High Performance Computing Facility, and associated support services at the University of Southampton, in the completion of this work.

To McGugsy,
I know you saw it first.

Definitions and Abbreviations

a/A	Italic letters denotes a scalar value
$\boldsymbol{a}$	Bold lower case letter denotes a vector
$\boldsymbol{A}$	Bold upper case letter denotes a matrix
$\boldsymbol{a}[b]$	The b$^{\text{th}}$ value of a vector $\boldsymbol{a}$
$\boldsymbol{a}[b_0 : b_1]$	The values from element b_0 to b_1 of a vector $\boldsymbol{a}$
$\boldsymbol{A}[b_0, ..., b_n]$	The value of the n^{th} dimensional matrix $\boldsymbol{A}$ corresponding to the element in position $(b_0, ..., b_n)$
$(\cdot)^T$	Transpose of a vector or matrix
$(\cdot)^*$	Complex conjugate of a vector or matrix
$(\cdot)^H$	Complex conjugate transpose of a vector or matrix
$(\cdot)^{-1}$	Inverse of a matrix
$\lfloor \cdot \rfloor$	Floor function
$\lceil \cdot \rceil$	Ceiling function
$\lfloor \cdot \rceil$	Rounding to nearest integer function
$\lfloor \cdot \rfloor_A$	Modulo operator using scalar A
$de2bi\,(\cdot)$	Decimal to binary integer conversion function
$\lvert \cdot \rvert$	Magnitude of a complex value
$\lvert\lvert \cdot \rvert\rvert$	Euclidean/2-norm
$diag(\boldsymbol{a})$	A diagonal matrix whose diagonal is the vector $\boldsymbol{a}$
$\mathcal{F}_D$	Discrete Fourier Transform (DFT) function
$\mathcal{F}_D^{-1}$	Inverse Discrete Fourier Transform (IDFT) function
$\mathbb{M}$	Modulation function
$\mathbb{M}^{-1}$	Demodulation function
$\boldsymbol{I}_{a\times b}$	a by b identity matrix
$\mathbf{1}_{a\times b}$	a by b matrix whose elements are 1
j	Square root of -1, $\sqrt{-1}$
c_0	Speed of light in a vacuum
$\bar{\boldsymbol{a}}$	FD and TF variables are denoted by a bar above the symbol
$\widetilde{\boldsymbol{a}}$	DD variables are denoted by a tilde above the symbol
$\ddot{\boldsymbol{a}}$	AFD variables are denoted by two dots above the symbol

Acronyms

AFD	Affine Frequency Domain
AFDM	Affine Frequency Division Multiplexing
AM	Amplitude Modulation
AoA	Angle of Attack
AoD	Angle of Departure
ASK	Amplitude Shift Keying
AWGN	Additive White Gaussian Noise
BER	Bit Error Rate
bpcu	Bits Per Channel Use
BPSK	Binary Phase Shift Keying
BS	Base Station
CCDF	Complementary Cumulative Distribution Function
CD-OFDM	Code-Division Orthogonal Frequency-Division Multiplexing
CDMA	Code Division Multiple Access
CDMA-OTFS	Code Division Multiple Access OTFS
CP	Cyclic Prefix
CPM	Continuous Phase Modulation
CPP	Chirp Periodic Prefix
CRB	Cramér-Rao Bound
CRLB	Cramér-Rao Lower Bound
CSI	Channel State Information
CSK	Code Shift Keying
CSS	Chirped Spread Spectrum
DAFT	Discrete Affine Fourier Transform
DCT	Discrete Cosine Transform
DD	Delay-Doppler Domain
DD-CDMA-OTFS	Delay Doppler Code Division Multiple Access OTFS
DFRC	Dual-Function Radar and Communication
DFT	Discrete Fourier Transform
Dl-CDMA-OTFS	Delay Code Division Multiple Access OTFS
DMMSE	Distortion Minimum Mean Square Error

Dp-CDMA-OTFS	Doppler Code Division Multiple Access OTFS
DPSK	Differential Phase Shift Keying
DS-UWB	Direct Sequence Ultra Wide Band
DSP	Digital Signal Processing
DSSS	Direct Sequence Spread Spectrum
E_b/N_0	Energy per bit over Noise power
EXIT	EXtrinsic Information Transfer
FAR	Frequency-Agile Radar
FD	Frequency Domain
FD-ZF	Fully Digital Zero-Forcing
FDA	Frequency-Diverse Array
FH	Frequency Hopping
FMCW	Frequency Modulated Continuous Wave
FSK	Frequency Shift Keying
GPS	Global Positioning System
HAD	Hybrid Analogue and Digital
IDFT	Inverse Discrete Fourier Transform
IFFT	Inverse Fast Fourier Transform
i.i.d.	Independent and Identically Distributed
IM	Index Modulation
IM-OFDM	Index Modulation Orthogonal Frequency-Division Multiplexing
IoT	Internet of Things
IQ	In-phase and Quadrature-phase
ISAC	Integrated Sensing and Communication
ISI	Inter-Symbol Interference
JCAS	Joint Communication and Sensing
JCR	Joint Communication and Radar
JRC	Joint Radar and Communication
LDPC	Low-Density Parity-Check
LEO	Low Earth Orbit
LFM	Linear Frequency Modulation
LLR	Log-Likelihood Ratio
LoS	Line of Sight
MF	Matched Filter
MI	Mutual Information
MIMO	Multiple Input Multiple Output
MISO	Multiple Input Single Output
ML	Maximum Likelihood
MMSE	Minimum Mean Square Error
MSE	Mean Square Error

MSK	Minimum Shift Keying
MUSIC	MUltiple SIgnal Classification
NDA	Non-Data Aided
NLoS	Non-Line of Sight
NOMA	Non-Orthogonal Multiple Access
ODDM	Orthogonal Delay-Doppler Division Multiplexing
OFDM	Orthogonal Frequency-Division Multiplexing
OFDMA	Orthogonal Frequency-Division Multiple Access
OTFS	Orthogonal Time Frequency Space
OTSM	Orthogonal Time Sequency Multiplexing
PAPR	Peak to Average Power Ratio
PM	Phase Modulation
PSK	Phase Shift Keying
PSLR	Peak to Side Lobe Ratio
QAM	Quadrature Amplitude Modulation
QPSK	Quadrature Phase Shift Keying
RadCom	Radar and Communication
RCC	Radar and Communication Coexistence
RDF	Radio Direction Finders
RF	Radio Frequency
RIS	Reconfigurable Intelligent Surface
RMSE	Root Mean Square Error
RSC	Recursive Systematic Convolutional
SC-FDMA	Single Carrier Frequency-Division Multiple Access
SCMA	Sparse Code Multiple Access
SD	Spectrum Division
SDFT	Symplectic Discrete Fourier Transform
SDMA	Space Division Multiple Access
SDR	SemiDefinite Relaxation
SE	Spectral Efficiency
SER	Symbol Error Rate
SINR	Signal to Interference and Noise Ratio
SNR	Signal to Noise Ratio
SS	Spread Spectrum
TD	Time Domain
TDD	Time Division Duplex
TDMA	Time Division Multiple Access
TF	Time Frequency Domain
UAV	Unmanned Aerial Vehicle
UE	User Equipment
ULA	Uniform Linear Array

URC	Unity Rate Convolutional
ZF	Zero-Forcing

Chapter 1

Introduction

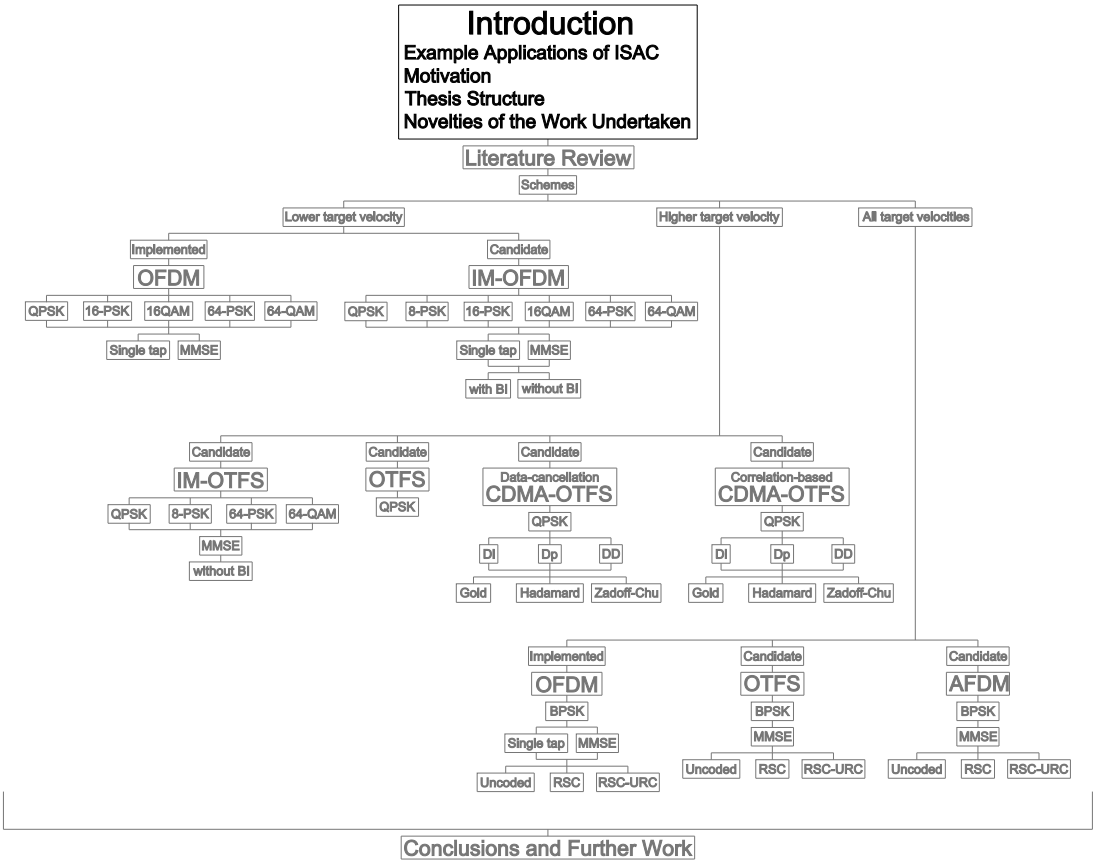

The concept of combining communication and sensing has been hypothesised since before the earliest use of radio. The induction of a signal from one momentarily excited coil to another adjacent coil had been illustrated by Prof. Joseph Henry in the 1830's [4]. The signal intensity was observed to be a function of the alignment of the coils, and thus in 1891 Prof. John Trowbridge proposed the use of large coils erected in the rigging of ships, which could be used to signal between two adjacent vessels in conditions of poor visibility using vessel-specific musical notes. These would be created by high frequency

interruption of the connection between the battery and the coil on the transmitting vessel, thereby identifying that vessel.

He proposed that, if the coil on the receiving vessel could be made to rotate, the direction to the transmitting ship could be also detected by the receiving vessel [5]. The physics of induction over suitable distances made this an impractical system, but the understanding of a dual use of the signal for both sensing and communication is clear. The demonstration of communication by radio by Guglielmo Marconi just four years later made this a practical proposition, and radio direction-finding systems were rapidly developed and deployed within the next 10 years. John Stone Stone is credited with the first patent of an effective Radio Direction Finders (RDF) system in 1902 as part of a group of three patents on tuning, whilst Lee de Forest, after some false starts, was also a significant contributor [6], being the first to propose measuring the attenuating signal strength to estimate distance as well as direction, coining the term ”wireless range finder”.

Early systems were basic directional sensing of analogue communication signals, which permitted some information about the signal source location even if the communication itself was encrypted. This was shown to be useful during the first world war, when changes in direction of an enemy communication signal could be combined with other intelligence to predict the mobilisation of an enemy asset, permitting the prompt dispatch of forces to intercept [7]. Direction-sensing equipment was refined between the world wars, permitting rapid and automated direction attainment. These would continue to use communication signals from known locations to triangulate a position, but as use became ubiquitous for ships and aircraft, networks of dedicated transmitting beacons were developed.

The signal from these dedicated beacons was primarily for direction sensing, but the signal from each beacon was customised with data added to directional signals for identification and meteorological information. Development was rapid, with bi-directional communication added, flight control information, landing controls, and anti-jamming systems. Detection techniques were improved so that both range and direction could be determined using a variety of techniques such as Doppler shift, frequency-based attenuation, signal time-of-flight, and interference between line-of-sight and reflected signals [6].

The use of reflected radio signals for sensing passive targets had been considered a possibility since Heinrich Hertz had shown that radio waves were reflected by metallic objects in 1887/8 [8]. Christian Hülsmeyer is considered the inventor of RADAR as, in 1904, he had a working device that could detect the return of a transmitted signal to indicate the direction to a reflective object up to 3km distant. The signal did not contain any data, so timing of the return signal was not possible, and he proposed to determine range by mounting the system on a tall tower, and scanning the horizon in

a vertical plane. The distance to the object could then be ascertained by triangulation using the angle at which the return signal was strongest. He intended the system to be used to detect ships to avoid collision. However, sea trials amongst ships that were, by this time, using radio for communication, meant that the reflected signal could not be differentiated, and the project was ultimately abandoned [9]. This illustrated that the signal must have some data content so that it could be identified amongst the already widely utilised spectrum.

RADAR systems improved during the inter-war years with data added in the form of pulse-modulated signals on a carrier wave providing both timing for distance estimation, and signal identification. By 1935 several countries had military-funded ground-based functioning systems for detection of aircraft and ships, and by the start of the second world war there were ship-borne and aircraft-mounted systems also available [10]. These developments tend to be poorly documented contemporaneously due to security concerns.

The modern understanding of ISAC, using digital signal processing, dates back to the 1960s. The requirement for ISAC has become more apparent in recent years as the spectrum has become more congested due to the increase in wireless devices and the data they produce. Conveniently, this has also become more viable due to improvements in technology, and similarities brought about by the convergence of the sensing and communication protocols [11].

1.1 Example Applications of ISAC

This field is likely to be a fundamental component in the development and exploitation of the future Internet of Things (IoT) environment. The number of connected devices is expected to increase from 19 billion in 2019 to 30 billion in 2030 [12]. In addition, the capabilities of each device will continue to expand, which will in turn increase the volume of data transmitted and received by each device. A large proportion of these devices will also be required to sense the locations of other devices, and objects both animate and inanimate.

The applications for this technology are wide ranging ([13]) and many will be critical for the maintenance of social and environmental standards. Additional examples of these include improved agricultural productivity, and the maintenance of social and cultural interactions whilst minimising the negative consequences, such as travel and inefficient utilisation of resources. There are obvious military applications for this technology, but these pale in comparison to the potential benefits that this could offer in the civilian sphere.

FIGURE 1.1: Example of robotic agricultural machinery that can benefit from ISAC, © Naïo Technologies, https://www.naio-technologies.com/en/home/

Using agriculture as an example, this technology will facilitate the use of small autonomous machines, such as that shown in Figure 1.1, to be capable of interacting with each other and their environment in sophisticated ways, allowing a step change in agricultural management. Such small machines permit the reduction or elimination of fertilisers, pesticides, herbicides and desiccants, essential given the changing regulatory requirements, e.g. [14], [15]. They allow efficient agriculture to move away from large monocultures, and allow breeding programs to focus on the quality of the product rather than processing limitations. They greatly reduce the energy input, water requirements, soil compaction, and the human burden, whilst at the same time opening up land for production that was previously unviable.

These changes will revolutionise, not just evolve, current agricultural practices, reversing the direction of development from mass production of reduced varieties to targeted production of a wide range of different produce in a competitive and sustainable manner. The reduced manual requirements will be critical, given the current trends in rural demographics (e.g. [16]), where manpower limitations will become critical as a shrinking working population seeks to sustain a disproportionately large retired cohort. The necessary technologies are already in place (e.g. [17–24]), the missing component is the interconnection between them [25]. In particular, the need for such machines to sense their local environment, sense the location of, and communicate with, their peers, and communicate in real time with sources of big agri-data to provide optimised, plant-by-plant interventions, will create a significant burden on the available bandwidth, given that many hundreds of small machines may be mobilised into an area where one large machine currently operates.

1.2 Motivation

The motivation of the work described in this Thesis is to investigate different communication waveforms, and characterise their performance when used for both communication and sensing. This then enables the identification of the relevant trade-offs between communication and sensing performance, which in turn aids in determining the conditions in which these different waveforms could be utilised. Since each application will have a different balance of requirements between communication and sensing, it is anticipated that no one single waveform will be optimal for all applications. Communication waveforms are investigated due to their widespread use, as there are many more communication systems in use compared to sensing systems.

A variant of the widely implemented OFDM waveform is first studied. The aim of the research on this waveform is to create an algorithm that would allow IM applied to OFDM to outperform OFDM for both sensing and communication. For the second system, the more recently proposed OTFS waveform was investigated, due to its greater resilience to Doppler shifts. The aim of the research is to generate a multi-user method for OTFS that allows for an improved sensing performance, whilst not negatively impacting the communication performance relative to single-user OTFS. Finally, the last system considers AFDM, a new waveform which possesses a higher resilience to Doppler shifts compared to OFDM. The aim of this research is to detail and analyse the performance of coded and uncoded AFDM, OTFS, and OFDM, using iterative channel equalisation and decoding methods, to identify the conditions in which AFDM would outperform OTFS and OFDM.

1.3 Thesis Structure

A literature review of the current work undertaken in ISAC has been presented in Chapter 2. Section 2.1 is a review of some of the earliest work and systems using both communication and sensing. Literature detailing trade-offs and foreseen advantages of ISAC are then discussed in Section 2.2. Papers on beamforming, beam sharing, beampattern and precoding optimisation are considered in Section 2.3. Data embedding methods in radar waveforms are discussed in Section 2.4, with communication waveforms used for sensing reviewed in Section 2.5. The use of frequency IM in ISAC is detailed in Section 2.6. Publications on Non-Orthogonal Multiple Access (NOMA) ISAC are considered in Section 2.7.1. Overviews of Reconfigurable Intelligent Surface (RIS)-aided and Low Earth Orbit (LEO) ISAC are presented in Sections 2.7.2 and 2.7.3.

The work undertaken is presented in Chapters 3-5. The first component focuses on the well established OFDM communication waveform in Chapter 3. IM applied to OFDM for both communication and sensing is investigated. FD IM is employed, as it reduces

the TD PAPR of the OFDM signal, and increases the transmit power on the activated subcarriers through power redistribution. The work presented has been published in [1]. An introduction is presented, which contains a brief background to the subject, the research problem and motivation behind the work, as well as a comparison of this work with others, highlighting this work's novelties. The system model is introduced, describing the transmitted signal, the channel models, the received signal processing, and a complexity analysis of the system. The simulation results are then presented and discussed, followed by the conclusions.

The second component focuses on the newer OTFS waveform in Chapter 4, which is designed to be less affected by the Doppler shift induced by large velocities. The merger of CDMA and OTFS is investigated, which allows for a simple multi-user communication methodology, which also reduces the variability in the transmit signal characteristics relative to OTFS, thereby aiding sensing. This is in contrast to the newer SCMA multi-user method, which increases the variability in the transmit signal characteristics. The CDMA-OTFS ISAC work has been published in [2]. The structure of this Chapter is similar to that of Chapter 3. The introduction provides a brief background to the subject, the research problem, the motivation behind the work, as well as a comparison of this work with others, highlighting this work's novelties. The system model is presented, with an analysis of the additional complexity imposed on the system by the multi-user communication and sensing methodologies. The simulation results are then presented and discussed, followed by the conclusions.

The third component focuses on the recently proposed AFDM waveform in Chapter 5. This waveform is a generalised version of OFDM, which can be tuned to possess characteristics and performance similar to OTFS, whilst remaining a single dimension waveform. This work has been submitted for publication. The combination of channel coding and soft-MMSE for AFDM is investigated, and the performance is compared to the older OFDM and OTFS waveforms. The structure of this Chapter is similar to that of Chapter 4. The introduction provides a brief background to the subject, the research problem, the motivation behind the work, as well as a comparison of this work with others, highlighting this work's novelties. The system model is presented, with an analysis of the additional complexity imposed on the system by the multi-user communication and sensing methodologies. The simulation results are then presented and discussed, followed by the conclusions.

The conclusion and future work are discussed in Chapter 6. The conclusions are reiterated in Section 6.1, with the proposed future work shown in Section 6.2.

1.4 Novelties of the Work Undertaken

The novelties of the IM-OFDM ISAC work, presented in Chapter 3, are outlined below:

- This is the first identified published work to demonstrate that IM-OFDM sensing can outperform OFDM sensing. IM-OFDM can do so whilst also outperforming OFDM in communication.
- A novel low complexity algorithm is conceived to "fill in" the "holes" in the sensing data created by IM-OFDM, whilst taking advantage of the increased subcarrier power gleaned from activating fewer subcarriers. This allows IM-OFDM sensing to outperform OFDM, with a slight increase in delay. As OFDM sensing assumes a low-Doppler environment, the impact of this sensing delay increase is negligible.
- An analysis of the impact of block interleaving and Quadrature Amplitude Modulation (QAM)/PSK on sensing performance of the symbol cancellation method.

The novelties of the CDMA-OTFS ISAC work, presented in Chapter 4, are outlined below:

- A detailed analysis of CDMA-OTFS in the context of ISAC is provided, where both fractional delay indices and fractional Doppler indices are considered.
- An in-depth analysis of the communication BER and sensing RMSE performance of delay only, Doppler only, and delay-Doppler sequence spreading for CDMA-OTFS.
- This work demonstrates that Zadoff-Chu Dl-CDMA-OTFS and DD-CDMA-OTFS are the configurations that consistently outperform pure OTFS sensing, whilst maintaining a similar communication performance at the same throughput.

The novelties of the iterative coded soft-AFDM work, presented in Chapter 5, are outlined below:

- Firstly, a parametric study of the communication performance of OFDM, AFDM and OTFS in doubly selective fading is performed for both coded and uncoded transmission. Multiple OTFS and AFDM configurations are investigated, since the existing publications tend to compare AFDM to OTFS with different subcarrier spacings and/or bandwidths.
- Secondly, a soft-MMSE equalisation method that is applicable to OFDM, AFDM and OTFS in an iterative turbo receiver architecture is proposed, that exchanges extrinsic information between the demapper and the channel decoder. Soft-MMSE refers to the holistic MMSE solution that updates its MMSE weighting matrix based on both the channel condition and the *a priori* probabilities gleaned from the channel decoder. EXtrinsic Information Transfer (EXIT) chart analysis is performed to investigate the performance of RSC-coded OFDM, AFDM and

OTFS. Moreover, URC coding is harnessed in order to improve the decoding convergence.

- It is demonstrated that for low-complexity transceivers having high coding rates, AFDM configurations exhibit a lower BER than their OTFS counterparts. Hence AFDM is better suited to low-complexity systems than OTFS at significant velocities.

Chapter 2

Literature Review of ISAC

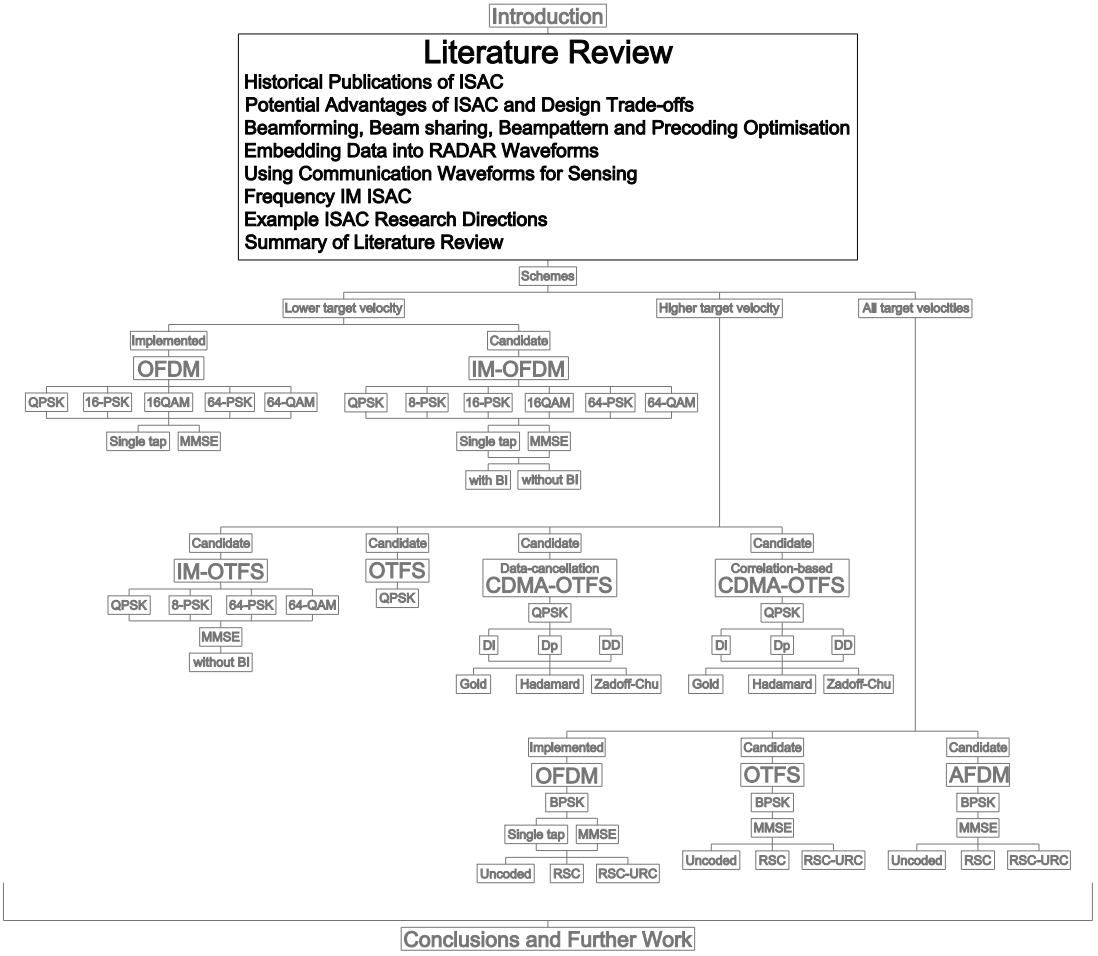

This chapter provides a critical survey of the ISAC literature. Section 2.1 is a review of some of the earliest work and systems using both communication and sensing. The literature detailing trade-offs and foreseen advantages of ISAC is then discussed in Section 2.2. Papers on beamforming, beam sharing, beampattern and precoding optimisation are considered in Section 2.3. Data embedding methods in radar waveforms

are then discussed in Section 2.4, with communication waveforms used for sensing reviewed in Section 2.5. The use of FD IM in ISAC is detailed in Section 2.6. Publications on NOMA ISAC are considered in Section 2.7.1, while overviews of RIS-aided and LEO ISAC are presented in Sections 2.7.2 and 2.7.3, respectively.

2.1 Historical Publications on ISAC

The potential to harness radio signals for sensing was recognised from the earliest use of radios for communication in the late 19th century, with a variety of systems in use by the early 20th century [26]. The military and commercial possibilities of this combination were also understood, leading to a dearth of contemporary sources outside of patent applications, but some reviews of this period are also available (e.g. [27,28]). The first operational navigation aids were direction finders, whereby a directional aerial is used either to transmit a radio signal, or to detect the heading towards an omni-directional radio source. Typically, the source would be transmitting data, initially in the form of Morse code, to identify the source and improve angular resolution.

These analogue systems rapidly developed to include bi-directional communication, triangulation, and Doppler shift sensing to provide both range, direction, and communication functions. Combining these with systems such as the Hellschreiber [27] permitted semi-automation of the sensing function and crude guidance indicators, along with improved communication. Whilst spectrum occupancy was not an issue in the early years, covert use of communication signals for sensing reduced jamming efficacy.

Similar systems, capable of utilising commercial Amplitude Modulation (AM) radio transmitters, remained standard equipment on aircraft until displaced by LORAN-C and Global Positioning System (GPS) at the end of the 20th century. Dedicated digital RDF systems are still used for aircraft approach and landing control, as well as for marine applications [29]. As the arms race prior to World War 2 commenced, research focus expanded to include radar sensing of passive targets, relying on a sensing-only function initially, but then communication components were rapidly added as counter-counter-measures.

The modern concept of ISAC has been in published scientific literature since at least 1963, with [30] detailing a system sending communication pulses on the radar pulse interval to convey information from a Base Station (BS) to vehicles for one way communication. The authors base the system on the capabilities of missile ranging equipment of the time, and also calculate the pulse code group and word error probabilities of the communication system.

The system has five pulse slots available per bit of information sent. The first two are interrogation signals, with the second being a reference signal. A pulse is transmitted

on the first of the three data slots when the information bit is 0, with a pulse on the second slot for a bit of 1. A pulse is sent on the last data slot to indicate the start of a word. The throughput of this early ISAC system is therefore low, as the rate of communication is dictated by the radar pulse interval, and only one bit is transmitted per pulse code group.

2.2 Potential Advantages of ISAC and Design Trade-offs

This section presents the trade-offs and potential advantages of ISAC as discussed in the literature.

2.2.1 Potential Advantages of ISAC

Some of the anticipated advantages discussed [31–33] include:

- *Integration gain*: integrated hardware can lower costs, reduce size [34] and increase energy efficiency, which reduces the amount of equipment on vehicles, both military and civilian [35]. An integrated system optimises both sensing and communication, and hence it can improve the Spectral Efficiency (SE) more efficiently [36]. Software defined radio relies on general signal processing hardware, instead of specialised circuits. Similar available hardware can be used for ISAC. However, these need to be improved as reconfiguration operations are time consuming. In the future, ISAC could be integrated on a chip, which could achieve high integration and coordination gains [37]. This hardware integration would diminish, and possibly dispense with, the need to isolate antennas from each other, as they would perform both functionalities.

- *Minimising spectrum congestion* [38], which is predicted to increase as the number of distinct communicating and sensing devices increases. The hardware integration leads to spectrum sharing and optimisation, hence reducing spectrum congestion.

- *Coordination gain*: sensing estimates can be used to improve the communication performance, and vice versa. For sensing-aided communication, the sensing parameters form a part of the Channel State Information (CSI), which can then be integrated into the channel estimation method to reduce the total computational burden, and potentially reduce the communication channel equalisation error. The estimated sensing parameters can also be utilised to improve the beamforming accuracy of the communication transmission. For communication-aided sensing, communication is utilised to transmit sensing information, to improve the

whole sensing system performance. For example, a distributed sensor arrangement can communicate with a centralised BS, which processes the information, and can then use the estimates to direct the sensors. Coordination gain also allows for full exploitation of the available degrees of freedom [39, 40].

These gains would allow for improved communication between equipment, due to the sensing aiding the beamforming algorithms, and improved reaction to changes in environment for both manned and unmanned vehicles. The hardware integration would be facilitated by the convergence of communication and radar requirements [32], such as high power, directionality, and resistance to interference, which result in improved quality, security and range.

There is also some signal processing [33] and hardware [41] convergence between communication and sensing. An example is the proliferation of Multiple Input Multiple Output (MIMO) and massive MIMO systems [33]. The shared advantages of MIMO for communication and sensing are [41]: spatial diversity [42, 43], and flexible adaptive beamforming [43, 44]. MIMO schemes also allow for communication spatial multiplexing [42].

When there are multiple antennas that are sufficiently spaced, the fading channels between each antenna and the target are independent of each other. This allows the communication system to improve the diversity gain, which reduces the outage probability [42]. Similarly, this allows a radar system to obtain many independent observations of a target, increasing the detection reliability of the system [43].

The independent paths offered by MIMO antennas can also be exploited to increase the throughput of the system through spatial multiplexing. As such, a communication system must consider the trade-offs between the spatial diversity and multiplexing, which are shown in [42], along with various spatial Digital Signal Processing (DSP) schemes.

The increased number of antennas also allows for directional beamforming, to one or more targets. For communications, this can allow the system to use available power more effectively, as less energy is transmitted in undesirable directions. More details on beamforming for mobile communications can be found in [44]. For radar, beamforming can improve detection reliability, as more power is focused in the target direction, reducing the number of reflections from other scatterers that are not of interest. More details on adaptive waveform modulation can be found in [43].

There are also suggestions that transmission performance is improved by the combination of radar and communication, which then provides advantages for radar [32]. It is also asserted that Joint Radar and Communication (JRC) will improve automation levels of dual-function systems. These claims may be of questionable value since most suggested advanced functionalities could be achieved through suitable external control

of separate systems. Further research, especially of an experimental nature, is required to comprehensively validate these claims.

These potential advantages are leading to an increased number of commercial entities investing in ISAC [33], with WiFi sensing being studied for indoor sensing.

2.2.2 Different Types of Communication and Radar Integration

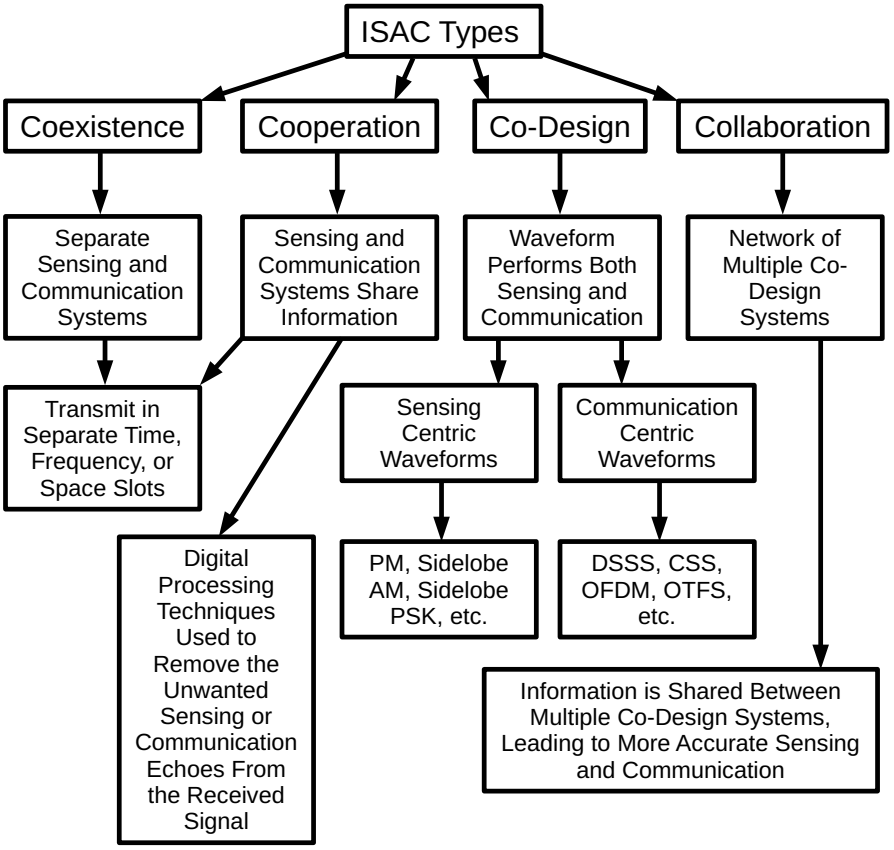

FIGURE 2.1: Summary of the different possible relationships between radar and communication

A range of different possible relationships between radar and wireless communications are proposed [32, 39]. These are shown in Figure 2.1, and are summarised below:

- *Coexistence*: radar and communication are isolated and treat each other as interference [45].
- *Cooperation*: radar and communication are independent but exploit joint knowledge [46].
- *Co-design*: joint unit which integrates both radar and communications [46].
- *Collaboration*: network of joint units that work together to fulfil tasks.

These have increasing levels of complexity in their design and implementation. Coexistence and Cooperation are sometimes bundled into Radar and Communication Coexistence (RCC), with systems based on co-design and collaboration defined as Dual-Function Radar and Communication (DFRC) schemes [39].

Coexistence is the current regime of radar and communication. Research has quantified the effects of radar on communications and vice-versa [47–56]. This has shown that separate time bands, frequency bands and/or spatial separation are required for communication and radar to coexist. For example, opportunistic spectrum access can be implemented, where the communication system transmits and receives when the spectrum (time/frequency/space resources) is not being used by radar. This is of limited applicability when MIMO radar is used, as it transmits near-continuously and omnidirectionally.

Interference cancellation schemes can be applied to mitigate the interference imposed by communication and radar waveforms on each other. The interference channel can also be estimated and this knowledge may be exploited to mitigate the interference, but to a limited extent, especially for coexistence-based systems [57, 58]. Closed form precoder designs are able to eliminate the interference, e.g. using null-space projections, but at the cost of potentially severe performance degradation. MIMO aided radar and communication schemes, where some antennas and receivers are used for communications and some for radar, selected in a way to avoid interference between them, have been considered [59]. Due to the increase in bandwidth and throughput demand for communications, there is a need for a more refined system.

Cooperation is the next step in which data from radar and communications work together to improve both systems. Interference between the systems persists, such as high power signal from radar drowning out the communication signals, or the communication signals interfering with radar echoes. Since both systems communicate with each other, radar echoes can be more easily distinguished from communications. Adding pilot symbols to communication signals, or developing other processing methods, help mitigate the interference [60]. MIMO radar and communications working together can improve performance of both systems [61].

The processing and precoding techniques employed for coexistence can also be applied to a greater extent to cooperation, as the communication and radar systems share information. This usually requires a control centre exchanging information with the radar and communications systems, which requires additional equipment, so it can be slow, bulky and expensive. This shared information can allow for an increased level of optimisation of signaling methodologies and beamforming, at the cost of increased computations [39].

Co-design offers further benefits [39]. As a single system performs both functionalities, greater optimisation of the resources and information is possible. By treating radar

targets as "virtual" communication users and vice versa, generalised beamforming algorithms can be utilised to improve the system performance, by leveraging sensing information for communication and vice versa.

Instead of the opportunistic spectrum access seen in coexistence, the same waveform can be used and tuned for both communication and sensing. MIMO radar can be applied in conjunction with Space Division Multiple Access (SDMA), transmitting the communication data in the radar sidelobes using Amplitude Shift Keying (ASK) or PSK [62]. The CSI can be estimated by the sensing and communication algorithms, which is then be shared and leveraged by both functionalities to improve their respective performances [33].

Feng *et al.* [32] note that the definitions of cooperation and co-design are somewhat blurred in the literature, with some researchers considering system functionality and others considering the design philosophy of the waveform to define the characteristics of their work.

Collaboration is the next step after co-design. When multiple co-designed systems must operate simultaneously, the potential for interference, similar to that observed for coexistence systems, remains [32]. Consequently, these systems have to collaborate to minimise this interference potential. However, collaboration also offers significant further benefits other than simply avoiding interference. These include the ability to combine systems to improve location estimation, extend sensing range, reduced data duplication, lower transmit power, etc. Little research has been done in this area.

Considering the requirement for further research, coexistence has already been extensively studied, and is reasonably well understood, as it is what is currently used commercially [32]. Cooperation has been widely researched, although there remains uncertainty as to how widely it has been implemented. Co-design is the next step that appears to be useful commercially. There is an increasingly large body of research in this area, but more in-depth studies are required to improve the current knowledge, for example, studying effects on multiple different types of channels, etc. Cooperation has relatively little research done, and potentially is the area that will offer the largest improvement in performance and functionality.

2.2.3 Overview of Waveform Co-design

2.2.3.1 Radar Centric Designs

Radar centric schemes use an existing radar waveform, with communication functionalities added to it [41]. Hence, the radar functionality is the primary function [33].

Examples of communications methods for these schemes are the use of waveform diversity for transmitting data [63], sidelobe AM [64], the combination of waveform diversity and AM [65], Phase Modulation (PM) [66], and ASK [62,67]. Adding communication signals into sidelobes of radar using beam control or waveform diversity leads to reduced SNR [32]. A similar system can be used along with MIMO arrays having varying frequencies for greater benefit. Embedded RF stenography schemes in radar signals can be used to conceal information [68]. These methods can offer high security at low data rates, and hence may be useful for military applications.

Other radar centric methods [41] include using different sets of Frequency Hopping (FH) codes to embed information [69], using FD IM with FH [70], or modulating information onto each hop, specifically PSK [71], coded PM [72], Frequency Shift Keying (FSK) [73] and Continuous Phase Modulation (CPM) [74] may be used. The authors of [73] also shows that the radar performance of a combination of FSK and PSK outperforms either stand-alone scheme. IM has little effect on radar performance, but allows for higher data rates than other modulation systems [75]. In contrast to the other methods, IM is complex to demodulate, and accurate channel estimation is essential for demodulation. To mitigate some of the effects of noise, specific sets of constellation points with large enough Euclidean distances need to be defined.

Linear Frequency Modulation (LFM) systems can also be employed for DFRC, e.g. in combination with Minimum Shift Keying (MSK) or CPM [76]. LFM and CPM with modified mapping codebooks can reduce the loss caused by the attenuation of the radar power amplifier and interference from other sources [32]. LFM DFRC systems are simpler to implement as there is already existing hardware, but require signal separation, which can be complex. LFM systems also suffer from low transmission rates and poor parameter flexibility.

These radar centric schemes provide a minimal communication performance, as they have low data rates, and tend to only communicate with a small number of users [39, 41]. The communication data of most of these methods can only be demodulated and decoded when there is Line of Sight (LoS) between the transmitter and receiver. For non-LoS cases, using the communication waveforms for target detection is preferred. More information on radar centric schemes in Section 2.5.

2.2.3.2 Communication Centric Designs

In communication centric schemes, communication is the primary function, with sensing performed using the communication waveform [32, 33]. Direct Sequence Spread Spectrum (DSSS) for Joint Communication and Radar (JCR) is investigated in [77]. This

scheme provides security, robustness, robust anti-jamming capabilities, can ensure orthogonality between radar and communication, and is already used in communications. The use of pseudo-noise codes can help reduce the likelihood of mutual jamming. Variations, such as Direct Sequence Ultra Wide Band (DS-UWB) and Chirped Spread Spectrum (CSS) have also been investigated [78]. These schemes have low data rates for communication systems, and require that the orthogonality needs to be maintained.

Other communication centric systems rely on Golay complementary sequences, which are embedded into the preamble of a single carrier frame IEEE 802.11ad [40], and OFDM, which is widespread in communications [32]. Using OFDM with interference cancellation methods improves Signal to Noise Ratio (SNR) [79, 80]. OFDM has good directionality but has high PAPR, which causes waveform distortion and therefore reduces the maximum detectable radar range [81]. OFDM is continuous, so if used for radar, good isolation of antennas is required, which can be expensive. Pucci *et al.* [82] analyse a system in which the available OFDM subcarriers are split into communication and sensing groups, with the trade-off between sensing and communication power allocation being considered. The authors state that the effects of imperfect conditions on the sensing performance still need more research, as they have yet to be fully explored.

MIMO OFDM can reduce the PAPR of OFDM and the sidelobe cross-correlation, and MIMO radar has higher resolution and range than classical radar [32]. Combining MIMO radar and communication improves throughput, but leads to an increase in clutter and interference in the receivers. MIMO OFDM JCR can partially mitigate these issues, leading to higher data rate for communications and angular resolution for radar. An illustration of a network in which the sensing signals would be used, along with an example of a MIMO OFDM DFRC transceiver, are shown in Figure 2.2, taken from [75].

More information on communication centric schemes is provided in Section 2.5.

2.2.3.3 Joint Design

Joint design tends to rely on novel waveforms that are designed to achieve both communication and sensing functionalities [33]. These are typically formulated as optimisation problems. Zhang *et al.* [75] provide examples of such designs. These include optimisation in time and frequency domains, an example of which is non-uniform spacing of subcarriers in OFDM, or waveform optimisation via spatial precoding optimisation, which can be Mutual Information (MI) based, waveform or beampattern similarity based, and estimation accuracy based.

There are also multi-beam analogue arrays [83–85]. These can allocate separate fixed direction sub-beams for communication and scanning subbeams for sensing [83, 84]. Alternatively, dynamic sub-beam allocation for both communication and sensing can be implemented, which is simple and flexible. This is beneficial for rapidly changing

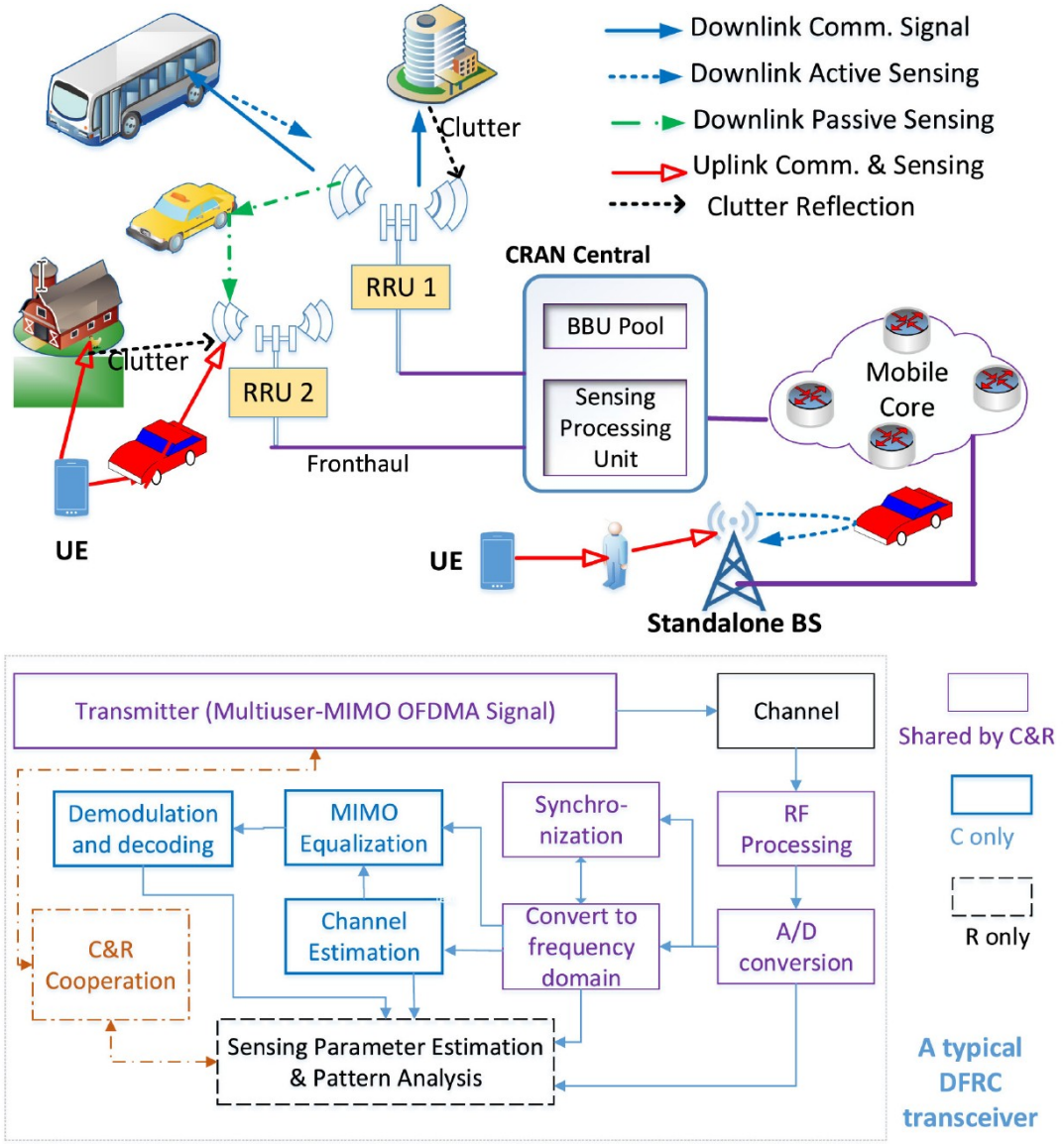

FIGURE 2.2: Illustration of a DFRC network in which the sensing signals would be used, along with an example block diagram of a MIMO OFDM DFRC transceiver, taken from [75]

conditions, but is sub-optimal. The largest multi-beam optimisation problems consider global optimisation [85], which yields an optimal system, but is typically complex and therefore is more difficult and time consuming to solve. This method provides a good benchmark for the dynamic subbeam allocation optimisations.

Array optimisation can be applied to the specific configuration of antennas [41]. A JCR system in can allocate separate antennas, and mainly focus on reducing the mutual interference between radar and communication [59, 86–89]. Integrated systems utilising the all antennas for both communication and sensing functionalities, but separate Radio Frequency (RF) chains can also be employed [90–94]. Completely integrated systems have also been investigated [95–100], details on which can be found in subsequent

sections of this chapter.

Feng *et al.* [32] carry out a study considering the performance of a joint system, characterised by the total volume of detection for multiple radars in communication with each other. The power allocated to the communication component was varied, and the results showed that a small amount of power allocated to communication increases the volume of detection, but that any further increase in the power allocated to communication decreases the volume of detection, as would be expected. The small initial improvement peaks at a communication power fraction of 0.1, but net gains are seen up to a communication power fraction of 0.5, compared to the scenarios with no communication. This would suggest that there is significant capacity for communication without impacting radar performance.

They also quantify the benefits of utilising radar to assist in the determination of the communication target locations in a wireless network. The results show that the number of time slots required to detect all the targets in the network is significantly reduced.

Insufficient details are provided on the basis for these studies, so further comment is not possible. Other examples for potential collaboration are given. Feng *et al.* [32] conclude that significant benefits can be derived by the combination of radar and communication, with collaboration being key to maximising these benefits.

2.2.4 Design Trade-offs

2.2.4.1 Performance Metrics

To characterise the performance of ISAC systems, bespoke metrics must be utilised. These metrics can be broadly split into three categories: communication-only metrics, sensing-only metrics, and shared metrics. Communication-only metrics include:

- **Bit Error Rate (BER)**: the BER is the number of errors in the estimated information bits divided by the number of information bits transmitted [1,2]. The Symbol Error Rate (SER) is also utilised [71, 101], which is the number of incorrectly estimated symbols divided by the total number of symbols transmitted. The BER is more commonly used. Both metric are unitless.
- **Achievable rate**: the maximum effective data throughput that can be transmitted [102, 103]. The effective data is the data that the transmitter can successfully estimate. It is partially proportional to the SNR/Signal to Interference and Noise Ratio (SINR). The units utilised in publications are bits/Hz/s, or Bits Per Channel Use (bpcu).
- **Outage probability**: the probability that the achievable rate is below the target rate/throughput [42, 104]. The outage probability is unitless.

- **Secrecy rate/secrecy capacity**: the difference between the rate/capacity of the main communication channel and the rate/capacity of the eavesdropper's channel [99, 100, 104]. The units utilised in publications are bits/Hz/s, or bpcu.

Sensing-only metrics include:

- **Probability of target detection**: the probability of successfully detecting a target [105–107]. This metric is unitless.
- **False alarm rate**: the probability that the system/scheme will detect a target that does not exist [108–110]. The false alarm rate is unitless.
- **Target estimation rate**: this metric considers the sensing target to be equivalent to a user who communicates unintentionally. More explicitly, it quantifies the amount of information concerning the target that can be gleaned from the received sensing signal given the specific propagation channel encountered. In other words, it is based on the amount of mutual information between the estimated and true target parameter value [111, 112]. The units utilised in the literature are bits/Hz/s, or bpcu, as for the communication rates.

The shared metrics used for both sensing and communication include:

- **Beam pattern**: it characterizes the specific shape of the transmit or receive beams. For the transmit beam, it may be illustrated by plotting the transmit signal magnitude versus the transmission angle [59, 97]. The magnitude is typically expressed in dB, and the angle in degrees or radians.
- **Peak to Side Lobe Ratio (PSLR)**: the ratio of the power in the main peak of the beampattern to the average power in the sidelobes [36, 113, 114]. This is used to characterise the beamforming performance. This metric is unitless, but it is also commonly presented in dB.
- **Mean Square Error (MSE)/Root Mean Square Error (RMSE)**: used to quantify the estimation of parameters, usually the channel matrix estimate for communication, or the estimation error of sensing parameters, such as the delay/range, Doppler shift/velocity, Angle of Attack (AoA), Angle of Departure (AoD), etc. [31, 39, 115–118]. The units depend on the parameter being estimated, e.g. for range/distance, the units are m^2 for MSE and m for RMSE.
- **Cramér-Rao Bound (CRB)/Cramér-Rao Lower Bound (CRLB)**: the bound of the MSE of the estimation error [40, 119]. The square root of the CRB and CRLB can be taken to obtain a bound for the RMSE. The CRLB is the lower bound [120, 121]. For some systems/schemes, the lower bound is difficult to derive, hence an average bound is derived instead (CRB). Many publication use CRB to refer to the

CRLB. The unit depends on the parameter being estimated, e.g. for range/distance, the unit are m^2.

- **Signal to Noise Ratio (SNR)**: the ratio of the average power of the transmitted signal to the average noise power [122–125]. Additive White Gaussian Noise (AWGN) is the most common noise considered, following a complex Gaussian/normal distribution. The E_b/N_0 is related to the SNR, and it is the ratio of the energy per information bit to the average noise power. SINR is an extension to the SNR, which considers the ratio of the average power of the transmitted signal to the addition of the average noise power and the average interference power [12,87,92]. The SNR and SINR are used for both communication and sensing. The E_b/N_0 is typically only utilised for communication. The SNR, E_b/N_0, and SINR are unitless, but are commonly presented in dB.

All the metrics discussed vary depending on the SNR/SINR, hence most publications will include results for an SNR or equivalent range, or specify an SNR or equivalent value.

2.2.4.2 Fundamental Trade-offs

The fundamental trade-offs of a point-to-point ISAC system in Gaussian channels, given a known pseudo-random waveform, are analysed in [102]. The metrics considered are the CRB and the maximum communication capacity of the system. Two main trade-offs are shown: the degree of randomness of the transmitted signal, and the bias of the received sensing covariance matrix towards the optimal communication or sensing bounds.

The two transmit signal types that represent the randomness extremes are a semi-unitary modulation scheme (e.g. PSK), the least random, and a Gaussian signaling modulation scheme, the most random. A theoretical outer bound of the CRB vs communication rate is also defined. The semi-unitary inner bound follows the theoretical sensing optimal bound, but cannot reach the maximum theoretical communication rate. Gaussian signaling has the opposite performance, as it can reach the maximum communication rate, but cannot achieve the theoretical minimum CRB. A time sharing scheme between semi-unitary and Gaussian signaling is deemed to be attractive as it most closely approaches the theoretical CRB vs communication rate outer bound.

As the sensing covariance matrix becomes more correlated to its communication counterpart, the theoretical outer bound and actual system bound increase. This is achieved in [102] by reducing the bearing angle of the communication receiver with respect to the sensing receiver. The results presented provide a framework for exploring the fundamental trade-offs of ISAC, but are limited in their scope. There needs to be a quantification of the ISAC parameter adjustments in practice. Cui *et al.* [33] is note that most

existing sensing receiver systems do not work well in a rich scattering environment, so ISAC receiver solutions need to be developed with improved functionality. There will be both issues and potential benefits with networks of ISAC devices, and work is required to explore these challenges. Hence, further research is required to derive and document the fundamental trade-offs of ISAC for a larger number of schemes and in a more diverse range of propagation environments.

2.2.4.3 Optimisation Methodologies

Using various performance metrics, such as those outlined in Section 2.2.4.1, optimisation problems can be formulated and solved to improve the performance of ISAC systems. Three types of optimisation problems dominate the literature: optimising communication performance given sensing performance constraints, optimising sensing performance given communication performance constraints, and jointly optimising communication and sensing performance. A problem with only a communication or sensing performance objective function is usually less complex to solve than one that considers both communication and sensing, and hence is more common. Optimising both functionalities allows one to tune the weighting between them, but increases the complexity of the problem.

Most problems are non-convex, which often require complex algorithms to solve. These algorithms generally do not guarantee that a global minima/maxima is obtained. Hence, a common method is to relax certain constraints to create a convex problem, which can then be solved by common algorithms. The solution to this convex approximation is unlikely to be the global optimum of the non-convex problem, but can approach this set of values. Further refinement of the output can be obtained by constructing and iterating between many different convex approximations, for each subset of variables, at the expense of additional computational complexity.

The most common communication metrics used are the communication SNR/SINR and the capacity/rate, as they are simpler to derive theoretically than the BER. For secure applications, the secrecy rate is also considered. The most common sensing metrics are the sensing SNR/SINR and the MSE or CRB. The SNR and SINR are popular choices as most metrics depend on them, hence an increase in SNR/SINR is usually correlated with increased communication or sensing performance. Most optimisation problems also include power constraints, jointly for communication and sensing, or using separate power constraints for each functionality.

The choice of which functionality is placed as a constraint depends on the conditions the system performs under. When resources are scarce, e.g. in small devices or sensors, constraints for the more essential functionality are present, as these must be maintained

at all times, whereas the less important functionality is relegated to the objective function. By contrast, when resources are more abundant, the functionality that is prioritised is included in the objective function so that the performance is maximised, with the secondary function placed as a set of constraints. A more fine-tuned approach can be implemented by specifying weighted metrics for both communication and sensing in the objective function as well as constraints. This method does increase the complexity of the optimisation problem.

2.2.5 ISAC Research Directions

The use of ISAC in conjunction with other emerging technologies has attracted research interest. Fang *et al.* [41] discuss novel combinations of Joint Communication and Sensing (JCAS) and emerging technologies, such as cooperative systems [126,127], dynamic 3D imaging [103,108,128], hybrid active and passive sensing [129–132], and IoT [115,133–136]. The authors of [41] state that IoT ISAC will have some key requirements, which include ubiquity, energy efficiency, and reduced complexity. For ubiquity, Unmanned Aerial Vehicles (UAVs) could be used, such as the systems investigated in [103,108,128]. An alternative would be to use LEO satellites, as advocated in [133]. For energy efficiency, the authors mention that OTFS ISAC, such as [115], is more energy efficient than OFDM ISAC, due to OTFS having a lower PAPR than OFDM.

Fang *et al.* [41] also mention different open issues for JCAS, which include: an integrated space, air and land network, the use of artificial intelligence, the combination of JCAS with computing and control, and security of JCAS systems. There is a concern that the systems may unintentionally give away sensitive information due to spectrum sharing of radar and communications. This has also been studied for civilian applications [99,100,132], but is naturally of more critical interest for military applications [39].

Liu *et al.* [39] note that, at the time of publication, most research is in the sub 6 GHz band, with there being a smaller body of research in 5G DFRC systems. There is a higher cost associated with digital hardware and greater computational costs associated with mmWave transmission and reception, hence there is an attraction to Hybrid Analogue and Digital (HAD) beamforming techniques for massive MIMO DFRC.

2.3 Beamforming, Beam Sharing, Beampattern and Precoding Optimisation

2.3.1 Multiple Input Single Output ISAC

Ni *et al.* [119] have created a pair of waveform precoder optimisation systems for Multiple Input Single Output (MISO) JCR. The proposed systems use a separate single receive antenna for radar sensing to facilitate duplex operation. This single receive antenna is separated from the transmit antennas to avoid any short range leakage effects. OFDM signals are used for communication and sensing, with only downlink communications existing.

Multiple metrics are used for the optimisation of communications and radar. For communication, two SINR expressions are used for optimisation. The first is a SemiDefinite Relaxation (SDR) of the SINR equation of the system, and the second is a rewritten form of the relaxed expression, in which rank reduction is no longer necessary. The latter SINR constraint equation is used in the paper.

For radar, two optimisation metrics are proposed, MI maximisation and the CRB. The maximisation of the MI maximises the channel information in the received radar signal. The CRB is defined as a theoretical lower bound of the estimation errors of the radar target parameters. When the waveform precoder is optimised around the CRB, the Euclidean distance is minimised between the JCR system precoder and the optimal radar precoder.

Both closed-form and iterative algorithms are given. The closed-form solution does not always exist, hence the simulations use the iterative algorithms. These algorithms iterate to the edge of the space created by the constraints, and then towards the tangent between the objective function and the constraint space.

The following assumptions are made:

- The BS uses a Uniform Linear Array (ULA).
- Each User Equipment (UE) has a single antenna.
- The Doppler shift of a given propagation path is invariant in time.

Another waveform precoder algorithm is taken from the literature for comparison, referred to as the weighted-sum JCAS system. The MI and the CRB algorithms have almost identical sum rates, being lower than that of a communication only system, but higher than the weighted-sum JCAS system.

The sensing MI for the MI precoder system is a little lower than that of a radar only system, but higher than that of the weighted-sum JCAS system. The estimation error of the CRB precoder system is a little higher than that of a radar only system, but lower than that of the weighted-sum JCAS system.

Naturally, each optimisation method proposed performs best when using their optimisation criteria as the measure of sensing performance. The paper does not include an independent sensing criterion as a benchmark of the proposed precoder optimisations. Both of these methods present a trade-off between communication and radar.

2.3.2 Multiple Input Multiple Output ISAC

Liu *et al.* [59] develop beamforming techniques for MIMO Radar and Communication (RadCom), where a single device simultaneously communicates and senses. They contrast the performance to that of a similar system in which communication and radar coexist. For coexisting, the beampattern has to meet two conditions, which are to guarantee the SINR level required for communication, and to avoid exceeding the maximum transmit power set. For the shared deployment, an additional condition is required, namely that the generated RadCom beampattern be a close match to the desired beampattern for radar detection.

Initially, the antennas are split into two groups, with set one communicating, whilst the other is used for radar. The interference by the radar signals imposed on the communication signals is removed by Zero-Forcing (ZF). The radar signals are therefore forced to lie within the null-space of the channel between the radar antennas and the communication users. The communication beampattern matches that of the radar. The algorithm to determine the communication beampattern, denoted as separated SDR, follows a procedure outlined below:

- The Rayleigh fading gains, SINR threshold, radar transmit power and beampattern requirement are set.
- The radar covariance matrix is calculated.
- The related optimisation problem is then solved through SDR, removing the rank 1 constraint.
- The rank 1 constraint is then approximated.
- The communication beampattern matrix becomes known.

For the second approach, each antenna is used for both communication and radar. The radar targets are treated as imaginary LoS communication users. The first beamforming

algorithm, termed as shared SDR, follows a procedure similar to separated SDR, and is described below:

- Calculate the radar beampattern.
- Solve the beamforming optimisation problem without the rank 1 constraint through SDR.
- Approximate the rank 1 constraint.
- The RadCom beampattern becomes known.

The problem is then reformulated as a weighted beamforming optimisation problem, which is solved through Riemannian manifold optimisation. Two algorithms, using two different penalty terms, are introduced. The first uses a sum-square penalty, which is introduced into the shared SDR problem. The sum-square penalty is the sum of the squares of the difference between the user SINR and the SINR thresholds specified. The second algorithm uses a maximum penalty system, where the minimum user SINR is maximised. There are both per-antenna power constraint and total power constraint variants of all the shared deployment algorithms.

The following assumptions are made:

- ULA antennas are used.
- Each communication user has a single antenna.
- The propagation channel is a flat Rayleigh fading channel.
- There is perfect channel estimation.
- For separate deployment, communication signals are statistically independent of the radar signals.
- For shared deployment, the communication signal can be used as the radar probing signal.

The results show that the separated SDR beampattern has lower peaks than a radar only system, whilst the shared SDR has higher peaks than the radar only system. For both SDR beampatterns, the PSLR decreases as the SINR threshold is increased, but there is an 8 dB increase in PSLR for the shared system. For all shared deployment algorithms considered, the average PSLR decreases as the average SINR increases, and the results appear insensitive to the specific choice of the weighting method. The total power constraint-based variant has a higher PSLR compared to the per-antenna power constraint variant.

The separated SDR beampattern is infeasible when the number of communication users is larger than the number of antennas allocated to communication, as there are too few degrees of freedom available. This issue is also seen in the shared SDR beampattern, when the number of users approaches the total number of antennas. The penalty algorithm-based beampatterns are always feasible when the number of communication users is equal to or less than the number of antennas.

The MSE of the beampattern produced by the algorithms compared to the optimal radar beampattern increases as the average SINR increases, as would be expected, since a higher communication performance results in a reduced radar performance.

In consideration of the results, it can be concluded that both SDR algorithms suffer from low feasibility, when a large number of users are considered relative to the number of antennas available for communication. The penalty-based algorithms do not appear to suffer from this, although no results are shown when the number of users exceeds the number of antennas. The shared SDR beampattern is better than the separated SDR beampattern, having higher and more distinct peaks, which is associated with an assumed superior radar performance. The shared SDR has a higher PSLR than the separated SDR for a given SINR threshold.

Some disadvantages of the shared SDR algorithm are that it has higher dimensions than the separated SDR algorithm, leading to higher computational loads. It is also difficult to approximate the rank 1 constraint, whilst satisfying strict equality of the per-antenna power constraint for this variant. The relaxed solution cannot take full advantage of the available power.

The penalty algorithms are more efficient than the other algorithms as there is no rank 1 approximation after solving the optimisation problems.

The per-antenna power constraint variants consistently have a lower PSLR and higher beampattern MSE than the total power constraint variants, which is associated with an assumed inferior radar performance.

The paper proposes that further work will consider receiver designs and temporal techniques for the proposed schemes. The authors of [89] propose a new low-complexity beamforming algorithm for a coexistence-based system similar to that shown in [59].

Liu *et al.* [118] design a transmit beamforming-based MIMO DFRC system that seeks to optimise both the radar transmit beam pattern and the SINR at the communication users. The joint transmitter utilises jointly precoded individual communication and radar waveforms. This maximises the degrees of freedom of the MIMO radar waveform. The design is formulated as a non-convex optimisation problem, which is tackled in two ways. The first forms an approximate convex problem through SDR, which is solved using conventional optimisation tools. The second is a ZF-based approach,

which zero-forces the inter-user and radar interference. This circumvents the computational burden of recovering the optimal precoders from the SDR approach.

The following assumptions are made:

- Both the radar and communication signals are zero-mean, temporally-white and wide-sense stationary stochastic processes.
- The communication symbols are uncorrelated with the radar waveforms.
- The communication symbols intended for different users are uncorrelated.
- The individual radar waveforms are generated by pseudo random coding, and are thus considered uncorrelated with each other.

A system using a sum-square penalty problem is simulated for comparison. The transmit beampatterns of the SDR and ZF methods are similar to those of the radar only system. When the number of users is lower than the number of main radar beams required, the benchmark systems cannot match the radar only beampattern. This is due to the decreased radar degrees of freedom of the baseline system. When the number of users is higher than the number of main radar beams required, the baseline system beampattern is similar to that of a radar only system.

When the communication SINR threshold is low, the SDR method is biased towards radar performance, whereas the ZF method leans towards communication performance. As the communication SINR threshold increases, the radar and communication performance of both methods converge, with the radar beampattern MSE and communication sum rate increasing. As the number of communication users increases, the radar beampattern MSE and communication sum rate increase for both methods.

As the number of users is increased, the SINR threshold at which the SDR and ZF optimisation problems become feasible decreases. The problems rapidly become unfeasible above a given SINR threshold. Both methods have identical feasibility curves.

The estimated angle RMSE and detection probability of the SDR method and the benchmark system are similar when the number of users is greater than the number of main radar beams required. When this is not the case, the SDR method outperforms the benchmark system.

It is stated that the SDR method generally outperforms the baseline method, although the results presented show that this appears to only be the case when the number of users is smaller than the number of main radar beams required.

Further work mentioned includes replacing the SINR constraint with a utility function for communication in the optimisation problems to prevent them becoming infeasible.

A multiple-user scenario, in which all users communicate and sense using the same spectrum, is considered in [94]. This system considers both local and off-site computing, with the cost of transferring data to outside systems for computation investigated. The authors of [41] claim that [94] is a pioneer for the study of the combination of ISAC and edge computing.

DFRC designs are proposed in [95] for both omnidirectional and directional radar beampatterns. Weighted optimisations are then developed for these beampatterns, with flexible trade-offs between sensing and communication performance. This system is then further developed in [96], where the sidelobe of the sensing signals is constrained. The results in [96] show that the communication performance is increased when the sensing sidelobe levels are constrained, with a smaller decrease in sensing performance.

Johnston *et al.* [97] consider a DFRC system using an OFDM waveform incorporating Differential Phase Shift Keying (DPSK) modulation, as imperfect channel estimation is assumed. An optimisation problem is derived for the transmit and receive resource allocation, which seeks to optimise the sensing performance, given specific power, beampattern and communication performance constraints. The optimisation problem is constructed to be able to consider a wide variety of sensing metrics, such the MI, Fisher information for delay estimation, or the weighted sum of the detection probability.

2.3.3 Hybrid Analogue and Digital MIMO ISAC

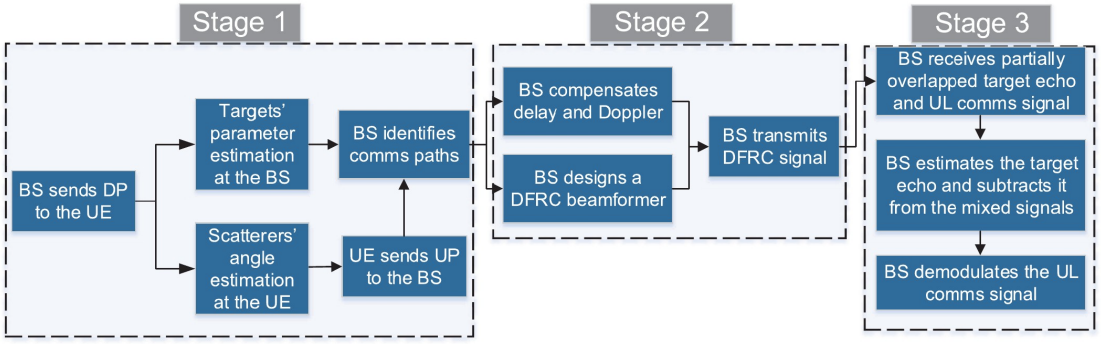

FIGURE 2.3: The three stages of transmission of a DFRC system combining HAD communications and phased MIMO radar, taken from [39]

Liu *et al.* [39], introduced above, also conceive a novel architecture for a DFRC system. This combines HAD communications and phased MIMO radar. Some of the unwanted targets are scatterers for the communication channel, and therefore radar signals are sent towards them, unlike with traditional radar. The proposed DFRC structure has three stages, which are also summarised in Figure 2.3:

- Stage 1: radar target detection and communication channel estimation.

- Stage 2: radar transmit beamforming and downlink communication.
- Stage 3: radar target tracking and uplink communication.

In stage 1, the radar detection waveform used is similar to a communication pilot waveform, and hence it is also used for CSI estimation. The waveform is an "OFDM" chirp signal, with a different starting frequency for each antenna. Using the echoes scattered by the targets and the signals from the UEs, the BS estimates the angle of arrival of the received signals, as well as the delay and Doppler shifts. The UEs estimate the angle parameters of the communication channel scatterers, then formulate a ZF beamformer. The BS then receives the UE signals, and estimates the remaining channel parameters.

In stage 2, the BS designs a DFRC beamformer based on the known and estimated information. Transmit and receive beamforming are required, as the communication channel matrix is non-invertible. This aims to approximate ZF beamforming, details of which are included in [39]. Several methodologies are applied for interference cancellation. These include the use of null-space projection, or zero-forcing the interference.

In stage 3, the BS tracks the targets and users, whilst decoding the communication signals. The paper focuses on calculating the AoAs and AoDs of the targets and users. A guard period is present between the downlink and uplink communications to partially mitigate the interference between the uplink signals and the echoes. The signals received at the BS are therefore partially overlapped radar echoes and UE signals. The BS formulates an analogue combiner using the previously estimated parameters. The new reflection coefficients are then estimated at each new transmit-receive cycle. Using this information, the radar echoes are estimated, then removed from the overlapped received signals to eliminate the echo interference from the UE signals. The BS then formulates a ZF beamformer to equalise the channel, and decodes the UE signals.

This methodology assumes the following:

- Each user equipment has multiple antennas.
- The BS knows the number of scatterers and targets, and well as the ones that contribute to the communication channel.
- The radar echoes are received before the signals from the UEs.
- The BS perfectly compensates for the delay and Doppler shifts caused by the channel after CSI estimation.

Results are presented showing that the system correctly estimates both the radar target and communication scatterer locations at an SNR of 10 dB, but makes errors at a SNR of -10 dB. The SE of the system when it estimates the CSI is close to that of a perfect CSI case. The Fully Digital Zero-Forcing (FD-ZF) beamformer maintains the same SE

for all numbers of users considered when perfect channel estimation is used. When the CSI is estimated, the SE slowly decreases as the number of users increases. For both the HAD-ZF and HAD null-space projection beamformers, the SE decreases as the number of users increases. The decrease is more pronounced when the CSI is estimated. The SE of Stage 3 improves as the SNR increases, for all the algorithms considered.

The overlap ratio is defined as the ratio of the time the radar echo overlaps with the received UE signal. As this increases, the SE remains unchanged for FD-ZF, and for HAD-ZF beamformers. For the other beamformer considered, the SE decreases as the overlap ratio increases. The angular tracking RMSE decreases as the SNR increases. The DFRC system successfully keeps track of the targets in the simulated case.

The DFRC system proposed in [39] can distinguish between two targets despite being close to each other, as the system uses the angle, Doppler shift and time delay information for target detection. The SE of the three CSI estimation techniques are close to the perfect channel estimation case. The HAD-ZF performance is similar to that of the ZF, whereas the HAD null-space projection method has a slightly lower performance.

However, the authors of [39] do not explore the impact of these assumptions or any variations. Future work has been suggested, to include learning-based communication and radar spectrum sharing, which would use machine learning to differentiate between echoes and UE signals. Also, extending the paper to vehicle-to-everything networks, and further investigation of the downlink DFRC channel using information theory are mentioned.

2.3.4 Other Schemes

Wu *et al.* [135] consider the use of fixed analogue devices to reduce the energy consumption of a JCAS system. Instead of more typical analogue and digital arrays, a multi-beam antenna array is introduced. The multi-beam array has fewer degrees of freedom, but can still create and steer beams to ensure adequate communication and sensing performances.

A pair of precoder designs are discussed in [87], the first of which maximises the sum rate, and the second improves the energy efficiency of the system. The precoders are optimised using common constraints, namely power and target SINR constraints, with only the objective function being changed.

A two-stage iterative algorithm is proposed in [90] to generate signals as a function of angle and time. The signals generated are spatially uncorrelated in their sidelobes, which minimises the interference imposed by radar and communication on each other. This system is then experimentally tested in [91].

A hybrid beamforming system is introduced in [92], in which a two-stage optimisation of the transmit signal is carried out. The transmit signal is designed to be as similar as possible to an ideal radar beampattern, whilst conforming to specific power and communication user SINR constraints.

An ISAC system using passive radar is proposed in [93], and its trade-offs are investigated. The system optimises the sensing signal, given particular communication data rate constraints.

2.4 Embedding Data into Radar Waveforms

2.4.1 Comparison of Different Methods

Hassanien *et al.* [38] provide a comparison of various signalling strategies employed to communicate using radar waveforms. The signalling strategies described are: waveform diversity based method [63, 65], PM [66], sidelobe AM [64, 65] and ASK [67].

The waveform diversity method, as shown in [63] and [65], creates a set of radar waveforms, with each one corresponding to a communication symbol. As many different waveforms are transmitted over a coherent processing interval, using a constant filter can lead to a reduction in clutter cancellation performance. To mitigate this, a filter has to be designed for each of the possible transmitted waveforms. This method broadcasts the communication information, which could pose a security risk.

The PM method of Hassanien *et al.* [66] varies the phase of the transmitted radar waveform, with a reference signal needed for non-coherent detection. The reference and embedded communication signals are transmitted simultaneously and propagate through the same channel, which allows any phase rotations induced by the propagation environment to be cancelled out. The user's choice of transmit beamforming weight vector allows the system to communicate directionally, or broadcast the embedded information.

Sidelobe AM modulates the amplitude of the sidelobe of the transmitted radar pulse. As the main lobe is not modified, the sensing performance remains unaffected, but the system cannot communicate with a target in the direction of the main lobe. In [64], a time-modulated array based method is used by Euzière *et al.*, which optimises the average array factor, based on the given weights set for each antenna of the system. In [67] and [65], convex optimisation is used to determine the beamforming weight vectors for each sidelobe AM level.

Sidelobe ASK creates many orthogonal radar waveforms, which are simultaneously transmitted, each with information embedded in the sidelobe, as shown in [67] and

[65]. Sidelobe ASK is a combination of the waveform diversity method and of sidelobe AM.

In [38], it is shown that sidelobe AM has the poorest BER performance, followed by sidelobe ASK, with PM modulation having the best BER performance both in the sidelobe and the main lobe. However, Hassanien *et al.* [38] do not provide any numeric comparison between a waveform diversity method and the other modulation schemes described.

2.4.2 Amplitude Shift Keying

Hassanien *et al.* [125] also develop a sidelode ASK scheme for DFRC systems using a radar signal as the base waveform. The modulation is imposed on the sidelobe of the instantaneous beampattern, which is designed to transmit a reference waveform and multiple orthogonal waveforms. Each transmitted waveform was set to have two sidelobe amplitude levels, corresponding to a single bit. A reference waveform is required to ensure communication demodulation at the receiver. The sidelobe is modulated once per radar pulse, limiting the communication rate. Orthogonal waveforms can be added to increase the radar performance and the communication rate. The propagation channel considered consists of a single time invariant coefficient.

An assumed beampattern is shown, with a heavily reduced sidelobe amplitude in the direction of the communication user to minimise the communication BER. A high BER is maintained in the other directions to maintain the security of the transmission. This scheme can only communicate with a user who is not in the direction of the main lobe of the radar waveform.

As the number of orthogonal waveforms is increased, the BER at a given SNR increases, at the expense of throughput. The probability of source resolution is extremely sensitive to SNR, with near-zero probability for an SNR below 5 dB, and a probability approaching unity above 10 dB. The system would therefore not be viable for radar detection when the SNR is below 10 dB. The RMSE of the target angle follows a similar pattern, where it is high at low SNRs, and low at high SNRs.

This scheme is compared to another ASK modulation scheme [137], and included references from the literature. Both systems have an identical BER when the number of transmitted bits is 1. When this number is increased, the novel scheme outperforms the baseline scheme. The novel scheme outperforms the baseline scheme in terms of target angle RMSE for all SNRs considered. The baseline scheme has a higher probability of source resolution than the novel scheme at low SNR, but a lower probability at high SNR.

Arik *et al.* [138] propose a novel ASK modulation scheme for JRC, and compare it to two other existing schemes from [65] and [67]. The scheme functions in a similar way to the previously reviewed paper [125]. The system uses a novel Non-Data Aided (NDA) channel estimation method that avoids both the requirement of an additional training signal, and the inherent reduction in capacity that this entails. The fading channel assumes a Rician distribution with at least one LoS path, with the k factor being varied. A ULA of antennas is assumed.

The proposed system has a slightly higher throughput than the baseline scheme using NDA at high SNRs under fast fading. Under slow fading, this baseline scheme's throughput is slightly improved, and greater than that of the novel scheme. The second baseline scheme ([67]), which does not appear to use NDA channel estimation, has a higher throughput than the other schemes at low SNRs. All three schemes have an almost identical BER at all the SNRs considered.

Future investigations are expected to include utilising different diversity combining techniques as a mitigation of the effects of multiple propagation paths.

2.4.3 Phase Modulation

Hassanien *et al.* [139] develop a phase modulation scheme for DFRC. Transmit beamforming weight vectors are created so that their transmit power radiation patterns are identical, but with the phase being specific to each weight vector. Each beamforming weight vector is associated with a specific point on the communication constellation. Consequently, this requires that there are as many beamforming weight vectors as the modulation order for coherent communication, and twice this number for non-coherent communication.

There are three transmit signalling strategies. The first is coherent communication, which is comprised of a transmitted radar waveform and the communication weight vectors. The communication data is transmitted in the direction of the communication receiver. The second strategy relies on non-coherent communication in the direction of the communication receiver. Two orthogonal waveforms are transmitted, both of which contain communication weight vectors. The phase difference between the two waveforms is the modulated phase. The third signalling strategy is non-coherent broadcasting, in which the non-coherent signal is communicated in all directions.

For all the strategies, a single constellation point is transmitted per radar pulse. For the non-coherent strategies, the orthogonal waveforms are transmitted simultaneously, which is assumed to preserve the transmitted phase difference. The scheme can communicate in the direction of the main radar lobe. The scheme assumes that a ULA of antennas is used.

The coherent strategy has a lower BER than the non-coherent strategies for a given SNR. Both non-coherent strategies have identical BER for the SNR considered. This trend is present when communicating both in the sidelobe and main lobe of the radar signal. The main lobe communication BER has a -20 dB SNR offset compared to the sidelobe communication, which corresponds to the sidelobe amplitude attenuation relative to the main lobe.

The schemes of [64] and [67] are introduced for comparison. Both of them use sidelobe AM, with one additionally employing waveform diversity, and can only communicate in directions other than the main lobe. Both of these comparison schemes have a higher BER than the novel scheme for the SNR considered.

When communicating in the main lobe, the BER for the coherent strategy is erratic for very small changes in angle. When communicating in the sidelobe, the BER of the AM scheme along with waveform diversity is lower than that of the non-coherent direction strategy, but higher than the BER for the coherent strategy, at the communication angle. The non-waveform diversity AM scheme has inferior performance compared to the other schemes. The non-coherent broadcasting strategy has an oscillating BER with respect to the transmission angle.

The radar detection angle RMSE is lower for the novel scheme than for the AM schemes when there is a low SNR. The probability of source detection is higher for the novel schemes than for the baseline schemes, and reaches a value of 1 at a lower SNR.

Hassanien *et al.* [71] also develop a PSK scheme for FH radar. A PSK symbol is embedded in each FH waveform used. The waveforms are orthogonal to each other. The number of transmitted communication symbols in each radar pulse is the number of antenna elements times the length of the FH codes. The data rate is proportional to the pulse repetition frequency, the number of transmit antenna elements, the FH code size, and the number of bits encoded into a PSK symbol. The channel is modelled as the collection of the reflected paths, each with a corresponding reflection coefficient that remains unchanged over the duration of a pulse.

The results show that the system performs as expected, with the SER decreasing as the SNR increases, and increasing when the modulation order is increased. The radar performance is said to be relatively unaffected by the modulation scheme, but no results are provided.

2.4.4 Quadrature Amplitude Modulation

Ahmed *et al.* [62] propose a novel QAM scheme for the sidelobes of radar signals in DFRC systems. The system transmits different sidelobe levels in the directions of the communication receivers, similar to ASK. The system also transmits a different phase in

the directions of the communication receivers using PSK. The two modulation schemes are then combined to form a scheme analogous to QAM in communications. The supported number of communication directions is one less than the number of antenna elements, due to one direction being used for the radar main lobe. The system can perform both coherent and non-coherent communication. The coherent communication uses all of the orthogonal communication waveforms, whereas the non-coherent communication requires a reference waveform.

The sum data rate of QAM increases by 4 bits for every additional orthogonal waveform available, which is four times the sum rate increase of ASK-only or PSK-only systems. This is because the QAM scheme allows a combination of both other schemes to multiple users per radar pulse. For a given sum data rate, the coherent QAM has a lower BER than non-coherent QAM, which in turn outperforms the ASK-only and PSK-only systems.

2.4.5 Code Shift Keying

Tedesso *et al.* [101] propose a Code Shift Keying (CSK)-based JRC system in a restricted electromagnetic emissions control environment for naval military applications. Gold or Kasami codes are used for communication, which are pseudo-random sequences. The communication system uses Binary Phase Shift Keying (BPSK) or Quadrature Phase Shift Keying (QPSK) modulation. The resulting waveform is a pseudo-random binary phase coded radar waveform, for continuous wave radar. The maximum range has an inverse relationship to the maximum Doppler shift. The communication signal is sent in all directions.

The results show that the SER of the CSK scheme is lower than that of the baseline M-ary FSK scheme at low SNR, but converges as the SNR increases. Both Kasami and Gold codes have almost identical SER performances. The longer the codes, the lower the side lobe levels, which is normally associated with improved sensing performance. The PSLR of the QPSK signal is within 3 dB of the PSLR of the BPSK signal.

Further work could consider increasing the number of communication users through the use of OFDM. This would increase the complexity of the system. The use of various pulse shaping techniques could decrease the Doppler sidelobes, and the application of filtering techniques could reduce the range sidelobes. Additionally, it is observed that the use of CDMA waveforms is a potential area for future research.

2.4.6 Multiple Input Multiple Output Radar

A DFRC system based on MIMO radar is considered in [99], in which the sensing targets may attempt to intercept communication information. A pseudo-random signal

is transmitted towards eavesdroppers to prevent them from intercepting communication information, whilst also being used for sensing. The covariance matrices of the pseudo-random sensing and communication signals are optimised based in part on the system's secrecy rate.

The addition of artificial noise to prevent sensing targets from potentially intercepting communication information is also proposed by Su *et al.* in [100]. This is optimised by minimising the SINR for the sensing targets, whilst ensuring a given SINR level for communication targets. This problem is first considered for perfect channel and target location information, and then when there is uncertainty in this information. The authors note that when the target location is uncertain, the main sensing beam is widened, which leads to an increase in the power allocated to artificial noise to ensure a given SINR for the sensing targets.

A power allocation system for a distributed DFRC MIMO radar system with embedded communication information is introduced in [126] by Ahmed *et al.*. A distributed system is defined in [41] as a system in which there are multiple nodes that transmit and/or receive, with the data being processed in a centralised unit. The authors claim that the proposed power allocation scheme allows the DFRC system's communication performance to be close to that of a communication only system. This is achieved whilst having a superior sensing performance compared to a single node radar only system, as the reflected sensing signals are received from multiple nodes.

2.5 Using Communication Waveforms for Sensing

Kumari *et al.* [40] propose a JCR waveform for long range radar based on mmWave consumer wireless local area network at the 60 GHz unlicensed band using the IEEE 802.11ad standard. Radar algorithms using single and multiple frames are developed to detect single and multiple targets, and estimate their range and velocity.

A preamble, consisting of a short training field and a channel training field, is inserted at the start of each frame. The short training field is used for communication frame synchronisation and frequency offset estimation. The channel training field is utilised for communication CSI estimation. Both training fields are composed of Golay sequences, which have been chosen due to their perfect auto-correlation property at a Doppler shift of zero.

The following assumptions are made:

- The target vehicle can be represented by a single point model for performance evaluation.

- The location, relative velocity, and radar cross section of the target remain constant during a coherent processing interval due to the small enough relative acceleration and velocity of a target vehicle.
- Full-duplex radar operation due to the recent development of systems with sufficient isolation and self-interference cancellation.
- A frequency flat fading channel is used.
- The AoA and AoD of the targets are known.

As with other JCR systems, there is a trade-off between velocity estimation and communication data rate. This is illustrated in the paper by varying the number of preamble sequences used in a frame, where an increase leads to fewer symbols available for communication, but a greater signal range available for velocity estimation.

The single frame algorithm's range MSE is lower than that of the comparison algorithms simulated, but is larger than the CRB, and plateaus as the noise and interference power are decreased. GB/s data rates and cm level range accuracy and cm/s level velocity accuracy are claimed. A single target is simulated for this case.

The multiple frame algorithm's velocity MSE are identical to the CRB for each number of frames considered, indicating an ideal performance. As the number of frames used for detection is increased, the velocity MSE and its associated CRB decrease. When two targets are simulated, cm level range accuracy and cm/s velocity accuracy are achieved, with a coherent processing interval smaller than that of other long range radar schemes.

No results illustrating the communication performance of the algorithms are presented.

The claimed advantages of the proposed systems include that they are based on an existing IEEE 802.11ad standard, stated to be a good baseline for future work in mmWave systems, and that they surpass the minimum requirements for long range radar, whilst maintaining a suitable communication performance. It is noted that the system is extendable to higher carrier frequencies.

Kumari *et al.* [140] develop a tunable JCR waveform structure. A novel metric to quantify the communication performance is proposed. This metric is comparable to the CRB for radar, and is termed the Distortion Minimum Mean Square Error (DMMSE). The tunable JCR waveform structure can be used to optimise JCR performance using sparse techniques. Specific virtual waveform configurations are used to reduce computational complexity, such as uniform waveforms, nested virtual waveforms or Wichmann virtual waveforms. Simulations are carried out to study the performance of the systems, based on the IEEE 802.11ad standard.

Three optimisation problems are formulated: minimising the radar CRB under the constraint of a minimum communication DMMSE, minimising the communication

DMMSE for a given minimum radar CRB, and a flexible weighted average of communication and radar performances. Radar processing exploits the preamble of the JCR frame that consists of training sequences with good auto-correlation properties. Convexity of the optimisation problem is achieved by discarding certain values from the non-convex objective function region.

The following assumptions are made:

- Location and relative velocity of a target remain constant during a coherent processing interval.
- Full-duplex radar operation is achievable due to sufficient antenna isolation and self-interference cancellation.
- Perfect data interference cancellation on the training portion of the received JCR waveform as the transmitted data is known to the radar receiver.
- The source and destination align their beams towards each other.
- The channel assumes LoS and frequency selective Rayleigh fading for the communication and radar channels.

The virtual waveforms achieve high velocity estimation accuracy with a slight reduction in communication data rate. Non-uniform waveforms have a superior performance than uniform waveforms, which is more pronounced at low SNR and high target density. Wichmann waveforms appear to perform slightly better than nested waveforms. The advantage of non-uniform waveforms over uniform waveforms increases with the target count, whereas it reduces with radar SNR at high target count due to the saturation effect.

The DMMSE-based optimised waveforms are compared with traditional virtual preamble count-based optimised waveforms. It is observed that traditional virtual preamble count-based optimisation can be used as a coarse estimate of the optimal solution of the proposed optimisation problems. The figures in the paper do not appear to support this.

The claimed advantages include high velocity estimation accuracy and that the new performance metric makes the study of communication and radar performance trade-off simpler. The noted disadvantage of the proposed waveforms is that there is a slight reduction in communication data rate.

Future work is mentioned. The use of other virtual waveforms, such as Golomb and coprime waveforms is suggested. It is noted that the impact of Ricean fading on the performance benefit of the non-uniform waveforms would be of interest. The use of more advanced estimation algorithms is also mentioned. Validation of the simulation results using experimental data, when available, is considered desirable.

2.5.1 Orthogonal Frequency-Division Multiplexing

Sturm and Wiesbeck [36] is one of the earlier papers to discuss and present some possibilities for RadCom using different waveforms and signal processing methods. Two main transmission methods are considered, Spread Spectrum (SS) single carrier transmission and OFDM.

The SS single carrier transmission has the following properties:

- Both SS communications and m-sequence radar use codes that have good autocorrelation properties.
- RadCom requires a sufficiently high spreading factor.
- Coding can be used for CDMA.
- The mentioned codes that can be used are m-sequences, preferentially selected m-sequences, Gold sequences, Kasami sequences and chaos sequences.
- Both short and long codes are considered.
- BPSK modulation is used.
- The estimation of targets parameters demands large computational resources.

The OFDM transmission has the following properties:

- The radar measurements are performed using the modulated symbols, not the baseband signals.
- Coding is not considered, and PSK modulation is used.
- As long as the OFDM signal bandwidth is much smaller than the carrier frequency, the Doppler shift causes an identical phase shift on every subcarrier.
- The Doppler shift introduces a linear phase shift between successive symbols in a given subcarrier.
- The time delay introduces a linear phase shift between subcarriers for a given symbol.
- The changes introduced by the Doppler shift and time delay are orthogonal to each other.
- The orthogonality holds as long as the sensed object remains in the same discretised point within the delay-Doppler grid for the duration of an observation.

- The process of detecting the range and velocity, referred to as the modulation symbol-based approach, is as follows:
  - Element wise division, in which the received signal is divided by the transmitted signal, is used to remove the communication symbol information.
  - The Inverse Discrete Fourier Transform (IDFT) on the vector containing the time delay phase shift and the Discrete Fourier Transform (DFT) on the vector containing the Doppler shift phase shift is performed.
  - The delay and Doppler information can then be extracted, and the target range and velocity estimated.
  - The detection process is completely independent of the transmitted information.
  - The detection process consists of linear operations, and can therefore be easily expanded to consider multiple targets.
- This system offers a similar radar performance to a correlation processor.
- The paper only considers one user operation.

The expansion of the transmission methods to MIMO is considered. A horizontal ULA of antennas with constant element spacing is assumed. The pre-processing method for sensing is similar to the single antenna case. Processing all the information simultaneously would be too costly at large scale. Two processing approaches are considered, classical Fourier transform-based and MUltiple SIgnal Classification (MUSIC).

The Fourier transform-based method creates a matrix with a similar structure to a DFT, with an added sinusoidal distortion in the frequency domain. This matrix is computed by squaring the magnitude of the output of the sensing pre-processing multiplied by the beam steering vector.

The MUSIC method operates on the eigen-structure of the correlation matrix of the output of the sensing pre-processing. The eigenvalues of the correlation matrix are used to determine the number of scatterers in each range resolution cell. A radar image pseudointensity is then calculated, with its peaks being in the target directions. This method is more complex than the Fourier-based method.

In simulations, propagation paths with more than 40 dB of attenuation compared to the strongest path are not considered by the algorithms. The range calculations assume LoS for communication and radar.

The different code sequences for SS transmission are compared. As the spreading factor is increased, the PSLR increases. Long codes have a higher PSLR than short codes, with little variation introduced by the code type. When the signal to interference ratio from another user is above 5 dB, the PSLR remains constant. Below 5 dB, the PSLR decreases

as the signal to interference ratio decreases. It is noted that the introduction noise leads to a similar PSLR trend for variation in SNR.

For small spreading factors, the PSLR is insensitive to Doppler shift. For large spreading factors, the PSLR decreases as the Doppler shift increases, until the phase shift introduced by the Doppler shift corresponds to a full phase rotation during the coherent processing interval, at which point the PSLR increases. Overall, single carrier SS can be used for RadCom, but is not suitable for vehicular applications as it would require too many computational resources for accurate velocity and range estimations.

The OFDM modulation symbol-based approach for OFDM is compared to a correlation-based detector. The modulation symbol-based method has a higher PSLR than the correlation based method, leading to more accurate sensing. As the number of OFDM symbols considered over a sensing frame is increased, the PSLR and sensing image SNR increase.

The OFDM system was tested in a real-world setting. The system has correctly identified the vehicles ahead of the user, despite the presence of a strongly reflecting target immediately in front of the user. The reflected signal from the strongly reflecting target generates high intensity sidelobes that form a visible line across the relative velocity axis at the target's range in the range-velocity grid. A line across the range axis at the user's velocity represents reflections from the road furniture.

It has been confirmed that OFDM transmission provides a high dynamic range, which makes it suitable for vehicular RadCom applications. It is noted that multi-user access techniques are required when multiple communication users are present.

The beampattern for both MIMO sensing algorithms are simulated using SS transmission. The Fourier-based method has a large main lobe, and therefore cannot distinguish between adjacent users 5 degrees apart. The low PSLR of this method can lead to erroneous detection, as the sidelobes can be powerful enough to be confused as targets. The MUSIC method can differentiate the adjacent users, as its main lobe is narrower, and has higher angular resolution. The MUSIC method's higher PSLR and amplification of weaker reflections lead to fewer erroneous target detections.

2.5.1.1 Code-Division Orthogonal Frequency-Division Multiplexing

Chen *et al.* [12] develop a novel Code-Division Orthogonal Frequency-Division Multiplexing (CD-OFDM) JCAS system for machine type communications. The system can switch between OFDM and CD-OFDM transmission depending on the SINR detected.

The CD-OFDM spreads the symbol across the frequency subcarriers using Walsh-Hadamard codes, thereby increasing the robustness of the communication whilst reducing the throughput. The codes are perfectly orthogonal to each other. Code multiplexing can be used to increase the CD-OFDM throughput, when the SINR is increased. QAM symbol modulation is used. Once the communication signal is received and demodulated, the reconstructed communication signal is removed from the received signal to allow the weaker received sensing signal to be detected. The system operates full-duplex sensing.

The following assumptions are made:

- The channel follows a Rayleigh distribution.
- One LoS propagation path is assumed.
- Each propagation path has a separate delay and Doppler shift associated with it.
- The AoA and AoD of the signals are assumed to be known.
- The transmit antenna elements signal leakage to the receive antenna elements in the same unit is blocked.
- The system uses the receive antenna elements for both sensing and communication.
- The antennas are ULA.
- The targets are assumed to have a small relative velocity.
- The targets have high radar cross section.
- The CSI is perfectly estimated.
- There is channel reciprocity between different users that exploit the same spectrum.

The BER of the two transmission methods when the SINR is varied follow similar trends, with a SINR offset being present as the CD-OFDM transmission can operate at lower SINR. This offset decreases as more symbols are multiplexed. The OFDM transmission is compared to an existing Time Division Duplex (TDD) system from literature, which has an identical BER performance.

The RMSE of the range and velocity estimations are large, until a SINR of between 5 and 10 dB is reached, at which point the RMSE falls to a insignificant value, for all the transmission modes and systems considered. For the novel system, this is due to the communication demodulation error, interference and noise levels no longer impeding the received sensing signal to an extent that prevents accurate sensing. A slight offset

is seen for the CD-OFDM transmission, with the accurate estimation being present at a SINR of 5 dB, compared to 10 dB SINR for OFDM transmission. The TDD system's performance is slightly superior to that of the OFDM transmission, with the increased performance becoming more prevalent as the modulation order increases.

The stated advantages of the novel system are the full-duplex transmission, with greater flexibility than the TDD comparison system from literature. The stated disadvantages are the increased complexity associated with CDMA, a large number of subcarriers and a large number of symbols in a sensing frame are required for accurate sensing, and communication reliability is essential for accurate sensing.

2.5.1.2 Other OFDM ISAC Schemes

In [119], two optimisation problems are formulated, based on minimising MI and CRLB using on OFDM waveform. Each optimisation method proposed performs best when using their optimisation criteria as the measure of sensing performance with no independent sensing criteria with which to compare the proposed precoder optimisations shown.

[136] proposes a low complexity algorithm for a standard OFDM JRC system. The novel target parameter estimation algorithm reduces the detection complexity by utilising a 1D Fourier transform instead of the more common 2D Fourier transform.

In [86], an OFDM radar signal is manipulated to reduce the interference it imposes on the communications signals by approximating a modulated communication waveform. This system is then further optimised in [87], where two new precoder designs are introduced, one to maximise the sum rate, and the other the energy efficiency of the system. The uplink communication and short range sensing for OFDM JRC is investigated in [88], for both perfect and imperfect channel information.

An adaptive OFDM ISAC waveform design based on the conditional MI and the data information rate of the system is presented in [34]. These metrics are first determined, then an optimisation problem is formulated, with the transmit power on each subcarrier being optimised to maximise the weighted conditional MI and data information rates. The results show that this adaptive power scheme can outperform a conventional OFDM ISAC system with equal power distribution for both sensing or communication. This allows the system to be tuned to the specific environment and requirements it is placed in.

A cooperative vehicular network is considered in [127], in which each vehicle transmits sensing and communication information to each other using an OFDM waveform. Target information is obtained through various means: OFDM sensing, receiving information of a target's location from other vehicles, and estimating the target's location parameters using the transmitted communication signals sent by the target. The method used integrates the above sets of information to improve the target location estimate's accuracy, and allows the system to more accurately differentiate between targets than a single vehicle system.

2.5.2 Orthogonal Time Frequency Space

Since the OTFS concept was first introduced [141, 142], its employment for ISAC [143] has been a topic of interest. This is due in part to OTFS being less affected by Doppler shift than OFDM, and to the DD channel being defined by the delay and Doppler shifts of the propagation paths. This leads to the DD channel fluctuating at a slower rate than its Time Frequency Domain (TF) and TD counterparts. When the delay and Doppler shifts of the propagation paths are perfectly synchronous with the system's sampling grid, the channel can be modelled using a sparse matrix. This can simplify the associated target parameter estimation algorithms [144]. However, in practice, the delay and Doppler shifts are rarely integer multiples of the system resolutions, hence more complex detection algorithms are required for accurate target estimation. The full-search based Maximum Likelihood (ML) attains the best performance at the highest complexity.

Gaudio *et al.* [122, 123] investigate the effectiveness of OTFS for JCR in vehicular applications, and compare it with OFDM and Frequency Modulated Continuous Wave (FMCW) radar. The OFDM system uses a typical OFDM signal model. For sensing, the receiver phase rotates the symbols in the received signal before using ML algorithm to estimate the sensing parameters for the entire possible set of delay and Doppler indices, at an unspecified resolution.

The OTFS model uses more realistic rectangular pulses, as opposed to ideal pulses which are physically impossible to create. The OTFS symbols are only used for communication, as delay and Doppler shift estimation is a channel estimation problem for OTFS. Separate soft-output detector and decoder are included. Soft-output refers to an output whose value is not part of a fixed set. This flexibility is used to indicate reliability of the data.

A ML parameter estimation algorithm is used for sensing estimation. The ML algorithm in [122] is derived for a LoS only case, which is then extended to include cases where additional propagation paths exist in [123]. The proposed ML algorithm considers the time delay and Doppler shift to be continuous values, as opposed to most other

systems in literature which assume them to be integer multiples of the delay-Doppler grid resolution. Three other detectors are considered for comparison, one ML from literature, one linear block-wise MMSE, and one reduced complexity linear block-wise MMSE from literature.

The CRB for range and velocity estimation is derived for both the OFDM and OTFS systems. For data rate calculations, the transmitted symbols are assumed to be Independent and Identically Distributed (i.i.d.) Gaussian variables. This allows the data rate to be calculated as a function of the communication SNR for both OTFS and OFDM.

The following assumptions are made:

- Receiver has been detected.
- Multipath time-frequency selective channel.
- Discrete channel paths.
- Each path has a complex amplitude, a delay and a Doppler shift.
- Sensing parameters of interest are the delay and Doppler shift of the shortest path, which is assumed to be LoS.
- Channel paths are sufficiently separated in the delay-Doppler domain.
- Perfect CSI estimation.
- Number of channel paths, as well as the presence of the target are known.

When comparing the OTFS system to the OFDM and FMCW systems, only LoS is considered. The OTFS system has a higher data rate than the OFDM system across all the communication SNR considered, as the OFDM cyclic prefix creates a higher overhead. The OFDM system can accurately sense when the sensing SNR is above -20 dB, whereas this is only occurs for the FMCW system above -19 dB and for the OTFS system above -18 dB. After these SNR values, the range and velocity RMSE fall onto the CRB.

As the number of propagation paths increases from 1 to 4, the OTFS system sensing RMSE reaches the CRB at -17 dB of sensing SNR. A small number of additional propagation paths appears to have little effect on the OTFS sensing performance.

The symbol detection performance of all the detectors decreases as the number of propagation increases. This decrease is most noticeable in the comparison ML algorithm, and least noticeable in the full complexity MMSE detector. The proposed ML and the full complexity MMSE detectors have the greatest symbol detection performances. When the delay and Doppler values are continuous, the comparison ML and reduced complexity MMSE detectors have a significant reduction in performance, whereas the proposed ML and full complexity MMSE detector performances show small variations.

The stated advantages of the proposed detector are that it has a superior performance to that of the lower complexity comparison detectors, with a similar performance to that of the complex MMSE detector.

2.5.2.1 Successive Interference Cancellation

Wu *et al.* [115] propose novel sensing processing and estimation algorithms for OTFS JCAS. Waveform pre-processing is performed at the receiver to ensure sub-carrier orthogonality. This involves splitting an OTFS block, the signals transmitted over a coherent processing interval, into multiple sub-blocks. The echo signal in each sub-block is transformed into a sum of scaled and circularly shifted versions of the same signal sequence, creating a virtual cyclic prefix. This allows the maximum detectable range to be unconstrained by the OTFS cyclic prefix length.

The communication data symbols are removed in the time-frequency domain without amplifying noise. This is achieved by dividing the DFT of the target echo after pre-processing by the DFT of the essential signal part of the sub-block multiplied by a scalar, which is configured to optimise performance.

An off-grid method of estimating target ranges and velocities is used. Initially, an estimate of the parameters for the target with the strongest signal is performed. Once this has been completed, the signal from the target whose parameters have just been estimated is removed. This is then continued until the parameters for all the targets have been estimated. This is compared to a ML estimation algorithm.

The following assumptions are made:

- The receiver and transmitter are in the same physical unit.
- There is one receive and one transmit antenna per unit.
- Both antennas are synchronised.
- Rectangular pulse shaping is used for OTFS.
- The scattering coefficient of a target remains constant throughout a coherent processing interval.
- The scattering coefficients of the targets are uncorrelated.
- The total number of targets is known.

Both the proposed and the ML estimation algorithms follow the same estimated velocity MSE trend as the CRB over the range of SNR considered. The proposed and

ML algorithms have a slight positive MSE offset from the CRB. Varying the number of samples in a sub-block has a small impact on the MSE for the proposed algorithm.

The ML algorithm has periodic inconsistencies in the velocity estimate MSE as the target velocity increases. These inconsistencies are not present in the proposed algorithm. There is an optimal value of the essential signal length, for which there is a peak in performance. Sub-optimal values can significantly increase the MSE of the estimated parameters.

Future work mentioned includes compensating for the timing and frequency offsets caused by asynchronicity between the transmitter and receiver, distributed sensing in a network, and sensing-assisted communications.

2.5.2.2 Data Cancellation

Zhang *et al.* [113] propose a novel modulation symbol cancellation scheme for OTFS RadCom. The symbols are cancelled from the received sensing echoes at the sensing receiver to obtain the targets' range and velocity estimates. The communication system follows existing OTFS schemes.

The input-output relationship of the general OTFS system is stated to be similar to a 2D circular convolution, but with added intra-pulse Doppler modulation and a linear phase. These added components complicate the recovery of the delay-Doppler channel. An embedded pilot is introduced to reduce the coupling of the linear phase, to create a full-guard embedded pilot OTFS waveform. The residual coupling is then treated as random noise by the system.

An MMSE-based matrix inversion method is used to estimate the frequency-Doppler radar spectrum. The pilot symbol power is adjusted to ensure that the modulation symbol matrix is non-singular and increase the accuracy of the channel estimate. The delay-Doppler channel estimate is then obtained using the Inverse Fast Fourier Transform (IFFT).

Another method proposed is a Spectrum Division (SD) based symbol cancellation method. When the maximum Doppler shifts of the targets are relatively small, the channel is quasi-static in the delay-Doppler domain, and the intra-pulse Doppler modulation is therefore considered negligible. This allows the input-output relationship to be simplified. The channel can therefore be more simply estimated in the frequency-time domain, and then converted to the delay-Doppler domain. The SD method is therefore less complex than the MMSE-based method.

The following assumptions are made:

- Mono-static radar is used to detect the target and communicate data simultaneously.
- The delay and Doppler shifts of targets and propagation paths are integer multiples of the delay and Doppler resolutions.

The results are compared to an OFDM RadCom system from literature, which has a different velocity resolution to the proposed system, and employs a spectrum division method. I.i.d. 16-QAM data is used as the input.

When the maximum target range is greater than half the maximum sensing range, there is residual coupling of the linear phase term in the echos, leading to a noisy signal even in noiseless conditions. When the maximum target range is smaller than half the maximum sensing range, this is no longer the case, which allows the transmitted symbols to be fully cancelled.

When all the transmitted symbols are identical, the modulation symbol matrix is singular, and the channel estimation can only be obtained using the pilot symbols, leading to a poor performance. When the transmitted symbols vary, the matrix is no longer singular, and a more accurate channel estimate is achieved.

The MMSE-based OTFS method produces the largest PSLR in the delay-Doppler grid at the target range and velocities, followed by the OFDM and SD OTFS methods, indicating a superior sensing performance. The three methods have a similar PSLR at low SNR. As the SNR increases, the PSLR for the MMSE-based method increases for all the SNR considered, in contrast to the OFDM method that plateaus beyond 16 dB SNR and the OTFS SD method that peaks at 12 dB SNR, then decreases as the SNR is further increased. As the target relative velocity or the number of targets increases, the PSLR decreases for all methods.

As the data symbol power to pilot power ratio increases, the PSLR increases for the MMSE-based method, but remains constant for the SD OFDM method. When the data rate is increased, there is a slight decrease in the PSLR for the SD OTFS method, but a significant decrease in the PSLR for the MMSE-based method, being lower than that seen for SD OTFS method at the higher data rates considered.

Future work mentioned is the analysis of the system when the delays and Doppler shifts are no longer integer multiples of the delay and Doppler resolutions.

2.5.2.3 Fractional Delay and Doppler Index Estimation Methods

In [145, 146], the authors conceive a two-dimensional correlation-based method for OTFS integer delay and Doppler index estimation. A generalised likelihood ratio test is developed to estimate the number of targets. The fractional indices of the estimated

targets are determined by comparing the power-ratio of the indices surrounding the estimated integer indices in the imaging matrix. This method requires each target to have unique integer delay and Doppler indices. The authors observe that the correlation-based method results in an error floor at high SNRs due to the inter-symbol interference caused by the multiple propagation paths in the channel. Tang *et al.* [147] propose a two-step sensing methodology to estimate the integer and fractional delay and Doppler indices of the targets for OTFS sensing. The first step employs a matched filter-based method to determine the integer indices. The second step utilises a Fibonacci-search based algorithm to iteratively determine the fractional indices. Unlike other parameter estimation methods, which reach an error floor at high SNRs, the estimation error of the Fibonacci-search based algorithm continues to decrease as the SNR increases.

In [148], Muppaneni *et al.* design a two-step method for sensing the target parameters of OTFS. Firstly, the integer indices are estimated by maximising a cost function for a fixed number of propagation paths. Secondly, the fractional indices are estimated using a matrix of all the integer indices and the previously estimated fractional indices. For the first path, only integer indices of the other paths are utilised to estimate the first path fractional indices. Once the fractional indices for a path have been estimated, the channel attenuation of the associated path is then estimated. After the fractional indices of a path are estimated, the difference between the received signal and the reconstructed received signal from the estimates is calculated. If this difference becomes smaller than a specific threshold, the sensing procedure is terminated, and path estimation is concluded. Otherwise, the algorithm continues until the fixed number of propagation path variables has been estimated. This method is also harnessed for communication channel estimation using pilot frames. The results presented in [148] show that the proposed algorithm leads to a lower sensing estimation error and communication BER than the modified ML benchmark used for comparison.

2.5.3 Affine Frequency Division Multiplexing

AFDM is a novel chirp-based waveform, first introduced in [149]. AFDM is similar to OFDM, with the DFT replaced by the Discrete Affine Fourier Transform (DAFT). The DAFT is a generalised transform, with the DFT being a specific form of the DAFT. It is characterised by two chirp parameters, named chirp parameter 1 (c_1) and chirp parameter 2 (c_2), which can be flexibly tuned to optimise the diversity and correlation properties of the signal. Other forms of OFDM utilising the DAFT [150] or chirps [151, 152] have been proposed, but these still lead to propagation paths being separable only by delay, not Doppler shift. The DAFT utilised in AFDM is configured such that the propagation paths are separable by both delay and Doppler shift, similar to OTFS. This allows AFDM to achieve full diversity, like OTFS. The communication performance of AFDM has also been shown to be similar to that of OTFS. Of concern is that the

maximum Doppler shift needs to be known at the transmitter to configure the DAFT. AFDM requires a prefix to be added, the Chirp Periodic Prefix (CPP), similar to the OFDM Cyclic Prefix (CP). The CPP reduces to a CP if the value of c_1 for the DAFT meets certain conditions. The correct configuration of the DAFT allows the Affine Frequency Domain (AFD) channel matrix to be sparse, similar to the OTFS DD channel matrix, but with a different structure.

An overview and comparison of various waveforms, including OTFS and AFDM, for various ISAC key performance indicators, is presented in [153]. The authors show that AFDM presents a mixture of characteristics of OFDM and OTFS for communication, and variable sensing characteristics, due to the flexibility offered by tuning the values of the DAFT chirp parameters. Tuning c_2 allows one to moderate the PAPR, the delay ambiguity, and the Doppler ambiguity of AFDM. Hence, AFDM presents a greater sensing flexibility than OFDM and OTFS.

Ni *et al.* [124] consider monostatic AFDM ISAC. Multiple AFDM frames are transmitted and received, to produce a received signal matrix, in a similar manner to symbol cancellation-based OFDM ISAC [36]. Two detection algorithms are implemented. The first utilises the TD signals, and utilises a method similar to symbol cancellation-based OFDM sensing. The second method operates on the AFD received signal. The AFD method is shown to only experience small fluctuations in image SNR as the Doppler shift is increased. By contrast, the image SNR of the TD and symbol cancellation-based OFDM methods degrades significantly as the Doppler shift is increased. The AFD method has a larger maximum unambiguous Doppler shift compared to the TD method, and is therefore capable of correctly estimating much larger velocities than the TD method. No comparison to OTFS sensing is presented.

Pilot symbol-based monostatic AFDM ISAC is considered in [154]. The pilot symbol is introduced into the transmit signal, with guard bands surrounding it to prevent interference between the pilot and data symbols, as in [155, 156]. Sensing is performed using the guard band and pilot symbol only. This allows for the simple removal of the self-interference imposed by the transmitter on the receiver. This pilot-based sensing method is shown to reach the sensing error floor at a higher SNR than a full signal sensing method, but with a much lower complexity. The performance of AFDM pilot sensing is shown to be comparable to that of OTFS sensing employing a more complex interference cancellation method.

Zhu *et al.* propose a bistatic AFDM method for static channels [157], where only range and fading gain estimation are considered. This method estimates the target parameters using a pilot frame. The DAFT chirp parameters are not configured to allow the propagation paths to be separable by Doppler shift, hence is not compared to OTFS. The ambiguity function of AFDM is analysed, and the optimal value of chirp parameter 2 with respect to the ambiguity function is determined to be 0. The value of chirp

parameter 1 chosen does not allow AFDM to separate the Doppler taps of the channel. A vector of 1s is transmitted in the first symbol slot for channel estimation, followed by the data symbols in successive symbol slots. A TD lower complexity pulse compression algorithm is utilised for sensing. The BER results show that this estimation method in the proposed form is incompatible with OTFS. The BERs of AFDM and OFDM are close to that of their respective perfect channel estimation counterparts, with the BER of AFDM significantly lower than that of OFDM at higher SNR. No OTFS estimation method is implemented as a comparison.

A monostatic and bistatic method are presented in [158], for AFDM, OFDM, and OTFS, utilising probabilistic data association-based message passing and parametric bilinear Gaussian belief propagation respectively. The performance of AFDM is similar to that of OTFS, with slightly lower BER and channel parameter MMSE at higher SNRs.

Xiao *et al.* [159] develop an AFDM sensing method utilising prior knowledge of the channel delay profile. This method assumes the number of resolvable paths as well as the relative delays between resolvable paths are known, and that there is a single target. This information is leveraged to estimate the target parameters under the assumption that their statistical distributions follow a Nakagami-m distribution. The proposed method is shown to leverage Non-Line of Sight (NLoS) path information, leading to a lower estimation error, unlike the comparison algorithm, and is more robust to incorrect information. The performance of the proposed method is more vulnerable to degradation caused by increases in target velocity.

A super-imposed pilot method is proposed [160] for AFDM monostatic ISAC and bistatic channel estimation. Channel estimation is performed by an MMSE algorithm, whilst target parameter estimation is achieved by implementing a TD compensation-based correlation method. The pilot symbols used are Zadoff-Chu sequences. The results presented show that the proposed system can outperform other AFDM pilot methods, including the method from [161]. Unlike the pilots from [161], the proposed pilot arrangement performance does not significantly deteriorate when large delays are present. The proposed pilot arrangement also leads to a lower probability of incorrect detection than the pilot method from [161]. No comparison method is offered to illustrate the target parameter estimation error performance.

Luo *et al.* develop an AFDM ISAC system [120] for a mixed near-field and far-field environment. The authors assume that a symmetrical ULA antenna with an odd number of elements is used, and that the number of targets is known. A tensor representation of the received signal without AWGN is formulated. This representation is than rewritten as a multiplication of submatrices using CANDECOMP/PARAFAC decomposition. Each submatrix contains information on different target parameters.

The AoD is directly obtained from the decomposition. The AoA is calculated using the covariance matrix of the estimated AoA vectors generated by the CANDECOMP/PARAFAC decomposition. This mitigates the effect of the coupling of AoA and distance due to the spherical shape of the near-field transmitted signal. A MUSIC algorithm can be used to extract the AoA, but an optimisation problem is formulated to reduce the complexity of this operation. 1D pulse compression is used to obtain the integer parts of the delay and Doppler indices. An iterative 1D golden section search method is implemented for fractional index estimation. The fractional delay and Doppler indices are estimated separately. The authors also derive the CRLB of this system. The complexity analysis of the estimation algorithms is given, but the complexity of these algorithms is not compared to the complexity of the alternative methods that are claimed to be more complex.

No comparison to OFDM or OTFS sensing is provided, but the proposed sensing method is only applicable to AFDM. The AoD estimation method approaches the CRLB, and exhibits a much lower normalised MSE than the comparison MUSIC and orthogonal matching pursuit methods over the SNR range considered. This is due to the performance of the novel method not being limited by the resolution and number of antennas of the system to the same extent as the comparison methods. The AoA estimation method approaches the CRLB, and exhibits a much lower normalised MSE than the comparison far-field and subspace methods. As this work considered a mixed near-field and far-field environment, the performance of the far-field method is compromised. The results show that the proposed delay and Doppler estimation algorithm only requires a maximum of three iterations to reach its error floor. The proposed method's normalised MSE is close to the CRLB, similar to the approximate ML comparison method with the finest grid resolution, and much lower than that of the comparison compressed sensing method. The complexity of the proposed method is $\approx O(10^4)$, whereas the approximate ML at the finest resolution is $\approx O(10^{12})$.

The effect of c_1 on the channel gain phase estimation performance of AFDM is analysed in [121]. Sensing is performed using multiple AFDM symbol slots, and the system assumes integer Doppler indices. The BER is shown to be at its lowest when c_1 is set to the optimum value that maximises the diversity order [149, 155, 156]. The results show that the CRLB is at is lowest when $c_1 = 0$, which is the special case where AFDM becomes OFDM. This conference is limited in scope, as it does not consider the CRLB of the channel gain magnitude, of the delay , and of the Doppler shift.

A sensing method for AFDM is developed in [162]. Hierarchical sparsity, defined in [163], of the channel matrix is assumed, with integer Doppler indices. The pilot-based sensing method from [154] is used as to obtain the set of receive signal vector used for estimation. This method allows for a lower sampling rate than the chirp subcarrier spacing, hence reducing complexity. A compressed sensing algorithm from [163] that

takes advantage of hierarchical sparsity is implemented for delay and Doppler estimation. The results show that sensing estimation MSE of AFDM is similar to that of OFDM and OTFS, but with a significant reduction in pilot overhead, as well as a reduction in the sensing sampling rate.

2.6 Frequency IM ISAC

There does not appear to be many publications on the subject of frequency IM ISAC. Some publications focus on IM-OFDM. Combining IM and OFDM has the potential to increase implementation and energy efficiencies, robustness to interference and noise, and therefore improve the communication BER performance [116]. IM-OFDM partitions the OFDM subcarriers into groups, with a subset of the subcarriers in each group being activated. The activated subcarriers transmit signals, with the indices of the activated subcarriers also conveying information.

The IM-OFDM structure leads to a condition in which IM-OFDM communication can always outperform OFDM: for an Γ-QAM/PSK OFDM system where each transmitted signal has an average power of 1, the IM-OFDM system should have Γ subcarriers with $\Gamma - 1$ activated subcarriers in each group. This allows the IM-OFDM system to use Γ-QAM/PSK, which maintains the throughput of the OFDM system, with each transmitted signal having an average power of $\sqrt{\frac{\Gamma}{\Gamma-1}}$.

The primary issue caused by IM-OFDM for ISAC is the lack of a signal transmitted on certain subcarriers, as this creates "holes" in the reflected signal from a sensing target. There have been different methods proposed to mitigate this issue.

One method is to use compressed sensing as in [164]. The transmitted signal is a typical IM-OFDM signal. The communication information embedded in the transmitted signal is then removed from the received signal. The resulting matrix is then formatted to remove the deactivated subcarriers, producing the matrix $\boldsymbol{B}$. A compressed sensing problem is then formulated. The assumption is that a processed matrix for all subcarriers $\boldsymbol{R}$ multiplied by a reduced DFT matrix would produce the matrix $\boldsymbol{B}$. A compressed sensing algorithm is then applied to interpolate $\boldsymbol{R}$ from $\boldsymbol{B}$ and the reduced DFT matrix.

This method leads to a slightly poorer sensing performance than OFDM sensing, but maintains the improved communication performance of IM-OFDM over OFDM.

A second method is to use frequency-agile radar in conjunction with IM-OFDM communication, as proposed by Sahin *et al.* [116]. In this system, radar signals are sent over some of the deactivated communication subcarriers, according to the activated communication subcarrier indices. The system ensures that there is at least one null subcarrier per group of subcarriers. Two Golay complementary sequences are transmitted over

the radar signals per time slot, with each radar signal comprising of a single element of one of the sequences. Low-density parity check codes are also implemented.

Unlike many other references, [116] considers bistatic sensing. This allows the communication receiver to use the radar signal for channel estimation. A null subcarrier estimation-based method is used for sensing. The system determines the null subcarrier(s) in each group, which allows it to identify the communication and radar subcarriers, following the activation pattern of the system for given subcarrier indices. Delay and Doppler estimation is performed similarly to conventional OFDM sensing, with all non-radar subcarriers set to 0.

Two communication decoding methods are applied. The first is the null subcarrier estimation-based decoding used for sensing. The communication symbols are then demodulated using conventional methods. The second communication decoding method is an ML-based decoding method. This decoding algorithm considers all possible communication and radar subcarrier combinations, and selects the most likely one.

Two comparison system are presented. The first is a similar IM-OFDM system utilising irregularly spaced pilot symbols for channel estimation, and the second is a JCR OFDM system with comb-type pilots. The channel is estimated through linear interpolation between the pilot symbols. The maximum delay of a target is less than the length of the cyclic prefix of the OFDM signal.

The comb-type pilot OFDM scheme exhibits periodicity in the range estimation, which limits its maximum detectable range. This is not present in the proposed IM-OFDM scheme. The OFDM and IM-OFDM interpolation channel estimation systems both exhibit similar radar MSE performances over the SNR range considered. The IM-OFDM radar-based channel estimation system has a much lower radar MSE than the other systems. As the number of moving targets is increased, the radar MSE performance for all of the systems increases.

For the OFDM system, a parity checking rate of 0.5 yields a lower BER than no parity checking, which has a lower BER than a rate of 0.75. A similar trend is seen at high SNR for the radar-based channel estimation with ML decoding IM-OFDM system. At lower SNR, the BER for the parity rate of 0.75 is lower than the BER for the uncoded signal. The null subcarrier-based decoding has a higher BER than the ML-based decoding over the range of SNR considered. The interpolation-based IM-OFDM system has a higher BER than the radar-based IM-OFDM system.

When there are one moving and two stationary targets, the OFDM system has a similar BER performance to the radar-based IM-OFDM system for a parity rate of 0.5. When the number of moving targets is increased, the BER of the OFDM system is greater at higher SNR than the radar-based IM-OFDM system, whose BER performance remains unaffected, for a parity rate of 0.5.

Future development of the proposed scheme will focus on its generalisation for different subblock and active subcarrier numbers. The method in [116] does not fully integrate sensing and communication, which can leads to larger hardware costs, as two separate types of signals are transmitted.

Alternative systems using frequency IM for ISAC have also been investigated. [165] uses circularly-shifted chirps based on the DFT-s-OFDM structure in conjunction with IM and PSK modulation for ISAC. The chirps are sent along frequencies dictated by the subcarrier indices. The transmitted signal is similar in structure to an IM-OFDM signal, with the signal on the activated subcarriers being chirps with embedded PSK symbols created through frequency domain spectral shaping. No comparisons are made with conventional OFDM ISAC.

Another system that incorporates frequency IM for ISAC is [166]. This system uses carrier agile phased array radar for sensing, whilst communicating using frequency and space IM. The available frequencies are divided into subcarrier groups, with the frequencies each antenna transmits being dictated by the frequency and space indices. This allows the radar functionality to be unimpeded by addition of the communication data, with the inherent randomness of communication data being exploited by the system. The throughput of this system remains much lower than if communication waveforms where used. A companion paper [167] to [166] considers the case where the system is only used for sensing. The results in [167] show that the system's sensing performance is lower than that of Frequency-Agile Radar (FAR) in all considered conditions.

The system in [168] considers the combination of IM and of the Frequency-Diverse Array (FDA) radar, with the addition of phase modulation applied to the transmitted radar signals. The introduction of IM leads to higher sidelobes in the beampattern used for range estimation, but it is shown to have no significant effect on the beampattern harnessed for angle estimation. The CRB of the proposed system is also shown to be lower than that of traditional FDA radar systems.

The authors of [70] develop a general FH MIMO model for ISAC, which can be tuned for harnessing multiple communication strategies. These are conventional data modulation, such as QAM or PSK, IM, and FH code selection. The transmitted signal is split into separate matrices, each representing a specific communication signaling strategy. The pair of hybrid communication strategies considered are the combination of PSK and FH code selection, as well as the combination of FH code selection and IM. The BER of the hybrid schemes constitutes a middle ground between the BER of the individual constituent signaling strategies. The sidelobe levels of the hybrid schemes are dominated by the highest sidelobe levels of the component signaling strategies. This leads to a trade-off between the communication throughput and sensing performance.

IM can also be implemented in conjunction with FAR. The authors of [31] undertake a numerical evaluation of OFDM and IM-FAR, under Rayleigh fading and without interference whilst ensuring that both systems have the same throughput. Their results show that both systems have a similar sensing MSE performance, with OFDM having a significantly superior BER performance over IM-FAR. The authors mention that the IM-FAR sensing performance would be greater than OFDM when there are multiple devices, as IM-FAR has a low mutual interference, as mentioned in [167].

2.7 Example ISAC Research Directions

2.7.1 Non-Orthogonal Multiple Access ISAC

As the number of connected devices is predicted to increase, the pressure on the available resources will naturally increase. To increase the number of devices serviced by the limited resources, new multi-user methods need to be developed and implemented. Many implemented systems utilise orthogonal access methods, such as Orthogonal Frequency-Division Multiple Access (OFDMA), but these present hard limits on the number of connected devices, imposed by the resources available. In contrast, NOMA methods allow a greater number of devices to be serviced for the same amount of resources, as they are not limited by the orthogonality requirement. This comes at the cost of increased interference between devices, due to the lack of orthogonality.

Mu *et al.* [169] develop a NOMA aided joint radar and multicast-unicast communication system. Multicast communication refers to communicating with both radar and communication users, whereas unicast communication refers to communicating with communication users only. Two methods are presented. The first is a beamforming-based approach for a single pair of communication and radar users. Separate beamformers are used for multicast and unicast transmission. The beamformers are optimised to maximise the communication rate for unicast transmission, whilst ensuring a minimum sensing and multicast performance. This method is used as a baseline for the second one. The second method is a cluster-based approach, using a single beamformer for both unicast and multicast per communication and radar user pair. The optimisation problems for both methods maximise the unicast rate given sensing and multicast constraints. These problems are non-convex, hence convex approximations are generated and solved. Successive interference cancellation is employed to reduce the inter-signal interference.

These methods are compared to a Time Division Multiple Access (TDMA) system, which uses TDMA to transmit the unicast and multicast signals, and a system that employs separate beamformers for unicast and multicast transmission, but uses both

beamformers for radar user detection, without successive interference cancellation being employed. The unicast rate of the proposed systems decreases as the multicast rate requirement is increased, and is higher than that of the TDMA scheme. It is indicated that a time allocation ratio of 0.5 has been applied, but the mechanism for this allocation is unclear. Consequently, this may not be an optimum arrangement for each minimum multicast rate requirement. As the beam pattern mismatch threshold is increased, the unicast rate increases for the beamforming-based and TDMA schemes, whilst it remains constant for the combined beamforming scheme. It is unclear whether the combined beamforming scheme lacks a beamforming mismatch constraint, or whether the lack of successive interference cancellation is the cause of the difference in response.

For the TDMA and cluster-based schemes, the total unicast rate increases as the number of radar and communication pairs increases from 2 to 3, before decreasing as the number of pairs further increases. This is deemed by the authors to be a characteristic of the increasing spatial degrees of freedom experienced for a low number of user pairs, accompanied by the escalating inter-user interference, when more user pairs are introduced. This in turn leads to a smaller fraction of power being allocated to unicast communication. However, the sensing performance is not investigated in this paper. A disadvantage of the beamforming-based scheme is that it requires two beamformers per user pair, hence potentially resulting in an excessive complexity, when multiple user pairs are considered. An advantage noted in the paper is that the proposed schemes have much higher unicast rates than the benchmark schemes.

Another NOMA ISAC system is considered in [98]. The results presented show that when the system is underloaded, NOMA has a lower combined communication and sensing performance than the comparison conventional ISAC model when there is low spatial correlation. When there is high spatial correlation, or when the system is overloaded, the NOMA system outperforms the comparison system using the same metrics.

2.7.2 Reconfigurable Intelligent Surface Aided ISAC

The propagation of signals is often blocked by the objects in the environment, leading to a lack of LoS paths. However, many estimation algorithms harnessed for sensing require LoS propagation. As a remedy, Reconfigurable Intelligent Surfaces (RISs) can be harnessed to improve the service for users roaming in complex NLoS environments. Some RISs are purely passive, only modifying the phase of the reflected signal. The more complex active RISs are also capable of manipulating the amplitude of the signals for the sake of enhancing the performance attained.

Hybrid active and passive sensing is being considered for ISAC [41]. This refers to systems that utilise active and passive methods of sensing, such as active and passive RIS, in addition to more typical sensing methods. [129] investigates the use of passive RIS to

reduce the multi-user interference introduced by DFRC systems. The DFRC waveform and RIS phase shift matrices are determined to minimise the multi-user interference. This is further developed in [130] with constant modulus and CRB constraints.

The combination of active and passive RIS elements for ISAC is proposed in [131]. The active elements contain amplifiers, in addition to the phase shifters present in passive RIS elements. The transmit beamformers and the RIS coefficients are optimised to maximise the worst case target illumination, given constraints including communication SINR.

[132] considers the issue of security in RIS-aided DFRC with multiple eavesdroppers, where the sensing targets are considered to be potential eavesdroppers. Artificial noise is introduced to reduce the sensing target SINR, as in [99,100].

A sensor-aided passive RIS solution is presented in [170]. The RIS is composed of three main elements: reflectors, radar sensors and energy harvesters. The sensing signal is either wirelessly transmitted by the RIS to the BS or conveyed through a direct physical connection. The energy harvesters harness a fraction of the impinging energy to power the RIS.

Three different transmission protocols for reflector and energy harvester elements are considered, with the location and number of radar sensor elements remains constant. The first protocol is "Element-splitting", where different elements are used for different functions. The second protocol is "Time-splitting", which is similar to TDMA, where elements are used as reflectors or energy harvesters at different time slots. More complex hardware is required compared to "Element-splitting", as the elements need to be capable of performing two functions. The last protocol presented is "Power-splitting", where the reflector and energy harvester elements are evenly spread throughout the RIS, with the proportion attributed to each function being variable. Again, this is a more complex protocol than the "Element-splitting" version.

RIS can be used for NLoS sensing, and to supplement LoS sensing. Sensor-aided zero-energy RIS has been shown to reduce the CRB of RIS sensing. Three different optimisation ideologies are presented. The first is the placement of a single function as the objective function, and the other functions are constraints in the optimisation problem. The second is the creation of objective functions for the three functions, and ranking them according to priority, while optimising each objective function in series. The third optimisation is the insertion of all three functions into a new composite objective function. It is more complex to generate and to optimise, but could lead to a superior performance.

The authors in [171] consider beyond diagonal RIS, where the reflection/scattering matrix has non-zero elements off the diagonal. Allowing the reflection matrix to be non-diagonal permits greater flexibility in optimising the RIS phase shifts. The addition of

the weighted communication and sensing SNRs is the objective function. As a result, a more complex algorithm is required to solve this problem compared to one with a diagonal reflection matrix constraint. Their results show that using a non-diagonal reflection matrix increases the communication and sensing SNRs compared to diagonal reflection matrices.

In [172], the authors introduce the combination of ISAC with symbiotic radio utilising RIS to improve the backscatter. The symbiotic radio is comprised of primary and secondary systems. The primary systems actively transmit, whilst the secondary systems transmit secondary data, such as propagation environment data, via backscatter. The backscatter transmission absorbs a portion of the energy of a received signal, then utilises the absorbed energy to transmit a modified version of the received signal. In the scenario considered by the authors, the backscatter includes additional sensing information produced by the sensors on the RIS. The symbol period of the backscatter signal is many times longer than that of the primary signal. The primary system is a BS, which transmits communication and sensing signals, and performs sensing parameter estimation in full-duplex. The authors assume any self-interference caused by the full-duplex operation is sufficiently mitigated. The additional information on the backscatter signal is modulated using BPSK. The communication user first demodulates the BS signal, then uses successive interference cancellation to estimate the encoded backscatter information.

An optimisation problem is proposed in which the objective function is the sum rate of the user, with the RIS backscatter information and BS sensing SNRs as constraints. The variables to optimise are the BS sensing receive beamforming vector, the BS communication and sensing transmit beamforming vectors, and the RIS reflection/phase shift matrix. As this is a complex problem, each set of variables is iteratively optimised, following the order in the previous paragraph using a block coordinate descent algorithm. The sum rate of the proposed method is significantly higher than that of the comparison scenarios where the RIS phase shifts are randomly generated, or where no RIS is present. The sum rate of the proposed method is slightly lower than that of the scenario where the BS only transmits a communication signal, and performs sensing only with this signal. The advantage of the proposed method over the communication signal only method is that the beampattern is more evenly spread between communication users and sensing target, allowing for a higher sensing SNR. The authors do no present any sensing results to show the impact of this beam-pattern difference on the sensing performance.

ISAC is considered with NOMA communication in [173]. The NOMA method employed is power domain NOMA, where there is a difference in power between transmitted signals. Successive interference cancellation is utilised to remove the interference of the stronger signals on the weaker ones. This work considers public and covert information transmission, where the covert signal is the weak one, and the public signal

is the strong one. The users receive the signal from the BS as well as the reflected signal from the RIS. The objective is to maximise the rate of the information transmitted to the covert user whilst ensuring that the covert information cannot be decoded by other users in the area. The public transmission rate, the sensing SNR, and the probability of the covert information being decoded are the constraints.

The optimisation problem assumes that the eavesdropping user has imperfect CSI. The beamforming vector for the public and covert transmission and the RIS reflection coefficients are the variables to be optimised. The algorithm proposed alternates between optimising the beamforming vectors and the RIS reflection coefficients. The results show that increasing the total transmit power and/or the number of RIS elements increases the covert information rate. Also, the covert information rate with the optimised RIS reflection coefficients is higher than when the RIS reflection coefficients are randomly generated. However, no alternative optimisation method is presented for comparison.

The authors of [104] consider NLoS sensing, and the users receive the signal from the BS as well as the reflected signal from the RIS. Active RIS is considered, where the RIS can amplify the reflected signal. A common signal is sent to the users, as well as a private signal sent to each individual user only, in addition to a radar signal sent to each sensing target. The RIS contains sensors, which detect the radar echoes from the targets and perform sensing parameter estimation. Each individual signal has its own beamforming vector associated with it, and assumes perfect successive interference cancellation to mitigate the interference of the signal from the BS on the signal reflected from the RIS.

The authors generate an optimisation problem to maximise the minimum sensing SINR, subject to the secrecy rate, security outage probability, and power constraints. The beamforming vectors and RIS reflection coefficients are the optimised variables. The proposed algorithm iterates between beamforming vector optimisation and RIS reflection coefficient optimisation. The results show that the beampattern produced has stronger peaks in the direction of the targets compared to a passive RIS sensing method. The minimum SINR of the proposed system is higher than that of the passive RIS method and a comparison method taken from the literature, where the sensing echo is reflected from the RIS to the BS for sensing parameter estimation. The additional propagation from the RIS to the BS leads to a additional attenuation imposed on the sensing echo, and hence seems to be a somewhat tenuous comparison. Nevertheless, this highlights the advantage of the RIS performing target estimation, but at the cost of additional resources at the RIS. As the secrecy rate constraint is increased, the minimum sensing SINR is reduced.

2.7.3 Low Earth Orbit aided ISAC

To increase spectrum coverage, LEO satellites are being considered [114, 133, 134, 174–176]. These systems have higher latency than terrestrial systems due to the increased propagation distances [133]. This leads to statistical channel information being used, since immediate channel information cannot be readily obtained. [133] also takes into account the effects of beam squinting. Communication and atmospheric sensing using THz waveforms in LEO systems is considered in [134]. CSS modulation is used, and is shown to outperform PSK modulation.

In [176], the combination of communication, remote sensing, and navigation using multiple clusters of LEO satellites is discussed. This combination is anticipated to offer improvement for vehicular transport, such as more accurate navigation based on the current road and traffic conditions, and improving the speed of the detection of emergency situations, such as accidents, in rural areas. The sensing is performed using synthetic aperture radar, which utilises multiple sensing images from different satellites in a given cluster throughout their orbit to build up a high resolution image of the target area. The authors describe four levels of integration of communication, sensing, and navigation: function-level, signal-level, data-level, and application-level. These are defined as follows:

- Function-level: where the different functionalities are present on each satellite, but function independently. The focus is on the management of the different functionalities.
- Signal-level: where a single waveform is used for the three functions, but the data of each function is only used for that given function, and is not shared between functionalities. The focus is on the waveform design and generation.
- Data-level: similar to signal-level, but with the data shared among all the functionalities. The focus is on using the combined data sets to further optimise the waveform and detection/estimation models.
- Application-level: where the functionalities are used to support the tasks undertaken by the vehicles, rather than meet pre-determined performance goals. It is data-level integration expanded to consider what is required by the vehicles on the ground, with the performance requirements changing over time depending on the vehicle's task.

A simulation example is provided to show the improvements presented by function-level and signal-level integration compared to no integration. Increasing the integration increases the communication, navigation and remote sensing performance. Suggested future research areas include satellite constellation design, satellite association optimisation for ISAC, and resource management.

An ISAC system for LEO satellite communication and sensing utilising Orthogonal Delay-Doppler Division Multiplexing (ODDM) is designed in [114]. ODDM is a DD waveform that was first introduced in [177], which is configured to ensure orthogonality between DD elements. Synthetic aperture radar is utilised for remote monostatic sensing by the satellite communicating to the users and sensing the environment on the ground. Each synthetic aperture focuses on a part of the satellite coverage area. There are time slots set for downlink transmission and sensing, and time slots set for uplink transmission.

In the first frame, a sequence of Zadoff-Chu pilot symbols, guard symbols, and control data symbols are transmitted. The subsequent frames transmit the data. MMSE channel equalisation is employed. ODDM's orthogonality reduces the complexity of MMSE equalisation, as the matrix inverse can be calculated using the Hadamard division. The sensing estimates are used to adjust and update the range estimate of the satellite to the users. The proposed method has the second lowest complexity of the benchmark channel estimation methods, whilst exhibiting the lowest PAPR of the more complex methods. The MSE of the proposed method is lower than that of the benchmark methods, while the BER of the ODDM modulation presents a 2 dB gain over the equivalent OFDM scheme, for both uncoded and coded transmission. This proposed method leads to a higher PSLR for range estimation than the benchmarks, but a similar PSLR for azimuth estimation. This proposed framework is implemented and validated in an experimental setting.

A bistatic sensing OFDM system is implemented in [175]. The transmitted signal from the satellite is reflected by the environment and received by UAVs, which perform the sensing parameter estimation. The satellite and the UAVs also communicate with each other. The authors assume the Doppler shift imposed on the communication signal by the satellite orbit is known, and that the satellite orbit and location, and the UAV locations, are also known. They assume the signals received by the UAV are synchronised with each other, whilst the transmitter on the satellite is not assumed to be synchronised with the receiver on the UAV. They also assume that the communication signal from the satellite to the UAV only consists of LoS propagation, and that the interference from the communication signal from the satellite to the UAV on the sensing signal is mitigated, and hence is not considered.

To produce the sensing image, range compression is performed by a Matched Filter (MF) method using the reconstructed communication information, and a back projection algorithm is employed for azimuth compression. The authors formulate an optimisation problem to achieve the largest image resolution by determining the optimal UAV velocity. The timing and carrier frequency offsets are determined by self-correlation of the reconstructed communication signal. The estimated timing and carrier frequency offsets are used as references to mitigate the effects of timing offsets and carrier frequency offsets on the sensing estimates.

In order to reduce the ambiguity in the sensing image, a 5G positioning reference signal consisting of a QPSK-modulated pseudo-random Gold sequence is inserted into the satellite transmit signal in a comb structure. The results shows a 61 % improvement in the resolution when the UAV velocity is optimised. The range resolution, image quality, and position estimate of the proposed synchronisation method approach that of the perfect synchronisation case, and outperform the benchmark method that estimates the offsets only through demodulation. When the communication SNR is above a threshold (-22 dB in the case simulated), the MSE of the time and phase offset estimations reach and follow the CRLB. No comparison method is shown for the MSE curves. The ambiguity suppression method is shown to suppress ambiguity, but is not compared to another method. The methods are then experimentally validated.

A study of satellites sensing, and communicating with, aerial terminals is presented in [178]. A combination of sensing and extended Kalmann filters is used to predict the location of the aerial terminals to reduce the signalling overhead and improve beamforming. The authors assume that the satellite has the same number of transmit and receive antennas. The delay and Doppler estimation is done using an MF method, whilst the estimated AoA is calculated using the delay and Doppler estimates. The channel is assumed to only contain LoS propagation. The beamforming optimisation problem is formulated with the transmission rate as the objective function, and the x-axis and y-axis AoA CRLBs as constraints.

This problem is then reformulated to reduce the optimisation complexity. A branch-and-reduce-and-bound algorithm is employed to solve this problem. A sub-optimal problem is also formulated, which is less complex to solve, and a lower complexity method is proposed to solve it. A long list of beamforming algorithms are then compared. The two proposed methods exhibit a tracking performance and CRLBs that are slightly inferior to those of the higher-complexity optimal benchmark method, but outperform most other methods to which they are compared. The proposed lower complexity method results in only a small performance degradation compared to the proposed higher complexity method.

[117] presents work on a satellite constellation structure which comprises of one central satellite, surrounded by many auxiliary satellites. The central satellite does not transmit to the ground, but only communicates with the auxiliary satellites using inter-satellite optical links. It assumes the optical links transmit information at a high enough rate to not limit the system's performance. All satellites use the same spectrum for transmission, and the transmit signal from each satellite is the addition of the communication signal and a TD location sensing waveform. Both communication and sensing signals are used for sensing, and the sensing waveform supplements the sensing capabilities of the communication signal.

The authors assume the user's equipment and the satellites apply techniques to mitigate the delay and frequency offsets. Some references to publications of such techniques are given, but no information on the techniques were provided. The achievable transmit rate is used as the communication metric, and the sensing echo received by the auxiliary satellites are transferred to the central satellite for processing. A ML method is used to estimate the target reflection coefficient and a particle swarm optimisation algorithm, based on bird swarm feeding behavior, is used to estimate the target coordinates, as this is less complex than ML. The authors derive the CRB of this estimation algorithm. The optimisation problem is defined as the minimisation of the CRB for the given power and individual user communication rate constraints. The variables are communication beamforming vectors and sensing waveforms.

The objective function is reformulated, and iterative approximations of the maximum eigenvalue of the non-convex objective function are used to create successive convex approximations of the objective function. The solution of each iteration can be calculated following a provided equation. A second optimisation problem with the communication rate as the objective function and the CRBs as constraints is also given. The problem is reformulated as a convex problem, which the authors state can be solved using standard convex methods by adding a penalty function.

The complexity analyses of the particle swarm estimation algorithm and the sensing objective optimisation problem are given. The sensing algorithm is shown to exhibit a significantly lower CRB than the comparison communication and sensing methods. A pure sensing method that disregards the communication rate constraint still exhibits a lower CRB than the proposed method, demonstrating the trade-off between communication and sensing performance. Increasing the number of antenna elements (both receive and transmit) decreases the CRB, as does increasing the total power available. However, increasing the power reduces the performance improvement derived from increasing the number of elements on the antennas. It is noted that the proposed sensing algorithm has a similar RMSE performance to an ML method with a grid size of 0.001 m, whilst having a much smaller computational complexity.

2.8 Summary of Literature Review

The literature review has sought to provide background and context to the combination of sensing and communication. The concept of combining communication and sensing has been understood and exploited since the earliest use of radio. Early systems were basic directional sensing of communication signals, or data added to directional signals for identification and meteorological information. Development was rapid, with bi-directional communication added, flight control information, landing controls, and

anti-jamming systems. The modern understanding of ISAC, using digital signal processing, dates back to the 1960s.

The efforts that have been invested show that there is an essential and increasing need for this technology, because of limited energy and spectral resources combined with an exponential growth in the predicted number of devices and the step change that is occurring in their functionality. An example of the latter is the move from sensing and communication functions that assist in a vehicle's control and operation to a system in which the vehicle represents one component of a network of integrated devices, all operating and controlled without human intervention.

The literature review includes a range of general papers, which are in themselves, surveys of other published work. These provide a convenient and focused overview of the subject. These illustrate that there has been quite extensive discussions and proposals on a wide range of potential directions for this research.

The actual work has been shown to be somewhat more limited, primarily comprising theoretical simulations of specific proposals, generally very restricted in their application, and severely constrained by their assumptions. Published results tend to present a restricted view on the relative performance of different methodologies, frequently leading to conclusions that have limited general applicability. Consequently, caution will need to be applied in using these results to extend the work in specific directions which may not align precisely with the published work.

An example of this is where comparisons are made between proposed systems and others from literature, in which the proposed systems are optimised for the specific problem considered, and the systems from literature do not appear to be similarly optimised. It is understood that this occurs because the authors wish to ensure that the systems have a common input data set, but this is not necessarily representative of how each individual system would be applied in a practical application. This is illustrated in the literature review when similar methodologies occur in multiple publications, but their relative performance is inconsistent.

Even rarer is real experimental data to support simulation results. Nevertheless, the few examples that do exist support the conclusion that the combination of communication and radar has great promise in providing enhancements to both functions as a consequence of their integration, as well as peripheral benefits such as reduced power consumption and reduced system size and weight.

It is observed that there are almost as many different metrics as there are proposals. This adds to the difficulty in drawing specific comparisons. There may be benefit in the development of a targeted set of metrics that are broad enough to cover all aspects of the field, whilst at the same time providing some consistency in quantifying performance. It is appreciated that this could be viewed as excessively restrictive in such

a young field, and thus perhaps this could take the form of a test suite rather than specific metrics. This would permit comparison on common problems of proposed systems with other optimised systems.

This leads to a philosophical question about the direction of development in this field. The reviewed work seeks to quantify the capabilities of their various systems, but it could be proposed that there is a need to define the requirements towards which these systems must be developed. A suitable test suite could be a means to define these goals in a consistent and coherent manner.

Papers are included to consider the two fundamental approaches to this problem, that is using radar waveforms for communication or communication waveforms for radar. It would be hoped that a literature review could identify which of the two approaches would give the best overall performance. Unfortunately, for the reasons noted above, this is difficult to do. Using radar waveforms for communication appears to be limited in applicability compared to the reverse, due to severely limited communication capacity. This occurs because the focus of these systems does not permit any compromise on sensing performance. The radar only systems used for comparison for systems in which a communication waveform is used for sensing do not appear to be defined using existing state of the art radar. This leads to a mismatch when comparing the two approaches.

In conclusion, this field is likely to be a fundamental component in the development and exploitation of the future IoT environment. The existing work provides a sound and reasonably comprehensive basis for the development of this topic, with the noted caveats. The potential to show performance improvements in both sensing and communication due to their combination is enticing and worthy of further exploration.

Chapter 3

Index Modulation OFDM ISAC

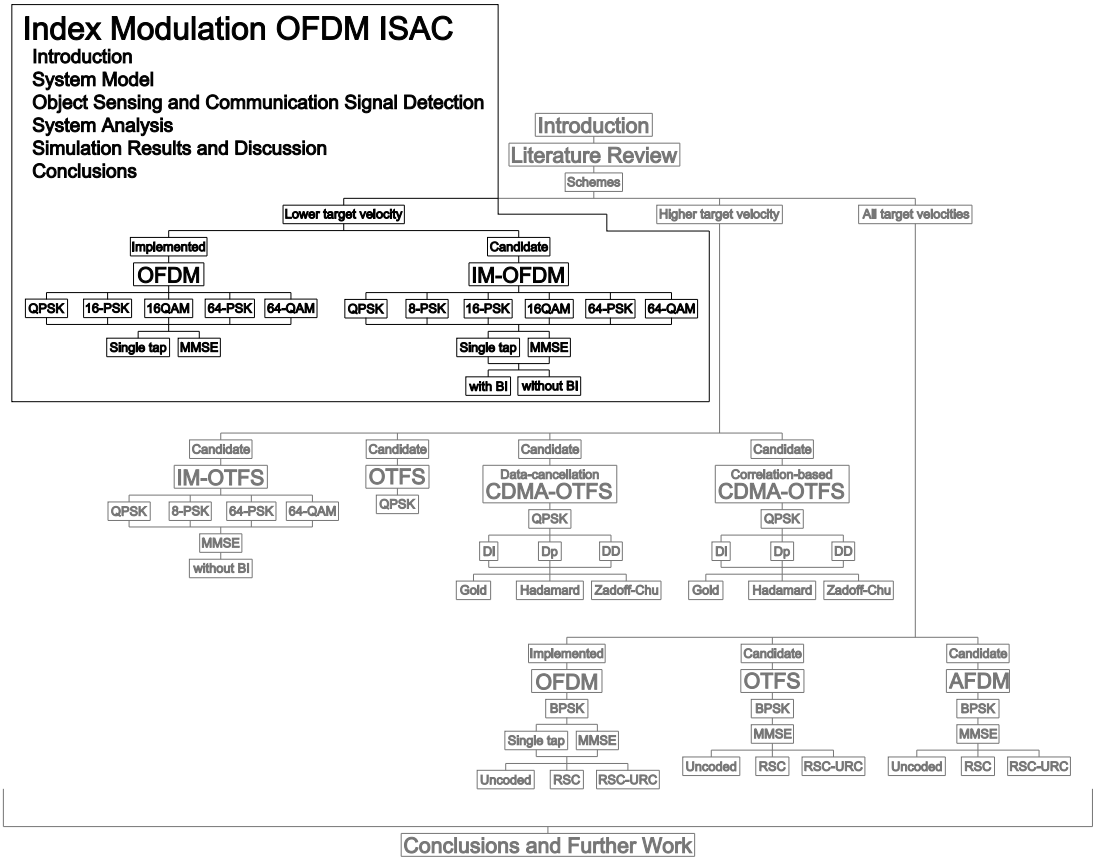

3.1 Introduction

OFDM is a well established waveform used in 4G and 5G standards, with much of the hardware in use supporting it. As the frequency subcarriers are orthogonal to each

other at lower Doppler shifts, simple equalisation and sensing methods can be implemented. Many propagation environments only contain users, objects, and targets that move at low velocities, such as in dense cities, where the speed of vehicles is limited. Hence, OFDM is likely to still play an important role in ISAC signaling in the next wireless generations.

This chapter describes the first published part of the research undertaken, on IM-OFDM ISAC [1]. FD IM reduces the TD PAPR of the OFDM signal, and increases the transmit power on the activated subcarriers through power redistribution. Although the communication performance of IM-OFDM has been characterised, little published work has investigated its use for sensing. The sensing methods previously utilised function either by inserting a separate sensing signal, or by accepting a sensing performance equal to or lower than that of OFDM. The sensing method proposed seeks to embrace the advantages of IM-OFDM to improve both the communication and sensing performance relative to OFDM.

Literature reviews of OFDM ISAC, and of FD IM and IM-OFDM ISAC are presented in Sections 2.5.1 and 2.6 of Chapter 2, and hence are not repeated here.

3.1.1 Motivation for the Proposed System

The objective is to develop an IM-OFDM ISAC system that outperforms an OFDM ISAC system for both communication and sensing. As previously mentioned in Section 2.6, the combination of IM and OFDM is potentially capable of improving both the implementation and energy efficiencies, as well as the robustness to interference and noise. These characteristics allows IM-OFDM to outperform OFDM based communication. Briefly, IM leads to an increased power on the activated subcarriers, which is capable of improving the sensing performance. Given these promising features, IM-OFDM is harnessed for ISAC applications.

The existing published work either inserts a radar signal into the deactivated subcarriers, thereby using a radar signal for sensing, or employs compressed sensing, which leads to a lower sensing performance than OFDM ISAC.

Hence, a novel low complexity algorithm is proposed that collects observations of the received signal to “fill in” the “holes” in the sensing data created by IM-OFDM, whilst taking advantage of the increased signal power gleaned from activating fewer subcarriers. This occurs over multiple transmit frames, which delays the target estimation. As OFDM sensing assumes low target velocities, this delay is shown to have a negligible impact on the sensing performance of IM-OFDM.

The simulation results will demonstrate that an IM-OFDM ISAC scheme is capable of outperforming its OFDM ISAC counterpart for both sensing and communication. The

impact of block interleaving and of the modulation type on the sensing performance are also discussed. Since IM-OFDM sensing removes the data from the received signal, block interleaving has no significant impact on the sensing performance, which is validated through the simulation results.

Two modulation types are considered, PSK and QAM. As PSK maintains a constant amplitude, the transmitted data has no significant effect on its sensing performance. This is true, regardless of the modulation order. By contrast, varying the QAM modulation order has a substantial impact on the system's sensing performance, caused by the increased number of possible amplitude levels, as the QAM modulation order is increased. Due to this, sensing using PSK outperforms sensing with QAM at modulation orders higher than 4, as BPSK and QPSK have the same constellations as 2-QAM and 4-QAM, respectively.

3.1.2 Contributions

TABLE 3.1: Contrasting on contributions to the literature

Papers / Topics	[164]	[165]	[166]	[116]	[36]	[12]	[123]	This work
Channel modeling								
Doubly selective channel model				✓		✓	✓	✓
System								
IM-OFDM	✓			✓				✓
Frequency IM	✓	✓	✓	✓				✓
Reduced PAPR compared to OFDM	✓	✓	✓	✓			✓	✓
Improved data efficiency compared to OFDM	✓	✓	✓				✓	✓
Combining multiple observations for sensing								✓
Results								
BER and RMSE improvements to OFDM sensing whilst maintaining throughput								✓
Effect of block interleaver on sensing RMSE								✓
Effect of PSK and QAM modulation on RMSE								✓

This work's contributions are contrasted with the literature in Table 3.1, and are detailed below:

- A novel low complexity algorithm is conceived to "fill in" the "holes" in the sensing data created by IM-OFDM, whilst taking advantage of the increased subcarrier power gleaned from activating fewer subcarriers. This allows IM-OFDM

sensing to outperform OFDM, with a slight increase in delay. As OFDM sensing assumes a low-Doppler environment, the impact of this sensing delay increase is negligible.

- An analysis of the impact of block interleaving and QAM/PSK on sensing performance.

3.2 System Model

This section presents the system model and its underlying assumptions. The system considers point-to-point transmission between two communication devices, and monostatic sensing of multiple targets.

It is assumed that there is no external interference during transmission. The CP is assumed to be sufficiently long to avoid Inter-Symbol Interference (ISI), which is perfectly removed from the received signal at the receiver. The channel's Doppler shifts are less than a tenth of the subcarrier spacing, to correlate with other studies, but this is not a limitation of this system, as a time and frequency selective channel is modeled. For communication, integer delay indices are assumed, as discussed in Section 3.2.2.2, along with perfect channel estimation.

For sensing, it is assumed that the self-interference between the transmit signal and received echos is perfectly mitigated, and that there is a single LoS path between the transmitter and each target, with the number and directions of the targets being known. The self-interference is assumed to be mitigated by appropriate shielding, signal processing methods, and/or an orthogonal signaling scheme (e.g. similar to TDMA). A single LoS path is assumed, since the system operates in the mmWave band, where the NLoS paths become attenuated to the extent that they are not significant for monostatic sensing. The number of targets is assumed to be known, either through prior knowledge, or by the use of a separate estimation algorithm, such as a generalised likelihood ratio test [145, 146]. The directions of the targets are assumed to be estimated by a separate method, for example by the popular MUSIC algorithm [39].

The block diagrams of the communication and sensing models are shown in Figures 3.1 and 3.2 respectively.

3.2.1 Transmitted Signal

To implement IM-OFDM, the M subcarriers of the system are partitioned into G subcarrier groups. Hence, each group contains $\frac{M}{G} = M_G$ subcarriers. For IM, M_A subcarriers are activated in each group at any given time, with $M_A < M_G$. Since the total available power is constant, additional power is allocated to the activated subcarriers when

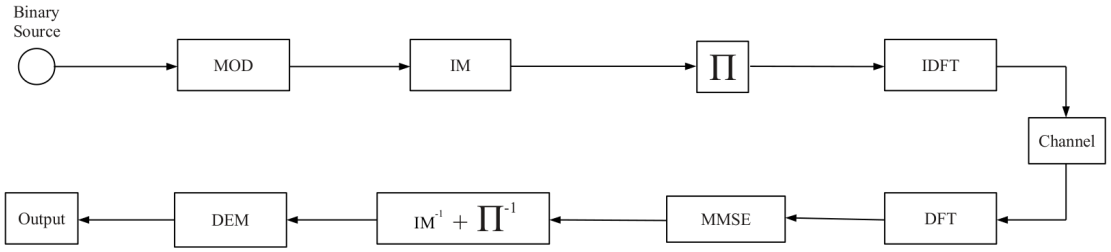

FIGURE 3.1: Block diagram of the communication model

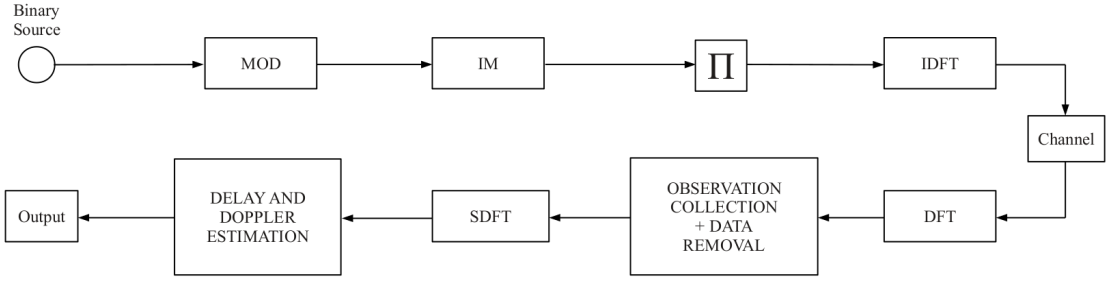

FIGURE 3.2: Block diagram of the sensing model

fewer subcarriers are activated. Therefore, the ratio of power assigned to each activated subcarrier of IM-OFDM compared to an equivalent OFDM system having the same throughput is $\frac{M_G}{M_A}$.

The number of bits determining the activated subcarrier indices of a group is $\beta_G = \lfloor log_2 \mathcal{C}_{M_G}^{M_A} \rfloor$, where $\lfloor \cdot \rfloor$ is the floor function, and $\mathcal{C}_{M_G}^{M_A}$ is the total number of permutations of M_A in M_G indices. Correspondingly, the number of possible subcarrier combinations used for IM within a group is $C_N = 2^{\beta_G}$. The C_N subcarrier combinations are collected to form a set, expressed as $\mathfrak{C}_N \in \mathbb{Z}^{C_N \times M_A}$. On each of the activated subcarrier, a Γ-PSK or Γ-QAM symbol is transmitted, with each symbol conveying $\beta_\Gamma = log_2(\Gamma)$ bits. Therefore, the total number of bits β transmitted per IM-OFDM symbol is $\beta = G\,(\beta_G + M_A \beta_\Gamma)$.

In this IM-OFDM system, block interleaving is employed for distributing the activated subcarriers from each group across the entire available bandwidth, dispersing the subcarriers across all groups. This minimises the probability that an entire group of subcarriers will experience similar fading, and hence increases the communication reliability. Specifically, the block interleaving process is described as:

$$\bar{\boldsymbol{x}}_{\infty,\,n}[\bar{m}_G G + g] = \bar{\boldsymbol{x}}_n[gG + \bar{m}_G]\,, \tag{3.1}$$

where $\bar{\boldsymbol{x}}_n \in \mathbb{C}^{M\times 1}$ is the vector of modulated data for the n^{th} IM-OFDM FD symbol, $\bar{\boldsymbol{x}}_{\infty,\,n} \in \mathbb{C}^{M\times 1}$ is the vector of modulated data after block interleaving, $n = [0, ..., N-1]$ is the IM-OFDM symbol index, with N being the number of IM-OFDM symbols transmitted in a frame, $\bar{m}_G = [0, ..., M_G - 1]$ is the subcarrier index within a group, and $g = [0, ..., G-1]$ is the subcarrier group index.

After block interleaving, the IDFT is applied to $\bar{\boldsymbol{x}}_{\infty,\,n}$ to determine the TD signals for transmission, which is expressed as:

$$\boldsymbol{x}_n = \mathcal{F}_M^{-1}\left(\bar{\boldsymbol{x}}_{\infty,\,n}\right) , \tag{3.2}$$

where $\boldsymbol{x}_n \in \mathbb{C}^{M\times 1}$ is the transmitted baseband TD signal, and $\mathcal{F}_M^{-1}$ is the M-point IDFT.

Again, it is assumed that the CP is long enough to guarantee that there is no ISI between adjacent OFDM symbols. It is also assumed that it is perfectly removed from the received signal, thereby having no detrimental effect on the system performance. Consequently, the CP is not considered any further.

3.2.2 Channel Models and Received Signal

The transmitted signal is passed through a time and frequency selective fading channel, as modelled in [179]. The DD representation of the fading channel is:

$$\widetilde{h}(\tau,\nu) = \sum_{p=0}^{P-1} \widetilde{h}_p \delta(\tau-\tau_p)\delta(\nu-\nu_p) , \tag{3.3}$$

where τ is the delay, ν is the Doppler shift, p is the propagation path index, P is the total number of propagation paths, τ_p is the delay associated with the p^{th} path, ν_p is the Doppler shift associated with the p^{th} path, $\widetilde{h}_p$ is the fading gain and path loss associated with the p^{th} path, and $\delta(\cdot)$ is the Dirac delta function.

When sampled in the DD, the channel can be represented by the time-invariant fading gain and path loss $\widetilde{h}_p$, the delay index l, and the Doppler index k. The delay and Doppler indices are defined as:

$$\widetilde{h}_p = \widetilde{\phi}_p \widetilde{\psi}_p , \tag{3.4}$$

$$l = (\Delta f M)\tau , \tag{3.5}$$

$$k = \frac{N}{\Delta f}\nu , \tag{3.6}$$

where $\widetilde{\phi}_p$ is the fading gain associated with the p^{th} path, $\widetilde{\psi}_p$ is the path loss associated with the p^{th} path, and Δf is the subcarrier spacing.

The TD representation of the fading channel is therefore:

$$h_{m,\,n,\,p} = \widetilde{h}_p e^{j2\pi k_p \frac{nM+m-l_p}{MN}} , \tag{3.7}$$

where $j = \sqrt{-1}$, m is the sample index, while l_p and k_p are the delay and Doppler indices associated with the l^{th} propagation path.

The received TD signal $\boldsymbol{y}_n \in \mathbb{C}^{M\times 1}$ is expressed as:

$$\boldsymbol{y}_n[m] = \sum_{p=0}^{P-1} h_{m,\,n,\,p}\, \boldsymbol{x}_n[m - l_p] + \boldsymbol{z}_n[m]\,, \tag{3.8}$$

where $\boldsymbol{z}_n$ is the complex AWGN, with mean $\mu_z = 0$ and variance σ_z^2, expressed as $\mathcal{N}(\mu_z, \sigma_z^2)$, and $\boldsymbol{x}_n[m - l_p]$ is the delayed transmitted baseband TD signal propagating through the l^{th} path, with $\boldsymbol{x}_n \in \mathbb{C}^{M\times 1}$.

When the delay indices of the propagation paths are assumed to be integers, the fading channel and the received signal can be modelled as in (3.8). When this assumption is discarded, the values of m, at which $m - l_p$ is an integer, no longer coincide with the integer matrix indices. As matrices do not have fractional indices, the channel has to be modelled differently. A portion of the fading channel is modelled in the FD, then converted to the TD as follows:

$$\boldsymbol{x}_n[m - l_p] = \frac{1}{\sqrt{M}} \sum_{\bar{m}=0}^{M-1} \bar{\boldsymbol{x}}_{\infty,\,n}[\bar{m}] e^{j2\pi \frac{(m-l_p)\bar{m}}{M}}\,, \tag{3.9}$$

where $\bar{m}$ is the subcarrier index.

The received TD signal becomes:

$$\boldsymbol{y}_n[m] = \frac{1}{\sqrt{M}} \sum_{p=0}^{P-1} h_{m,\,n,\,p} \sum_{\bar{m}=0}^{M-1} \bar{\boldsymbol{x}}_{\infty,\,n}[\bar{m}] e^{j2\pi \frac{(m-l_p)\bar{m}}{M}} + \boldsymbol{z}_n[m]\,. \tag{3.10}$$

Equation (3.10) is more computationally demanding than equation (3.8), because for each IM-OFDM symbol, ML IDFTs are taken, as opposed to having a single IDFT for integer indices.

3.2.2.1 Sensing

For simplicity, having a single propagation path spanning from the source to the sensing target is assumed, since the power of the scattered NLoS paths is considered negligible compared to the power of the LoS paths. The fading gain $\widetilde{\phi}_{p,\,sen}$ and the path loss $\widetilde{\psi}_{p,\,sen}$ for the p_{sen}^{th} target are:

$$\widetilde{\phi}_{p,\,sen} = 1\,, \tag{3.11}$$

$$\widetilde{\psi}_{p,\,sen} = \sqrt{\frac{c_0^2 \gamma_p}{(4\pi)^3 f_c^2 R_{p,\,sen}^4}}\,, \tag{3.12}$$

where $(\cdot)_{sen}$ denotes a sensing variable, c_0 is the speed of light, f_c is the carrier frequency, γ_p is the radar cross-section of target p_{sen}, and $R_{p,\,sen}$ is the distance between the sensing target p_{sen} and the transmitter. The total number of sensing targets is P_{sen}.

Given $R_{p,\,sen}$ and the velocity $V_{p,\,sen}$ of the p_{sen}^{th} target, the delay $\tau_{p,\,sen}$ and Doppler shift $\nu_{p,\,sen}$ of the p_{sen}^{th} target are:

$$\tau_{p,\,sen} = \frac{2}{c_0} R_{p,\,sen}\,, \tag{3.13}$$

$$\nu_{p,\,sen} = \frac{2f_c}{c_0} V_{p,\,sen}\,. \tag{3.14}$$

The associated delay and Doppler indices are determined following (3.5) and (3.6).

3.2.2.2 Communication

The communication path loss is formulated as:

$$\widetilde{\psi}_{p,\,com} = \sqrt{\frac{c_0^2}{(4\pi)^2 f_c^2 R_{com}^2}}\,, \tag{3.15}$$

where $(\cdot)_{com}$ denotes a communication variable, while R_{com} is the distance from the transmitter to the receiver.

The communication channel is assumed to have P_{com} propagation paths, where the first path of $p_{com} = 0$ is the LoS path, and the subsequent $P_{com} - 1$ paths are NLoS paths. Hence, following [179], the fading gains of the communication paths can be expressed as:

$$\widetilde{\phi}_{p,com} = \begin{cases} \sqrt{\frac{\kappa}{\kappa+1}}, & \text{if } p_{com} = 0 \\ \sqrt{\frac{1}{(\kappa+1)(P_{com}-1)}}\zeta_{l,com}, & \text{if } 0 < p_{com} \leq L-1, \end{cases} \tag{3.16}$$

where κ is the Rician K factor, and $\zeta_{l,\,com}$ is a complex Gaussian random variable having a mean of $\mu_{com} = 0$ and a variance of $\sigma_{com}^2 = 1$, expressed as $\mathcal{N}(0, \sigma_{com}^2)$.

As the signal transmitted along the LoS path is the first to arrive at the receiver, its delay can be set to 0. The delays associated with the propagation paths for communication are denoted as:

$$\tau_{p,\,com} = \begin{cases} 0\,, & \text{if } l = 0 \\ \tau_{max,\,com}\eta_\tau\,, & \text{if } 0 < p_{com} \leq L-1\,, \end{cases} \tag{3.17}$$

where η_τ is a random variable following a uniform distribution between 0 and 1, and $\tau_{max,\,com}$ is the maximum propagation path delay, defined as:

$$\tau_{max,\,com} = \frac{P_{com}}{\Delta f M}\,. \tag{3.18}$$

The Doppler shift of each communication path is:

$$\nu_{p,com} = \begin{cases} \nu_{com}, & \text{if } l = 0 \\ \nu_{max,com}(\eta_\nu - 0.5), & \text{if } 0 < p_{com} \leq L-1, \end{cases} \tag{3.19}$$

where ν_{com} is the Doppler shift of the communication receiver, $\nu_{max,\,com}$ is the maximum Doppler shift, and η_ν is a random variable following a uniform distribution between 0 and 1. The Doppler shift and maximum Doppler shift of the communication receiver are:

$$\nu_{com} = \frac{f_c}{c_0} V_{com}\ , \tag{3.20}$$

$$\nu_{max,\,com} = \frac{\Delta f}{N} \lceil \frac{N}{\Delta f} \nu_{com} \rceil\ , \tag{3.21}$$

where V_{com} is the communication target velocity, and $\lceil \cdot \rceil$ is the ceiling function.

3.3 Object Sensing and Communication Signal Detection

This section describes the target detection and parameter estimation for sensing, and the signal detection considered in communication. For both sensing and communication, the received TD signal $\boldsymbol{y_n}$ is first converted to the FD before processing:

$$\bar{\boldsymbol{y}}_n = \mathcal{F}_M\left(\boldsymbol{y}_n\right)\ , \tag{3.22}$$

where $\mathcal{F}_M$ is the M-point DFT.

3.3.1 Object Sensing

Following [12], when subcarrier orthogonality is assumed, the FD received signal can be simplified to:

$$\bar{\boldsymbol{y}}_{n,\,sen}[\bar{m}] = \bar{\boldsymbol{x}}_{\infty,\,n}[\bar{m}] \sum_{p_{sen}=0}^{P_{sen}-1} \widetilde{h}_{p,\,sen} \left(\boldsymbol{a}(l_{p,\,sen})\boldsymbol{a}(k_{p,\,sen})^T\right)_{\bar{m},\,n} + \bar{\boldsymbol{z}}_n[\bar{m}]\ , \tag{3.23}$$

where $\bar{m} = 0, ..., M-1$, $n = 0, ..., N-1$, $\bar{\boldsymbol{z}}_n$ is the FD AWGN, while $\boldsymbol{a}(l_{p,\,sen}) \in \mathbb{C}^{M\times 1}$ and $\boldsymbol{a}(k_{p,\,sen}) \in \mathbb{C}^{N\times 1}$ are the delay and Doppler shift index steering vectors, respectively, defined as:

$$\boldsymbol{a}(l_{p,\,sen})[\bar{m}] = e^{-j2\pi \frac{\bar{m} l_{p,\,sen}}{M}}\ , \tag{3.24}$$

$$\boldsymbol{a}(k_{p,\,sen})[n] = e^{j2\pi \frac{n k_{p,\,sen}}{N}}\ . \tag{3.25}$$

Although this representation is used in this Section to describe the sensing method, the simulations in Section 3.5 assume the channel model from Section 3.2.2, where the subcarrier orthogonality is not assumed, and can be degraded at large velocities.

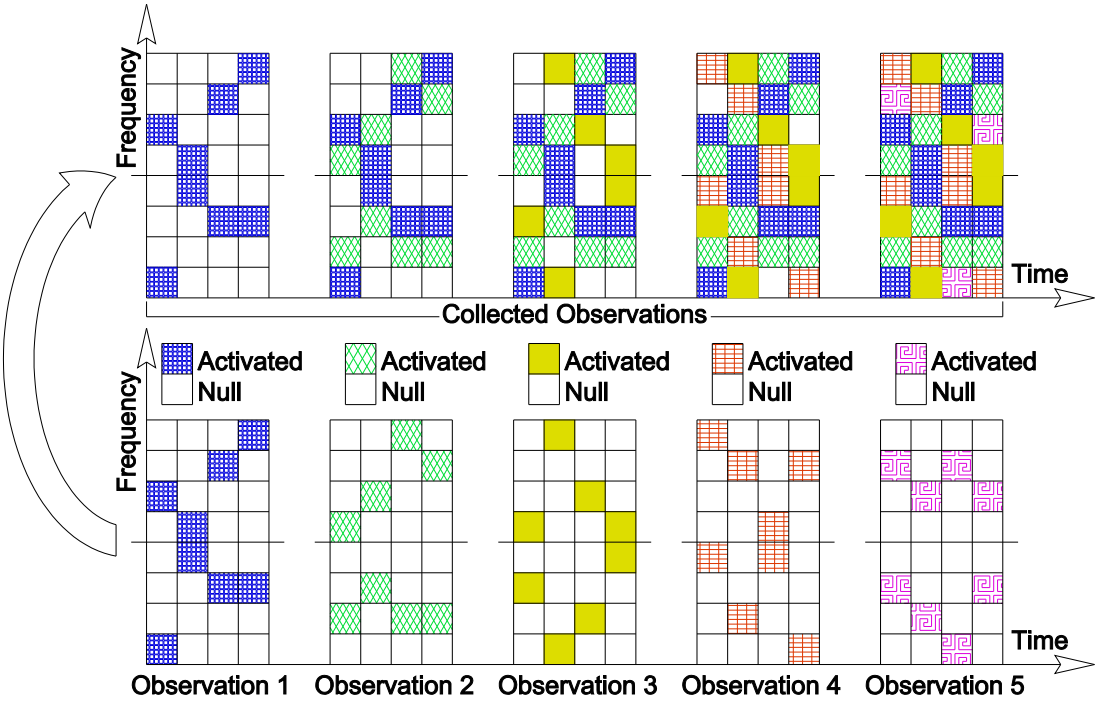

FIGURE 3.3: Example to illustrate the observation collection for $M = 8$, $N = 4$, $M_G = 4$, $M_A = 1$, and $N_{CL} = 5$

The delay and Doppler shift information of the target can be determined from the received signal, as long as there are signals transmitted on a sufficient number of subcarriers. However, IM-OFDM does not transmit signals on all subcarriers within each time-slot, as seen in the bottom row of Figure 3.3, which leads to a lack of target information in the reflected signal. To mitigate this problem, an observation collection matrix is constructed by collecting observations over N_{CL} transmit frames so that most of the missing subcarriers can be filled by signals. This is illustrated in Figure 3.3, for an IM-OFDM system having 2 groups of 4 subcarriers, where 1 subcarrier is activated in each group. Furthermore, each frame contains 4 IM-OFDM symbols, and 5 frames are collected to form the time-frequency observation matrix for sensing.

To elaborate, in Figure 3.3, the top row depicts the matrix of collected observations $\bar{\boldsymbol{Y}}_{CL} \in \mathbb{C}^{M \times N}$ filled with the newly received observations, once they become available. The bottom row shows the individual observations of the 5 frames, each representing a time-frequency matrix $\bar{\boldsymbol{Y}}_{n_{CL}} = \left(\bar{\boldsymbol{y}}_{0,\, n_{CL},\, sen}, \bar{\boldsymbol{y}}_{1,\, n_{CL},\, sen}, \cdots, \bar{\boldsymbol{y}}_{N-1,\, n_{CL},\, sen}\right)$ of a specific frame. Prior to an observation matrix being collected, the modulated communication

data symbols are removed from the received reflected signals by the transmitter, producing the matrix $\bar{\boldsymbol{U}}_{n_{CL}} \in \mathbb{C}^{M\times N}$, by relying on the operation expressed as:

$$\bar{\boldsymbol{U}}_{n_{CL}} = \bar{\boldsymbol{Y}}_{n_{CL}} \oslash \bar{\boldsymbol{X}}_{\infty,\, n_{CL}} \,, \tag{3.26}$$

where $\bar{\boldsymbol{X}}_{\infty,\, n_{CL}} = (\bar{\boldsymbol{x}}_{\infty,\, 0,\, n_{CL}}, \bar{\boldsymbol{x}}_{\infty,\, 1,\, n_{CL}}, ..., \bar{\boldsymbol{x}}_{\infty,\, N-1,\, n_{CL}})$ are the data symbols for the n_{CL}^{th} frame, and $\oslash$ is the Hadamard division or element-wise division. When an element of $\bar{\boldsymbol{X}}_{\infty,\, n_{CL}}$ is 0, the corresponding element of $\bar{\boldsymbol{U}}_{n_{CL}}$ is set to 0.

Then, as a new observation matrix is collected, the matrix of collected observations $\bar{\boldsymbol{Y}}_{CL}$ in the top row of Figure 3.3 is updated with the new observation. If there is an overlap between an existing and a new element of an observation, the oldest element is retained. Once all observations over N_{CL} frames have been collected, the delay and Doppler indices of the targets are estimated from the matrix of collected observations $\bar{\boldsymbol{Y}}_{CL}$. This is achieved, following [12], by applying the N-point DFT to the rows and the M-point IDFT to the columns of the matrix of collected observations $\bar{\boldsymbol{Y}}_{CL}$, converting the time-frequency $\bar{\boldsymbol{Y}}_{CL}$ into the DD $\widetilde{\boldsymbol{Y}}_{CL} \in \mathbb{C}^{M\times N}$:

$$\widetilde{\boldsymbol{Y}}_{CL}[l,k] = \frac{1}{\sqrt{MN}} \sum_{p=0}^{P-1} \widetilde{\psi}_{p,\, sen} \widetilde{h}_{p,\, sen} \left(\sum_{\bar{m}=0}^{M-1} e^{j2\pi \frac{\bar{m}(l-l_{p,\, sen})}{M}} \right) \left(\sum_{n=0}^{N-1} e^{j2\pi \frac{n(k_{p,\, sen}-k)}{N}} \right) + \widetilde{\boldsymbol{Z}}_{CL}[l,k] \,, \tag{3.27}$$

where $\widetilde{\boldsymbol{Z}}_{CL} \in \mathbb{C}^{M\times N}$ is the DD matrix of the time-frequency AWGN $\bar{\boldsymbol{Z}}_{n_{CL}} \oslash \bar{\boldsymbol{X}}_{\infty,\, n_{CL}}$ collected.

The modulus peaks of $\widetilde{\boldsymbol{Y}}_{CL}$ are at $\sum_{p=0}^{P-1} \left[l = \lfloor l_{p,\, sen} \rceil, k = \lfloor k_{p,\, sen} \rceil \right]$ in the absence of noise, where $\lfloor \cdot \rceil$ is the rounding function. Hence, the sensing algorithm estimates the sensing delay indices $\hat{l}_{p,\, sen}$ and Doppler shift indices $\hat{k}_{p,\, sen}$ of the targets by selecting the L modulus peaks of $\widetilde{\boldsymbol{Y}}_{CL}$. The estimated target range $\hat{R}_{l,\, sen}$ and velocity $\hat{V}_{l,\, sen}$ are then formulated as:

$$\hat{R}_{l,\, sen} = \hat{l}_{p,\, sen} \frac{c_0}{2\Delta f M} \,, \tag{3.28}$$

$$\hat{V}_{l,\, sen} = \begin{cases} \hat{k}_{p,\, sen} \frac{\Delta f c_0}{2N f_c} \,, & \text{if } \hat{k}_{p,\, sen} \leq \frac{N}{2} \\ \left(\hat{k}_{p,\, sen} - N \right) \frac{\Delta f c_0}{2N f_c} \,, & \text{if } \hat{k}_{p,\, sen} > \frac{N}{2} \,. \end{cases} \tag{3.29}$$

Note that for the estimated Doppler index, a value higher than $\frac{N}{2}$ indicates a target having a negative velocity.

When the delay and Doppler indices for a target do not coincide with an integer multiple of the estimation resolution, a finer estimation of the target delay and Doppler indices is beneficial. Following [122, 123], the N-point DFT and M-point IDFT matrices applied to $\bar{\boldsymbol{Y}}_{CL}$ are substituted by a $(N \times NN_{ML})$ DFT matrix $\boldsymbol{F}_{N\times NN_{ML}}$ and a

$(MN_{ML} \times M)$ IDFT matrix $\boldsymbol{F}^{-i}_{MN_{ML}\times M}$, respectively, defined as:

$$\boldsymbol{F}_{N\times NN_{ML}}[n, n_{ML}] = \frac{1}{\sqrt{N}} e^{-j2\pi n \frac{n_{ml}}{NN_{ML}}} , \tag{3.30}$$

$$\boldsymbol{F}^{-i}_{MN_{ML}\times M}[\bar{m}_{ML}, \bar{m}] = \frac{1}{\sqrt{M}} e^{j2\pi \bar{m} \frac{\bar{m}_{ml}}{MN_{ML}}} , \tag{3.31}$$

where n_{ML} = (0, 1, ..., $NN_{ML} - 1$), $\bar{m}_{ML}$ = (0, 1, ..., $MN_{ML} - 1$), and N_{ML} is a resolution refinement factor.

The resultant sensing imaging matrix is $\widetilde{\boldsymbol{Y}}_{ML} \in \mathbb{C}^{MN_{ML}\times NN_{ML}}$. It is important to note that the range of delay and Doppler shift that can be estimated from $\widetilde{\boldsymbol{Y}}_{ML}$ is the same as that from $\widetilde{\boldsymbol{Y}}_{CL}$, since the estimation range of delay and Doppler shift is defined by the system parameters, not by the sensing algorithm. As $\widetilde{\boldsymbol{Y}}_{ML}$ has more elements than $\widetilde{\boldsymbol{Y}}_{CL}$, the delay and Doppler estimation resolution is increased by a factor of N_{ML}.

The target range and velocity are then estimated similarly, with M and N in (3.28) and (3.29) replaced by MN_{ML} and NN_{ML}, respectively, yielding:

$$\hat{R}_{l,\,sen} = \hat{l}_{p,\,sen} \frac{c_0}{2\Delta f M N_{ML}} , \tag{3.32}$$

$$\hat{V}_{l,sen} = \begin{cases} \hat{k}_{p,sen} \frac{\Delta f c_0}{2NN_{ML} f_c}, & \text{if } \hat{k}_{p,sen} \leq \frac{NN_{ML}}{2} \\ \left(\hat{k}_{p,sen} - NN_{ML}\right) \frac{\Delta f c_0}{2NN_{ML} f_c}, & \text{if } \hat{k}_{p,sen} > \frac{NN_{ML}}{2}. \end{cases} \tag{3.33}$$

3.3.2 Signal Detection in Communication

Again, it is assumed that there is perfect channel estimation at the receiver. A pair of demodulation schemes are considered, namely single-tap and MMSE demodulation. Both schemes operate in the FD. Hence, the TD channel $\boldsymbol{H}_{n,\,com} \in \mathbb{C}^{M\times M}$ is converted to the FD as follows:

$$\bar{\boldsymbol{H}}_{n,\,com} = \mathcal{F}_M \left(\boldsymbol{H}_{n,\,com}\right) . \tag{3.34}$$

The received signal in the FD $\bar{\boldsymbol{y}}_n$ can then be expressed as:

$$\bar{\boldsymbol{y}}_{n,\,com} = \bar{\boldsymbol{H}}_{n,\,com} \bar{\boldsymbol{x}}_{\infty,\,com} , \tag{3.35}$$

where $\bar{\boldsymbol{x}}_{\infty,\,com}$ is defined in (3.1).

In the context of single-tap demodulation, the communication information is detected for each subcarrier group separately. The system firstly assumes that all of the subcarriers within a group are activated, then it demodulates and remodulates the information on each subcarrier, in an attempt to recreate the transmitted signal on the subcarrier,

formulated as:

$$\hat{\boldsymbol{x}}_{g,\,n}[\bar{m}_G] = \mathbb{M}\left[\mathbb{M}^{-1}\left(\boldsymbol{\varphi}_g[\bar{m}_G]\right)\right] , \tag{3.36}$$

where $\hat{\boldsymbol{x}}_{g,\,n} \in \mathbb{C}^{M_G \times 1}$ is the vector of estimated communication symbols transmitted on the subcarriers within the g^{th} subcarrier group, $\mathbb{M}(\cdot)$ is the modulation function, $\mathbb{M}^{-1}(\cdot)$ is the demodulation function, and $\boldsymbol{\varphi}_g \in \mathbb{C}^{M_G \times 1}$ is defined as:

$$\boldsymbol{\varphi}_g[\bar{m}_G]] = \bar{\boldsymbol{y}}_{n,\,com}[gM_G + \bar{m}_G]\frac{(\bar{h}_{\bar{m}_G,\,g,\,n})^*}{||\bar{h}_{\bar{m}_G,\,g,\,n}||^2} , \tag{3.37}$$

where $\bar{h}_{\bar{m}_G,\,g,\,n} = \bar{\boldsymbol{H}}_{n,\,com}[gM_G + \bar{m}_G,\, gM_G + \bar{m}_G]$, $||\cdot||$ is the Euclidean norm, and $(\cdot)^*$ is the complex conjugate.

The differences between the received signal and the estimated transmitted signal for all possible C_N subcarrier index combinations are calculated, with the combination yielding the smallest error being chosen according to:

$$\begin{aligned}\hat{C} = \arg\min_{\forall c} \sum_{\bar{m}_A=0}^{M_A-1} \big(&||\boldsymbol{\varphi}_g[\mathfrak{C}_N[c,\,\bar{m}_A]] - \hat{\boldsymbol{x}}_{g,\,n}[\mathfrak{C}_N[c,\,\bar{m}_A]]||^2 \\ &-||\boldsymbol{\varphi}_g[\mathfrak{C}_N[c,\,\bar{m}_A]]||^2\big)\boldsymbol{\kappa}_g[\mathfrak{C}_N[c,\,\bar{m}_A]] ,\end{aligned} \tag{3.38}$$

where $c = [0,\,1,\,...,\,C_N - 1]$ is the subcarrier combination index in a combination, $\hat{C}$ is the estimated activated subcarrier combination, $\bar{m}_A$ is the activated subcarrier index, and $\boldsymbol{\kappa}_g \in \mathbb{C}^{M_G \times 1}$ is defined as:

$$\boldsymbol{\kappa}_g[\bar{m}_G] = ||\bar{h}_{\bar{m}_G,\,g,\,n}||^2 . \tag{3.39}$$

Once the activated subcarrier index combination having the smallest error is estimated, the transmitted bits are determined based on the estimated activated subcarrier combination and the associated modulated symbols.

The MMSE demodulation is similar to single-tap demodulation, but with the channel matrix $\bar{\boldsymbol{H}}_{n,\,com}$ replaced by $\bar{\boldsymbol{H}}_{mmse,\,n}$, and $\bar{\boldsymbol{y}}_{n,\,com}$ replaced by $\bar{\boldsymbol{y}}_{mmse,\,n}$, which are defined as:

$$\bar{\boldsymbol{H}}_{mmse,\,n} = \bar{\boldsymbol{G}}_n\bar{\boldsymbol{H}}_{n,\,com} , \tag{3.40}$$

$$\bar{\boldsymbol{y}}_{mmse,\,n} = \bar{\boldsymbol{G}}_n\bar{\boldsymbol{y}}_{n,\,com} , \tag{3.41}$$

where $\bar{\boldsymbol{G}}_n \in \mathbb{C}^{M \times M}$ is given by:

$$\bar{\boldsymbol{G}}_n = \left(\bar{\boldsymbol{H}}^H_{n,\,com}\bar{\boldsymbol{H}}_{n,\,com} + N_0\boldsymbol{I}_{M\times M}\right)^{-1}\bar{\boldsymbol{H}}^H_{n,\,com} , \tag{3.42}$$

with N_0 being the AWGN power, and $\boldsymbol{I}_{M\times M}$ the M by M identity matrix.

Note that, for OFDM demodulation, $G = M$ and $M_G = M_A = 1$, since all subcarriers are activated.

3.4 System Analysis

3.4.1 Cramér-Rao Bound

According to [123], the average unbiased estimator CRB for the associated range and velocity estimation are defined as:

$$\hat{\sigma}_{l,R}^2 \geq \frac{6N_0}{\widetilde{\psi}_{p,sen}^2 P_{avg} P_{im} (2\pi)^2 MN(M^2-1)} \left(\frac{c_0}{2\Delta f}\right)^2, \tag{3.43}$$

$$\hat{\sigma}_{l,V}^2 \geq \frac{6N_0}{\widetilde{\psi}_{p,sen}^2 P_{avg} P_{im} (2\pi)^2 MN(N^2-1)} \left(\frac{c_0 \Delta f}{2f_c}\right)^2, \tag{3.44}$$

where $\hat{\sigma}_{l,R}^2$ and $\hat{\sigma}_{l,V}^2$ are the variance of the target range and velocity estimation errors, respectively, P_{avg} is the average transmit power of the modulated communication symbols before the power allocation due to IM, and P_{im} is the additional power allocated to each activated subcarrier due to IM.

The CRB assumes the best case for IM-OFDM, where there is a complete set of information of the reflected signal. As the RMSE is the metric used for sensing, the standard deviation is utilised:

$$\hat{\sigma}_{l,R} \geq \sqrt{\frac{6N_0}{\widetilde{\psi}_{p,sen}^2 P_{avg} P_{im} (2\pi)^2 MN(M^2-1)}} \frac{c_0}{2\Delta f}, \tag{3.45}$$

$$\hat{\sigma}_{l,V} \geq \sqrt{\frac{6N_0}{\widetilde{\psi}_{p,sen}^2 P_{avg} P_{im} (2\pi)^2 MN(N^2-1)}} \frac{c_0 \Delta f}{2f_c}, \tag{3.46}$$

where $\hat{\sigma}_{l,R}$ and $\hat{\sigma}_{l,V}$ are the standard deviations of the target range and velocity estimation errors, respectively.

It is important to note that, as stated in [123], this CRB is an average CRB, not a true lower bound, and it is only applicable when M and N are sufficiently large.

3.4.2 Complexity Analysis

The observation collection algorithm searches through an $N \times M$ matrix for N_{CL} observations. The complexity of such an operation is negligible compared to the other operations of the system, such as the IDFT and DFT utilised by OFDM-based transmit pre-processing and receive post-processing.

The interpolation algorithm operates using an $N \times NN_{ML}$ DFT matrix and an $MN_{ML} \times M$ IDFT matrix during the delay and Doppler shift estimation, compared to an $N \times N$ DFT matrix and an $M \times M$ IDFT matrix in the absence of interpolation, leading to an increase in complexity. The complexity of the DFT and IDFT operations depends on the specific implementation utilised, therefore no complexity order is given.

The complexity of subcarrier index activation is negligible, as it relies on a lookup table. The activated index is estimated by a ML detector, which has a complexity order of $\mathcal{O}(M_G)$ [180]. Hence, IM-OFDM has a larger demodulation complexity than OFDM.

The single-tap demodulation relies on the ML detector for IM-OFDM, hence it has the same complexity order of $\mathcal{O}(M_G)$. The MMSE demodulation is similar to single-tap demodulation, but with the addition of N matrix inversions applied to matrices of size $M \times M$. The complexity order for matrix inversions is proportional to M^3 [181], but again, it is dependent on the specific implementation utilised.

3.5 Simulation Results and Discussion

TABLE 3.2: Default variable values

Variable	Value
Carrier frequency f_c	40 GHz
Subcarrier spacing Δf	120 kHz
Number of observations collected N_{CL}	4
Number of sensing frames simulated	2000
Minimum number of bit errors	800
Maximum number of bits simulated	4×10^7
Minimum number of communication frames simulated	200
Number of communication paths P_{com}	3
Number of sensing targets P_{sen}	1
Rician K factor κ	0 dB
Number of subcarriers M	256
Number of symbol sent per frame N	64
Integer delay and Doppler indices	
Target velocity	$6 \times 7.03 = 42.18$ m/s
Target range	$29 \times 4.88 = 141.52$ m
Fractional delay and Doppler indices	
Target velocity	40 m/s
Target range	140 m
Interpolation factor N_{ML}	4

Unless otherwise stated, the simulation parameters used are given in Table 3.2. The IM-OFDM system is compared to an OFDM benchmark using QPSK modulation. Since classic OFDM activates all the subcarriers, no block interleaving is employed.

Three combinations of M_G and M_A are considered: $M_G = 4$ and $M_A = 3$ (4,3); $M_G = 2$ and $M_A = 1$ (2,1); and $M_G = 4$ and $M_A = 1$ (4,1). To maintain an equal throughput of 2 bits per channel use (bpcu) for the above schemes, (4,3) uses QPSK modulation, (2,1) 8-PSK, and (4,1) 64-QAM.

When the communication signal is received, it is sampled to obtain the discrete received signal. This creates delay bins into which the received signal paths fall. As a fractional delay index is considered to be equivalent to an integer delay index as long as it lies within the same delay bin, only integer delay indices are considered. This allows the simpler form of the received signal given in (3.8) to be used, which reduces the simulation duration. This simplification is included because the performance of IM-OFDM communication is well understood, so the focus of this work is on the sensing behaviour.

This assumption is valid for communication as the individual path or paths the signal has travelled through do not have to be separately identified. By contrast, this is not the case for sensing, as each individual propagation path has to be separately identified, because it could be associated with a separate target, as mentioned in Section 3.2.2.1.

For integer indices, the target range and velocity are set to a multiple of the approximate range and velocity resolutions of the system. An approximation is used, as the range and velocity resolutions are a function of c_0, which is not an integer.

The communication SNR is used for sensing. This is calculated based on the path loss for a communication target at the range shown in the table, in order to illustrate the performance trade-offs between communication and sensing.

The proposed sensing algorithm retains the oldest information. An alternative would be to retain the newest information. To investigate the effect of this choice, consideration is given to the maximum detectable velocity, approximately 225 m/s, and the range resolution in the absence of interpolation, approximately 4.88 m. For the system parameters chosen, the distance travelled over 16 consecutive observations is 0.03 m. This is expected to be insignificant relative to the more coarse resolution of the system. Thus, it can be concluded that the choice of retaining the first or the last information will not materially impact the accuracy of the range estimate. If the interpolation factor is above 64, then the resolution of the system increases to a level where this choice may be revisited.

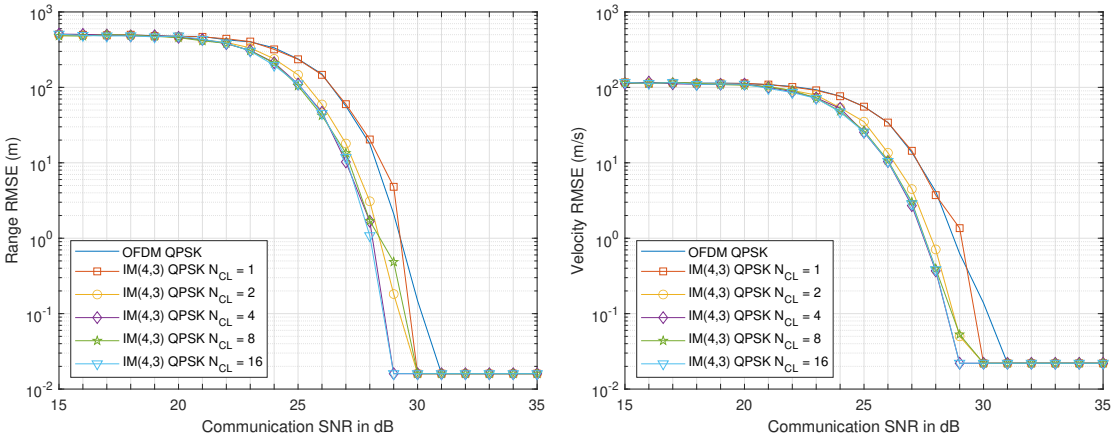

(A) Range RMSE (B) Velocity RMSE

FIGURE 3.4: IM-OFDM(4,3) QPSK RMSE for $N_{CL} = 1, 2, 4, 8, 16$ for integer indices

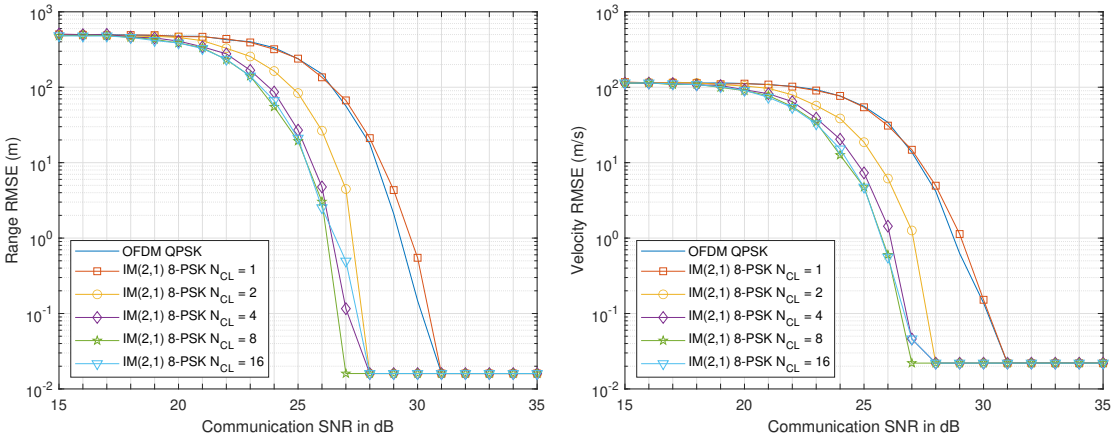

(A) Range RMSE (B) Velocity RMSE

FIGURE 3.5: IM-OFDM(2,1) 8-PSK RMSE for $N_{CL} = 1, 2, 4, 8, 16$ for integer indices

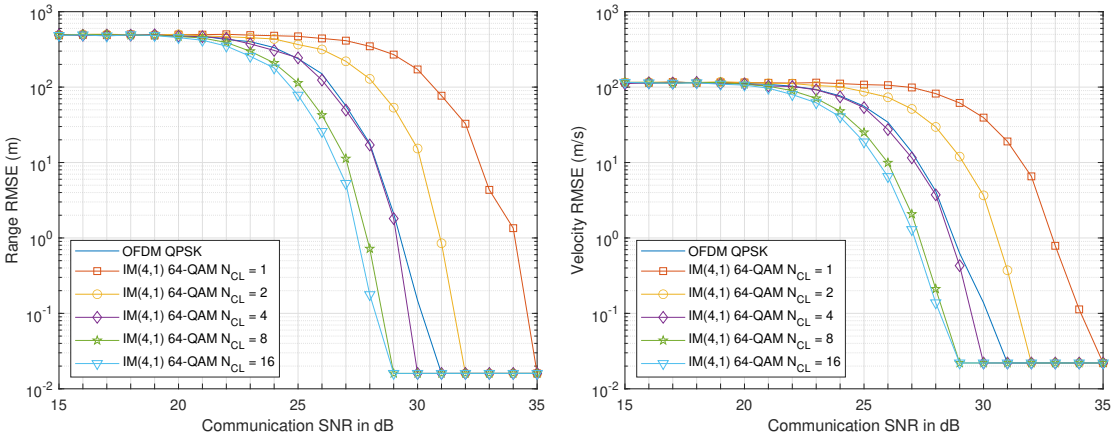

(A) Range RMSE (B) Velocity RMSE

FIGURE 3.6: IM-OFDM(4,1) 64-QAM RMSE for $N_{CL} = 1, 2, 4, 8, 16$ for integer indices

3.5.1 Integer Indices

3.5.1.1 Varying the Number of Observations Collected

The number N_{CL} of observations collected is varied, as shown in Figures 3.4-3.6. There is an improvement in the RMSE *vs.* SNR trend as N_{CL} is increased, which is in line with expectations as the missing information in the matrix of collected observations is filled in, hence increasing the accuracy of the sensing algorithm. This improvement then stagnates above certain N_{CL} values. The value of N_{CL} at which this stagnation occurs increases as the number of activated subcarriers is reduced, which is due to the reduction of the information conveyed by using IM.

For both (4,3) and (2,1), increasing N_{CL} beyond 4 has no significant impact on the sensing performance. This is illustrated by the lines lying close to each other throughout the communication SNR range considered, once N_{CL} exceeds this threshold. For (4,1), N_{CL} has to be increased to 8 for the sensing performance to plateau. For all other results in this section, the value of N_{CL} will be set to 4.

As shown in Figures 3.4 and 3.6, increasing N_{CL} has no impact on the error floor. This occurs because, firstly, as OFDM sensing assumes relatively low target velocities, where the Doppler shift associated with the target is less than $\frac{\Delta f}{10}$, the target is unlikely to have moved a significant distance whilst the observations are collected, as previously discussed.

Secondly, the size of the sensing imaging matrix is independent of N_{CL}. The sensing resolution is proportional to the size of the imaging matrix. The error floor is the difference between the value output by the estimator and the target parameter value when the noise level is no longer significant. As the output of the sensing algorithm is an integer multiple of the system resolution, the error floor is not affected by N_{CL}.

3.5.1.2 Default Values

Figure 3.7a shows the BER performance of the system for all the configurations considered. The configuration of (4,3) has the lowest BER at higher SNR, followed by OFDM. This is expected, as both the (4,3) and the OFDM schemes have the same modulation order, with the signal power on each activated subcarrier for (4,3) being $\sqrt{\frac{4}{3}}$ instead of 1, where the latter is the case for OFDM. As the number of activated subcarriers is reduced, the modulation order is increased to maintain the total data throughput of 2 bpcu, which erodes the overall BER performance.

Single-tap demodulation exhibits an error floor higher than 8×10^{-4} for all systems, which is unsuited for practical use. MMSE demodulation does not have an error floor and exhibits a lower BER than single-tap demodulation at higher SNRs. The emergence

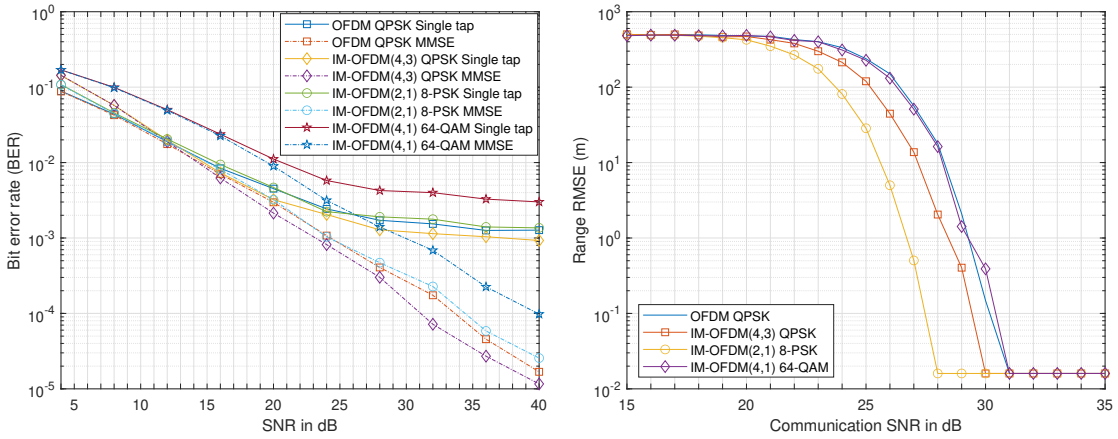

(A) BER for single-tap and MMSE demodulation

(B) Range RMSE for $N_{CL} = 4$

FIGURE 3.7: BER and range RMSE for OFDM and IM-OFDM for integer indices

of an error floor for single-tap demodulation is because this algorithm only utilises the diagonal values of the FD channel matrix. By contrast, MMSE demodulation operates on the channel matrix prior to demodulation, as described in Section 3.3.2. Hence, single-tap demodulation results in an inaccurate demodulation, when a significant Doppler shift is present, which manifests itself as an error floor. This error floor may be mitigated by utilising error correction coding techniques.

Figure 3.7b characterises the sensing performance of the systems for $N_{CL} = 4$. As the sensing performance is similar for both range and velocity estimation, only the range RMSE is shown. The scheme (2,1) reaches the RMSE error floor at the lowest SNR, followed by the (4,3), OFDM and (4,1) arrangements. As the number of subcarriers activated in an IM block is decreased, the per-carrier power is increased, which in turn increases the detection reliability. At $N_{CL} = 4$, the probability of having missing information in the imaging matrix is low for (2,1) and (4,3), but higher for the (4,1) scheme. Hence, the performance of (4,1) is similar to that of OFDM for $N_{CL} = 4$.

3.5.1.3 Effects of Block Interleaving

The subcarrier block interleaving employed for IM-OFDM separates the grouped subcarriers. This leads to the subcarriers within a group being spread across the available bandwidth, shown in (3.1), as opposed to having the subcarriers within a group next to each other, as in conventional IM-OFDM. This reduces the probability of all the subcarriers within a group experiencing a deep fade, which increases the activated subcarrier index detection reliability.

Figure 3.8 shows the BER performance of the IM-OFDM systems both with (w/) and without (w/o) block interleaving, using the OFDM performance as a benchmark. The presence of block interleaving does not make single-tap detection viable for all systems.

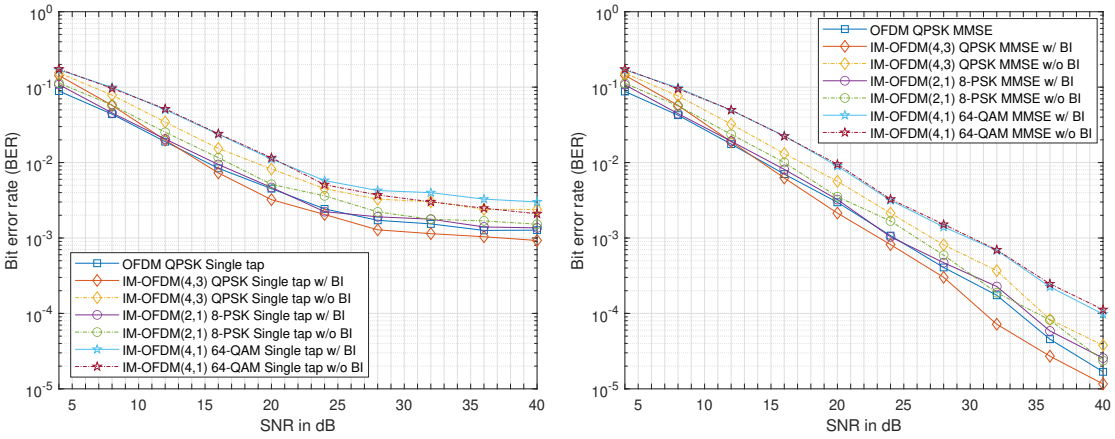

(A) Single-tap demodulation (B) MMSE demodulation

FIGURE 3.8: BER for single-tap and MMSE demodulation for OFDM and IM-OFDM with (w/) and without (w/o) block interleaving for integer indices

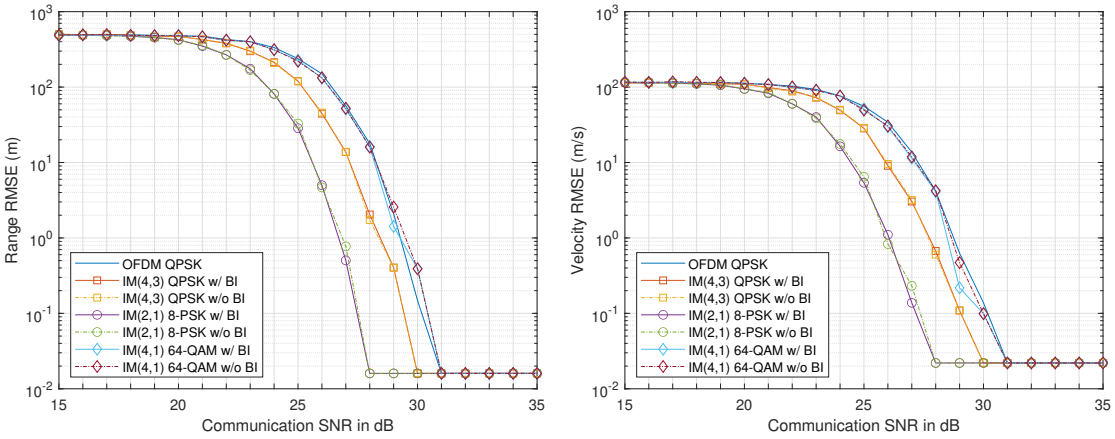

(A) Range RMSE (B) Velocity RMSE

FIGURE 3.9: RMSE for OFDM and IM-OFDM for $N_{CL} = 4$ with (w/) and without (w/o) block interleaving for integer indices

The performance of the (4,3) and (2,1) schemes is degraded, when no block interleaving is used in support of MMSE demodulation. However, the absence of interleaving does not affect the (4,1) scheme. The performance of (4,3) is worse than that of OFDM, when no block interleaving is employed.

When multiple subcarriers are activated within a group, a more dramatic potential variability is introduced, as the detection algorithms demodulate multiple signals at a time in an attempt to identify the activated subcarriers. The above-mentioned advantages of block interleaving therefore improve the BER performance attained.

Figure 3.9 shows that block interleaving has little to no effect on the sensing performance. As the sensing algorithm has *a priori* knowledge of the transmitted signal, and removes the transmitted information from the received signal, the specific ordering of the transmitted data has no effect on the sensing performance.

3.5.1.4 Effects of PSK and QAM Modulation on the Sensing Performance

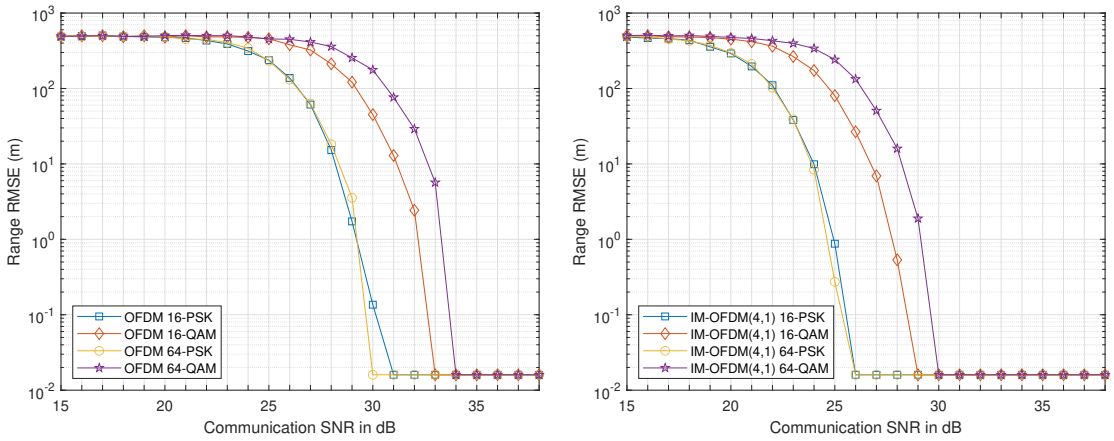

(A) OFDM (B) IM-OFDM(4,1)

FIGURE 3.10: Range RMSE for modulation of 16- and 64-PSK and 16- and 64-QAM for integer indices

The effect of the PSK and QAM and their bit per symbol throughput on the sensing performance is shown in Figure 3.10. Increasing the modulation order has little effect on the sensing performance of PSK, but degrades the sensing performance as the QAM order is increased. It can also be seen that QAM reaches the RMSE error floor at a higher SNR than PSK modulation.

Again, these trends occur due to the QAM symbols' variable amplitude. When the data is removed from the received sensing signal, the time-frequency matrix produced will have noise levels that are less statistically uniform, due to the varied amplitude of the data symbols. Once this matrix is converted to the DD, these varied noise levels reduce the detection reliability by increasing the probability of false peaks.

These results are supported by [102], which investigates the effect of the transmit signal randomness on the sensing performance attained. As QAM varies both the amplitude and phase of a signal, it produces a signal for sensing that is more "random" than PSK, which only varies the phase, but not the magnitude.

3.5.1.5 Effects of Increasing the Number of Objects on the Sensing Performance

To characterise the system's sensing performance in more complex environments, simulations have been performed where 3 additional reflecting objects have been added that are not desired targets. The range and velocity of these additional objects are randomly chosen to be: R_2 = 175.68 m, R_3 = 175.68 m, R_4 = 219.6 m, V_2 = -14.06 m/s, V_3 = 70.3 m/s, and V_4 = -21.09 m/s. The sensing RMSE results recorded for a single target and for multiple objects are shown in Figure 3.11.

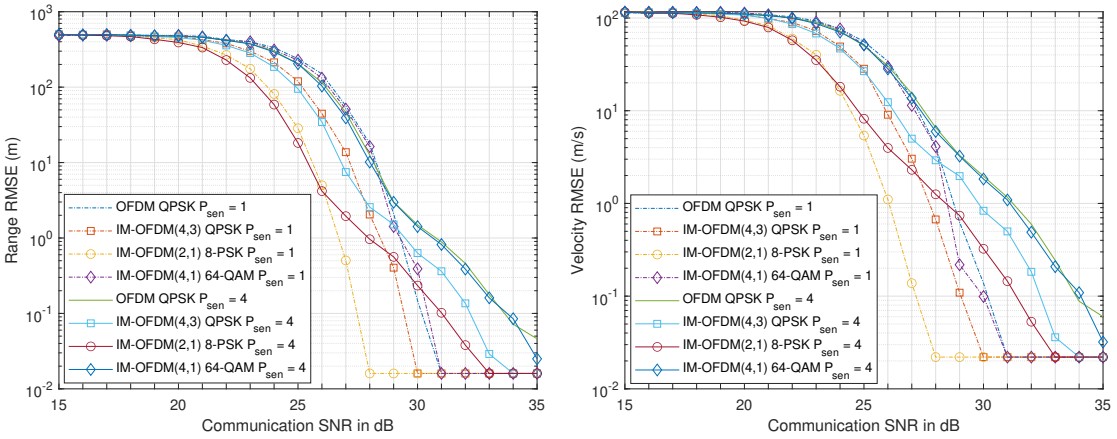

(A) Range (B) Velocity

FIGURE 3.11: Sensing RMSE of the OFDM and IM-OFDM systems for one target P_{sen} = 1 and multiple objects P_{sen} = 4

Although the sensing performance of all the systems is reduced when additional reflective objects are introduced, their relative sensing performance remains similar. The performance reduction is due to the additional peaks in the DD image matrix corresponding to the additional objects, hence requiring a smaller noise amplitude for an erroneous target estimation.

3.5.1.6 Comparison with Partial-Activation Based OFDM

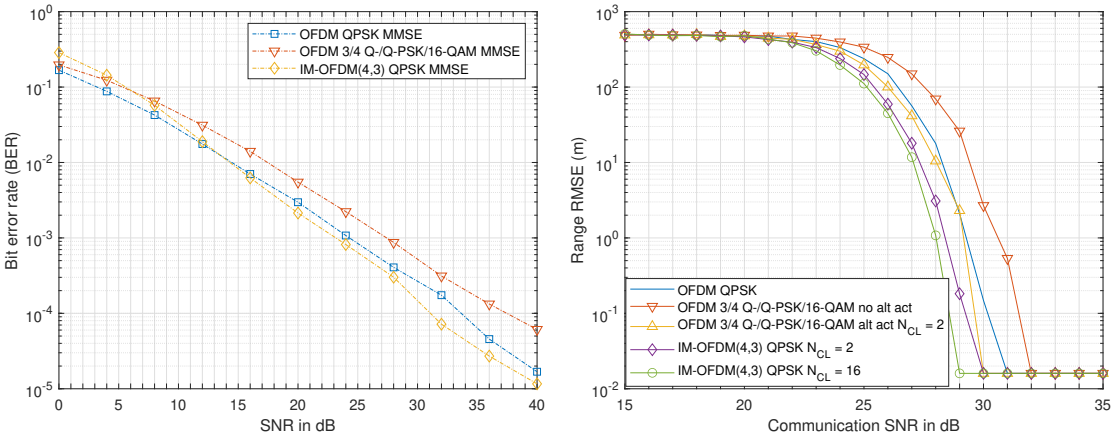

(A) BER (B) Range RMSE

FIGURE 3.12: BER and range RMSE of OFDM QPSK, OFDM-3/4 QPSK QPSK 16-QAM and IM-OFDM(4,3) QPSK

The use of IM in the spatial domain is shown to result in a lower system performance than other techniques [182]. To demonstrate the effectiveness of IM in the FD, partial-activation based OFDM is investigated. By activating only a subset of the available subcarriers for OFDM, the modulation order on the activated subcarriers has to be increased to maintain the system throughput for a fair comparison. IM provides an

additional dimension to transmit information, thereby allowing the modulation order to remain the same as for standard OFDM. Therefore, IM-OFDM will always have the potential to outperform OFDM partial subcarrier activation for communication and sensing.

To illustrate this, an additional partial-activation based OFDM benchmark scheme has been created: OFDM-3/4. This scheme employs OFDM, whilst only activating three-quarters of the subcarriers, without employing index modulation. Since fewer subcarriers are used, the power on the activated subcarriers is increased by a factor of $\frac{4}{3}$. To maintain the throughput of 2 bpcu, OFDM-3/4 uses QPSK, QPSK, and 16-QAM on each group of three activated subcarriers, and it is compared to IM-OFDM(4,3) QPSK.

The BER results of MMSE demodulation are shown in Figure 3.12a. The increased modulation order of OFDM-3/4 leads to a higher BER than that of IM-OFDM(4,3) and OFDM for SNRs above 10 dB. The BER of partial-activation based OFDM is higher than that of IM-OFDM for the majority of the SNR range considered.

Since partial-activation based OFDM does not transmit on all subcarriers, there is some missing target information, similarly to IM-OFDM. Since partial-activation based OFDM always transmits on the same subcarriers, the collection algorithm would not "fill in" the missing information. Thus, partial-activation based OFDM would never outperform its equivalent IM-OFDM system for sensing.

The sensing performance of partial-activation based OFDM can be improved if there is an alternating subcarrier activation pattern, which increases the system complexity. This modification arranges for partial-activation based OFDM to alternate between multiple sets of subcarriers. For OFDM-3/4, two sets of subcarriers are considered. This allows the system to receive full target information, once two observations are collected. The range RMSE of sensing is shown in Figures 3.12b. For partial-activation based OFDM, "no alt act" refers to the system operating without alternating activation. By contrast, "alt act" represents the system employing alternating activation.

OFDM-3/4 operating without alternating activation reaches the RMSE error floor at a higher SNR than OFDM, since the amplitude variation of the individual QAM symbols reduces the sensing performance, despite the increased power on the activated subcarriers. When alternating activation is used, OFDM-3/4 reaches the error floor at the same SNR as IM-OFDM(4,3) using $N_{CL} = 2$, since the amplitude variation of 16-QAM offsets the performance improvement from receiving full target information. IM-OFDM(4,3) using $N_{CL} = 16$ outperforms OFDM-3/4 employing alternating activation.

Thus, IM-OFDM is capable of outperforming partial-activation based OFDM for both sensing and communication, even when a more complex alternating activation pattern is employed.

3.5.2 Fractional Indices

3.5.2.1 Varying the Interpolation Factor

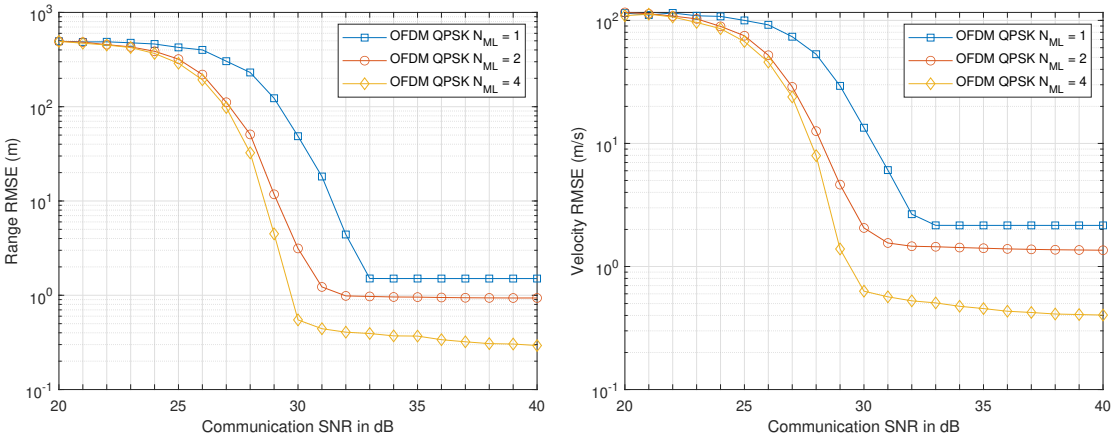

(A) Range RMSE (B) Velocity RMSE

FIGURE 3.13: OFDM QPSK RMSE for $N_{ML} = 1, 2, 4$ for fractional indices

The effect of varying N_{ML} on the RMSE is shown in Figure 3.13 for OFDM. The trends are similar for all the other considered systems, hence only the OFDM results are shown. The error floor is higher than for integer indices, because there is a larger discrepancy between the estimator output values and the target parameters. As N_{ML} is increased, both the error floor and the SNR at which the error floor is reached are reduced. This is because the system resolution is increased as N_{ML} is increased.

3.5.2.2 Default Values

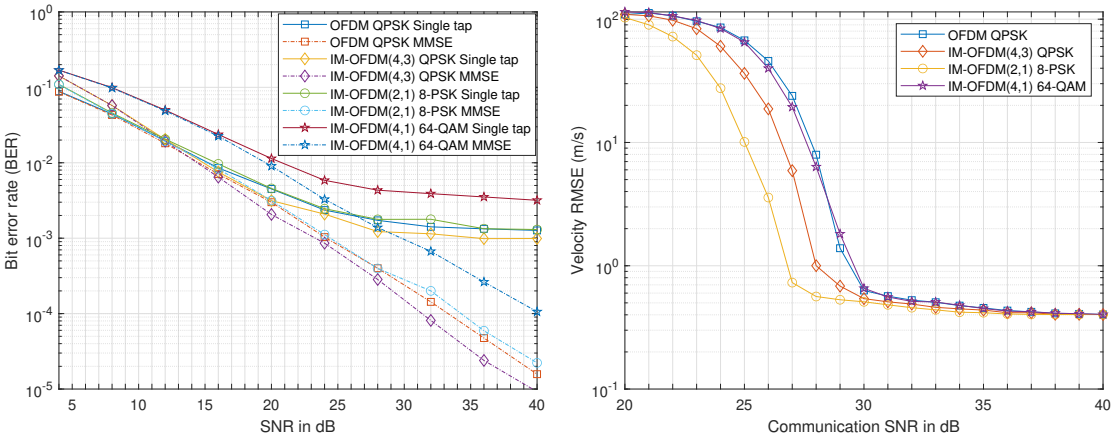

(A) BER for single-tap and MMSE demodulation (B) Velocity RMSE for $N_{CL} = 4$ for $N_{ML} = 4$

FIGURE 3.14: BER and velocity RMSE for OFDM and IM-OFDM for fractional indices

Figure 3.14a shows the BER performance of the system for all the configurations considered for integer delay and fractional Doppler indices. The trends in Figure 3.14a are

identical to those of integer indices, shown in Figure 3.7a. Switching from integer to fractional Doppler indices has no effect on the BER of the systems.

Figure 3.14b shows the range RMSE performance of all systems for $N_{ML} = 4$. The trends across the systems are the same as observed for integer indices in Figure 3.7b, with the (2,1) scheme having the best performance, followed by the (4,3) scheme, with the OFDM benchmark and the (4,1) scheme.

3.5.3 Cramér-Rao Bound

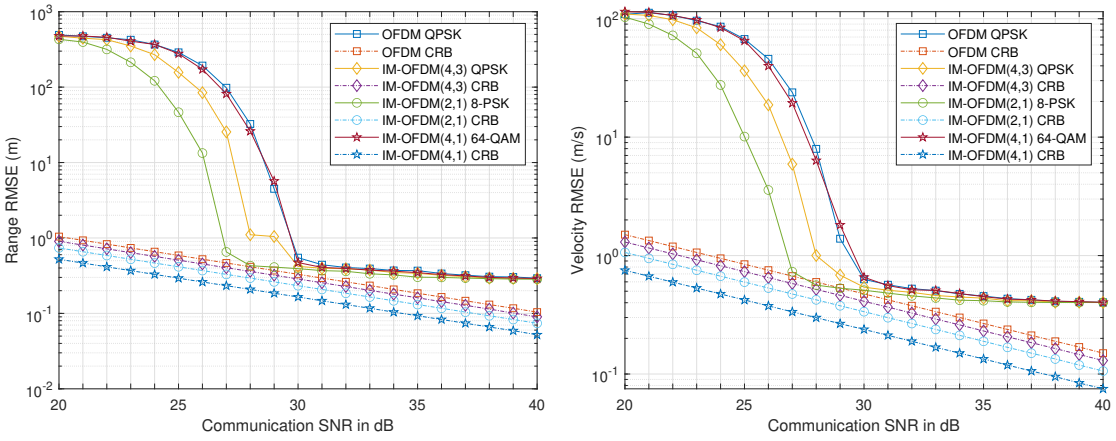

(A) Range RMSE (B) Velocity RMSE

FIGURE 3.15: CRB and RMSE for OFDM and IM-OFDM for $N_{CL} = 4$ for $N_{ML} = 4$ for fractional indices

The CRB with the RMSE results of the systems considered are shown in Figure 3.15, for the default fractional index values. As the CRB assumes having a complete set of information concerning the reflected signal, the system having the highest average power on each activated subcarrier, namely (4,1), has the lowest CRB. By contrast, the OFDM benchmark has the highest CRB. The systems (2,1), (4,3) and OFDM approach their respective CRBs as they reach their error floors, but they then diverge from the CRB as the SNR increases. Further, the RMSE of the (4,1) scheme does not approach its CRB, because too few observations are collected to fully exploit the increased power of each activated subcarrier of this IM configuration.

3.5.4 Peak to Average Power Ratio

The PAPR of the TD transmitted signals of the OFDM and IM-OFDM systems have been calculated over 20,000 frames, with the Complementary Cumulative Distribution Function (CCDF) of the PAPR for $M = 4$, 16, 64, and 256 subcarriers shown in Figure 3.16. For each frame, a vector of random bits is generated, which are then modulated. The resulting TF signal is converted to the TD, and the PAPR of this TD signal is

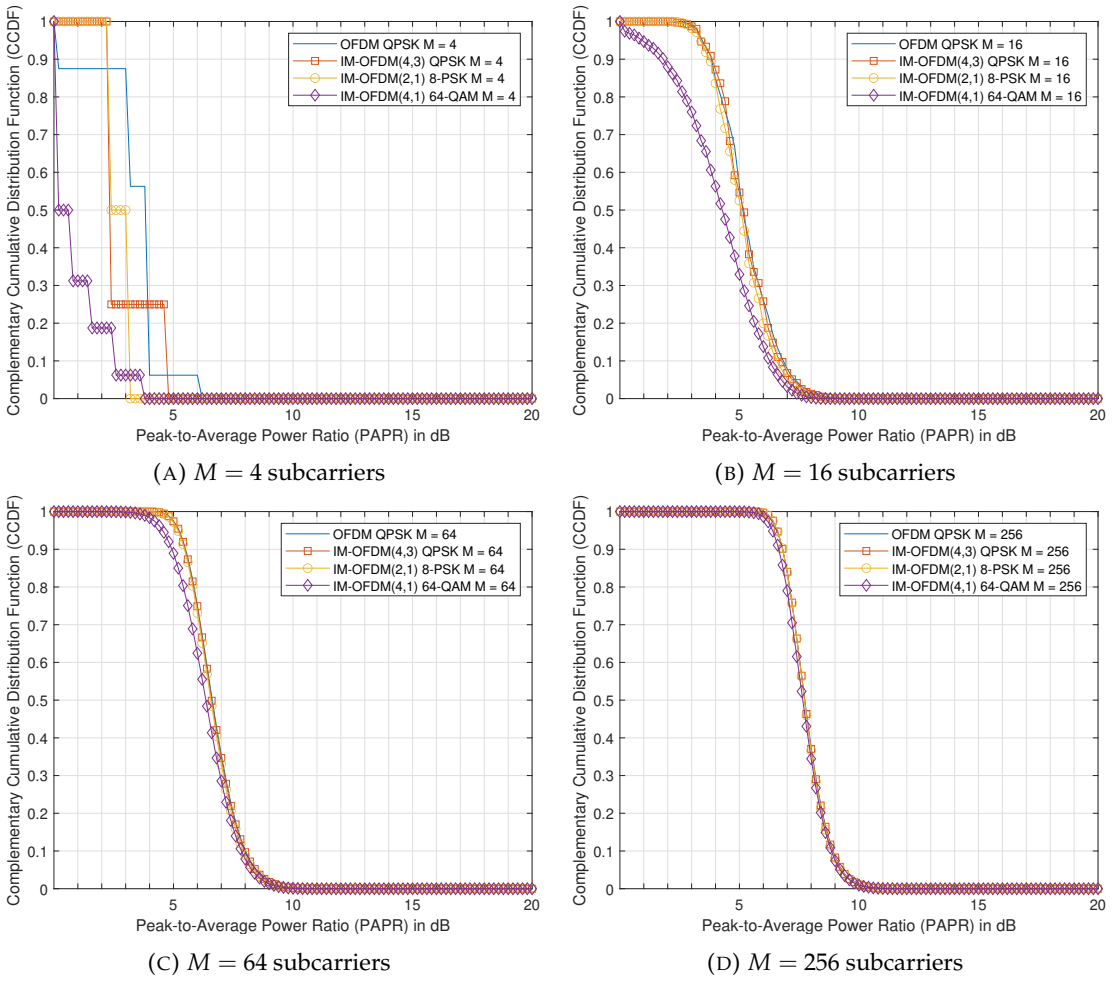

(A) $M = 4$ subcarriers

(B) $M = 16$ subcarriers

(C) $M = 64$ subcarriers

(D) $M = 256$ subcarriers

FIGURE 3.16: CCDF of the PAPR of all the considered systems

calculated. Although the power assigned to the activated subcarriers is increased in the FD for IM-OFDM, this does not necessarily lead to an increase in the PAPR in the TD, since the blank/deactivated subcarriers reduce the likelihood of a peak generated by the IDFT used in the conversion from FD to TD. The PAPR of IM-OFDM is lower than that of OFDM for a small number of subcarriers, but approaches the PAPR of OFDM as the number of subcarriers is increased. Thus, the use of IM does not increase the PAPR of OFDM, but reduces it when a small number of subcarriers is employed, and remains unchanged when a large number of subcarriers is utilised.

3.6 Conclusions

A novel IM-OFDM ISAC solution was conceived, which outperforms OFDM ISAC by collecting multiple sensing observations. The delay caused by the collection of multiple observations has no impact on the sensing performance, as the error floors remain constant when N_{CL} is varied. For $N_{CL} = 4$, the (4,3) scheme is shown to outperform

TABLE 3.3: Results Summary for Default Integer Index Values

System	SNR at which the RMSE error floor is reached	SNR at which 10^{-4} BER is reached
OFDM QPSK	31 dB	33.5 dB
IM-OFDM(4,3) QPSK	30 dB	31 dB
IM-OFDM(2,1) 8-PSK	28 dB	34.5 dB
IM-OFDM(4,1) 64-QAM	31 dB	40 dB

OFDM both in terms of sensing and communication. A summary of the results for the default integer index scenario is shown in Table 3.3.

A range of trade-offs was characterised in terms of the subcarrier grouping, communication throughput, and the number of sensing observation collected. If a modest sensing and communication performance improvement is deemed sufficient, the (4,3) configuration may be recommended. If a higher sensing performance is desired at the cost of communication performance erosion, the (2,1) or (4,1) schemes may be employed, depending on the target velocity and the required throughput. It can also be seen that the (4,1) scheme using PSK modulation has a better sensing performance than the other systems. As noted in the complexity analysis, the demodulation complexity is proportional to the number of subcarriers in a group, with (2,1) having the lowest demodulation complexity amongst the IM-OFDM systems.

Increasing the interpolation factor leads to a similar improvement in sensing performance in all systems, albeit at the cost of increased complexity. Increasing M and N will also increase the sensing resolution, but would require a substantial system modification.

The communication-oriented results show that OFDM waveforms require a large SNR to attain a low BER at higher velocities. This is due to the subcarrier orthogonality being partially compromised by the Doppler shifts. Hence, a different waveform has to be invoked to attain satisfactory communication and sensing performance at higher velocities.

Chapter 4

Code Division Multiple Access OTFS ISAC

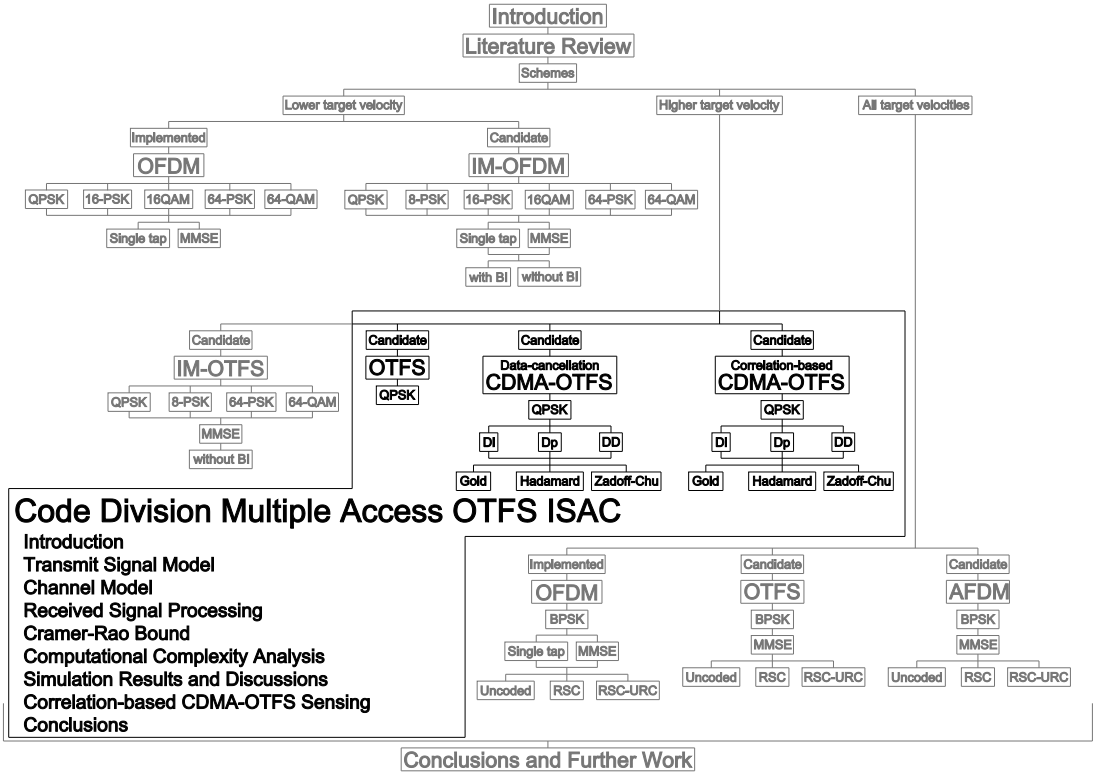

4.1 Introduction

This chapter describes the published part of the research undertaken on CDMA-OTFS [2]. ISAC is expected to be required in a multitude of environments, including high

mobility scenarios. As was shown in Chapter 3, the widely implemented OFDM waveform suffers from a reduced performance at higher velocities, due to the large Doppler shifts compromising the subcarrier orthogonality. Hence, the OTFS waveform is chosen as it is designed to be less affected by the Doppler shift induced by large velocities. There are many publications that investigate the communication performance of multi-user OTFS, but few consider their sensing capabilities. Hence, CDMA is employed to provide multi-user communication capabilities, whilst also allowing for monostatic sensing. CDMA is chosen due to its simplicity and its ability to reduce the variability in the transmit signal characteristics relative to OTFS, thereby aiding sensing. This is in contrast to the other multi-user methodologies, such as the newer SCMA multi-user method, which increases the variability in the transmit signal characteristics.

4.1.1 Literature Review

ISAC is a subject of considerable interest for future wireless generations [39,59,183,184], as the number of wireless devices is expected to drastically increase. Since the OTFS concept was first introduced [141, 142], its employment for ISAC [143] has been a topic of interest. This is due in part to OTFS being less affected by Doppler shift than OFDM, and to the DD channel being defined by the delay and Doppler shifts of the propagation paths. This leads to the DD channel fluctuating at a slower rate than its TF and TD counterparts. When the delay and Doppler shifts of the propagation paths are perfectly synchronous with the system's sampling grid, the channel can be modelled using a sparse matrix. This can simplify the associated target parameter estimation algorithms [144]. A literature review of OTFS ISAC is presented in Section 2.5.2 of Chapter 2, and hence is not repeated here. Below is a literature review on work not covered in Chapter 2.

4.1.1.1 OTFS Variants

A low-complexity variant of OTFS, known as Orthogonal Time Sequency Multiplexing (OTSM), was first introduced by Thaj *et al.* [185]. This waveform modulates the symbols in the delay-sequency (sic) domain, as opposed to the DD of OTFS. This is achieved by replacing the IDFT along the Doppler axis by the Walsh-Hadamard transform. Since this is a purely real-valued transform, a real-valued transmitted signal can be generated by employing a real-valued modulation scheme. The Hadamard transform is also more computationally efficient than the DFT and the IDFT used for OTFS. However, since the modulated waveform is constructed in the delay-sequency domain, not the DD, the propagation paths with identical delays cannot be separated without more complex detection methods, even if they have different Doppler shifts. Thaj *et al.* [185] show that OTSM has a similar BER performance to OTFS, but it is computationally more

efficient due to the use of the Hadamard transform. The pilot power and PAPR of OTSM is reduced by Neelam and Sahuin [186], by superimposing the pilot symbols on the data, and employing a low complexity iterative channel estimator. Moreover, the BER upper bound of OTSM is determined by Sui *et al.* [187], and a novel vector approximate message passing-based expectation-maximization detector is developed to improve the BER performance of OTSM.

Doosti-Aref *et al.* [188] harness IM in the sequency domain, to improve both the spectral efficiency and BER of OTSM. This method is further developed in [189], where pairs of sequence indices of the sequency domain are determined by IM, as opposed to detecting individual indices. This improves the energy efficiency of the system, and reduces the error propagation imposed by erroneous activated index estimation.

The estimation and compensation of the In-phase and Quadrature-phase (IQ) imbalance in the received signal caused by the hardware at high frequencies is investigated for OTSM and OTFS by Neelam and Sahu [190]. The estimation is achieved by placing two pilot symbols in the delay-sequency domain transmitted signal, and then estimating the imbalance based on these symbols in the delay-time domain. The addition of a second pilot symbol decreases the number of indices available for data, since guard bands are also required between the pilot symbols, in addition to the guard band between the pilot symbols and the data. The IQ compensation is implemented in the delay-time domain. The compensation of the imbalance is improved as the pilot power is increased. This work is then also extended to determine both the carrier frequency offset and the channel parameters by Neelam and Sahu [191], where both integer delay and fractional Doppler indices are considered.

The work in [190] is further extended to transmitter and receiver imbalance estimation and compensation as well as channel estimation by the same authors [192]. A complex pseudo noise-based training sequence is placed in the indices allocated to the pilot symbols. The imaginary part of the sequence is a cyclic shift of the real part of the sequence. The channel is estimated at discrete intervals, where the initial estimations are further refined by linear interpolation. An iterative algorithm is conceived for estimating and compensating the IQ imbalance.

Singh *et al.* [193] implement a deep learning-based detector for OTSM to compensate for hardware impairments. This deep learning-based detector involves a convolutional neural network, which is trained on the transmitted, received, and MMSE detector outputs. A data augmentation scheme is then developed to further enhance the input data to the neural network. The resultant detector has a slightly higher complexity than an MMSE detector, whilst reducing the BER.

Reddy *et al.* [194] design a multi-user uplink method based on upsampled and circularly shifted OFDM. These signals, when combined at the base station, are equivalent to single-user OTFS, OTSM, or block-based single carrier signals. This is equivalent to a

system that allocates delay indices to users, where the secondary domain of the data can be selected simply by interchanging the matrix multiplying the modulated data. Specifically, the system may opt for the IDFT for OTFS/Zak-OTFS, the Hadamard transform for OTSM, or the identity matrix for single carrier TD schemes. The BER performance of the OTSM method is comparable to that of the OTFS method.

Another method applying a real-valued transform to OTFS is proposed by Kalpage *et al.* [195]. A modified Zak-OTFS method relying on the Discrete Cosine Transform (DCT) is developed to reduce the PAPR of OTFS. Replacing the DFT by the DCT reduces both the PAPR and the complexity of the system, without eroding the BER for the conditions considered by the authors.

4.1.1.2 Multi-user OTFS Methodologies

Surabhi *et al.* [196] design a multi-user OTFS system that splits the available DD indices into multiple sub-groups, each of which is allocated to a user. The sub-groups can be along the delay axis, the Doppler axis, or both axes. The BER of the schemes relying on index groups along the delay or Doppler axis is lower than that of the schemes that allocate indices for a user along two axes. The BER of this system using ML or message passing-based detection is lower than that of OFDMA and Single Carrier Frequency-Division Multiple Access (SC-FDMA).

Khammammetti and Mohammed [197] propose a DD index allocation method for multi-user communications similar to that of [196], but place guard bands between the indices assigned to users, to minimise the inter-user interference. This leads to a simpler detector, at the cost of an eroded throughput.

Ge *et al.* [198] apply the DD matrix partitioning method to uplink communication, separating stationary and mobile devices. The stationary devices modulate along the delay axis, and the mobile devices modulate along the Doppler axis. As the base station is static, the stationary users do not experience Doppler shift. A successive interference cancellation aided iterative turbo receiver utilising soft inputs and outputs is developed for detecting the uplink signals. The stationary user signals are decoded, followed by the information arriving from the mobile devices.

4.1.1.3 Sparse Code Multiple Access-OTFS

SCMA has been amalgamated in conjunction with OTFS in [199–202], relying on NOMA for supporting a higher number of users than the number of available resources blocks, albeit at the cost of increased inter-user interference.

Thomas *et al.* [199] allocate the modulated symbols along either the delay or Doppler axes using sparse codes. Both the uplink and downlink are considered. In the downlink, a single pilot symbol associated with an appropriate guard band is used for channel estimation, to achieve a communication performance close to the perfect channel estimation case. For the uplink, a sophisticated channel estimation method is developed without excessive guard band overhead, as the effect of the sparse codes on the symbols cannot be separated from the multipath channel effects. Convolutional sparse coding techniques are utilised for uplink channel estimation, as the pilot symbols also rely on sparse codes in the pilot band, surrounded by guard bands.

Wen at al. [200, 201] allocate the symbols based on each user's sparse code along the delay and Doppler indices. The system firstly estimates the vector of superimposed transmitted symbols from all users in the TD, then decodes the symbols gleaned from each user in the DD employing a message passing algorithm. The system iterates between the two domains to accurately estimate the transmitted symbols.

Deka *et al.* [202] harness SCMA OTFS for both uplink and downlink communication, with the sparse codes aligned either along the delay axis, or the Doppler axis. Channel estimation is performed by embedding a pilot symbol surrounded by guard bands in the transmitted signal. The results show a lower BER for SCMA OTFS than for power-domain OTFS NOMA and DD index allocation OTFS for the same normalised user load.

Although SCMA-OTFS is a promising multi-user method, the characteristics of the transmitted signal are not optimal for sensing, since signals exhibiting a higher degree of randomness lead to an eroded sensing performance [102]. The sparsity of the codes is beneficial for reducing the detection and demodulation complexity, but increases the signal variability. This issue is also observed when IM is harnessed [1].

4.1.1.4 Dense Sequence Spreading OTFS

There are also a few publications on dense sequence spreading OTFS [203–205]. In [203], Sun *et al.* spread the symbols along the delay axis of the DD matrix. Two spreading sequence methods are considered: a single spreading sequence used to spread each symbol, or separate sequences used to spread each symbol. In the first case, a sequence having good autocorrelation properties is designed. In the second case, the optimisation problem is too complex, due to the immense variety of possible sequence combinations. Gold and m-sequences are used in this case. The BER of spread OTFS is shown to be lower than that of DSSS or spread OFDM.

In Cao *et al.* [204], each symbol is spread along the Doppler axis using m-sequences. A rake receiver is designed to detect the symbols. The channel is assumed to have two

paths, each with identical delays. This novel receiver leads to a lower BER than conventional MMSE detection in the limited channel conditions considered. The performance difference is more pronounced if the gains of each path are of similar magnitude.

In Ma *et al.* [205], the users are assigned to groups. Each user group is allocated a Doppler index, with each user symbol spread over the delay indices at the user group Doppler index. The sequences utilised are cyclically orthogonal, such as the columns or rows of a DFT matrix. The spread symbols are interleaved along the delay axis. However, no performance comparison to OTFS is provided.

4.1.2 Contributions

Again, there is a paucity of publications on the subject of dense sequence spreading OTFS, especially for ISAC. Hence, this work analyses the communication BER and sensing RMSE performance of CDMA-OTFS, and contrasts them with pure OTFS. Table 4.1 explicitly juxtaposes the novelties of the proposed system to the existing literature, which are detailed below:

- A detailed analysis of CDMA-OTFS in the context of ISAC is provided, where both fractional delay indices and fractional Doppler indices are considered.
- An in-depth analysis of the communication BER and sensing RMSE performance of delay only, Doppler only, and delay-Doppler sequence spreading for CDMA-OTFS.
- This work demonstrates that Zadoff-Chu Dl-CDMA-OTFS and DD-CDMA-OTFS are the configurations that consistently outperform pure OTFS sensing, whilst maintaining a similar communication performance at the same throughput.

4.2 Transmit Signal Model

The block diagrams of the communication and sensing models are shown in Figures 4.1 and 4.2 respectively. For sensing, the transmit signal is reflected off the objects in the environment, and these reflected echos are then detected by the receiver.

Sequence spreading across the delay, Doppler, or delay and Doppler indices is applied to OTFS, relying on Gold, Hadamard, and Zadoff-Chu sequences. A sequence of length M is used for delay-domain spreading, of length N for Doppler-domain spreading, and of length MN for DD spreading, where M is the number of subcarriers, and N is the number of symbols slots.

TABLE 4.1: Contrasting contributions to the literature

Topics \ Papers	[205]	[199]	[202]	[201]	[194]	[196]	[203]	[204]	[200]	This work
Channel modeling										
Fractional delay indices										✓
Fractional Doppler indices			✓	✓		✓			✓	✓
Sequence spreading										
Sequence spreading	✓	✓	✓	✓	✓		✓	✓	✓	✓
Dense sequences[1]	✓				✓		✓	✓		✓
Multi-user methods										
Multi-user communication	✓	✓	✓	✓	✓	✓			✓	✓
Resource allocation on delay only	✓	✓	✓			✓	✓			✓
Resource allocation on Doppler only		✓	✓			✓		✓		✓
Resource allocation on DD indices				✓		✓			✓	✓
Code multiple access methods	✓	✓	✓	✓					✓	✓
Code multiple access along the delay only, Doppler only, and DD indices										✓
ISAC										
Code multiple access OTFS communication and sensing										✓
Effect of spreading on the sensing RMSE performance										✓

[1] Dense sequences: all or the majority of the elements have a non-zero value, as opposed to sparse sequences

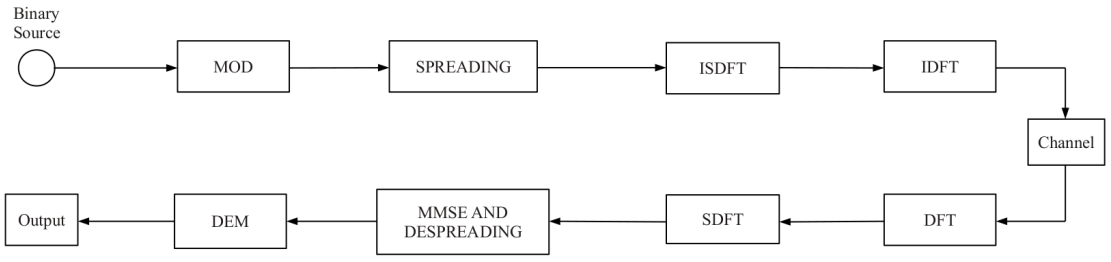

FIGURE 4.1: Block diagram of the communication model

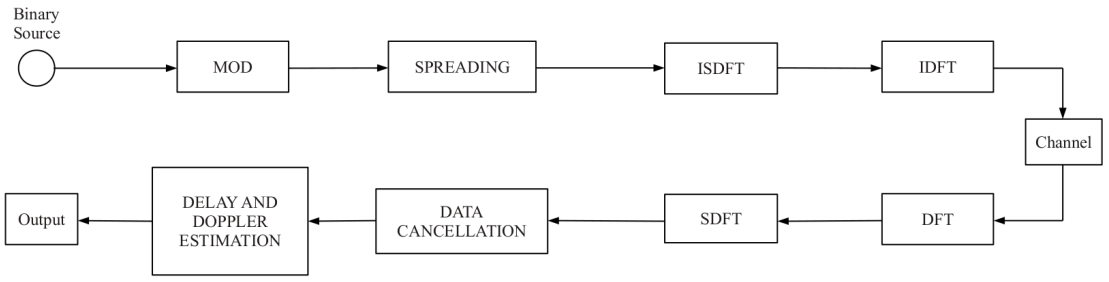

FIGURE 4.2: Block diagram of the sensing model

Each sequence $\boldsymbol{c}$ is power-normalised, hence:

$$\boldsymbol{c}^H \boldsymbol{c} = 1 \,, \tag{4.1}$$

where $(\cdot)^H$ is the Hermitian/complex transpose.

The matrix $\boldsymbol{C}$ containing all of the spreading sequences utilised is:

$$\boldsymbol{C} = (\boldsymbol{c}_0, \boldsymbol{c}_1, ..., \boldsymbol{c}_{N_{mult}-1}) \,, \tag{4.2}$$

where N_{mult} is the number of multiplexed modulated sequences.

The DD transmitted signal vector $\widetilde{\boldsymbol{x}} \in \mathbb{C}^{MN \times 1}$ is expressed as:

$$\widetilde{\boldsymbol{x}} = \mathfrak{C}\boldsymbol{s} \,, \tag{4.3}$$

where $\boldsymbol{s} \in \mathbb{C}^{N_s \times 1}$ is the vector of the modulated symbols, $\mathfrak{C} \in \mathbb{C}^{MN \times N_s}$ is the spreading matrix containing the spreading sequences, where the arrangement of the sequences is dependent on the specific CDMA-OTFS scheme implemented. Furthermore, N_s denotes the number of symbols transmitted in a frame. The system throughput is $\frac{\beta N_s}{MN}$ bpcu, where β is the number of bits per symbol. The CP is assumed to be sufficiently long, and it is perfectly removed from the received signal at the receiver.

4.2.1 Delay Code Division Multiple Access OTFS

For Dl-CDMA-OTFS, each modulated symbol $s_{n_{mult},\, n}$ is multiplied by a spreading sequence $\boldsymbol{c}_{n_{mult}} \in \mathbb{C}^{M \times 1}$, where $n_{mult} = (0,\, 1,\, ...,\, N_{mult} - 1)$, and $n = (0,\, 1,\, ...,\, N - 1)$. The total number of transmitted symbols $N_s = N_{mult}N$, and the maximum number of multiplexed sequences is M, hence $1 \leq N_{mult} \leq M$.

The DD transmitted signal matrix representation $\widetilde{\boldsymbol{X}} \in \mathbb{C}^{M \times N}$ is:

$$\widetilde{\boldsymbol{X}} = \boldsymbol{C}\boldsymbol{S} \,, \tag{4.4}$$

where $\boldsymbol{C} \in \mathbb{C}^{M \times N_{mult}}$, $\boldsymbol{S} \in \mathbb{C}^{N_{mult} \times N}$, and $\boldsymbol{S}[n_{mult},\, n] = s_{n_{mult},\, n}$.

The columns of $\widetilde{\boldsymbol{X}}$ are stacked to create the DD transmitted signal vector $\widetilde{\boldsymbol{x}}$:

$$\widetilde{\boldsymbol{x}}[nM : (n+1)M-1] = \widetilde{\boldsymbol{X}}[0 : M-1, n] \,, \tag{4.5}$$

where $n = (0, 1, ..., N-1)$.

The symbols can also be directly spread to form $\widetilde{\boldsymbol{x}}$, as in (4.3), where:

$$\boldsymbol{s}[nN_{mult} + n_{mult}] = s_{n_{mult},\, n} \,, \tag{4.6}$$

$$\mathfrak{C} = \mathrm{diag}(\boldsymbol{C}) \,, \tag{4.7}$$

and $\mathrm{diag}(\boldsymbol{C})$ is the diagonal operator, which creates a matrix whose diagonal elements are $\boldsymbol{C}$.

As an example, for $M = 4$, $N = 3$, $N_{mult} = 2$, $\boldsymbol{C} \in \mathbb{C}^{M \times N_{mult}} = \mathbb{C}^{4\times 2}$, and $\mathfrak{C}$ is:

$$\mathfrak{C} = \begin{bmatrix} \boldsymbol{C} & \boldsymbol{0}_{4\times 2} & \boldsymbol{0}_{4\times 2} \\ \boldsymbol{0}_{4\times 2} & \boldsymbol{C} & \boldsymbol{0}_{4\times 2} \\ \boldsymbol{0}_{4\times 2} & \boldsymbol{0}_{4\times 2} & \boldsymbol{C} \end{bmatrix} \,, \tag{4.8}$$

where $\boldsymbol{0}_{4\times 2}$ is a 4×2 matrix of 0.

4.2.2 Doppler Code Division Multiple Access OTFS

For Doppler Code Division Multiple Access OTFS (Dp-CDMA-OTFS), each modulated symbol $s_{m,\, n_{mult}}$ is multiplied by a spreading sequence $\boldsymbol{c}_{n_{mult}} \in \mathbb{C}^{N\times 1}$, where $m = (0, 1, ..., M-1)$. The total number of transmitted symbols is $N_s = N_{mult}M$, and the maximum number of multiplexed sequences is N, hence $1 \leq N_{mult} \leq N$.

The DD transmitted signal matrix representation $\widetilde{\boldsymbol{X}}$ is:

$$\widetilde{\boldsymbol{X}} = \boldsymbol{S}\boldsymbol{C}^T \,, \tag{4.9}$$

where $(\cdot)^T$ is the transpose operation, $\boldsymbol{C} \in \mathbb{C}^{N\times N_{mult}}$, $\boldsymbol{S} \in \mathbb{C}^{M\times N_{mult}}$, $\boldsymbol{S}[m, n_{mult}] = s_{m,\, n_{mult}}$, and $m = (0, 1, ..., M-1)$.

The columns of $\widetilde{\boldsymbol{X}}$ are stacked to create the DD transmitted signal vector $\widetilde{\boldsymbol{x}}$, as shown in (4.5). The symbols can also be directly spread to form $\widetilde{\boldsymbol{x}}$, as in (4.3), where:

$$\boldsymbol{s}[mN_{mult} + n_{mult}] = s_{m,\, n_{mult}} \,, \tag{4.10}$$

$$\mathfrak{C}[nM + m,\, mN_{mult} : (m+1)N_{mult} - 1] = \boldsymbol{C}[n, 0 : N_{mult} - 1] \,, \tag{4.11}$$

with $m = (0, 1, ..., M-1)$, and $n = (0, 1, ..., N-1)$.

As an example, for $M = 4$, $N = 3$, $N_{mult} = 2$, $\boldsymbol{C} \in \mathbb{C}^{N \times N_{mult}} = \mathbb{C}^{3\times 2}$, and $\mathfrak{C}$:

$$\mathfrak{C} = \begin{bmatrix} \boldsymbol{C}[0,0] & \boldsymbol{C}[0,1] & 0 & 0 & 0 & 0 & 0 & 0 \\ 0 & 0 & \boldsymbol{C}[0,0] & \boldsymbol{C}[0,1] & 0 & 0 & 0 & 0 \\ 0 & 0 & 0 & 0 & \boldsymbol{C}[0,0] & \boldsymbol{C}[0,1] & 0 & 0 \\ 0 & 0 & 0 & 0 & 0 & 0 & \boldsymbol{C}[0,0] & \boldsymbol{C}[0,1] \\ \boldsymbol{C}[1,0] & \boldsymbol{C}[1,1] & 0 & 0 & 0 & 0 & 0 & 0 \\ 0 & 0 & \boldsymbol{C}[1,0] & \boldsymbol{C}[1,1] & 0 & 0 & 0 & 0 \\ 0 & 0 & 0 & 0 & \boldsymbol{C}[1,0] & \boldsymbol{C}[1,1] & 0 & 0 \\ 0 & 0 & 0 & 0 & 0 & 0 & \boldsymbol{C}[1,0] & \boldsymbol{C}[1,1] \\ \boldsymbol{C}[2,0] & \boldsymbol{C}[2,1] & 0 & 0 & 0 & 0 & 0 & 0 \\ 0 & 0 & \boldsymbol{C}[2,0] & \boldsymbol{C}[2,1] & 0 & 0 & 0 & 0 \\ 0 & 0 & 0 & 0 & \boldsymbol{C}[2,0] & \boldsymbol{C}[2,1] & 0 & 0 \\ 0 & 0 & 0 & 0 & 0 & 0 & \boldsymbol{C}[2,0] & \boldsymbol{C}[2,1] \end{bmatrix}. \tag{4.12}$$

4.2.3 Delay Doppler Code Division Multiple Access OTFS

For DD-CDMA-OTFS, each modulated symbol $s_{n_{mult}}$ is multiplied by a spreading sequence $\boldsymbol{c}_{n_{mult}} \in \mathbb{C}^{MN\times 1}$. The total number of transmitted symbols $N_s = N_{mult}$, and the maximum number of multiplexed sequences is MN, hence $1 \leq N_{mult} \leq MN$. The DD-CDMA-OTFS scheme can therefore support more users by relying on a greater number of unique spreading sequences than Dl-CDMA-OTFS and Dp-CDMA-OTFS.

The symbols are directly spread to form $\widetilde{\boldsymbol{x}}$, as in (4.3):

$$\widetilde{\boldsymbol{x}} = \sum_{n_{mult}=0}^{N_{mult}-1} \boldsymbol{c}_{n_{mult}} s_{n_{mult}} = \boldsymbol{C}\boldsymbol{s}\,, \tag{4.13}$$

where $\boldsymbol{s} \in \mathbb{C}^{N_{mult}}$, $\boldsymbol{C} \in \mathbb{C}^{MN\times N_{mult}}$, and $\mathfrak{C} = \boldsymbol{C}$.

4.3 Channel Model

In this section, the channel models are introduced. The generalised TD, TF, and DD channel models are described in Section 4.3.1. The communication channel parameters are presented in Section 4.3.2, while the sensing channel parameters are discussed in Section 4.3.3.

4.3.1 Generalised Channel Model

It is assumed that there is no external interference during transmission. The transmitted signal is passed through a time-varying and frequency-selective fading channel, as modelled in [179]. The DD representation of the fading channel is:

$$\widetilde{h}(\tau, \nu) = \sum_{p=0}^{P-1} \widetilde{h}_p \delta(\tau - \tau_p)\delta(\nu - \nu_p) \,, \tag{4.14}$$

where τ is the delay, ν is the Doppler shift, $p = [0, 1, ..., P-1]$ is the propagation path index, and P is the total number of propagation paths. Furthermore, τ_p is the delay associated with the p^{th} path, ν_p is the Doppler shift associated with the p^{th} path, $\widetilde{h}_p$ is the fading gain and path loss associated with the p^{th} path, and $\delta(\cdot)$ is the Dirac delta function.

When sampled in the DD, the channel can be represented by the time-invariant parameter $\widetilde{h}_p$, the delay index l, and the Doppler index k. The delay and Doppler indices are defined as:

$$l = (\Delta f M)\tau \,, \tag{4.15}$$

$$k = \frac{N}{\Delta f}\nu \,, \tag{4.16}$$

where Δf is the subcarrier spacing.

The TD representation of the fading channel is:

$$h_{m,\,n,\,p} = \widetilde{h}_p e^{j2\pi k_p \frac{nM+m-l_p}{MN}} \,, \tag{4.17}$$

where $j = \sqrt{-1}$, l_p is the delay index associated with the p^{th} propagation path, and k_p is the Doppler index associated with the p^{th} propagation path.

The TD channel matrix $\boldsymbol{H}_n \in \mathbb{C}^{M \times M}$ is:

$$\boldsymbol{H}_n[m, \lfloor m - l_p \rfloor_M] = \sum_{p=0}^{P-1} h_{m,\,n,\,p} \,, \tag{4.18}$$

where $\lfloor \cdot \rfloor_M$ is the modulo M operator.

When the delay indices are assumed to be integers, the TD received signal $\boldsymbol{y} \in \mathbb{C}^{M \times 1}$ is

$$\boldsymbol{y}_n = \boldsymbol{H}_n \boldsymbol{x}_n + \boldsymbol{z} \,, \tag{4.19}$$

where $\boldsymbol{x}_n \in \mathbb{C}^{M \times 1}$ is the TD transmitted signal, and $\boldsymbol{z}$ is the complex TD AWGN, with mean $\mu_z = 0$ and variance σ_z^2, expressed as $\mathcal{N}(\mu_z, \sigma_z^2)$.

When the integer delay index assumption is discarded, $(m - l_p)$ is not an integer for $m = (0, 1, ..., M-1)$. As matrices do not have fractional indices, the channel must to be modelled differently. A portion of the fading channel is modelled in the TF and then converted to the TD as follows:

$$\boldsymbol{y}_n[m] = \frac{1}{\sqrt{M}} \sum_{p=0}^{P-1} h_{m,\,n,\,p} \sum_{\bar{m}=0}^{M-1} \bar{\boldsymbol{x}}_n[\bar{m}] e^{j2\pi \frac{(m-l_p)\bar{m}}{M}} + \boldsymbol{z}_n[m]\,, \tag{4.20}$$

where $\bar{\boldsymbol{x}} \in \mathbb{C}^{M\times N}$ is the TF transmitted signal, and $\bar{m} = [0, 1, ..., M-1]$.

The TF channel matrix $\bar{\boldsymbol{H}}_n \in \mathbb{C}^{M\times M}$ is:

$$\bar{\boldsymbol{H}}_n = \mathcal{F}_M \boldsymbol{H}_n \mathcal{F}_M^H\,, \tag{4.21}$$

where $\mathcal{F}_M$ is the M-point DFT and $\mathcal{F}_M^H$ is the M-point IDFT.

The DD channel matrix $\widetilde{\boldsymbol{H}} \in \mathbb{C}^{MN\times MN}$ is:

$$\widetilde{\boldsymbol{H}} = \left(\mathcal{F}_N \otimes \mathcal{F}_M^H\right) \bar{\boldsymbol{H}}_X \left(\mathcal{F}_N^H \otimes \mathcal{F}_M\right)\,, \tag{4.22}$$

where $\otimes$ is the Kronecker product, and

$$\bar{\boldsymbol{H}}_X = \operatorname{diag}\left(\bar{\boldsymbol{H}}_n\right) = \begin{bmatrix} \bar{\boldsymbol{H}}_0 & \boldsymbol{0}_{M\times M} & \cdots & \boldsymbol{0}_{M\times M} \\ \boldsymbol{0}_{M\times M} & \bar{\boldsymbol{H}}_1 & \cdots & \boldsymbol{0}_{M\times M} \\ \vdots & \vdots & \ddots & \vdots \\ \boldsymbol{0}_{M\times M} & \boldsymbol{0}_{M\times M} & \cdots & \bar{\boldsymbol{H}}_{N-1} \end{bmatrix}\,. \tag{4.23}$$

4.3.2 Communication Channel Parameters

Integer delay indices, fractional Doppler indices, and Rician fading are assumed for communication. There are P_{com} propagation paths. The first path $p_{com} = 0$ is the LoS path, and the remaining $P_{com} - 1$ paths are NLoS paths. The fading gain $\widetilde{h}_{p,\,com}$ of the $p_{com}{}^{\text{th}}$ propagation path is:

$$\widetilde{h}_{p,\,com} = \begin{cases} \sqrt{\frac{\kappa_{com}}{\kappa_{com}+1}}, & \text{if } p_{com} = 0 \\ \sqrt{\frac{1}{(\kappa_{com}+1)(P_{com}-1)}}\zeta_{p,\,com}, & \text{if } p_{com} > 0\,, \end{cases} \tag{4.24}$$

where κ_{com} is the Rician K factor, and $\zeta_{p,\,com}$ is a complex Gaussian random variable with mean $\mu_{com} = 0$ and variance $\sigma_{com}^2 = 1$, expressed as $\mathcal{N}(\mu_{com}, \sigma_{com}^2)$.

The integer delay index $l_{p,\,com}$ is:

$$l_{p,\,com} = \begin{cases} 0, & \text{if } p_{com} = 0 \\ p_{com} \,\%\, L_{com}, & \text{if } p_{com} > 0 \;\&\; P_{com} \geq L_{com} \\ \lfloor L_{com}\eta_{\tau,\,com} \rceil, & \text{if } p_{com} > 0 \;\&\; P_{com} < L_{com}, \end{cases} \tag{4.25}$$

where L_{com} is the number of delay taps, $p_{com} = [0,\, 1,\, ...,\, P_{com} - 1]$, % is the remainder or modulus operator, $\eta_{\tau,\,com}$ is a random variable following a uniform distribution between 0 and 1, and $\lfloor \cdot \rceil$ is the rounding function.

If $P_{com} < L_{com}$, no pair of propagation paths will have the same delay index, yielding: $l_{p_1,\,com} \neq l_{p_2,\,com}$, where $p_1 = [0,\, 1,\, ...\, P_{com} - 1]$, $p_2 = [0,\, 1,\, ...\, P_{com} - 1]$, and $p_1 \neq p_2$.

The fractional Doppler index $k_{p,\,com}$ is:

$$k_{p,\,com} = \begin{cases} k_{com,\,max}, & \text{if } p_{com} = 0 \\ \lfloor 2k_{com,\,max}\,(\eta_{v,\,com} - 0.5) \rceil, & \text{if } p_{com} > 0\,, \end{cases} \tag{4.26}$$

where $\eta_{v,\,com}$ is a random variable following a uniform distribution between 0 and 1, and $k_{com,\,max}$ is the maximum integer Doppler index:

$$k_{com,\,max} = \lceil \frac{f_c N V_{com}}{\Delta f c_0} \rceil\,, \tag{4.27}$$

with V_{com} representing the velocity of the communication receiver, f_c is the carrier frequency, c_0 is the speed of light, and $\lceil \cdot \rceil$ is the ceiling function.

4.3.3 Sensing Channel Parameters

The delay and Doppler indices for sensing, $l_{p,\,sen}$ and $k_{p,\,sen}$ respectively, are:

$$l_{p,\,sen} = \frac{2\Delta f M R_{p,\,sen}}{c_0}\,, \tag{4.28}$$

$$k_{p,\,sen} = \frac{2 f_c N V_{p,\,sen}}{\Delta f c_0}\,, \tag{4.29}$$

where $R_{p,\,sen}$ is the range of the ${p_{sen}}^{\text{th}}$ path, $V_{p,\,sen}$ is the velocity of the ${p_{sen}}^{\text{th}}$ path, $p_{sen} = [0,\, 1,\, ...,\, P_{sen} - 1]$, and P_{sen} is the number of sensing propagation paths.

As monostatic sensing is assumed, the transmitted signal is reflected from the target to the sensing receiver attached or adjacent to the transmitter, hence a factor of 2 is present in (4.28) and (4.29). It is assumed that the self-interference between the transmit signal and received echos is perfectly mitigated by appropriate shielding, signal processing methods, and/or an orthogonal signaling scheme (e.g. similar to TDMA). The first P_t

propagation paths are LoS paths associated with each sensing target, and the remaining P_n paths are NLoS paths. The total number of sensing propagation paths P_{sen} is:

$$P_{sen} = P_t + P_n \ . \tag{4.30}$$

The fading gain $\widetilde{h}_{p_t,\,sen}$ of the $p_t{}^{\text{th}}$ target is:

$$\widetilde{h}_{p_t,\,sen} = \sqrt{\frac{\kappa_{sen}}{\kappa_{sen}+1}}\sqrt{\widetilde{\psi}^2_{p_t}} \ , \tag{4.31}$$

where κ_{sen} is the sensing Rician K factor, and $\widetilde{\psi}^2_{p_t}$ is the power gain associated with the $p_t{}^{\text{th}}$ LoS path, defined as:

$$\widetilde{\psi}^2_{p_t} = \frac{c_0^2\sigma_{p_t}}{(4\pi)^3 f_c^2 R^4_{p,\,sen}} \ , \tag{4.32}$$

where σ_{p_t} is the radar cross-section of the $p_t{}^{\text{th}}$ target.

The fading gain $\widetilde{h}_{p_n,\,sen}$ of the $p_n{}^{\text{th}}$ NLoS path is:

$$\widetilde{h}_{p_n,\,sen} = \sqrt{\frac{1}{P_n(\kappa_{sen}+1)}}\zeta_{p_n,\,sen}\min_{\forall p_t}\left(\sqrt{\widetilde{\psi}^2_{p_t}}\right) \ , \tag{4.33}$$

where $\zeta_{p_n,\,sen}$ is a complex Gaussian random variable with mean $\mu_{sen} = 0$ and variance $\sigma^2_{sen} = 1$, expressed as $\mathcal{N}(\mu_{sen}, \sigma^2_{sen})$.

The NLoS power is set relative to the smallest value of $\widetilde{\psi}^2_{p_t}$, which is associated with the weakest target signal. The smallest value of $\widetilde{\psi}^2_{p_t}$ is used to ensure that no NLoS paths have an average power higher than $\sqrt{\frac{1}{P_n(\kappa_{sen}+1)}}$ relative to any of the targets. As the system is operating in the mmWave band, the NLoS reflections are assumed, on average, to be weaker than the LoS signals.

The range and velocity of the NLoS paths, $R_{p_n,\,sen}$ and $V_{p_n,\,sen}$, are:

$$R_{p_n,\,sen} = R_{n,\,max}\eta_{\tau,\,sen} \ , \tag{4.34}$$

$$V_{p_n,\,sen} = 2V_{n,\,max}\left(\eta_{v,\,sen} - 0.5\right) \ , \tag{4.35}$$

where $\eta_{\tau,\,sen}$ and $\eta_{v,\,sen}$ are random variables following a uniform distribution between 0 and 1, and:

$$R_{n,\,max} = \sqrt[4]{\kappa_{sen}}\max_{\forall p_t}\left(R_{p_t,\,sen}\right) \ , \tag{4.36}$$

$$V_{n,\,max} = \frac{\Delta f c_0}{4 f_c} \ , \tag{4.37}$$

The fourth root of κ_{sen} is present in (4.36) as the power gain is inversely proportional to R^4, as seen in (4.32). A maximum range is fixed, because the reflected signals having

NLoS paths associated with delays larger than the maximum in (4.36) are assumed to not significantly interfere, due to the high attenuation associated with a greater range.

4.4 Received Signal Processing

4.4.1 Communication Data Detection

The DD received signal $\widetilde{\boldsymbol{y}} \in \mathbb{C}^{MN\times 1}$ can be represented as:

$$\widetilde{\boldsymbol{y}} = \widetilde{\boldsymbol{H}}\widetilde{\boldsymbol{x}} + \widetilde{\boldsymbol{z}}\,, \tag{4.38}$$

where and $\widetilde{\boldsymbol{z}}$ is the complex-valued AWGN in the DD.

MMSE demodulation is applied at the receiver, with perfect channel estimation assumed. The vector of estimated symbols $\hat{\boldsymbol{s}} \in \mathbb{C}^{N_s\times 1}$ is formulated as:

$$\hat{\boldsymbol{s}} = \widetilde{\boldsymbol{G}}^H \widetilde{\boldsymbol{y}}\,, \tag{4.39}$$

where $\widetilde{\boldsymbol{G}}$ is:

$$\widetilde{\boldsymbol{G}} = \left(\widetilde{\boldsymbol{H}}\mathfrak{C}\mathfrak{C}^H\widetilde{\boldsymbol{H}}^H + N_0\boldsymbol{I}_{MN\times MN}\right)^{-1}\widetilde{\boldsymbol{H}}\mathfrak{C}\,, \tag{4.40}$$

where N_0 is the AWGN power, and $\boldsymbol{I}_{MN\times MN}$ is the $MN \times MN$ identity matrix. The estimated symbols are then demodulated to obtain the estimated bits.

4.4.2 Sensing Target Parameter Estimation

For sensing, the number of targets is assumed to be known, either through prior knowledge, or by the use of a separate estimation algorithm, such as a generalised likelihood ratio test [145, 146]. The directions of the targets are assumed to be estimated by a separate method, for example by the popular MUSIC algorithm [39].

A two step sensing method is applied. The first step utilises a data cancellation-based method to estimate the integer indices of the targets. The accuracy of this step is limited by the system parameters. The second step employs ML detection to estimate the fractional component of the indices estimated in step 1. The resolution of the fractional index estimation is a separate system parameter N_{ML}.

The first step is a modified data cancellation method adapted from [144]. The DD received signal can be represented as in (4.38), or as:

$$\widetilde{\boldsymbol{y}} = \widetilde{\boldsymbol{X}}_X\widetilde{\boldsymbol{h}} + \widetilde{\boldsymbol{z}}\,, \tag{4.41}$$

where $\widetilde{\boldsymbol{h}} \in \mathbb{C}^{MN\times 1}$ is the vector containing the propagation path gains at the associated delay-Doppler indices, and $\widetilde{\boldsymbol{X}}_X \in \mathbb{C}^{MN\times MN}$ is an expanded matrix of the DD transmitted signal matrix $\widetilde{\boldsymbol{X}}$:

$$\widetilde{\boldsymbol{X}}_X[l_1+Mk_1, l_2+Mk_2] = \begin{cases} \widetilde{\boldsymbol{X}}[l_1-l_2+M, k_{diff}]e^{\frac{j2\pi k_2(l_1-l_2)}{MN}}, & \text{if } l_1-l_2<0 \\ \widetilde{\boldsymbol{X}}[l_1-l_2, k_{diff}]e^{\frac{j2\pi k_2(l_1-l_2)}{MN}}, & \text{if } l_1-l_2>0\,, \end{cases} \tag{4.42}$$

where l_1 and $l_2 = [0, 1, ..., M-1]$, k_1 and $k_2 = [0, 1, ..., N-1]$, and:

$$k_{diff} = \begin{cases} k_1-k_2+N, & \text{if } k_1-k_2<0 \\ k_1-k_2, & \text{if } k_1-k_2>0\,. \end{cases} \tag{4.43}$$

The estimated channel parameter vector $\hat{\boldsymbol{h}}$ is calculated as follows:

$$\hat{\boldsymbol{h}} = \widetilde{\boldsymbol{X}}_X^H \widetilde{\boldsymbol{y}}\,. \tag{4.44}$$

The indices at which the P_t peak amplitudes of $||\hat{\boldsymbol{h}}||^2$ occur are the estimated integer delay and Doppler indices $\hat{l}_{p_t}^{dc}$ and $\hat{k}_{p_t}^{dc}$ of the first step, where $||\cdot||$ is the Euclidean norm.

The ML second step used for fractional index estimation applies ML estimation to the indices adjacent to the P_t delay and Doppler integer indices gleaned from the first step. The delay indices $\boldsymbol{l}_{p_t}^{ml}$ and Doppler indices $\boldsymbol{k}_{p_t}^{ml}$ considered for the $p_t{}^{\text{th}}$ target are:

$$\boldsymbol{l}_{p_t}^{ml} = \hat{l}_{p_t}^{dc}\mathbf{1}_{(2N_{ML}+1)\times 1} + \frac{\boldsymbol{n_l}}{N_{ML}}\,, \tag{4.45}$$

$$\boldsymbol{k}_{p_t}^{ml} = \hat{k}_{p_t}^{dc}\mathbf{1}_{(2N_{ML}+1)\times 1} + \frac{\boldsymbol{n_k}}{N_{ML}}\,, \tag{4.46}$$

where $\mathbf{1}_{(2N_{ML}+1)\times 1}$ is a $[(2N_{ML}+1)\times 1]$ vector of 1, $\boldsymbol{n_l} = \big[-N_{ML}, -N_{ML}+1, ..., 0, ..., N_{ML}-1, N_{ML}\big]$, $\boldsymbol{n_k} = \big[-N_{ML}, -N_{ML}+1, ..., 0, ..., N_{ML}-1, N_{ML}\big]$, and N_{ML} is the interpolation or resolution refinement factor.

The ML algorithm creates a set of equivalent channels $\hat{\boldsymbol{H}}_{l_{p_t}^{ml}, k_{p_t}^{ml}}$, with a gain of 1, for the sets $\boldsymbol{l}_{p_t}^{ml}$ and $\boldsymbol{k}_{p_t}^{ml}$. The gain is set to 1 since no channel gain estimation is performed. The algorithm calculates the peak associated with each combination, and determines the indices $\hat{l}_{p_t}^{ml}$ and $\hat{k}_{p_t}^{ml}$ estimated by selecting the combination with the largest peak, following [122]:

$$(\hat{l}_{p_t}^{ml}, \hat{k}_{p_t}^{ml}) = \arg\max_{\forall l_{p_t}^{ml}, k_{p_t}^{ml}} \frac{||\widetilde{\boldsymbol{x}}^H \hat{\boldsymbol{H}}_{l_{p_t}^{ml}, k_{p_t}^{ml}}^H \widetilde{\boldsymbol{y}}||^2}{\widetilde{\boldsymbol{x}}^H \hat{\boldsymbol{H}}_{l_{p_t}^{ml}, k_{p_t}^{ml}}^H \hat{\boldsymbol{H}}_{l_{p_t}^{ml}, k_{p_t}^{ml}} \widetilde{\boldsymbol{x}}}\,, \tag{4.47}$$

where $\widetilde{\boldsymbol{y}}$ is the DD received signal vector.

The indices $\hat{l}_{p_t}^{ml}$ and $\hat{k}_{p_t}^{ml}$ are then used to calculate the target range $\hat{R}_{p_t,\,sen}$ and velocity $\hat{V}_{p_t,\,sen}$, following [1]:

$$\hat{R}_{p_t,\,sen} = \frac{\hat{l}_{p_t}^{ml} c_0}{2Mf_s}\,, \tag{4.48}$$

$$\hat{V}_{p_t,\,sen} = \frac{\hat{k}_{p_t}^{ml} \Delta f c_0}{2Nf_c}\,. \tag{4.49}$$

4.5 Cramér-Rao Bound

Following [206], the average unbiased estimator CRBs for the associated range and velocity estimation are defined as:

$$\hat{\sigma}_{l,\,R}^2 \geq \frac{N_0}{P_{avg}|\widetilde{h}_{p_t,\,sen}|^2 \pi^2 MN(M-1)^2} \left(\frac{c_0}{2\Delta f}\right)^2\,, \tag{4.50}$$

$$\hat{\sigma}_{l,\,V}^2 \geq \frac{N_0}{P_{avg}|\widetilde{h}_{p_t,\,sen}|^2 \pi^2 MN(N-1)^2} \left(\frac{c_0 \Delta f}{2f_c}\right)^2\,, \tag{4.51}$$

where $\hat{\sigma}_{l,\,R}^2$ and $\hat{\sigma}_{l,\,V}^2$ are the variance of the target range and of the velocity estimation errors, respectively, while P_{avg} is the average power of the transmitted signal.

As the RMSE is the metric used for sensing, the standard deviation is utilised:

$$\hat{\sigma}_{l,\,R} \geq \sqrt{\frac{N_0}{P_{avg}|\widetilde{h}_{p_t,\,sen}|^2 \pi^2 MN(M-1)^2}}\,\frac{c_0}{2\Delta f}\,, \tag{4.52}$$

$$\hat{\sigma}_{l,\,V} \geq \sqrt{\frac{N_0}{P_{avg}|\widetilde{h}_{p_t,\,sen}|^2 \pi^2 MN(N-1)^2}}\,\frac{c_0 \Delta f}{2f_c}\,, \tag{4.53}$$

where $\hat{\sigma}_{l,\,R}$ and $\hat{\sigma}_{l,\,V}$ are the standard deviations of the target range and velocity estimation errors, respectively.

It is important to note that this CRB is an average CRB, not a true lower bound.

4.6 Computational Complexity Analysis

This section quantifies the additional complexity introduced by CDMA-OTFS to the modulation and communication demodulation compared to OTFS, and the complexity of the target parameter estimation methods.

4.6.1 Additional Modulation and Demodulation Complexity Compared to OTFS

In (4.3), the modulation relies on a multiplication of an $(MN \times N_s)$ matrix by an $(N_s \times 1)$ vector. The computational complexity of this operation is on the order of $O(MNN_s)$, for all the CDMA-OTFS schemes.

For Dl-CDMA-OTFS, $N_s = N_{mult}N$, $1 \leq N_{mult} \leq M$, hence the complexity at the minimum and maximum throughputs is $O(MN^2)$ and $O(M^2N^2)$, respectively.

For Dp-CDMA-OTFS, $N_s = N_{mult}M$, $1 \leq N_{mult} \leq N$, hence the complexity at the minimum and maximum throughputs is $O(M^2N)$ and $O(M^2N^2)$, respectively.

For DD-CDMA-OTFS, $N_s = N_{mult}$, $1 \leq N_{mult} \leq MN$, hence the complexity at the minimum and maximum throughputs is $O(MN)$ and $O(M^2N^2)$, respectively.

The computational complexity of all the CDMA-OTFS schemes is the same for the same throughput. Modulating using (4.4) for Dl-CDMA-OTFS and (4.9) for Dp-CDMA-OTFS leads to the same complexity.

For MMSE demodulation, there is an additional matrix multiplication required in (4.40), where the channel matrix $(MN \times MN)$ is multiplied by the spreading matrix $(MN \times N_s)$. This multiplication can be performed once, with the resulting matrix used three times in (4.40). The complexity of the multiplication is on the order of $O(M^2N^2N_s)$.

4.6.2 Complexity of the Sensing Methods

There are $MN \times MN$ operations required for the creation of the expanded matrix of the DD transmitted signal (4.42), hence the complexity is $O(M^2N^2)$. The complexity of the matrix multiplication of the data cancellation method (4.44) is $O(MN \times MN \times 1) = O(M^2N^2)$, since an $(MN \times MN)$ matrix is multiplied by an $(MN \times 1)$ vector. The total complexity of this algorithm is therefore $O(2M^2N^2)$.

The computational complexity of (4.47) for fractional index estimation is $O(2MN)$. This operation is repeated $(2N_{ML}+1)^2$ times, hence the total complexity of the ML fractional index estimation is $O(2MN(2N_{ML}+1)^2)$.

4.6.3 Discussions

The additional complexity imposed on the modulation by CDMA-OTFS is comparable to that of SCMA OTFS schemes, as both involve the spreading of symbols across the available resources. There exist certain matrix multiplication methods having reduced

complexity for sparse matrices, so the additional complexity of SCMA OTFS may be reduced, depending on the spreading matrix structure. Other multi-user methods, such as directly allocating DD indices to users [196–198], may have a lower modulation complexity, depending on their modulation structure.

The additional demodulation complexity of CDMA-OTFS is much lower than that of DD index allocation, because the properties of the dense sequences chosen for CDMA-OTFS allow for a relatively simple demodulation, due to their desirable cross-correlation properties. Although no correlation operations are harnessed for communication detection and demodulation, the low cross-correlation of the sequences mitigates inter-user/inter-symbol interference. This trend becomes more pronounced when perfectly orthogonal sequences having zero-cross-correlation are employed. DD index allocation requires more complex demodulation methods, for example, iterative methods such as successive interference cancellation, in order to mitigate the inter-symbol and inter-user interference.

4.7 Simulation Results and Discussions

This section discusses the BER results and sensing RMSE results of both multi-user CDMA-OTFS and single-user OTFS. The single-user OTFS system assigns a single symbol to each DD resource, hence transmitting MN symbols in a frame. In the legend, "Gold" refers to Gold sequence spreading, "Had" refers to Hadamard sequence spreading, and "ZC" refers to Zadoff-Chu sequence spreading.

4.7.1 Communication BER Results

TABLE 4.2: Communication simulation parameters

Variable	Value
Carrier frequency f_c	40 GHz
Subcarrier spacing Δf	120 kHz
Number of communication delay taps L_{com}	3
Number of communication propagation paths P_{com}	3
Rician K factor κ_{com}	0 dB
Number of subcarriers M	64
Number of symbols sent per frame N	64
Communication receiver velocity	200 m/s
Minimum number of bit errors	600
Maximum number of bits simulated	1×10^7

The simulation parameters used are shown in Table 4.2. The BER of QPSK Gold, Hadamard, and Zadoff-Chu sequence spreading for Dl-CDMA-OTFS, Dp-CDMA-OTFS, and DD-CDMA-OTFS is portrayed in Figure 4.4 for $N_{mult} = 1$. The BER of

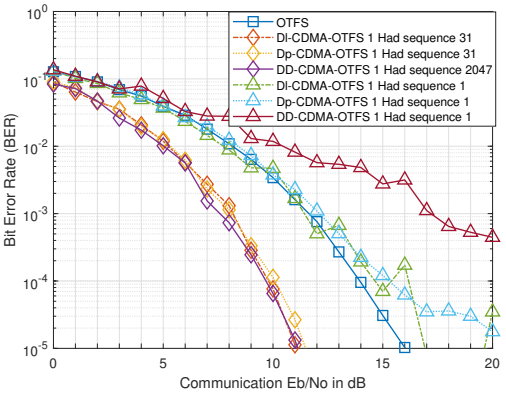

FIGURE 4.3: BER of QPSK Hadamard sequences 1 and 31 spreading for $N_{mult} = 1$ for Dl-CDMA-OTFS and Dp-CDMA-OTFS, Hadamard sequences 1 and 2047 spreading for DD-CDMA-OTFS, and of OTFS QPSK

OTFS QPSK is also shown in Figure 4.4. At the minimum throughput, all system configurations relying on the three sequences have similar BER performances. The BER of CDMA-OTFS for $N_{mult} = 1$ is much lower than that of OTFS, albeit at a large cost of throughput, which is reduced by a factor of 64 for Dl-CDMA-OTFS and Dp-CDMA-OTFS, and a factor of 4096 for DD-CDMA-OTFS.

The performance of Hadamard sequences for $N_{mult} = 1$ depends on the specific Hadamard sequence selected, as shown in Figure 4.3. When the first Hadamard sequence of the Hadamard matrix is selected (Hadamard sequence 1), the BER for CDMA-OTFS is higher than that of OTFS, as this sequence is a vector of 1.

The BER of QPSK Gold, Hadamard, and Zadoff-Chu sequence spreading for $N_{mult} = 32$ for Dl-CDMA-OTFS and Dp-CDMA-OTFS, $N_{mult} = 2048$ for DD-CDMA-OTFS, and of OTFS QPSK is shown in Figure 4.5 for a throughput of 1 bpcu for CDMA-OTFS. For 1 bpcu, the Zadoff-Chu sequence outperforms OTFS for all spreading configurations, as Zadoff-Chu sequences are resistant to delay and Doppler interference. The BER of Gold sequence spreading is similar to that of OTFS for all spreading configurations, with the BER of Gold DD-CDMA-OTFS slightly lower than that of OTFS at high E_b/N_0. This is because the length of the Gold sequences for DD-CDMA-OTFS is longer than for Dl-CDMA-OTFS and Dp-CDMA-OTFS. The BER performance of Hadamard Dl-CDMA-OTFS and Dp-CDMA-OTFS is similar to OTFS for the majority of the E_b/N_0 range, but its BER is slightly higher at larger E_b/N_0, as Hadamard sequences are vulnerable to multi-path interference. The BER of Hadamard DD-CDMA-OTFS is higher than that of OTFS, since the spreading sequence experiences multi-path interference in both the delay and Doppler domains.

The BER of QPSK Gold, Hadamard, and Zadoff-Chu sequence spreading for $N_{mult} = 64$ for Dl-CDMA-OTFS and Dp-CDMA-OTFS, $N_{mult} = 4096$ for DD-CDMA-OTFS, and of

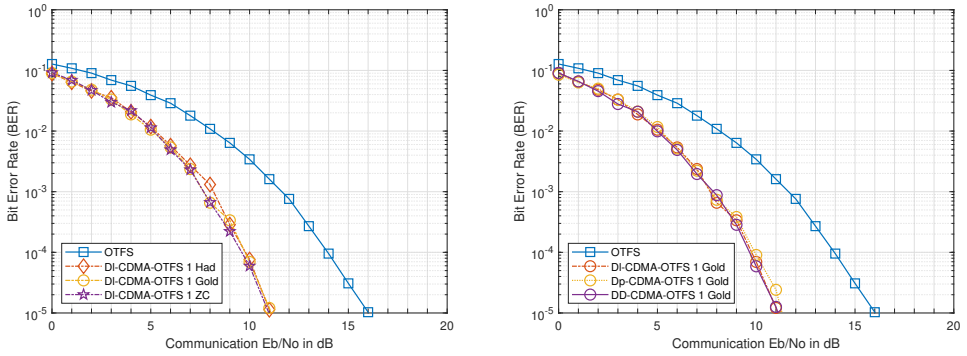

(A) OTFS and Dl-CDMA-OTFS

(B) OTFS and Gold sequence

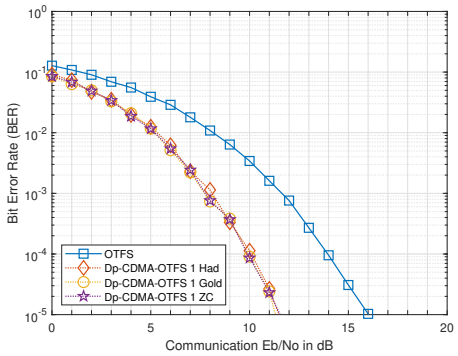

(C) OTFS and Dp-CDMA-OTFS

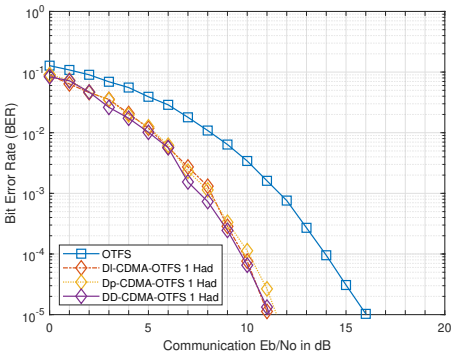

(D) OTFS and Hadamard sequence

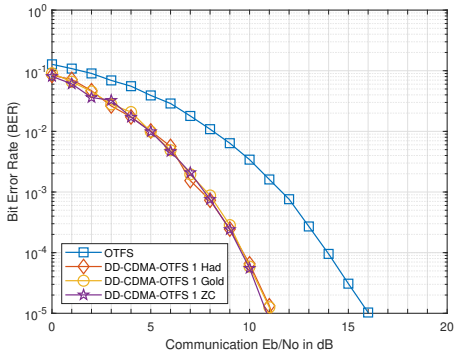

(E) OTFS and DD-CDMA-OTFS

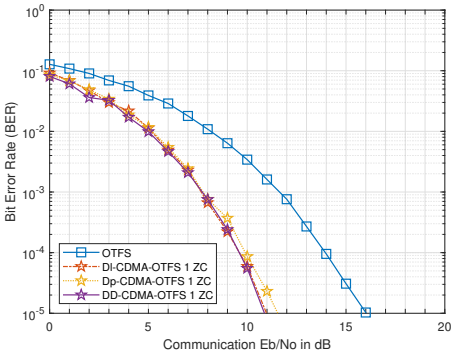

(F) OTFS and Zadoff-Chu sequence

FIGURE 4.4: BER of QPSK Gold, Hadamard, and Zadoff-Chu sequence spreading for $N_{mult} = 1$ for Dl-CDMA-OTFS, Dp-CDMA-OTFS, and DD-CDMA-OTFS, and of OTFS QPSK

OTFS QPSK is shown in Figure 4.6, for a throughput of 2 bpcu. At 2 bpcu, the performance of Gold sequences is poor, as their lack of orthogonality leads to increased inter-symbol interference. The BER of Zadoff-Chu sequences is almost identical to OTFS. The BER for 2 bpcu is higher than for a throughput of 1 bpcu, as the sequences experience a small amount of inter-symbol interference, despite their orthogonality. The performance of Hadamard sequences is similar to the half throughput case of 1 bpcu, as the sequences experience little inter-symbol interference due to their orthogonality to each other.

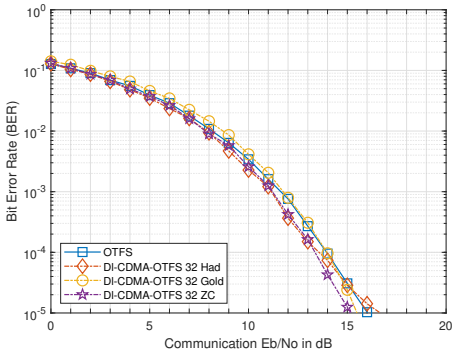

(A) OTFS and Dl-CDMA-OTFS

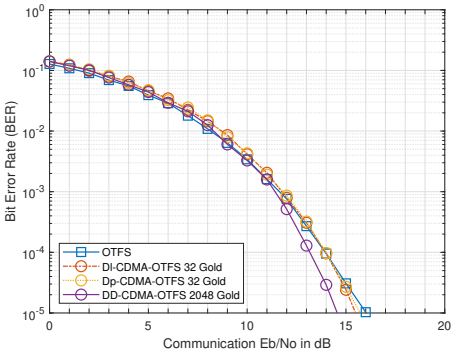

(B) OTFS and Gold sequence

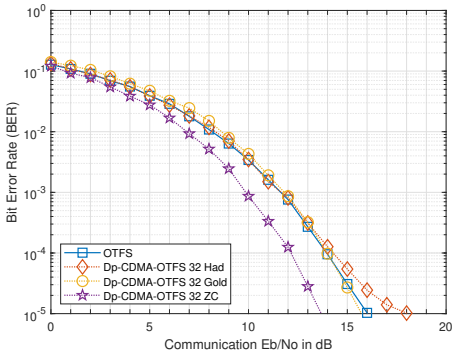

(C) OTFS and Dp-CDMA-OTFS

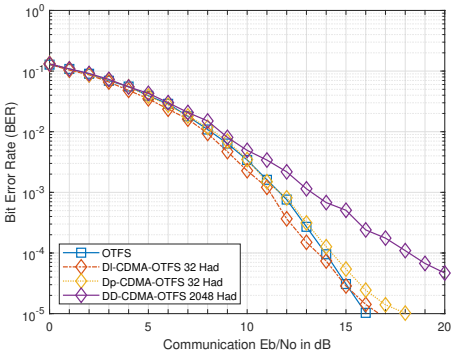

(D) OTFS and Hadamard sequence

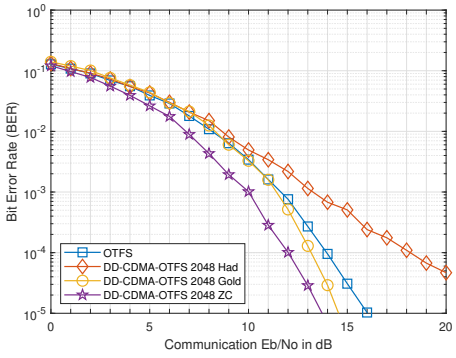

(E) OTFS and DD-CDMA-OTFS

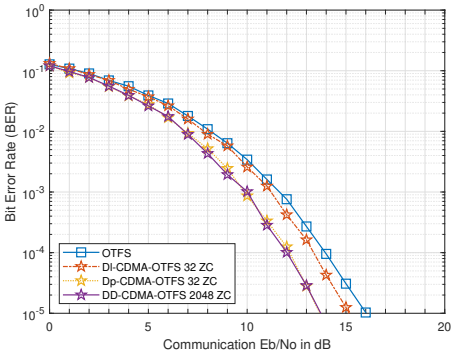

(F) OTFS and Zadoff-Chu sequence

FIGURE 4.5: BER of QPSK Gold, Hadamard, and Zadoff-Chu sequence spreading for $N_{mult} = 32$ for Dl-CDMA-OTFS and Dp-CDMA-OTFS, $N_{mult} = 2048$ for DD-CDMA-OTFS, and of OTFS QPSK

4.7.2 Sensing RMSE Results

The simulation parameters used are shown in Table 4.3. The range and velocity RMSE of QPSK OTFS are shown in Figure 4.7 for $N_{ML} = 1$, 4, and 8, $R_t = 500$ m, $V_t = 200$ m/s, and $P_n = 0$ NLoS paths. The RMSE is dominated by the integer index estimation at E_b/N_0 below -18 dB, but by the fractional index estimation at higher E_b/N_0. As N_{ML} is increased, the system resolution is increased, which leads to a potentially lower error floor, as seen in Figure 4.7a.

In Figure 4.7b, the closest fractional index to the target velocity is unchanged for $N_{ML} =$

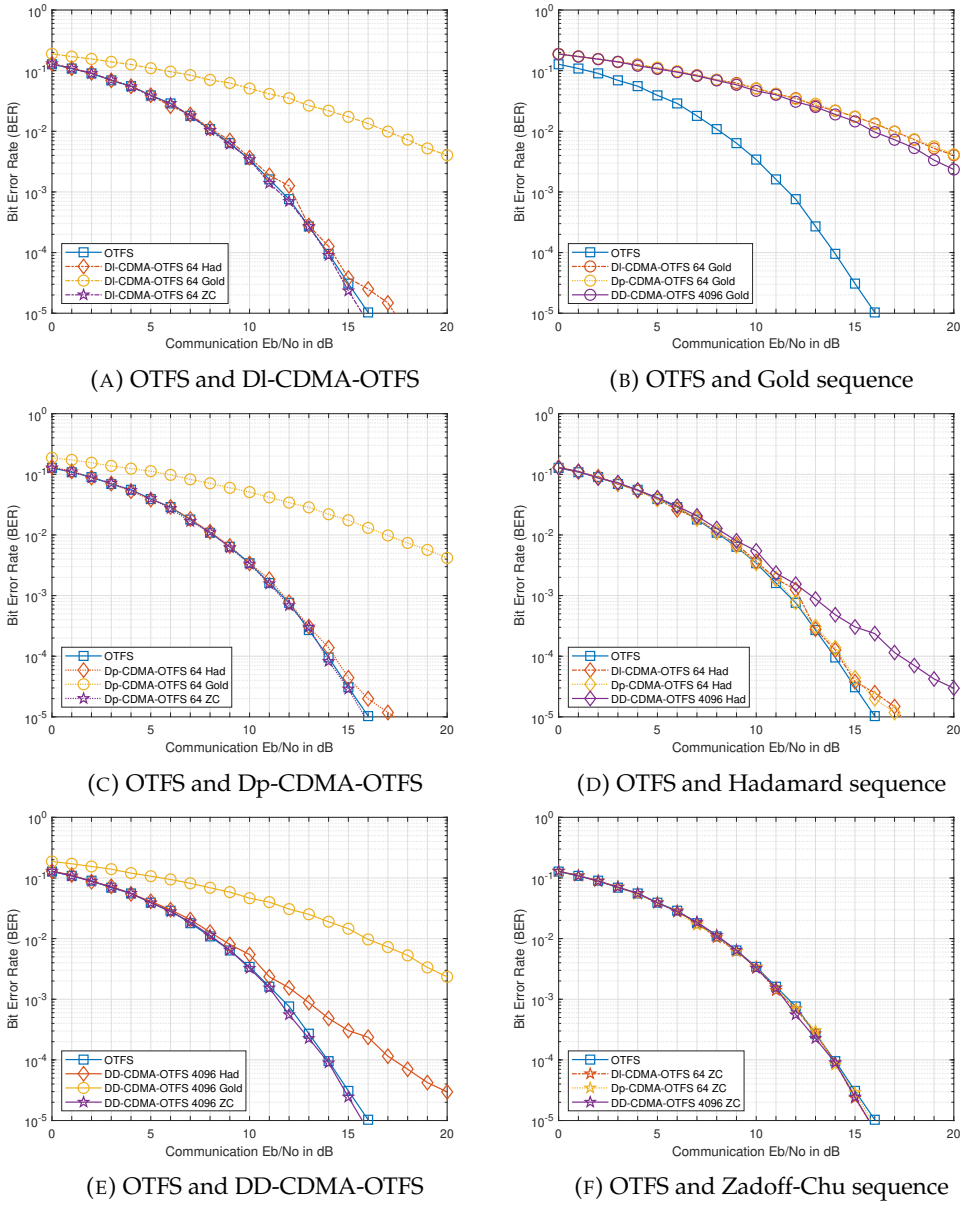

(A) OTFS and Dl-CDMA-OTFS

(B) OTFS and Gold sequence

(C) OTFS and Dp-CDMA-OTFS

(D) OTFS and Hadamard sequence

(E) OTFS and DD-CDMA-OTFS

(F) OTFS and Zadoff-Chu sequence

FIGURE 4.6: BER of QPSK Gold, Hadamard, and Zadoff-Chu sequence spreading for $N_{mult} = 64$ for Dl-CDMA-OTFS and Dp-CDMA-OTFS, $N_{mult} = 4096$ for DD-CDMA-OTFS, and of OTFS QPSK

TABLE 4.3: Sensing simulation parameters

Variable	Value
Carrier frequency f_c	40 GHz
Subcarrier spacing Δf	120 kHz
Number of sensing targets P_t	1
Rician K factor κ_{sen}	10 dB
Number of subcarriers M	64
Number of symbols sent per frame N	64
Number of frames simulated per E_b/N_0	4000

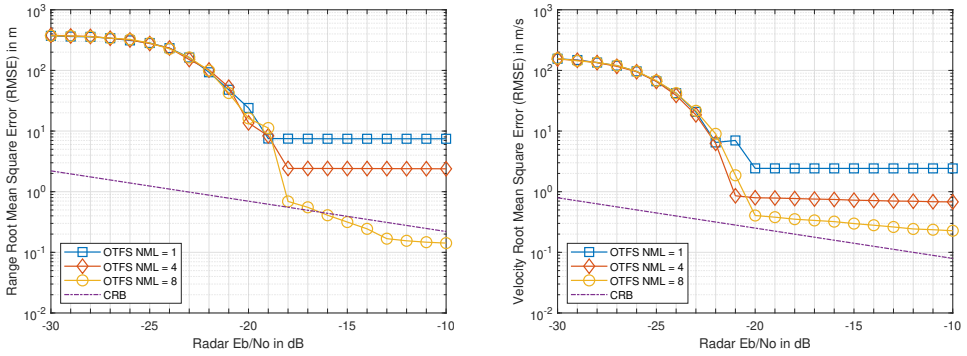

(A) Range RMSE (B) Velocity RMSE

FIGURE 4.7: Range and velocity RMSE of OTFS QPSK for $N_{ML} = 1$, 4, and 8, $R_t = 500$ m, $V_t = 200$ m/s, and $P_n = 0$ NLoS paths

4 and 8, hence the error floor is identical. As N_{ML} is increased, the fractional index detection algorithm becomes more sensitive to AWGN, which leads to the RMSE of the estimate reaching the error floor at higher E_b/N_0 than for $N_{ML} = 4$. All subsequent results use $N_{ML} = 8$.

In Figure 4.7b, the error floor is higher than the CRB, but in Figure 4.7a, the error floor is lower than the CRB for $N_{ML} = 8$. This is due to the discrete properties of the estimator. The target parameter estimator outputs a value from a discrete set, whereas the CRB assumes a continuous set. Hence, when the discrete estimator output is close to the target parameter value, the sensing error can be smaller than the CRB in the E_b/N_0 range considered. At higher E_b/N_0, the CRB will reduce further, below the error floor.

As similar trends are observed for range and velocity estimation, only the range RMSE results will be presented.

The range RMSE of QPSK Gold, Hadamard, and Zadoff-Chu sequence spreading are shown in Figure 4.8 for $N_{mult} = 64$ for Dl-CDMA-OTFS and Dp-CDMA-OTFS, $N_{mult} = 4096$ for DD-CDMA-OTFS, and of OTFS QPSK for $N_{ML} = 8$, $R_t = 500$ m, $V_t = 200$ m/s, and $P_n = 0$ NLoS paths.

For most of the CDMA-OTFS systems, the E_b/N_0 at which the RMSE is dominated by the fractional index estimation error is 1 dB lower than for OTFS, except for Hadamard Dl-CDMA-OTFS, Gold and Zadoff-Chu Dp-CDMA-OTFS, where it is 2dB lower than for OTFS. This is because the spreading codes distribute the signal over multiple indices, thereby creating a more uniform transmitted signal compared to OTFS. It has been shown [102] that more deterministic signals lead to a superior sensing performance.

The range RMSE of QPSK Gold, Hadamard, and Zadoff-Chu sequence spreading are shown in Figure 4.9 for $N_{mult} = 64$ for Dl-CDMA-OTFS and Dp-CDMA-OTFS, $N_{mult} =$

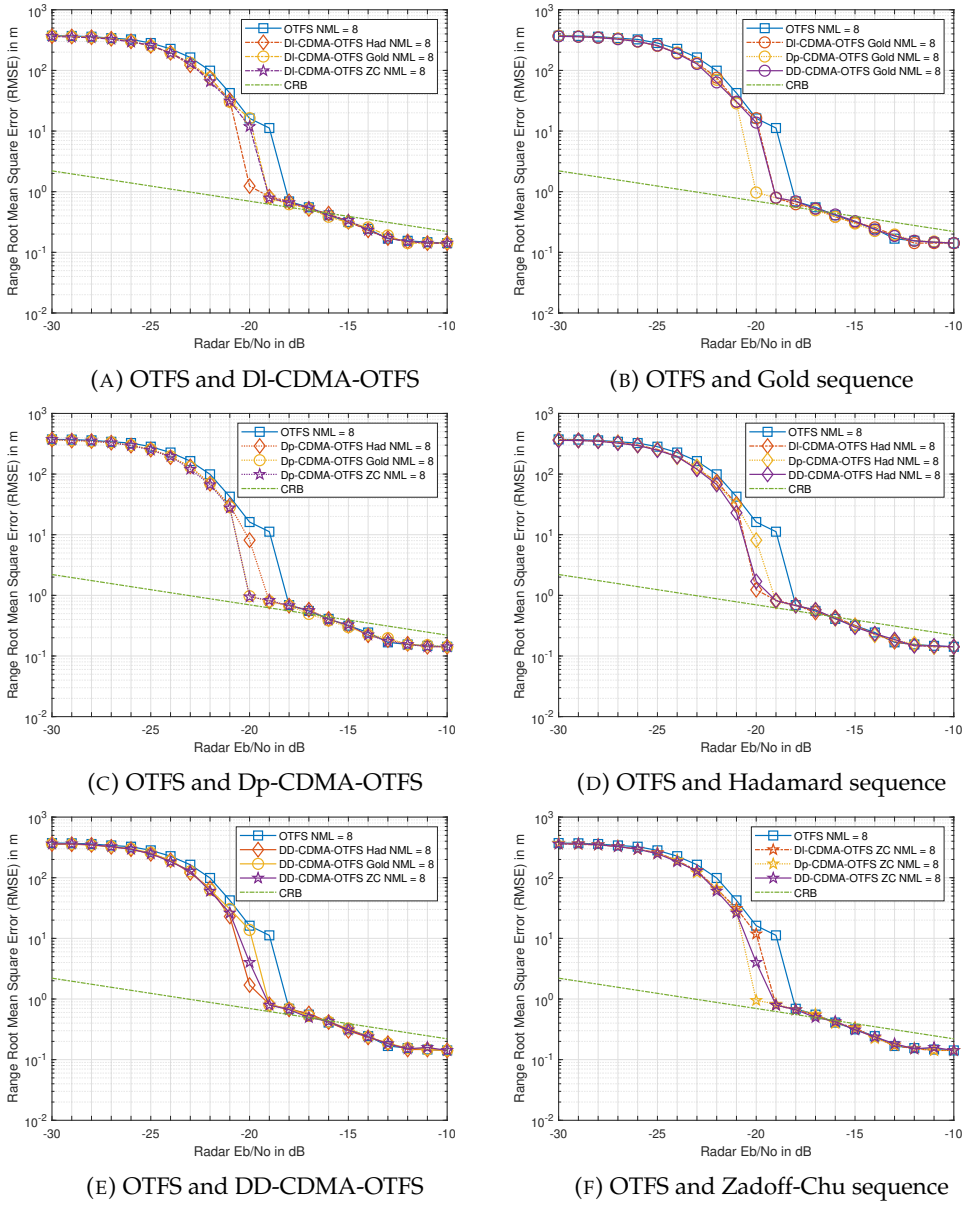

(A) OTFS and Dl-CDMA-OTFS

(B) OTFS and Gold sequence

(C) OTFS and Dp-CDMA-OTFS

(D) OTFS and Hadamard sequence

(E) OTFS and DD-CDMA-OTFS

(F) OTFS and Zadoff-Chu sequence

FIGURE 4.8: Range RMSE of QPSK Gold, Hadamard, and Zadoff-Chu sequence spreading for $N_{mult} = 64$ for Dl-CDMA-OTFS and Dp-CDMA-OTFS, $N_{mult} = 4096$ for DD-CDMA-OTFS, and of OTFS QPSK for $N_{ML} = 8$, $R_t = 500$ m, $V_t = 200$ m/s, and $P_n = 0$ NLoS paths

4096 for DD-CDMA-OTFS, and of OTFS QPSK for $N_{ML} = 8$, $R_t = 200$ m, $V_t = 110$ m/s, and $P_n = 7$ NLoS paths.

For most of the CDMA-OTFS systems, the E_b/N_0 at which the RMSE is dominated by the fractional index estimation error is 1 dB lower than for OTFS, except for Zadoff-Chu Dp-CDMA-OTFS and Gold DD-CDMA-OTFS, where it is at the same E_b/N_0 as OTFS. As the velocity is decreased, the sensing performance advantage of CDMA-OTFS is slightly decreased, as the distortion caused by the Doppler shifts of the propagation paths is reduced.

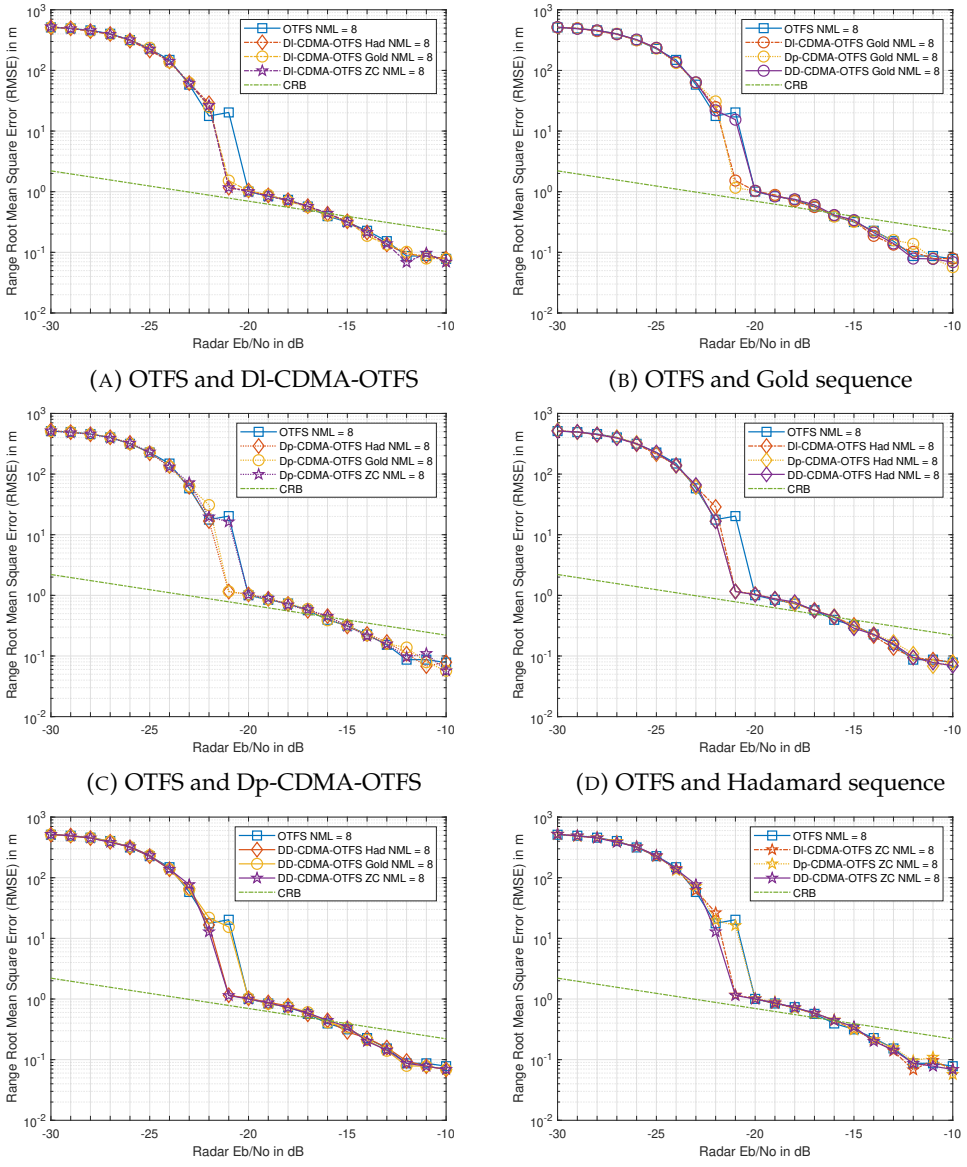

(A) OTFS and Dl-CDMA-OTFS

(B) OTFS and Gold sequence

(C) OTFS and Dp-CDMA-OTFS

(D) OTFS and Hadamard sequence

(E) OTFS and DD-CDMA-OTFS

(F) OTFS and Zadoff-Chu sequence

FIGURE 4.9: Range RMSE of QPSK Gold, Hadamard, and Zadoff-Chu sequence spreading for $N_{mult} = 64$ for Dl-CDMA-OTFS and Dp-CDMA-OTFS, $N_{mult} = 4096$ for DD-CDMA-OTFS, and of OTFS QPSK for $N_{ML} = 8$, $R_t = 200$ m, $V_t = 110$ m/s, and $P_n = 7$ NLoS paths

4.8 Correlation-based CDMA-OTFS Sensing

As the spreading sequences used also possess good autocorrelation properties, the use of a correlation-based sensing method was also investigated. The correlation operation is:

$$\widetilde{\boldsymbol{Y}}_{imag}[m_1, n_1] = \sum_{m=0}^{M-1} \sum_{n=0}^{N-1} \left(\widetilde{\boldsymbol{X}}[m, n]\right)^* \widetilde{\boldsymbol{Y}}[\lfloor m - m_1 \rfloor_M, \lfloor n - n_1 \rfloor_N] \,, \tag{4.54}$$

where $\widetilde{\boldsymbol{Y}}_{imag} \in \mathbb{C}^{M \times N}$ is the imaging matrix, $\widetilde{\boldsymbol{X}} \in \mathbb{C}^{M \times N}$ is the DD transmit signal matrix, $\widetilde{\boldsymbol{Y}} \in \mathbb{C}^{M \times N}$ is the DD received signal matrix, $m_1 = [0, 1, ..., M-1]$ and $n_1 = [0,$

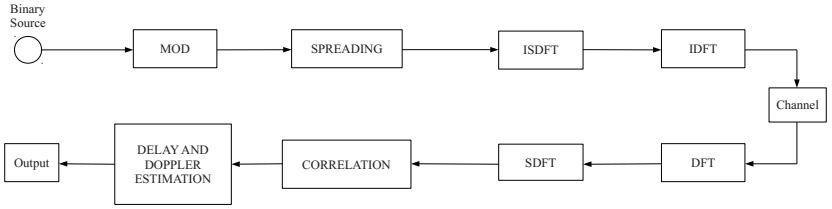

FIGURE 4.10: Block diagram of the CDMA-OTFS correlation-based sensing model

TABLE 4.4: Sensing simulation parameters for CDMA-OTFS

Variable	Value
Carrier frequency f_c	40 GHz
Subcarrier spacing Δf	120 kHz
Number of sensing targets P_t	1
Number of subcarriers M	64
Number of symbols sent per frame N	64
Number of frames simulated per E_b/N_0	4000
Target range R_t	500 m
Target velocity V_t	200 m/s
Number of NLoS paths P_n	0
Resolution refinement factor N_{ML}	8

$1, ..., N-1]$ are the lag/offset indices, $(\cdot)^*$ is the complex conjugate operation, and $\lfloor \cdot \rfloor_A$ is the modulo operator.

Due to the nature of the effective channel matrix, a circular shift is applied for each lag/offset. Hence, the modulo operator is present. A block diagram of this sensing system is shown in Figure 4.10.

The simulation parameters are shown in Table 4.4. The RMSEs of QPSK Gold, Hadamard, and Zadoff-Chu sequence spreading for $N_{mult} = 64$ for Dl-CDMA-OTFS and Dp-CDMA-OTFS, $N_{mult} = 4096$ for DD-CDMA-OTFS, and of OTFS QPSK are shown in Figures 4.11 and 4.12, for range and velocity respectively. It can be seen that the various CDMA-OTFS schemes do not outperform OTFS. Hence, these results were not included in the published work [2], and this sensing method was not pursued further.

4.9 Conclusions

Three different configurations of CDMA-OTFS were introduced. The multi-user communication performance of Zadoff-Chu CDMA-OTFS is similar to that of single user OTFS at an equal throughput. When fewer users are present, the multi-user throughput is diminished, and Zadoff-Chu CDMA-OTFS has a lower BER than single user OTFS. The communication performance of Zadoff-Chu sequences is similar for all three

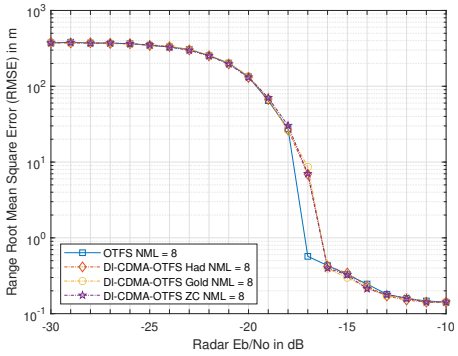

(A) OTFS and Dl-CDMA-OTFS

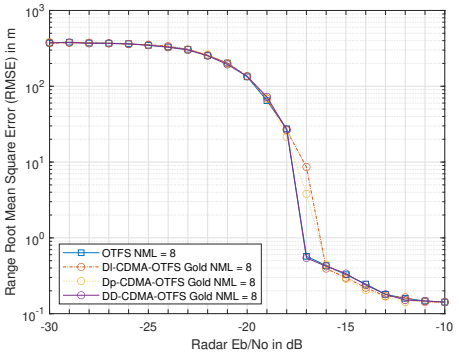

(B) OTFS and Gold sequence

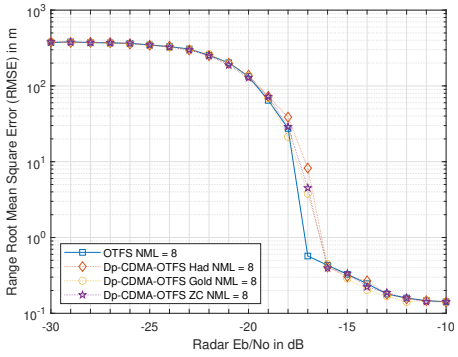

(C) OTFS and Dp-CDMA-OTFS

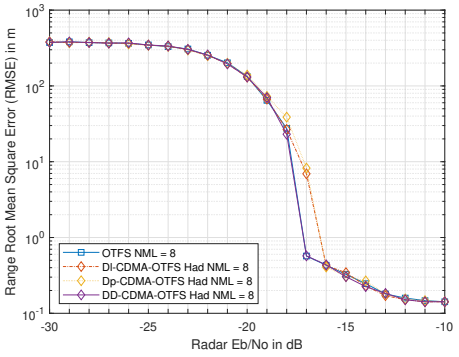

(D) OTFS and Hadamard sequence

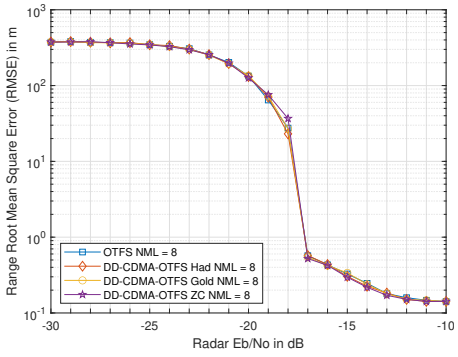

(E) OTFS and DD-CDMA-OTFS

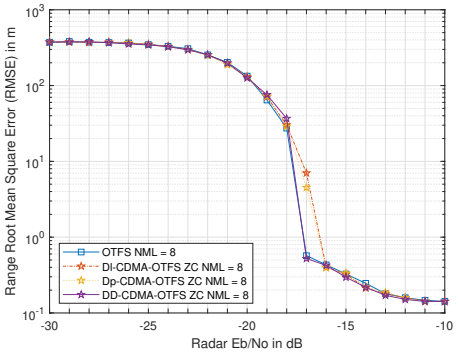

(F) OTFS and Zadoff-Chu sequence

FIGURE 4.11: Range RMSE of QPSK Gold, Hadamard, and Zadoff-Chu sequence spreading for $N_{mult} = 64$ for Dl-CDMA-OTFS and Dp-CDMA-OTFS, $N_{mult} = 4096$ for DD-CDMA-OTFS, and of OTFS QPSK

TABLE 4.5: E_b/N_0 at which a BER of 10^{-4} is reached for CDMA-OTFS at half load relative to OTFS

Configuration \ Sequence	Gold	Hadamard	Zadoff-Chu
Dl-CDMA-OTFS	0 dB	0 dB	−0.5 dB
Dp-CDMA-OTFS	0 dB	0 dB	−2 dB
DD-CDMA-OTFS	−1 dB	+4 dB	−2 dB

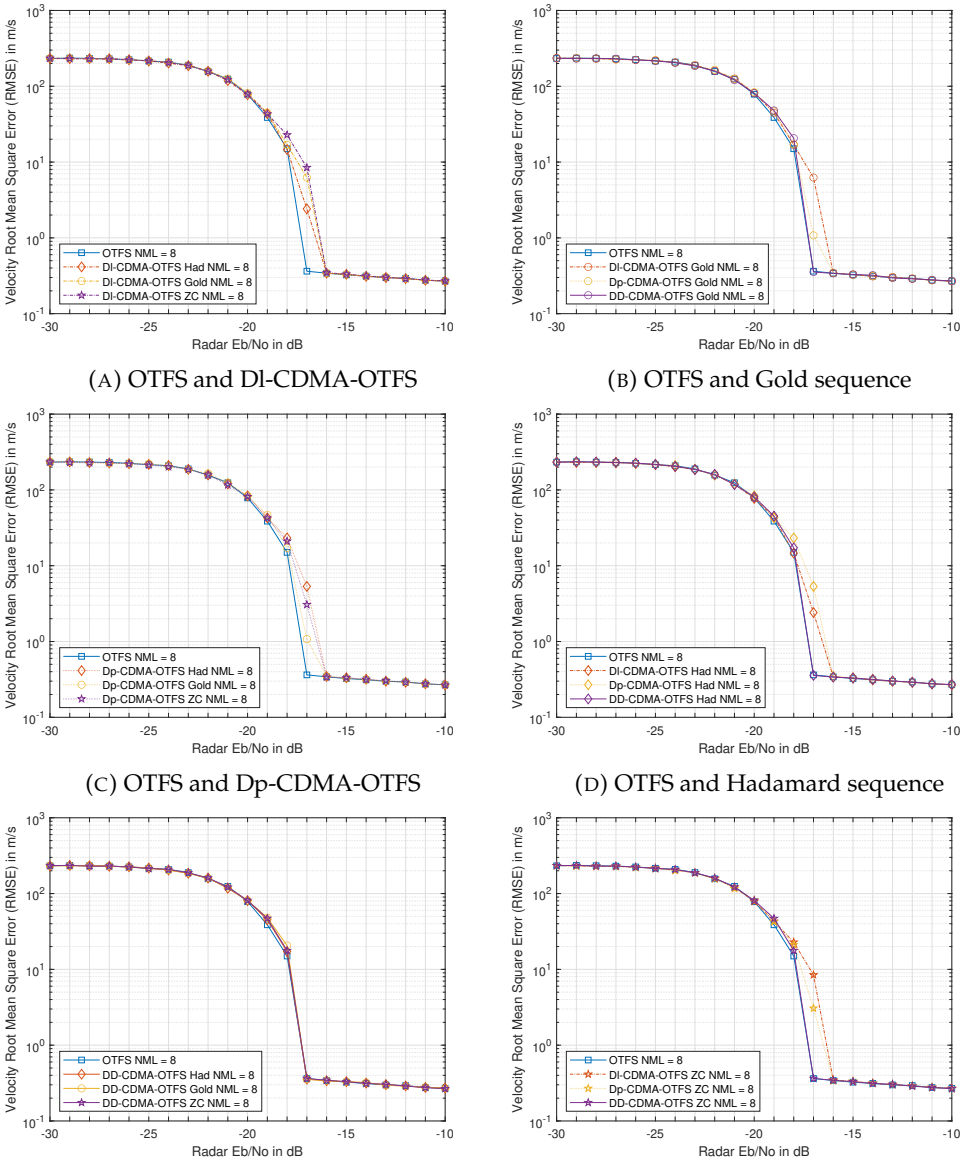

(A) OTFS and Dl-CDMA-OTFS

(B) OTFS and Gold sequence

(C) OTFS and Dp-CDMA-OTFS

(D) OTFS and Hadamard sequence

(E) OTFS and DD-CDMA-OTFS

(F) OTFS and Zadoff-Chu sequence

FIGURE 4.12: Velocity RMSE of QPSK Gold, Hadamard, and Zadoff-Chu sequence spreading for $N_{mult} = 64$ for Dl-CDMA-OTFS and Dp-CDMA-OTFS, $N_{mult} = 4096$ for DD-CDMA-OTFS, and of OTFS QPSK

TABLE 4.6: E_b/N_0 at which a BER of 10^{-4} is reached for CDMA-OTFS at full load relative to OTFS

Configuration \ Sequence	Gold	Hadamard	Zadoff-Chu
Dl-CDMA-OTFS	N/A	0 dB	0 dB
Dp-CDMA-OTFS	N/A	0 dB	0 dB
DD-CDMA-OTFS	N/A	+3 dB	0 dB

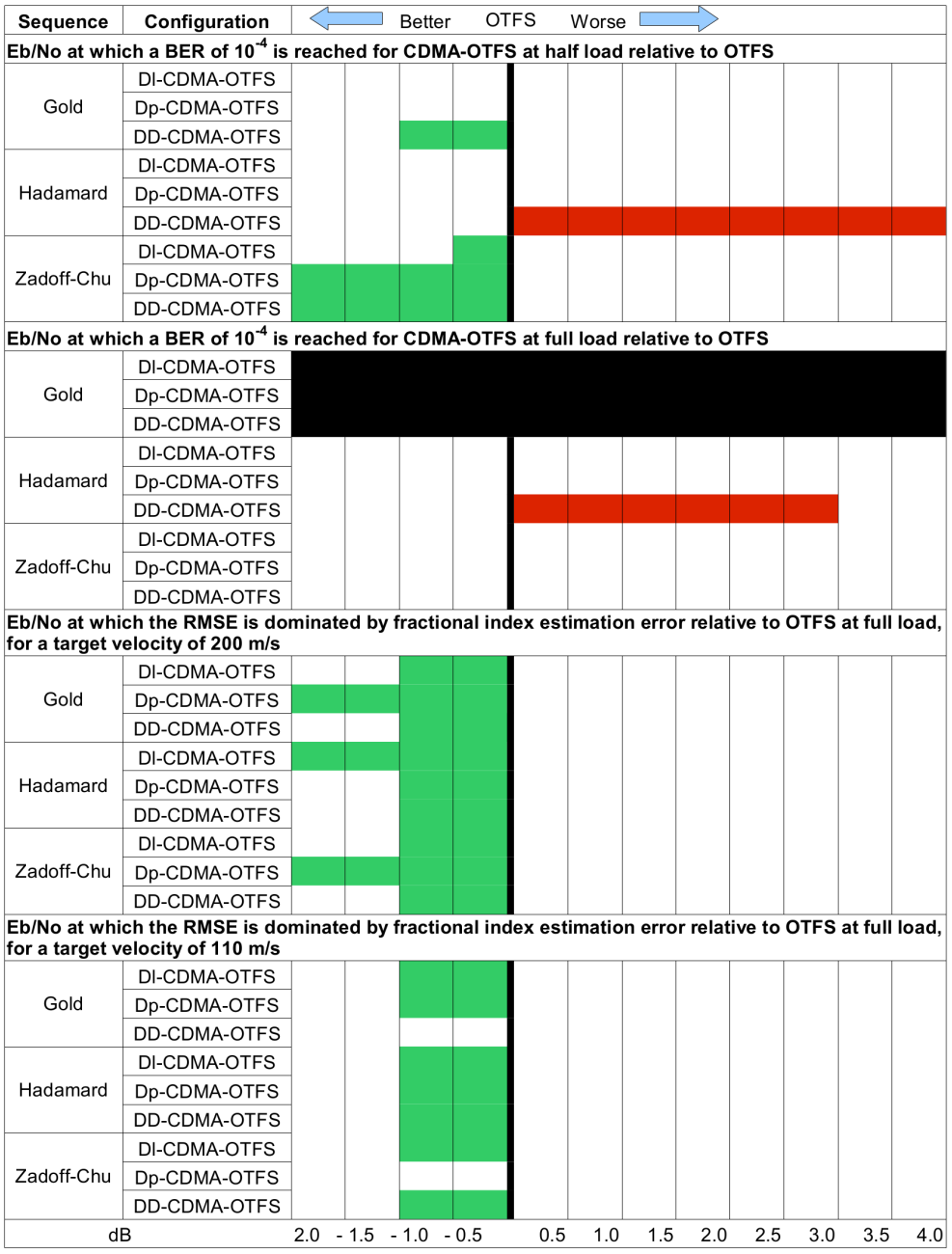

FIGURE 4.13: Comparison of relative performance of different configurations and sequences relative to OTFS for communication and sensing

TABLE 4.7: E_b/N_0 at which the RMSE is dominated by fractional index estimation error relative to OTFS at full load, for a target velocity of 200 m/s

Configuration \ Sequence	Gold	Hadamard	Zadoff-Chu
Dl-CDMA-OTFS	−1 dB	−2 dB	−1 dB
Dp-CDMA-OTFS	−2 dB	−1 dB	−2 dB
DD-CDMA-OTFS	−1 dB	−1 dB	−1 dB

TABLE 4.8: E_b/N_0 at which the RMSE is dominated by fractional index estimation error relative to OTFS at full load, for a target velocity of 110 m/s

Configuration \ Sequence	Gold	Hadamard	Zadoff-Chu
Dl-CDMA-OTFS	−1 dB	−1 dB	−1 dB
Dp-CDMA-OTFS	−1 dB	−1 dB	0 dB
DD-CDMA-OTFS	0 dB	−1 dB	−1 dB

CDMA-OTFS spreading configurations. Gold and Hadamard sequences do not consistently outperform single user OTFS communication. The communication performance of the different configurations relative to OTFS at the normalised half and full load are summarised in Tables 4.5 and 4.6, respectively, and illustrated in Figure 4.13.

The three CDMA-OTFS spreading configurations outperform pure OTFS sensing for all the velocities considered. Hadamard sequences lead to a superior sensing performance for Dl-CDMA-OTFS at high velocities, but the three sequences have a similar performance at lower velocities. Gold sequences increase the sensing performance of Dp-CDMA-OTFS at high velocities, whereas Zadoff-Chu sequences lead to the similar sensing performance as pure OTFS at lower velocities. The sensing performance of DD-CDMA-OTFS is similar for all three sequence types at high velocities, but Gold sequences lead to an inferior sensing performance at low velocities. The sensing performance of the different configurations relative to OTFS at full load are summarised in Tables 4.7 and 4.8, for target velocities of 200 m/s and 110 m/s respectively, and also illustrated in Figure 4.13.

Following these results, Zadoff-Chu Dl-CDMA-OTFS and DD-CDMA-OTFS are the configurations that consistently outperform pure OTFS sensing, whilst maintaining a similar communication performance at the same throughput.

The added modulation complexity of CDMA-OTFS is similar to other OTFS multi-user methodologies, but the demodulation complexity of CDMA-OTFS is lower than that of some other OTFS multi-user methodologies. CDMA-OTFS sensing can also consistently outperform OTFS sensing whilst not requiring any additional complexity for target parameter estimation. Hence, CDMA-OTFS is a computationally more attractive multi-user approach for OTFS ISAC than the alternatives in the literature.

A correlation-based method for CDMA-OTFS sensing was utilised. In contrast to the data cancellation method, the correlation-based method leads to CDMA-OTFS sensing having an inferior performance compared to OTFS sensing. Having identified this shortcoming, further work on correlation-based CDMA-OTFS has been deferred to permit the prioritising of more promising schemes.

Although OTFS is more resilient to Doppler shifts than OFDM, its implementation would require modifications to the existing systems, due to the presence of the Symplectic Discrete Fourier Transform (SDFT), as shown in Figures 4.1 and 4.2. The SDFT based OTFS may be viewed as an OFDM precoding scheme. Ideally, a waveform imposing a lower implementation complexity, while retaining the advantages of OTFS, would be preferred for ISAC.

Chapter 5

Coded Soft-MMSE AFDM ISAC

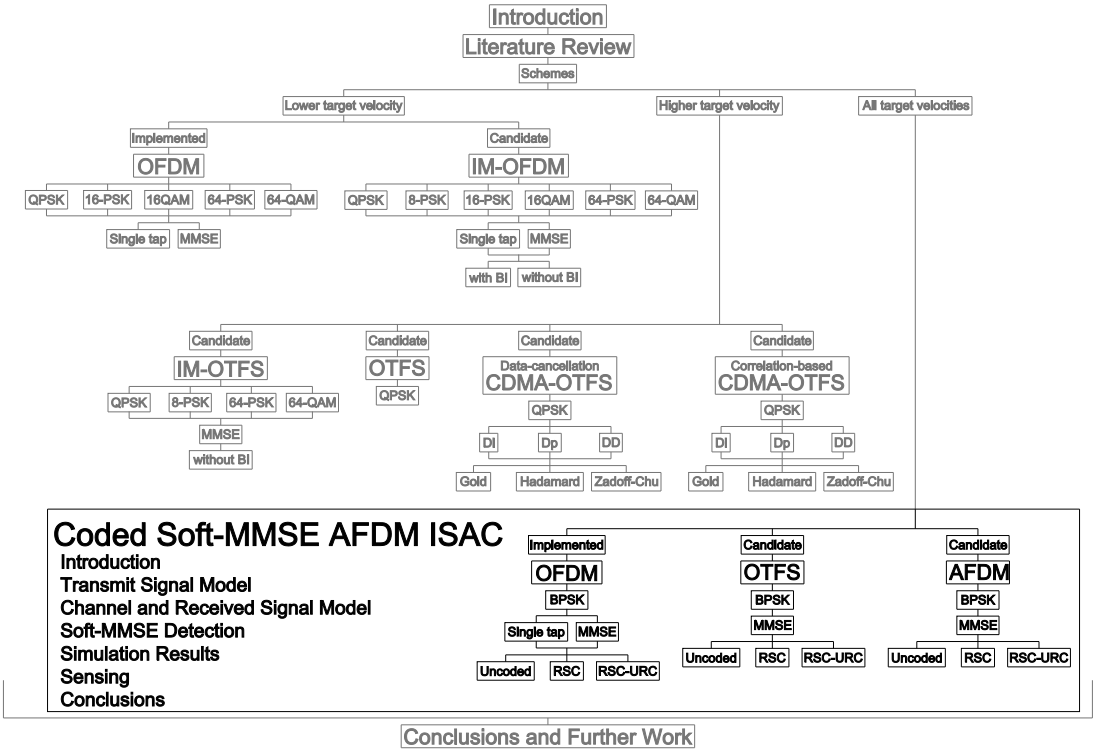

5.1 Introduction

This chapter describes the third part of the research undertaken, on iterative soft-MMSE and channel decoding aided AFDM, which has been published [3], with the exception of Section 5.6. AFDM is a generalised form of OFDM, which can be tuned to exhibit similar characteristics to OTFS. These similarities to OTFS allow AFDM to mitigate the effects of large Doppler shifts, and to separate propagation paths by their associated

delays and Doppler shifts, whilst reducing the implementation costs, due to AFDM's similarity to OFDM. Hence, AFDM is an attractive alternative to OTFS, especially for ISAC. As AFDM is a novel waveform, there is a paucity of publications considering iterative equalisation and decoding methods. This turbo architecture allows for improved communication performance, and may be leveraged to improve the sensing capabilities of the system. Hence, a study of such an architecture for AFDM is performed, with comparisons to OFDM and multiple OTFS configurations. Multiple OTFS configurations are investigated as OTFS is a two dimensional waveform, whereas AFDM is a single dimension waveform, which leads to there being no consensus on the best OTFS and AFDM configurations to implement for a fair comparison.

5.1.1 Literature Review

AFDM is a novel chirp-based waveform [149], and it may be deemed reminiscent of OFDM, where the DFT is replaced by the DAFT. The DAFT is a generalised transform, with the DFT being a specific form of the DAFT. It is characterised by two chirp parameters, namely chirp parameter 1 (c_1) and chirp parameter 2 (c_2), which can be flexibly tuned for optimising the diversity and correlation properties of the signal. Other forms of OFDM utilising the DAFT [150] or chirps [151, 152] have been proposed, but these still lead to propagation paths being separable only by delay, not Doppler shift. By contrast, the DAFT utilised in AFDM is specifically configured to ensure that the propagation paths are separable by both delay and Doppler shift, similar to OTFS schemes [141, 142]. This allows AFDM to achieve full diversity, like OTFS. The communication performance of AFDM has also been shown to be similar to that of OTFS [149]. However, the maximum Doppler shift must be known at the transmitter to configure the DAFT. AFDM also requires a prefix to be added, the CPP, similarly to the OFDM CP. The CPP reduces to a CP if the value of c_1 for the DAFT meets certain conditions. The correct configuration of the DAFT allows the AFD channel matrix to be sparse, similar to the OTFS DD channel matrix, but with a different structure.

The similarities between OFDM and AFDM have led to research in many areas of communication [207], such as satellite communication [208], secure transmission [209, 210], and DFT-based AFDM [211]. The DFT-based AFDM may be viewed as a precoded OFDM scheme, to align its implementation more closely to that of OFDM [211].

A literature review of AFDM ISAC is presented in Section 2.5.3 of Chapter 2, and hence is not repeated here. Below is a literature review on work not covered in Chapter 2.

5.1.1.1 Spectral Efficiency

AFDM has been shown to possess a higher spectral efficiency than OTFS when conventional pilot symbol-based channel estimation is employed [155, 156, 212]. This is due to the lower number of guard symbols required by AFDM compared to OTFS, as AFDM is a single-domain waveform, whereas OTFS requires guard symbols along both the delay and Doppler domains. However, this spectral efficiency improvement is not seen when other pilot methods are harnessed [161, 213]. For example, when superimposed pilot symbols are considered, this spectral efficiency improvement is no longer observed [161], but superimposed symbols require more complex detection methods for mitigating the interference between pilot and data symbols.

5.1.1.2 Peak to Average Power Ratio

As a drawback, AFDM suffers from high PAPR, as its structure is similar to OFDM, but it can be reduced by adjusting c_2 of the DAFT [214]. This creates a DAFT with multiple groups of c_2 values within the transform. The authors show that increasing the number of chirp parameter groups decreases the PAPR. This variability in the transmit DAFT leads to a higher BER, when the receiver does not know which c_2 values have been employed. Reddy *et al.* [215] propose to reduce the PAPR by applying μ-law companding and decompanding in the TD, prior to transmission and after reception respectively. This μ-law companding reduces the PAPR of AFDM to a greater extent than the method in [214], with no substantial impact on the BER for moderate companding.

5.1.1.3 Index Modulation

As for OTFS and OFDM, there has also been keen interest in the combination of AFDM and IM [216–220]. Standard IM applied to AFDM has been shown to slightly reduce the BER of AFDM [216] for both coded and uncoded transmission. This combination has been extended to a multi-antenna scenario in [217], where the transmission from each antenna is shifted by a fixed delay. The addition of IM is shown to reduce the BER of AFDM in this scenario, albeit at the expense of additional complexity. As expected, the BER of the cyclic transmission method decreases as the number of transmit antennas is increased.

Applying IM to the DAFT parameters has also been proposed [218]. The values of c_2 within groups are varied based on the input bits, in a similar manner to standard IM. This method is shown to result in a lower BER than standard AFDM-IM for ML detection. Another innovative IM scheme relies on Walsh-Hadamard sequence based spreading [219]. This is applied on a per-group basis of chirp subcarriers, and it is

shown to lead to a lower BER than both AFDM and standard AFDM-IM for a given throughput at sufficiently high SNRs.

5.1.1.4 Sparse Code Multiple Access

The employment of spreading sequences has also been investigated in multi-user communication. Multi-user SCMA aided AFDM is proposed in [221], for both uplink and downlink communications. The authors develop a SCMA codebook design to simplify the input-output relationship in the AFD, thereby allowing for a simpler receiver. The detector proposed for coded transmission iterates between a linear MMSE receiver and a Low-Density Parity-Check (LDPC) decoder, whose performance is enhanced by the addition of orthogonal approximate message passing. The uncoded and coded AFDM-SCMA schemes are shown to consistently outperform the equivalent OFDM schemes in both uplink and downlink transmission. The equivalent OTFS schemes are shown to have a similar performance to their AFDM counterparts.

5.1.1.5 Iterative Equalisation and Channel Coding

Due to the relative novelty of AFDM, there is a paucity of publications investigating the benefits of iterative equalisation and channel coding on the performance of AFDM. Nonetheless, a low complexity iterative linear-MMSE-based equalisation method is proposed for AFDM in [222]. The authors first determine the optimum DAFT chirp parameter values to minimise the BER when MMSE equalisation is employed. An iterative TD MMSE method is developed to reduce the complexity of soft linear-MMSE detection. The authors show that the proposed chirp parameter selection method allows the system to reach the BER lower bound. This advantage becomes more apparent when the propagation channel is doubly selective. The proposed iterative TD MMSE method is shown to have a slightly higher BER than iterative linear-MMSE. The performances of AFDM and OTFS are similar to each other for both equalisation methods. Soft-MMSE has also been utilised to improve the BER performance of AFDM in wideband channels [223].

Channel coding has also been investigated in [216, 224]. Xu *et al.* [224] develop a multi-block unitary transform-based approximate message passing algorithm for AFDM under fractional delay and Doppler indices. Fractional delay indices are scarcely covered in the AFDM literature. This algorithm is conceived to mitigate the energy dispersion effects of the fractional channel indices on the received signal. The proposed algorithm is shown to exhibit a higher iterative gain, illustrated by "empirical" EXIT chart analysis, and a lower BER than the Gaussian approximate message passing benchmark. This

algorithm also allows AFDM to exhibit a lower BER than OTFS, since AFDM only experiences interference in a single dimension, as opposed to two dimensions for OTFS. Channel coding was not the focus of the contributions of [216] and [224].

The only currently published work that considers the combination of iterative equalisation and channel coding for AFDM communication is [221]. The soft-MMSE method implemented is specifically designed for SCMA, and hence is not generally applicable to AFDM systems.

5.1.2 Motivation and Contributions

TABLE 5.1: Comparison of contributions from the literature

Papers / Topics	[156]	[216]	[217]	[221]	[158]	[222]	[224]	This work
System overview								
Doubly selective channel	✓	✓	✓	✓	✓	✓	✓	✓
Channel coding		✓		✓			✓	✓
Comparison between AFDM, OTFS and OFDM	✓			✓	✓	✓	✓	✓
Receive signal processing								
Iterative detection			✓	✓	✓	✓	✓	✓
Soft-MMSE				✓		✓		✓
URC code assisted decoding								✓
Iterative soft-MMSE and RSC decoding								✓
Performance analysis								
EXIT chart and trajectory analysis							✓	✓
Scalable numerology for AFDM and OTFS configurations		✓	✓					✓
Respective application domains of AFDM and OTFS configurations are identified								✓

As discussed above, AFDM has attracted substantial interest due to its similarity in implementation to OFDM, whilst allowing for comparable performance to OTFS. Although some publications consider coded AFDM and soft-MMSE, there is no in-depth comparison of coded AFDM to its equivalent OTFS counterpart. Hence, the current work addresses this knowledge gap. Table 5.1 boldly contrasts the novelties of the proposed system to the existing literature. The specific contributions of this work are detailed below:

TABLE 5.2: OFDM, OTFS and AFDM configurations

	OFDM	AFDM 1	OTFS 1	AFDM 2	OTFS 2	OTFS 3
Dimension	M	$\ddot{N}_1 = MN$	MN	M	$M_2N_2 = M$	MN
Subcarrier spacing	Δf	$\Delta f_1 = \frac{\Delta f}{N}$	Δf	Δf	$\Delta f_2 = N_2\Delta f$	Δf_1
Bandwidth	$M\Delta f$	$\ddot{N}_1\Delta f_1 = M\Delta f$	$M\Delta f$	$M\Delta f$	$M_2\Delta f_2 = M\Delta f$	$M\Delta f_1 = \frac{M\Delta f}{N}$
Duration	T	$\frac{1}{\Delta f_1} = NT$	NT	T	$\frac{N_2}{\Delta f_2} = T$	$\frac{N}{\Delta f_1} = N^2T$
Delay resolution	$\frac{1}{M\Delta f}$	$\frac{1}{M\Delta f}$	$\frac{1}{M\Delta f}$	$\frac{1}{M\Delta f}$	$\frac{1}{M\Delta f}$	$\frac{N}{M\Delta f}$
Doppler resolution	$\frac{\Delta f}{N}$	$\frac{\Delta f}{N}$	$\frac{\Delta f}{N}$	Δf	Δf	$\frac{\Delta f}{N^2}$
Throughput	B_S	B_S	B_S	B_S	B_S	$\frac{B_S}{N}$
Complexity per block	M	MN	MN	M	M	MN
References	[124, 208, 215, 216, 218]	[149, 155–157, 161, 210, 212, 217, 222–225]	[149, 155–157, 161, 207, 211, 212, 222, 223, 225]	[124, 207, 208, 211, 215, 216, 218]	[217]	[210, 221, 224]

- Firstly, a parametric study of the communication performance of OFDM, AFDM and OTFS in doubly selective fading is performed for both coded and uncoded transmission. Multiple OTFS and AFDM configurations, defined in Table 5.2, are investigated, since the existing publications tend to compare AFDM to OTFS with different subcarrier spacings and/or bandwidths [156, 210, 217]. M is the number of OFDM subcarriers, N is the number of symbol slots, $\ddot{N}$ is the number of AFDM chirp subcarriers, Δf is the subcarrier spacing, T is the symbol period, and B_S is the number of bits per symbol. OTFS 1 is the original OTFS configuration of [141, 142] whose subcarrier spacing and number of subcarriers are identical to OFDM. The AFDM 1 scheme of [149, 155, 156] is equivalent to OTFS 1, where both schemes share the same matrix dimension. Furthermore, OTFS 2 [217] and AFDM 2 [157, 161, 222] have the same matrix dimension as a single OFDM symbol. These five configurations utilise the same bandwidth. The last configuration, OTFS 3 [210, 221, 224], has the same matrix dimension as OTFS 1, but its subcarrier spacing is identical to that of AFDM 1.

- Secondly, a soft-MMSE equalisation method that is applicable to OFDM, AFDM and OTFS in an iterative turbo receiver architecture is proposed, that exchanges extrinsic information between the demapper and the channel decoder. Soft-MMSE refers to the holistic MMSE solution that updates its MMSE weighting matrix based on both the channel condition and the *a priori* probabilities gleaned from the channel decoder. EXIT chart analysis is performed to investigate the performance of RSC-coded OFDM, AFDM and OTFS. Moreover, URC coding is harnessed in order to improve the decoding convergence.

- It is demonstrated that for low-complexity transceivers having high coding rates, AFDM configurations exhibit a lower BER than their OTFS counterparts. Hence AFDM is better suited to low-complexity systems than OTFS at significant velocities.

5.2 Transmit Signal Model

The data bit vector $\boldsymbol{b}_D \in \mathbb{C}^{R_c B_S \ddot{N} \Xi \times 1}$ is encoded to produce the transmit bit vector $\boldsymbol{b} \in \mathbb{C}^{B_S \ddot{N} \Xi \times 1}$, where R_c is the channel coding rate, $B_S = log_2(\Gamma)$ is the number of bits per symbol, Γ is the modulation order, $\ddot{N}$ is the number of AFDM chirp subcarriers, and Ξ is the number of transmission blocks within a frame. A transmission block refers to a set of $\ddot{N}$ symbols (or equivalent for other waveforms) sent by the transmitter, and the channel parameters are assumed to be constant for the Ξ transmission blocks within a frame.

The transmit bits $\boldsymbol{b}$ are then interleaved using a random interleaver, where the interleave pattern is generated by a random number generator following a normal distribution, in order to generate $\overset{\infty}{\boldsymbol{b}}$. When URC coding is employed in conjunction with another coding method, a second interleaving operation is performed after URC encoding using a second random interleaver. The block diagrams of RSC-AFDM and RSC-URC-AFDM are shown in Figures 5.1 and 5.2, respectively.

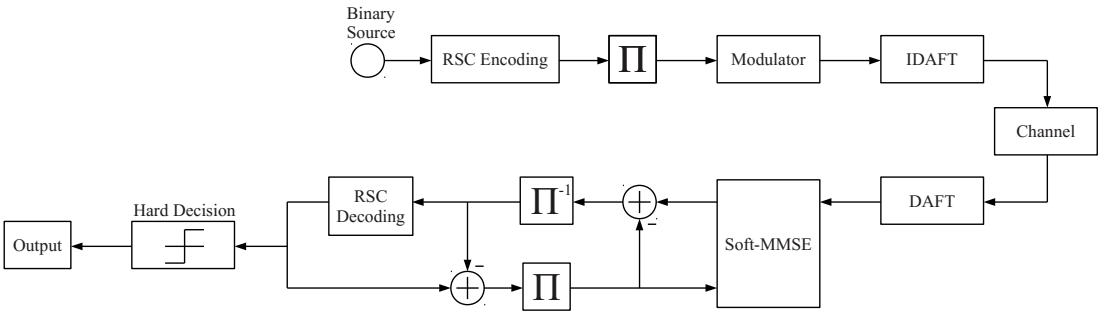

FIGURE 5.1: Block diagram of RSC-AFDM

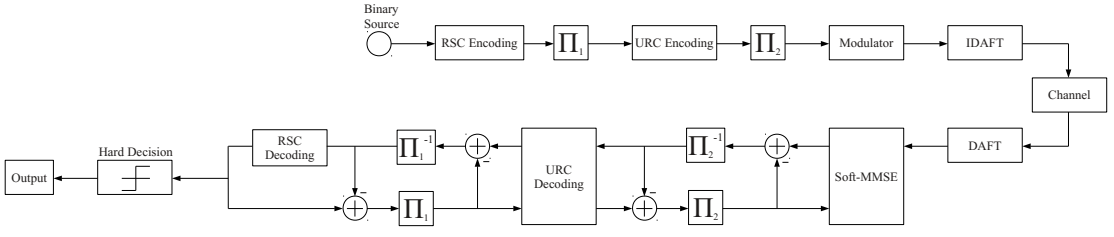

FIGURE 5.2: Block diagram of RSC-URC-AFDM

The interleaved bits $\overset{\infty}{\boldsymbol{b}}$ are modulated using PSK or QAM to form the AFD transmit signal $\ddot{\boldsymbol{x}} \in \mathbb{C}^{\ddot{N}\Xi \times 1}$. $\ddot{\boldsymbol{x}}$ is then converted to the TD:

$$\boldsymbol{x}_{\xi} = \boldsymbol{A}_{\ddot{N}}^{H} \ddot{\boldsymbol{x}}_{\xi} \,, \tag{5.1}$$

where $\boldsymbol{x}_{\xi} \in \mathbb{C}^{\ddot{N} \times 1}$ is the TD transmit signal for the ξ^{th} transmit block, $\xi = [0, 1, ..., \Xi - 1]$ is the block index, and $\boldsymbol{A}_{\ddot{N}}$ is the $\ddot{N} \times \ddot{N}$ DAFT, defined as:

$$\boldsymbol{A}_{\ddot{N}} = \boldsymbol{\Lambda}_{c_2} \boldsymbol{F}_{\ddot{N}} \boldsymbol{\Lambda}_{c_1} \,, \tag{5.2}$$

where $\boldsymbol{F}_{\ddot{N}}$ is the $\ddot{N} \times \ddot{N}$ DFT, c_1 and c_2 are the chirp parameters 1 and 2, and:

$$\boldsymbol{\Lambda}_{c} = \text{diag}(e^{-j2\pi c(\ddot{n})^2}) \,, \tag{5.3}$$

where $\ddot{n} = [0, 1, ..., \ddot{N} - 1]$ is the AFDM chirp subcarrier index, and $\text{diag}(\boldsymbol{v})$ generates a square diagonal matrix whose diagonal elements are the elements of $\boldsymbol{v}$.

Following the conditions outlined in [156], c_1 is set to:

$$c_1 = \frac{2(\ddot{k}_{max} + k_{\nu}) + 1}{2\ddot{N}} \,, \tag{5.4}$$

where $\ddot{k}_{max}$ is the maximum AFDM Doppler index, defined in (5.18) further below, and k_{ν} is the AFDM guard for fractional indices.

Furthermore, c_2 is set to a small arbitrary irrational number:

$$c_2 = \frac{1}{9^{2\pi}} \,. \tag{5.5}$$

Detailed information on the basic concepts of the DAFT and of AFDM can be found in [156].

5.3 Channel and Received Signal Model

It is assumed that there is no external interference during transmission, that the CPP for AFDM and the CP for OTFS and OFDM are perfectly removed, and that their lengths are in excess of the maximum channel delay-spread.

The transmitted signal is passed through a typical time-varying and frequency-selective fading channel used in the OTFS literature, as modelled in [179]. The TD representation of this channel for OTFS is:

$$h_{m,\,n,\,p,\,\xi} = \widetilde{h}_p e^{j2\pi \widetilde{k}_p \frac{\xi MN + nM + m - \widetilde{l}_p}{MN}} \,, \tag{5.6}$$

where $j = \sqrt{-1}$, $p = [0, 1, ..., P-1]$ is the propagation path index, P is the total number of propagation paths, $m = [0, 1, ..., M-1]$ denotes the OTFS subcarrier index, M is the number of OTFS subcarriers, $n = [0, 1, ..., N-1]$ is the OTFS symbol slot index, N is the number of OTFS symbol slots, $\widetilde{h}_p$ is the fading gain and path loss, while $\widetilde{l}_p$ and $\widetilde{k}_p$ are the OTFS delay and Doppler indices associated with the p^{th} propagation path respectively, defined as:

$$\widetilde{l}_p = (\Delta f M)\, \tau_p \,, \tag{5.7}$$

$$\widetilde{k}_p = \frac{N}{\Delta f} \nu_p \,, \tag{5.8}$$

where Δf is the OTFS subcarrier spacing, τ_p is the delay associated with the p^{th} path, and ν_p is the Doppler shift associated with the p^{th} path.

This representation assumes integer delay indices, as the delay resolution is assumed to be sufficiently large. The propagation path variables are assumed to be constant over the Ξ transmission blocks. The equivalent AFDM channel is attained upon substituting MN with $\ddot{N}$ and Δf with $\ddot{\Delta} f$. Hence, the TD representation of the channel for AFDM is:

$$h_{\ddot{n},\, p,\, \xi} = \widetilde{h}_p e^{j2\pi \ddot{k}_p \frac{\xi \ddot{N} + \ddot{n} - \ddot{l}_p}{\ddot{N}}} \,, \tag{5.9}$$

where $\ddot{l}_p$ and $\ddot{k}_p$ are the AFDM delay and Doppler indices associated with the p^{th} propagation path respectively:

$$\ddot{l}_p = \left(\ddot{\Delta} f \ddot{N}\right) \tau_p \,, \tag{5.10}$$

$$\ddot{k}_p = \frac{\nu_p}{\ddot{\Delta} f} \,, \tag{5.11}$$

where $\ddot{\Delta} f$ is the AFDM subcarrier spacing.

Therefore, in order to have consistent delay and Doppler indices between (5.7)-(5.8) and (5.10)-(5.11), $\ddot{N} = MN$, $\ddot{n} = nM + m$, and $\ddot{\Delta} f = \frac{\Delta f}{N}$.

Each index can be decomposed into its integer- and fractionally-spaced counterparts, e.g.:

$$\widetilde{k}_p = \underline{\widetilde{k}_p} + \delta \widetilde{k}_p \,, \tag{5.12}$$

where the $\underline{\widetilde{k}_p} = \lfloor \widetilde{k}_p \rceil$ is the integer part of the index, $\delta \widetilde{k}_p = \widetilde{k}_p - \underline{\widetilde{k}_p}$ is the fractional component, and $\lfloor \cdot \rceil$ is the rounding function.

Using this notation, the TD channel representations in (5.6) and (5.9) can be respectively rewritten as:

$$h_{m,\,n,\,p,\,\xi} = \left(\widetilde{h}_p e^{j2\pi\widetilde{k}_p \frac{nM+m-\widetilde{l}_p}{MN}}\right) e^{j2\pi\delta\widetilde{k}_p\xi}\,, \tag{5.13}$$

$$h_{\ddot{n},\,p,\,\xi} = \left(\widetilde{h}_p e^{j2\pi\ddot{k}_p \frac{\ddot{n}-\ddot{l}_p}{\ddot{N}}}\right) e^{j2\pi\delta\ddot{k}_p\xi}\,. \tag{5.14}$$

It can be readily seen that when the fractional component of the Doppler indices is 0, the channel does not vary with respect to the block index ξ. When δk_p is non zero, the additional blocks impose a phase shift to the TD channel.

The channel is specifically defined for OTFS and AFDM for explicit clarity, since multiple OTFS and AFDM configurations are considered, as shown in Table 5.2. Once again, it can be seen that AFDM is equivalent to OTFS when $\ddot{N} = MN$, $\ddot{n} = nM + m$, and $\ddot{\Delta f} = \frac{\Delta f}{N}$. The OTFS TD channel representation is also directly applied to OFDM, as OTFS and OFDM utilise the same system parameters.

5.3.1 Propagation Path Parameter Generation

The first path $p = 0$ is the LoS path, while the remaining $P - 1$ paths are NLoS paths. The fading gain and path loss $\widetilde{h}_p$ is:

$$\widetilde{h}_p = \begin{cases} \sqrt{\frac{\kappa}{\kappa+1}}, & \text{if } p = 0 \\ \sqrt{\frac{1}{(\kappa+1)(P-1)}}\zeta_p, & \text{if } p > 0\,, \end{cases} \tag{5.15}$$

where κ is the Rician K factor, and ζ_p is a complex Gaussian random variable with mean $\mu_h = 0$ and variance $\sigma_h^2 = 1$, expressed as $\mathcal{N}(\mu_h, \sigma_h^2)$.

The delay index l_p is:

$$l_p = \begin{cases} 0, & \text{if } p = 0 \\ \lfloor (D_T - 1)\eta_l \rceil, & \text{if } p > 0, \end{cases} \tag{5.16}$$

where D_T is the number of delay taps, and η_l is a random variable obeying a uniform distribution between 0 and 1.

The number of delay taps D_T defines the maximum delay index, and hence the maximum propagation path delay. No pair of propagation paths will have the same delay index, yielding: $l_{p_1} \neq l_{p_2}$, where $p_1 = [0, 1, \ldots P-1]$, $p_2 = [0, 1, \ldots P-1]$, and $p_1 \neq p_2$.

The fractional Doppler index k_p is:

$$k_p = \lfloor 2k_{max}\,(\eta_k - 0.5) \rceil, \tag{5.17}$$

where η_k is a random variable following a uniform distribution between 0 and 1, and k_{max} is the maximum integer Doppler index, defined as:

$$k_{max} = \lfloor \frac{1}{\ddot{\Delta f}} \frac{f_c V}{c_0} \rceil = \lfloor \frac{N}{\Delta f} \frac{f_c V}{c_0} \rceil \,, \tag{5.18}$$

where V is the velocity of the communication receiver, f_c is the carrier frequency, and c_0 is the speed of light. The equality holds when equivalent AFDM and OTFS configurations are compared.

5.3.2 Channel Matrix and Received Signal Definition

The TD channel matrix for block ξ, $\boldsymbol{H}_\xi \in \mathbb{C}^{\ddot{N}\times\ddot{N}}$, is formulated as:

$$\boldsymbol{H}_\xi[\ddot{n},\, \lfloor \ddot{n} - \ddot{l}_p \rfloor_{\ddot{N}}] = \sum_{p=0}^{P-1} h_{\ddot{n},\,p,\,\xi} \,, \tag{5.19}$$

where $\lfloor \cdot \rfloor_{\ddot{N}}$ is the modulo $\ddot{N}$ operator.

For OTFS, the $h_{\ddot{n},\,p,\,\xi}$ is replaced by $h_{m,\,n,\,p,\,\xi}$, with $nM + m$ instead of $\ddot{n}$, $\ddot{N}$ substituted by MN, and the OTFS delay and Doppler indices utilised.

The TD received signal for block ξ, $\boldsymbol{y}_\xi \in \mathbb{C}^{\ddot{N}\times 1}$, is:

$$\boldsymbol{y}_\xi = \boldsymbol{H}_\xi \boldsymbol{x}_\xi + \boldsymbol{z}_\xi \,, \tag{5.20}$$

where $\boldsymbol{z}_\xi$ is the AWGN for block ξ, with mean $\mu_z = 0$ and variance N_0, expressed as $\mathcal{N}(\mu_z, N_0)$, and N_0 is the noise power.

The AFD received signal for block ξ, $\ddot{\boldsymbol{y}}_\xi \in \mathbb{C}^{\ddot{N}\times 1}$, is:

$$\begin{aligned} \ddot{\boldsymbol{y}}_\xi &= \boldsymbol{A}_{\ddot{N}} \boldsymbol{y}_\xi = \boldsymbol{A}_{\ddot{N}} \boldsymbol{H}_\xi \boldsymbol{A}_{\ddot{N}}^H \ddot{\boldsymbol{x}}_\xi + \boldsymbol{A}_{\ddot{N}} \boldsymbol{z}_\xi, \\ \ddot{\boldsymbol{y}}_\xi &= \ddot{\boldsymbol{H}}_\xi \ddot{\boldsymbol{x}}_\xi + \boldsymbol{A}_{\ddot{N}} \boldsymbol{z}_\xi, \end{aligned} \tag{5.21}$$

where $\ddot{\boldsymbol{H}}_\xi$ is the AFD equivalent channel:

$$\ddot{\boldsymbol{H}}_\xi = \boldsymbol{A}_{\ddot{N}} \boldsymbol{H}_\xi \boldsymbol{A}_{\ddot{N}}^H \,. \tag{5.22}$$

5.4 Soft-MMSE Detection

Soft-MMSE equalisation [226] is applied at the receiver, with perfect channel estimation assumed. Due to the interleaving applied to the coded bits, the channel decoder's *a*

posteriori Log-Likelihood Ratios (LLRs) $\mathcal{L}^{\rho,\delta}$ are interleaved to generate the soft-MMSE *a priori* LLRs $\mathcal{L}^{\alpha,\mu}$.

For each transmit block ξ, a transmit symbol estimate $\varepsilon\{\ddot{\boldsymbol{x}}_{\xi}\}$ is formulated using the soft-MMSE *a priori* LLRs $\mathcal{L}_{\xi}^{\alpha,\mu}$ for the ξ^{th} transmit block as:

$$\begin{aligned}\varepsilon\{\ddot{\boldsymbol{x}}_{\xi}[\ddot{n}]\} &= \sum_{\gamma=0}^{\Gamma-1} s_{\gamma}\mathcal{P}\left(\ddot{\boldsymbol{x}}_{\xi}[\ddot{n}] = s_{\gamma}\right) \ , \\ &= \sum_{\gamma=0}^{\Gamma-1} s_{\gamma}\frac{\exp\left(\sum_{\beta=0}^{B_S-1} b_{\beta}^{\gamma}\mathcal{L}_{\xi}^{\alpha,\mu}[\ddot{n}B_S+\beta]\right)}{\prod_{\beta=0}^{B_S-1}\left(1+\exp\left(\mathcal{L}_{\xi}^{\alpha,\mu}[\ddot{n}B_S+\beta]\right)\right)} \ , \end{aligned} \tag{5.23}$$

where $\mathcal{P}\left(a=b\right)$ denotes the probability of $a=b$, s_{γ} is the modulated symbol corresponding to the integer value γ, $\gamma=[0,1,...,\Gamma-1]$ is the modulation index, $\beta=[0,1,...\ B_S-1]$ is the index of bits in a symbol, and $\exp(\cdot)$ is the natural exponential function.

A diagonal matrix $\boldsymbol{E}$ of the squared magnitude of $\varepsilon\{\ddot{\boldsymbol{x}}_{\xi}\}$ is then generated as:

$$\boldsymbol{E} = \text{diag}\left(\varepsilon\{\ddot{\boldsymbol{x}}_{\xi}\}\otimes\varepsilon\{\ddot{\boldsymbol{x}}_{\xi}\}^{*}\right) \ , \tag{5.24}$$

where $\otimes$ is the element-wise multiplication, and $(\cdot)^{*}$ is the complex conjugate operation.

The AFDM MMSE matrix $\ddot{\boldsymbol{G}}_{\xi}$ for the ξ^{th} transmit block is:

$$\ddot{\boldsymbol{G}}_{\xi} = \left(\ddot{\boldsymbol{H}}_{\xi}^{*}\left(\boldsymbol{R}_{SX}+\boldsymbol{E}\right)\ddot{\boldsymbol{H}}_{\xi}^{T}+N_0\boldsymbol{I}_{\ddot{N}\times\ddot{N}}\right)^{-1}\ddot{\boldsymbol{H}}_{\xi}^{*} \ , \tag{5.25}$$

where $(\cdot)^{T}$ is the transpose operation, $\boldsymbol{I}_{\ddot{N}\times\ddot{N}}$ is the $\ddot{N}\times\ddot{N}$ identity matrix, and $\boldsymbol{R}_{SX}$ is the covariance matrix of the transmit symbols, which is set to $\boldsymbol{I}_{\ddot{N}\times\ddot{N}}$, since the average transmit symbols power is normalised to 1.

The soft-MMSE transmit signal estimate $\overset{\mu}{\boldsymbol{x}}$ is expressed:

$$\overset{\mu}{\boldsymbol{x}}[\ddot{n}] = \left(\left(\ddot{\boldsymbol{y}}_{\xi}\right)^{T}\ddot{\boldsymbol{g}}_{\xi,\ddot{n}} - \iota_{\xi,\ddot{n}}\right)\frac{\left(\overset{\mu}{h}_{\xi,\ddot{n}}\right)^{*}}{|\overset{\mu}{h}_{\xi,\ddot{n}}|^{2}} \ , \tag{5.26}$$

where $|\cdot|$ is the magnitude operator, $\ddot{\boldsymbol{g}}_{\xi,\ddot{n}}$ is the $\ddot{n}^{\text{th}}$ column of $\ddot{\boldsymbol{G}}_{\xi}$, $\iota_{\xi,\ddot{n}}$ is the interference imposed upon the $\ddot{n}^{\text{th}}$ symbol by the other $\ddot{N}-1$ symbols in the ξ^{th} transmit block, and $\overset{\mu}{h}_{\xi,\ddot{n}}$ is:

$$\overset{\mu}{h}_{\xi,\ddot{n}} = \left(\ddot{\boldsymbol{h}}_{\xi,\ddot{n}}\right)^{T}\ddot{\boldsymbol{g}}_{\xi,\ddot{n}} \ . \tag{5.27}$$

The interference imposed upon the $\ddot{n}^{\text{th}}$ symbol by the other $\ddot{N}-1$ symbols in the ξ^{th} transmit block $\iota_{\xi,\ddot{n}}$ is:

$$\iota_{\xi,\ddot{n}} = \sum_{\ddot{n}_2=0,\,\ddot{n}_2\neq\ddot{n}}^{\ddot{N}-1} \varepsilon\{\ddot{\boldsymbol{x}}_{\xi}[\ddot{n}_2]\} \left(\ddot{\boldsymbol{h}}_{\xi,\ddot{n}_2}\right)^T \ddot{\boldsymbol{g}}_{\xi,\ddot{n}} \,. \tag{5.28}$$

The equivalent soft-MMSE AWGN noise power $\overset{\mu}{N}_{0,\xi}$ for each symbol is expressed as:

$$\overset{\mu}{N}_{0,\xi}[\ddot{n}] = \frac{1}{|\overset{\mu}{h}_{\xi,\ddot{n}}|} + (\boldsymbol{E}[\ddot{n},\ddot{n}]-1) \,. \tag{5.29}$$

The approximate maximum probability metric $\overset{\mu}{d}_{\overset{\mu}{m},\gamma}$ describing the probability of the transmit symbol $\ddot{\boldsymbol{x}}[\overset{\mu}{m}]$ being s_γ can then be generated using $\overset{\mu}{\boldsymbol{x}}[\overset{\mu}{m}]$ and $\overset{\mu}{N}_{0,\xi}$:

$$\overset{\mu}{d}_{\overset{\mu}{m},\gamma} = -\frac{\left|\overset{\mu}{\boldsymbol{x}}[\overset{\mu}{m}]-s_\gamma\right|^2}{\overset{\mu}{N}_0[\overset{\mu}{m}]} + \sum_{\beta=0}^{B_S-1} b_\beta^\gamma \mathcal{L}_{\xi}^{\alpha,\mu}[\ddot{b}] \,, \tag{5.30}$$

where $\ddot{b}=[0,1,...,\ddot{N}B_S-1]$ is the bit index within the transmit block ξ, $\overset{\mu}{m}=\lfloor\frac{\ddot{b}}{B_S}\rfloor$, and $\lfloor\cdot\rfloor$ is the floor function.

TABLE 5.3: Lookup table for the Jacobian algorithm

Value of $\lvert d_1-d_2\rvert$	Value of $\Theta(\lvert d_1-d_2\rvert)$
$\lvert d_1-d_2\rvert > 3.7$	0
$2.25 < \lvert d_1-d_2\rvert \leq 3.7$	0.05
$1.5 < \lvert d_1-d_2\rvert \leq 2.25$	0.15
$1.05 < \lvert d_1-d_2\rvert \leq 1.5$	0.25
$0.7 < \lvert d_1-d_2\rvert \leq 1.05$	0.35
$0.43 < \lvert d_1-d_2\rvert \leq 0.7$	0.45
$0.2 < \lvert d_1-d_2\rvert \leq 0.43$	0.55
$\lvert d_1-d_2\rvert \leq 0.2$	0.65

The soft-MMSE *a posteriori* LLRs $\mathcal{L}_{\xi}^{\rho,\mu}$ for the ξ^{th} transmit block are then calculated using the Approx-Log-MAP algorithm from [226, 227]:

$$\mathcal{L}_{\xi}^{\rho,\mu}[\ddot{b}] = \underset{s_\gamma\in\mathcal{S}_{b_\xi=1}}{\text{jac}}\left(\overset{\mu}{d}_{\overset{\mu}{m},\gamma}\right) - \underset{s_\gamma\in\mathcal{S}_{b_\xi=0}}{\text{jac}}\left(\overset{\mu}{d}_{\overset{\mu}{m},\gamma}\right) \,, \tag{5.31}$$

where $\text{jac}(\cdot)$ is the Jacobian function:

$$\text{jac}\,(d_1,d_2) = \max(d_1,d_2) + \Theta(|d_1-d_2|) \,, \tag{5.32}$$

where max is the maximum function that returns the highest value, and $\Theta(|d_1 - d_2|)$ is an additional term whose value is specified by Table 5.3 [228, 229].

The soft-MMSE *a posteriori* LLRs for the Ξ transmit blocks $\mathcal{L}^{\rho,\mu}$ are de-interleaved to produce the channel decoder's *a priori* LLRs $\mathcal{L}^{\alpha,\delta}$.

5.5 Simulation Results

TABLE 5.4: Simulation parameter values

Parameter	OFDM	AFDM 1	OTFS 1	AFDM 2	OTFS 2	OTFS 3
Modulation order Γ	2					
Number of propagation paths P	4					
Number of delay taps D_T	5					
Communication receiver velocity V	150 m/s					
Rician K factor κ	0 dB					
Carrier frequency f_c	38.5 GHz					
Maximum propagation delay τ_{max}	10.4167 μs					
AFDM guard for fractional indices k_ν	N/A	1	N/A	1	N/A	N/A
Set 1						
Number of subcarriers	32	512	32	32	8	32
Number of symbol slots	16	N/A	16	N/A	4	16
Subcarrier spacing	15 kHz	$\frac{15}{16}$ kHz	15 kHz	15 kHz	60 kHz	$\frac{15}{16}$ kHz
Set 2						
Number of subcarriers	16	128	16	16	8	16
Number of symbol slots	8	N/A	8	N/A	2	8
Subcarrier spacing	30 kHz	$\frac{15}{4}$ kHz	30 kHz	30 kHz	60 kHz	$\frac{15}{4}$ kHz
Set 3						
Number of subcarriers	8	32	8	8	4	8
Number of symbol slots	4	N/A	4	N/A	2	4
Subcarrier spacing	60 kHz	15 kHz	60 kHz	60 kHz	120 kHz	15 kHz
Set 4						
Number of subcarriers	4	8	4	4	2	4
Number of symbol slots	2	N/A	2	N/A	2	2
Subcarrier spacing	120 kHz	60 kHz	120 kHz	120 kHz	240 kHz	60 kHz

The simulation parameters are shown in Table 5.4. The number of subcarriers refers to OFDM-type subcarriers for OFDM and OTFS, and to chirp subcarriers for AFDM. Different random interleavers are generated for each frame. The same interleaver is utilised across transmission blocks within a frame, and the interleaver length is 10 000 bits.

The five configurations outlined in Table 5.2 are characterised by simulations. OFDM is configured to match OTFS 1, with multiple symbol slots. AFDM 1 is equivalent to

OTFS 1, hence it possesses a smaller subcarrier spacing than OFDM and OTFS 1, to ensure that the same frequency resources are utilised. The duration of AFDM 2 is equal to that of a single OFDM symbol, and has the same subcarrier spacing as OFDM. OTFS 2 is the configuration that is equivalent to AFDM 2. OTFS 3 has the same matrix dimension and subcarrier spacing as AFDM 1, hence it has a lower bandwidth. OTFS 3 is included since some references utilise this OTFS configuration to compare with AFDM.

Four parameter value groups are investigated, named Set 1, 2, 3, and 4. The matrix dimensions of OFDM, OTFS 1, and AFDM 1 are divided by 4 every time the Set index is increased. The values of the base variables defined in Table 5.2 are, for each Set:

- Set 1: $M = 32$, $N = 16$, $\Delta f = 15$ kHz.
- Set 2: $M = 16$, $N = 8$, $\Delta f = 30$ kHz.
- Set 3: $M = 8$, $N = 4$, $\Delta f = 60$ kHz.
- Set 4: $M = 4$, $N = 2$, $\Delta f = 120$ kHz.

5.5.1 Uncoded BER

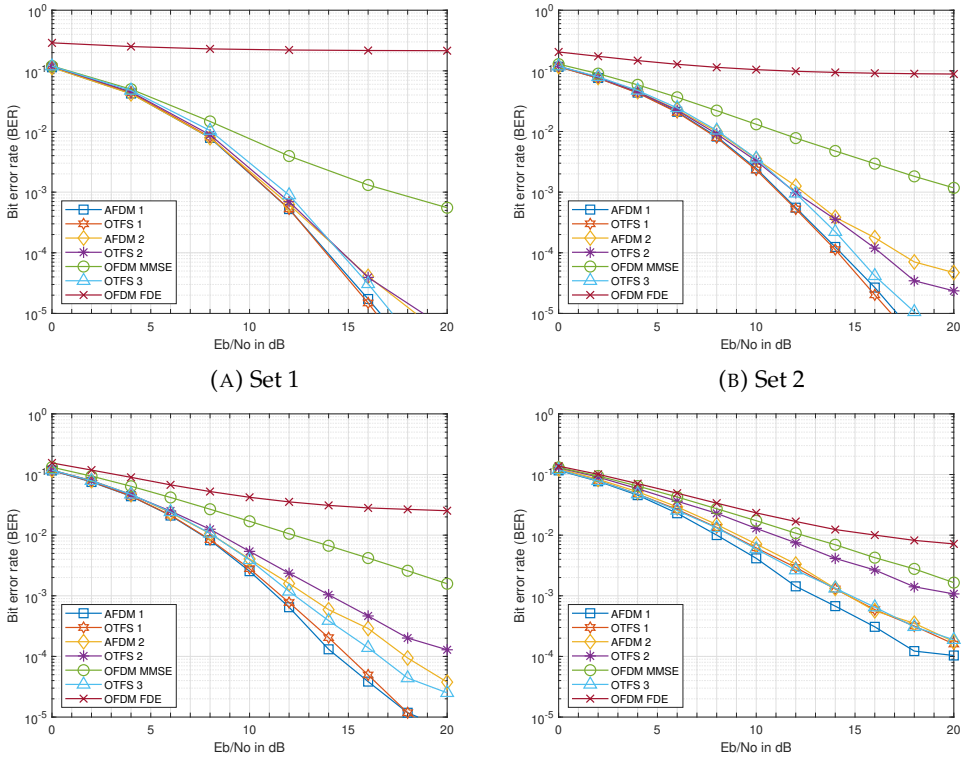

(A) Set 1 (B) Set 2

(C) Set 3 (D) Set 4

FIGURE 5.3: BER of uncoded BPSK AFDM 1 and 2, OFDM, and OTFS 1, 2 and 3

The BERs of uncoded BPSK AFDM 1 and 2, OTFS 1, 2, and 3, and OFDM utilising hard-MMSE are shown in Figure 5.3. The BER of OFDM using single tap FD equalisation,

denoted as "FDE", is also shown. Hard-MMSE refers to the MMSE equalisation that outputs bit estimates (hard values), as opposed to LLRs (soft values). For Set 1, the BERs of the AFDM and OTFS configurations are similar to each other. The BER of hard-MMSE OFDM is higher than that of AFDM and OTFS, with the BER of "FDE" OFDM remaining above 0.3 for the E_b/N_0 range considered.

When the Set index is increased, the dimension of the configurations is reduced, and the BERs of the AFDM configurations do not increase to the same extent as the BERs of their OTFS counterparts at high E_b/N_0. AFDM 1 is the counterpart to OTFS 1, and AFDM 2 is the counterpart to OTFS 2. OTFS 3 has no direct counterpart, and it is included to illustrate how a non-equivalent configuration may result in an unfair comparison between OTFS and AFDM. OTFS 3 has the same subcarrier spacing and dimension as AFDM 1, which results in OTFS 3 possessing a smaller bandwidth than AFDM 1.

It can be observed from Figure 5.3 that for Set 1, associated with the largest matrix dimension, AFDM 1 and OTFS 1 exhibit a similar BER, while the BER of AFDM 2 is comparable to that of OTFS 2. However, as the matrix dimension is reduced from that of Set 1 to Set 4, the AFDM configurations gradually start to outperform their OTFS counterparts. This is because to AFDM's diversity gain only presenting a significant advantage when the codeword differences are small, for small matrix dimensions. Therefore, Set 4 is utilised for the majority of the following results, as it is the parameter Set for which AFDM exhibits the most substantial BER improvement over OTFS.

5.5.2 EXIT Chart Analysis

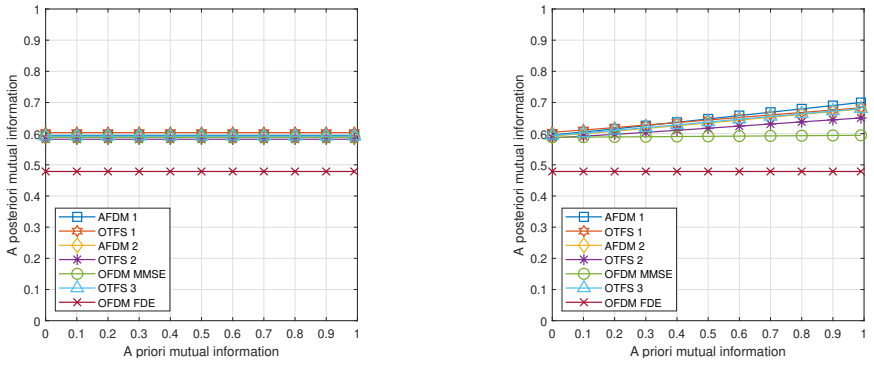

(A) Hard-MMSE (B) Soft-MMSE

FIGURE 5.4: EXIT chart of Set 4 hard- and soft-MMSE BPSK AFDM 1 and 2, OFDM, and OTFS 1 and 2 for 0 dB E_b/N_0

The EXIT charts of Set 4 hard- and soft-MMSE BPSK AFDM 1 and 2, OTFS 1, 2, and 3, and OFDM for 0 dB E_b/N_0 are shown in Figure 5.4. For hard-MMSE, the *a posteriori* mutual information remains constant when the *a priori* mutual information varies. In contrast, the *a posteriori* mutual information is increased when the *a priori* mutual information is increased for soft-MMSE. This demonstrates that the soft-MMSE method is

capable of improving the performance compared to hard MMSE. The EXIT curves of AFDM 1 and OTFS 1 are similar to each other, indicating a similar performance. The EXIT curve of AFDM 2 has a steeper gradient than that of OTFS 2, which suggests that AFDM 2 has a superior detection capability to OTFS 2. The EXIT curve of soft-MMSE OFDM is at a higher ordinate value than that of hard-MMSE OFDM, but maintains the same 0 gradient, which indicates that soft-MMSE OFDM cannot provide an iteration gain. The EXIT curve of soft-MMSE OFDM is also at a lower ordinate value than those of AFDM and OTFS. The lack of gradient in the soft-MMSE OFDM EXIT curve is due to the lack of correlation between the OFDM subcarriers, when no AFDM or OTFS precoding is implemented.

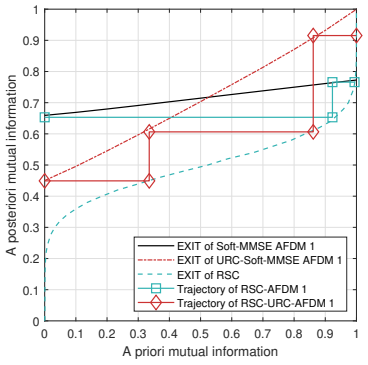

(A) AFDM 1, $R_c = 0.5$

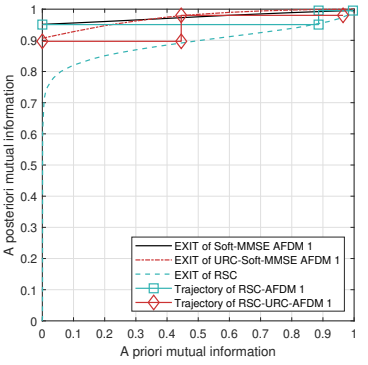

(B) AFDM 1, $R_c = 0.9$

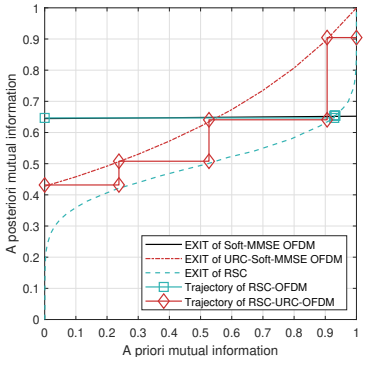

(C) OFDM, $R_c = 0.5$

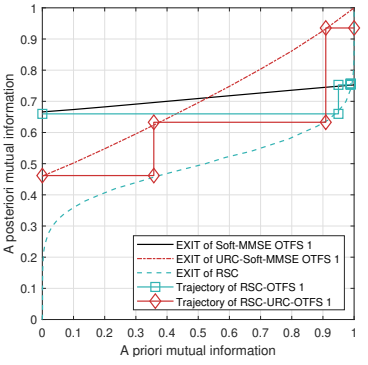

(D) OTFS 1, $R_c = 0.5$

FIGURE 5.5: EXIT chart and trajectory of Set 4 RSC- (square) and RSC-URC-coded (diamond) BPSK AFDM 1, OFDM, and OTFS 1 for 4 dB E_b/N_0

The EXIT charts and trajectories of Set 4 RSC- and RSC-URC-coded BPSK AFDM 1, OTFS 1 and OFDM for soft-MMSE are shown in Figure 5.5, for 4 dB E_b/N_0. The trajectories of AFDM 1 and OTFS 1 are similar, which reflects the general trend of approximately similar performance between AFDM and OTFS. Due to the flat EXIT chart of soft-MMSE OFDM, there is little iterative gain is attained for RSC coding.

The trajectories of RSC coding reach their end points in 1 or 2 iterations for AFDM 1 and OTFS 1. At a coding rate of 0.9, the minimum *a posteriori* mutual information is 0.9, which only leaves room for modest iteration gain. Hence, the RSC coded AFDM 1 and OTFS 1 trajectories approach the ideal (1, 1) point of perfect convergence.

When URC is harnessed, the EXIT chart performance of soft-MMSE is improved for all three waveforms for $R_c = 0.5$, which leads to a higher iterative gain for RSC coding, as the trajectory end point is closer to the ideal (1, 1) point. This is a benefit of the URC increasing the open tunnel. A greater number of iterations is required to reach the (1, 1) point when URC is employed, but this phenomenon no longer persists at higher coding rates, as shown in Figure 5.5b for $R_c = 0.9$, as the initial *a posteriori* mutual information is very high (0.9). The performance of RSC-URC-OFDM remains lower than that of RSC-URC-AFDM 1 and RSC-URC-OTFS 1.

5.5.3 Comparison of RSC and RSC-URC AFDM

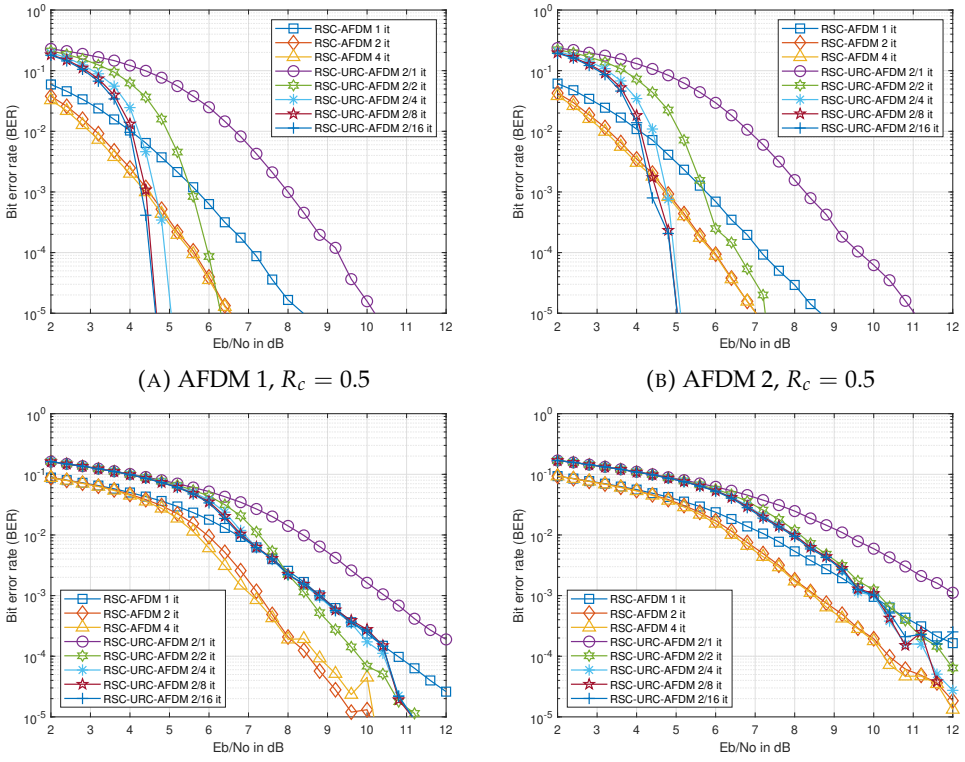

(A) AFDM 1, $R_c = 0.5$ (B) AFDM 2, $R_c = 0.5$

(C) AFDM 1, $R_c = 0.9$ (D) AFDM 2, $R_c = 0.9$

FIGURE 5.6: BER of Set 4 RSC- and RSC-URC-coded BPSK AFDM 1 and 2

The BERs of Set 4 RSC- and RSC-URC-coded BPSK AFDM 1 and 2 are shown in Figure 5.6, for $R_c = 0.5$ and 0.9. "RSC-AFDM 1 it" refers to RSC-AFDM relying on a single iteration, and "RSC-URC-AFDM 2/4 it" refers to RSC-URC-AFDM having 2 inner and 4 outer iterations. For RSC-URC coding, the inner iterations are between URC decoding and soft-MMSE equalisation. The outer iterations are between the RSC decoder and the combined URC-equaliser block.

As expected, increasing the coding rate increases the BER for both AFDM configurations and for both coding methods. The BER of RSC-AFDM 1 is lower than that of RSC-AFDM 2 at high E_b/N_0 and for a sufficiently high number of iterations, following

the trend for uncoded hard-MMSE AFDM simulated with the Set 4 variable values. The BER difference is accentuated when the coding rate is increased, as fewer errors can be corrected at high coding rates. The BER of RSC-URC-AFDM 1 is lower than that of AFDM 2 for both coding rates and for the specific number of inner and outer iterations considered.

For RSC coding, increasing the number of iterations from 1 to 2 drastically reduces the BER for both coding rates. By contrast, increasing the number of iterations from 2 to 4 no longer significantly improves the BER for a coding rate of 0.5, but slightly lowers it for a coding rate of 0.9. This result is consistent with the EXIT chart based prediction, where the trajectory end point is reached within a low number of iterations. The drastic BER reduction of RSC coding as the number of iterations increases is indeed expected as an explicit benefit of having iteratively improved extrinsic LLRs.

The BER of RSC-URC coding is higher for both coding rates than that of stand-alone RSC coding when a similar complexity is considered, which is a plausible reflection of the fact that RSC-URC can only improve the BER at an increased complexity. To elaborate, at a coding rate of 0.5, the BER of RSC-URC coding decreases as the number of outer iterations is increased up to 8. Further increase in the number of iterations does not significantly improve the BER performance. Again, RSC-URC is capable of outperforming RSC coding at the lower coding rates, but only at higher numbers of iterations. This is consistent with the EXIT chart predictions, where the trajectory end point for RSC-URC is only reached at a higher number of iterations than for RSC coding, but it is closer to the ideal (1, 1) point. At a coding rate of 0.9, the BER of RSC-URC is higher than that of RSC coding, even when a higher number of outer iterations is utilised. This is also shown in the EXIT chart results, where the addition of URC does not significantly impact the EXIT curve gradient of soft-MMSE equalisation at this coding rate. At small matrix dimensions, high code rates and many outer iterations, the BER of RSC-URC coding becomes unstable at high E_b/N_0, as shown in Figure 5.6d.

5.5.4 BER of RSC-coded OFDM, AFDM, and OTFS

The BERs of Set 4 RSC-coded BPSK AFDM 1 and 2, OFDM, and OTFS 1, 2, and 3 are shown in Figure 5.7, for coding rates of 0.5, 0.7, and 0.9, and for $It_{outer} = 2$. For all coding rates, OFDM has the highest BER trend, as its subcarrier orthogonality is partially compromised at the high velocity considered.

For all coding rates, the BER of AFDM 1 is generally lower than that OTFS 1 and OTFS 3. The BER difference is accentuated at $R_c = 0.9$. The BER of AFDM 2 is similar to that of OTFS 1 and OTFS 3 at $R_c = 0.5$, but gradually diverges as the coding rate is increased. For all coding rates, OTFS 2 has a higher BER than AFDM 2, and OFDM

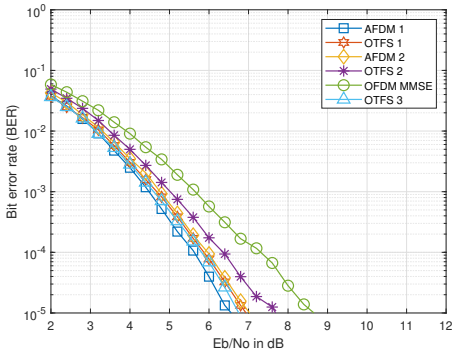

(A) $R_c = 0.5$, $\text{It}_{\text{outer}} = 2$

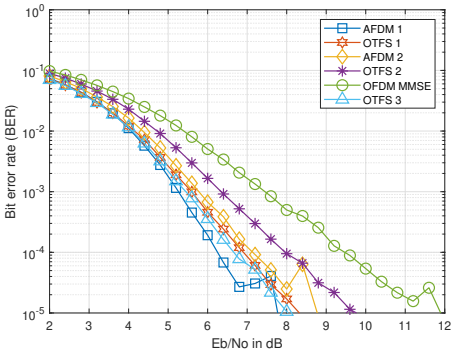

(B) $R_c = 0.7$, $\text{It}_{\text{outer}} = 2$

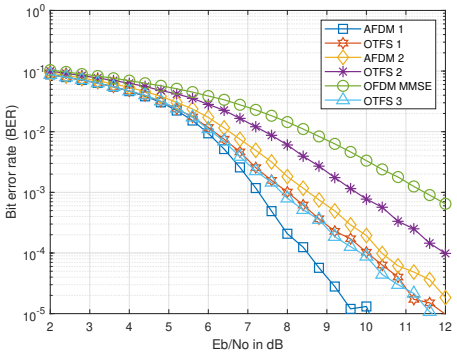

(C) $R_c = 0.9$, $\text{It}_{\text{outer}} = 2$

FIGURE 5.7: BER of Set 4 RSC-coded BPSK AFDM 1 and 2, OFDM, and OTFS 1, 2, and 3 for $\text{It}_{\text{outer}} = 2$

exhibits a higher BER than OTFS 2. AFDM 1, OTFS 1, and OTFS 3 have the larger matrix dimensions, hence they combat the effect of the channel and AWGN better than the other configurations, albeit at the expense of increased complexity. The AFDM configurations have a lower BER than their OTFS counterparts due to AFDM possessing higher degrees of freedom.

5.5.5 BER of RSC-URC coded OFDM, AFDM, and OTFS

The BERs of Set 4 RSC-URC-coded BPSK AFDM 1 and 2, OFDM, and OTFS 1, 2, and 3 are shown in Figure 5.8, for coding rates of 0.5, 0.7, and 0.9, and for $\text{It}_{\text{inner}} = 2$, and $\text{It}_{\text{outer}} = 2$ and 8. For all coding rates and number of outer iterations, OFDM has the highest BER trend.

For $R_c = 0.5$, the BER of AFDM 1, OTFS 1 and OTFS 3 are similar to each other, with OTFS 2, AFDM 2, and OFDM exhibiting a higher BER. For $\text{It}_{\text{outer}} = 2$, increasing R_c increases the relative BER difference of the configurations. AFDM 1 has the lowest BER, followed by OTFS 1 and 3, then AFDM 2, OTFS 2, and OFDM. Recall that AFDM 1, OTFS 1, and OTFS 3 have the larger matrix dimensions, hence they combat the effect of the channel and AWGN better, albeit at the expense of increased complexity. Furthermore, AFDM 2 and OTFS 2 have lower matrix dimensions, which leads to a higher

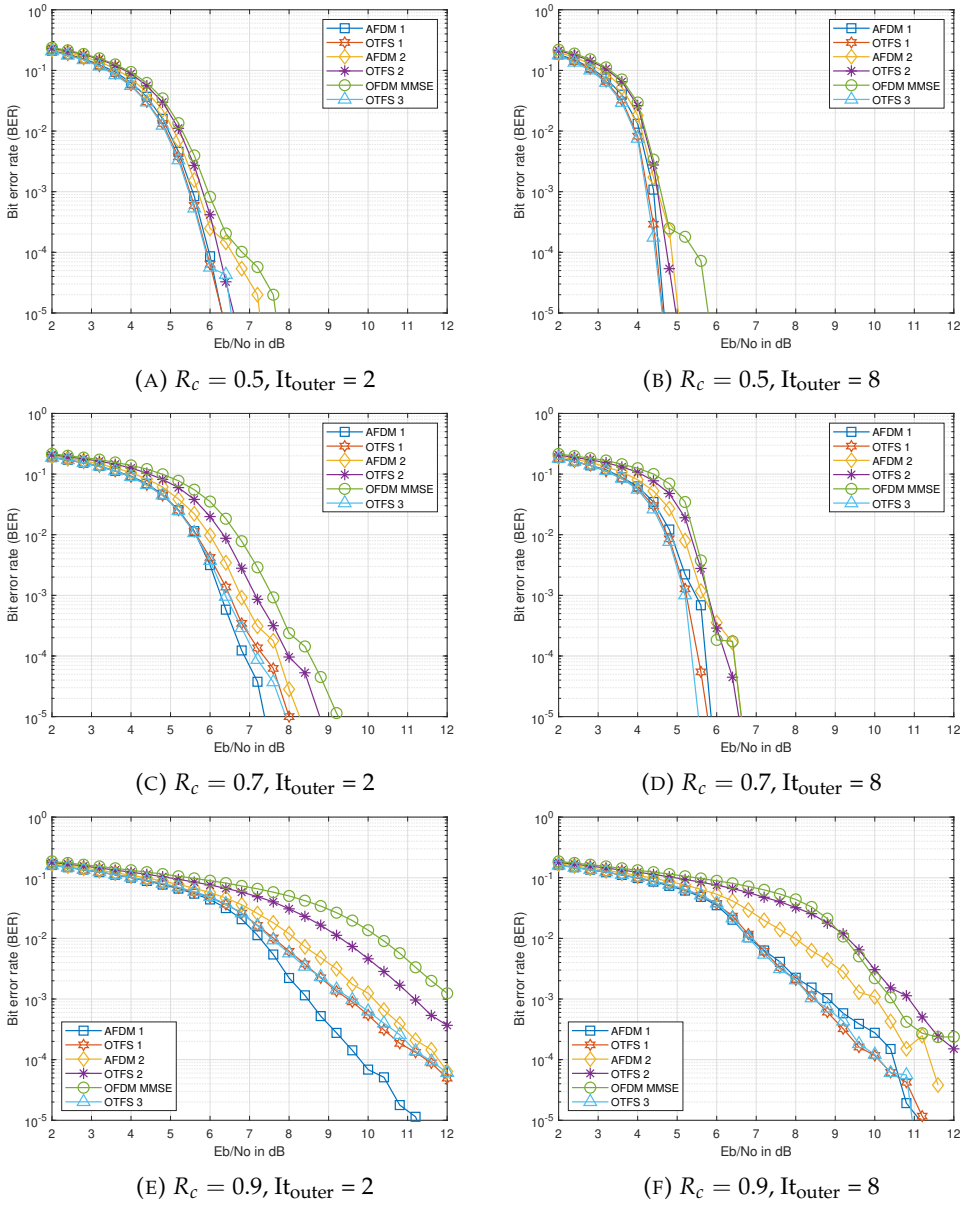

(A) $R_c = 0.5$, $\text{It}_{\text{outer}} = 2$ (B) $R_c = 0.5$, $\text{It}_{\text{outer}} = 8$

(C) $R_c = 0.7$, $\text{It}_{\text{outer}} = 2$ (D) $R_c = 0.7$, $\text{It}_{\text{outer}} = 8$

(E) $R_c = 0.9$, $\text{It}_{\text{outer}} = 2$ (F) $R_c = 0.9$, $\text{It}_{\text{outer}} = 8$

FIGURE 5.8: BER of Set 4 RSC-URC-coded BPSK AFDM 1 and 2, OFDM, and OTFS 1, 2, and 3 for $\text{It}_{\text{inner}} = 2$

BER, but a lower complexity. At the high velocity considered, the subcarrier orthogonality of OFDM is partially compromised, leading to higher BERs. These trends follow those observed for uncoded transmissions in Figure 5.3d.

When the number of outer iterations is increased to $\text{It}_{\text{outer}} = 8$, the relative difference in BER between the configurations is reduced. The BER trends of AFDM 1, OTFS 1, and OTFS 3 are similar to each other. Observe that AFDM 2, OTFS 2, and OFDM have similar BER trends to each other for $R_c = 0.5$ and 0.7, with a higher BER than AFDM 1, OTFS 1, and OTFS 3. At $R_c = 0.9$, the BER of AFDM 2 is higher than that of AFDM 1, OTFS 1, and OTFS 3, but lower than that of OTFS 2 and OFDM. This is an explicit

benefit of AFDM's higher degrees of freedom than those of OTFS and OFDM, which effects the BER performance at low matrix dimensions.

5.5.6 Effect of the Matrix Dimensions on the BER of RSC-URC coded OFDM, AFDM, and OTFS

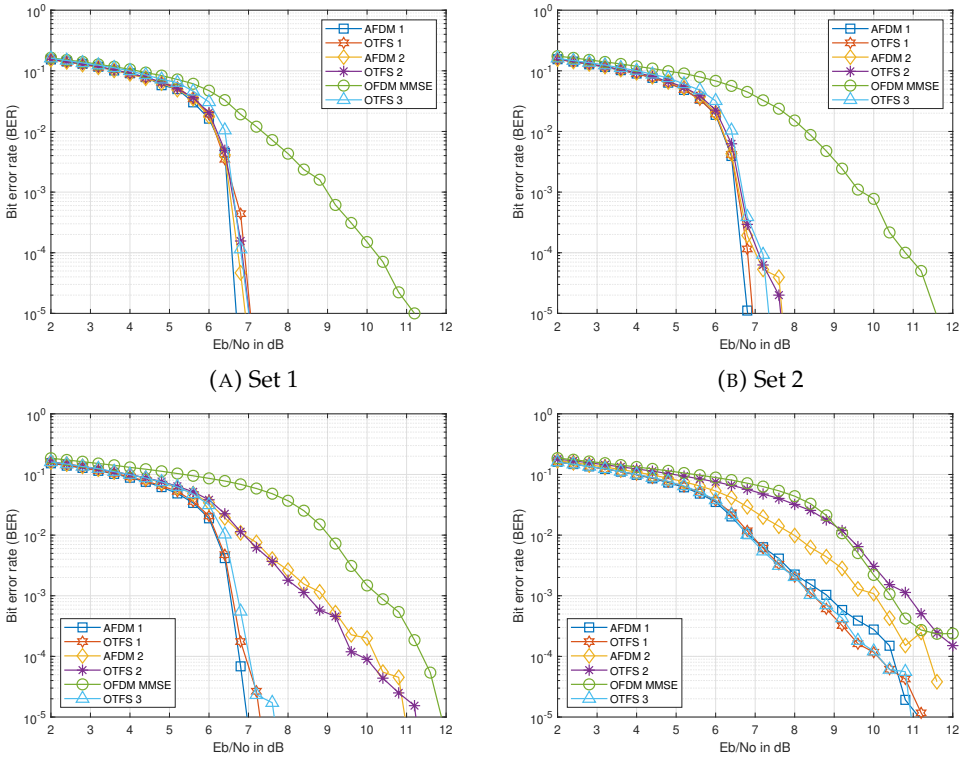

(A) Set 1 (B) Set 2

(C) Set 3 (D) Set 4

FIGURE 5.9: BER of Set 1, 2, 3, and 4 RSC-URC-coded BPSK AFDM 1 and 2, OFDM, and OTFS 1, 2 and 3 for $R_c = 0.9$ and $\text{It}_{\text{inner}} = 2$ and $\text{It}_{\text{outer}} = 8$ iterations

The BERs of RSC-URC-coded BPSK AFDM 1 and 2, OFDM, and OTFS 1, 2 and 3 are shown in Figure 5.9 for $R_c = 0.9$ and $\text{It}_{\text{inner}} = 2$ and $\text{It}_{\text{outer}} = 8$ iterations, for the variable values of Set 1, 2, 3 and 4. When the Set index is reduced, the dimension of the system configurations is increased. As the matrix dimensions are increased, the BER trends of the AFDM and OTFS configurations converge, since the effect of the matrix dimensions is diminished.

5.5.7 E_b/N_0 gain of RSC-URC Coding Relative to Uncoded Transmission

The E_b/N_0 gains of Set 4 RSC-URC-coded BPSK AFDM 1 and 2, OFDM, and OTFS 1 and 2 relative to uncoded transmission for $R_c = 0.5$ to 0.9 and $\text{It}_{\text{inner}} = 2$ and $\text{It}_{\text{outer}} = 8$ iterations at a BER of 10^{-3} is shown in Figure 5.10. The effective throughput in bpcu for each code rate is also shown. As expected, the E_b/N_0 gain reduces as the coding rate

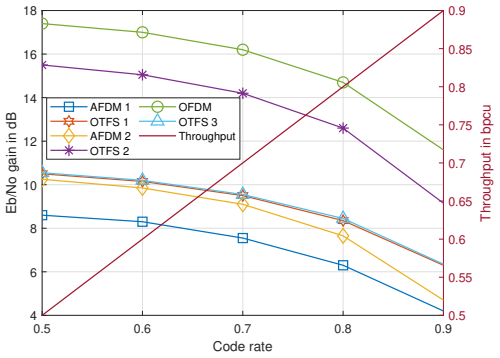

FIGURE 5.10: E_b/N_0 gains of Set 4 RSC-URC-coded BPSK AFDM 1 and 2, OFDM, and OTFS 1 and 2 relative to uncoded transmission for $R_c = 0.5$ to 0.9 and $It_{inner} = 2$ and $It_{outer} = 8$ iterations at a BER of 10^{-3}

increases, since fewer errors can be corrected at higher coding rates. The E_b/N_0 gain is largest for the configurations with the worst uncoded BER performance, as the coding allows the OTFS and OFDM configurations to overcome the higher diversity gain of AFDM.

5.5.8 Summary Table of the Communication BER Results

TABLE 5.5: E_b/N_0 in dB at which a BER of 10^{-4} is achieved for $R_c = 0.9$, for RSC coding and RSC-URC coding

Coding	AFDM 1	OTFS 1	AFDM 2	OTFS 2	OTFS 3	OFDM
RSC $It_{outer} = 2$	**8.5**	10	10.4	12	9.9	N/A
RSC-URC, $It_{outer} = 2$	**9.8**	11.5	11.8	N/A	11.5	N/A
RSC-URC, $It_{outer} = 8$	10.2	**10**	11.4	N/A	**10**	N/A

The E_b/N_0 at which a BER of 10^{-4} is achieved for $R_c = 0.9$ and different coding types and number of iterations are summarised in Table 5.5. For the lower complexity RSC coding and RSC-URC coding with $It_{outer} = 2$, AFDM 1 reaches a BER of 10^{-4} at a lower E_b/N_0 than the other configurations.

5.6 Sensing

Monostatic sensing functionality has been employed using a single pilot symbol in a pilot block. The pilot block is transmitted before the data blocks, with the pilot symbol placed in the first element of the transmit symbol vector. The power of the pilot symbol is $\ddot{N}$ for AFDM and MN for OTFS. The delay and Doppler indices for the $p_t{}^{\text{th}}$ target

are:

$$\widetilde{l}_{p_t} = \frac{2\Delta f M R_{p_t}}{c_0}\,, \tag{5.33}$$

$$\widetilde{k}_{p_t} = \frac{2 f_c N V_{p_t}}{\Delta f c_0}\,, \tag{5.34}$$

$$\ddot{l}_{p_t} = \frac{2\ddot{\Delta} f \ddot{N} R_{p_t}}{c_0}\,, \tag{5.35}$$

$$\ddot{k}_{p_t} = \frac{2 f_c V_{p_t}}{\ddot{\Delta} f c_0}\,, \tag{5.36}$$

where R_{p_t} is the range of the $p_t{}^{\text{th}}$ target and V_{p_t} is the velocity of the $p_t{}^{\text{th}}$ target.

A scalar of 2 is present in (5.33)-(5.36) because the signal is reflected by the target to the receiver in the monostatic sensing considered. It is assumed that the self-interference between the transmit signal and received echos is perfectly mitigated by appropriate shielding and/or signal processing methods.

For AFDM, a circular correlation operation is performed in the AFD on the received pilot block:

$$\ddot{\boldsymbol{y}}_{imag}[\ddot{n}_1] = \sum_{\ddot{n}=0}^{\ddot{N}-1} \left(\ddot{\boldsymbol{x}}_{pi}[\ddot{n}]\right)^* \ddot{\boldsymbol{y}}_{pi}[\lfloor \ddot{n} - \ddot{n}_1 \rfloor_{\ddot{N}}]\,, \tag{5.37}$$

where $\ddot{\boldsymbol{y}}_{imag} \in \mathbb{C}^{\ddot{N}\times 1}$ is the imaging vector, $\ddot{\boldsymbol{x}}_{pi} \in \mathbb{C}^{\ddot{N}\times 1}$ is the transmitted pilot block, and $\ddot{\boldsymbol{y}}_{pi} \in \mathbb{C}^{\ddot{N}\times 1}$ is the received pilot block.

An equivalent circular correlation operation is applied in the DD for OTFS. The P_t magnitude peaks of the $\ddot{\boldsymbol{y}}_{imag}$ are the estimates of the P_t target integer delay and Doppler indices.

A channel matrix is constructed utilising the estimated delay and Doppler indices, and the data in the data blocks are decoded. Two scoring methods are harnessed to determine the accuracy of the channel data: $(1 - \text{BER})$ and $-\log(\text{BER})$. The weights of each channel estimate are then normalised to calculate the weighted RMSE.

TABLE 5.6: Sensing parameter values

Parameter	Value
Number of targets P_t	1
System parameter Set	3
Target range	$\approx 312.5 + 0.001$ m
Target velocity	$\approx 233.8 + 0.001$ m/s

The simulation parameters for the preliminary sensing results are shown in Table 5.6. The range and velocity values are integer multiples of the resolutions of the configurations, with a shift of 0.001 added. This addition is present as the RMSE figures utilise

a logarithmic axis. If the range and velocity values were exact multiples of the range and velocity resolutions, the RMSE at higher SNRs would be 0, and hence could not be shown on the graphs.

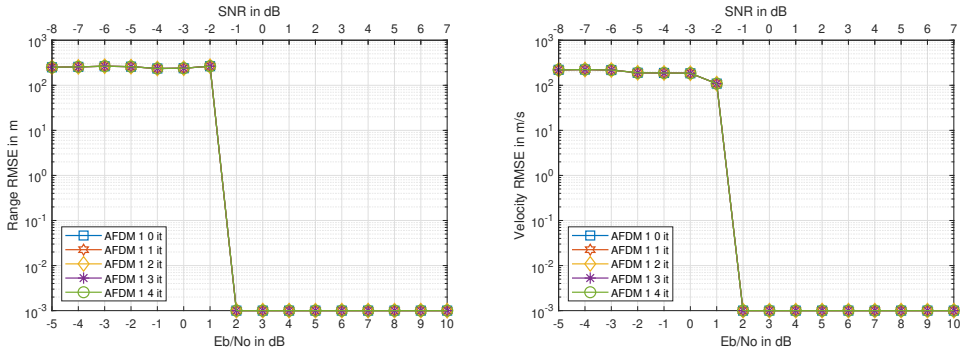

(A) Range (B) Velocity

FIGURE 5.11: RMSE of Set 3 RSC-coded BPSK AFDM 1 for $R_c = 0.5$ and It_{outer} = 0, 1, 2, 3, and 4 iterations for the $(1 - \text{BER})$ scoring method

The range and velocity RMSEs of Set 3 RSC-coded BPSK AFDM 1 for $R_c = 0.5$ and It_{outer} = 0, 1, 2, 3, and 4 iterations are shown in Figure 5.11 for the $(1 - \text{BER})$ scoring method. It_{outer} = 0 indicates that no decoding has been employed. The decoding has no impact on the integer index RMSE performance as the system reaches the RMSE error floor at an $\text{E}_\text{b}/\text{N}_0$ of 2 dB, at which the BER is still approximately 2×10^{-1}, an inadequate level for communication (shown in Figure 5.6a).

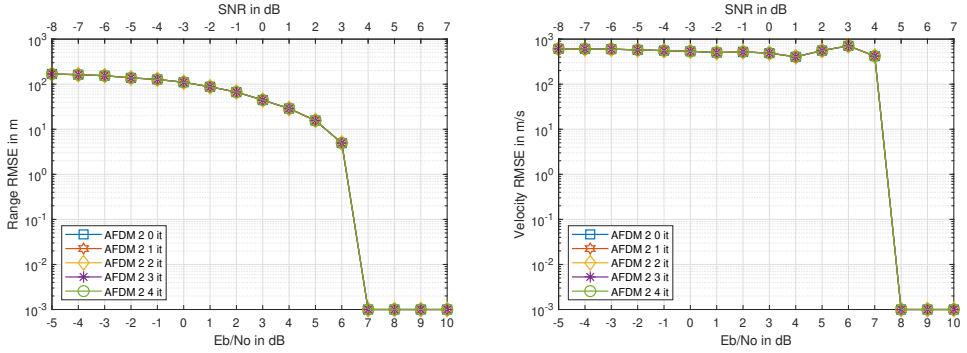

(A) Range (B) Velocity

FIGURE 5.12: RMSE of Set 3 RSC-coded BPSK AFDM 2 for $R_c = 0.5$ and It_{outer} = 0, 1, 2, 3, and 4 iterations for the $(1 - \text{BER})$ scoring method

The range and velocity RMSEs of Set 3 RSC-coded BPSK AFDM 2 for $R_c = 0.5$ and It_{outer} = 0, 1, 2, 3, and 4 iterations are shown in Figures 5.12 and 5.13, for the $(1 - \text{BER})$ and $-\log(\text{BER})$ scoring methods, respectively. Neither scoring improves the performance of the sensing method, despite the RMSE reaching the error floor at 7 and 8 dB $\text{E}_\text{b}/\text{N}_0$ for range and velocity, which corresponds to a BER of 10^{-5} or lower in Figure 5.6b. The AFDM 2 RMSE floor is reached at a higher $\text{E}_\text{b}/\text{N}_0$ than AFDM 1 as there is less power in the pilot symbol, due to the smaller matrix dimension of AFDM 2.

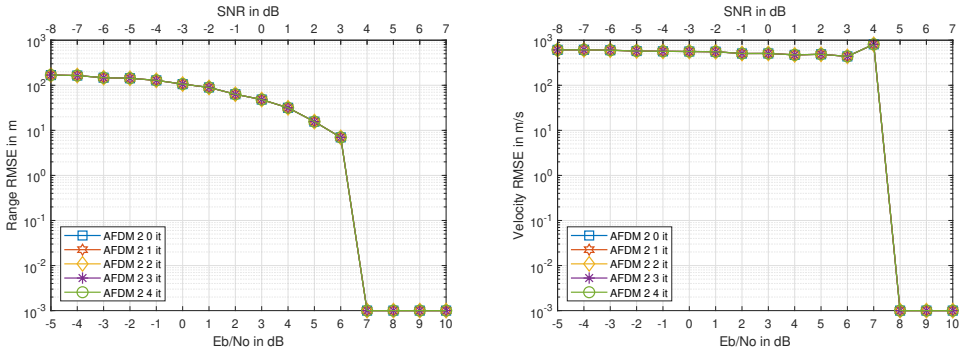

(A) Range (B) Velocity

FIGURE 5.13: RMSE of Set 3 RSC-coded BPSK AFDM 2 for $R_c = 0.5$ and $\mathrm{It}_{\mathrm{outer}} = 0$, 1, 2, 3, and 4 iterations for the $-\log(\mathrm{BER})$ scoring method

As the integer index resolutions of Set 3 AFDM 1 and 2 are quite poor ($\approx$ 312.5 m for AFDM 1 and 2, $\approx$ 58.4 m/s for AFDM 1, and $\approx$ 233.8 m/s for AFDM 2), an incorrect estimate leads to a large error, hence the weighting based on decoding has no significant impact on the performance.

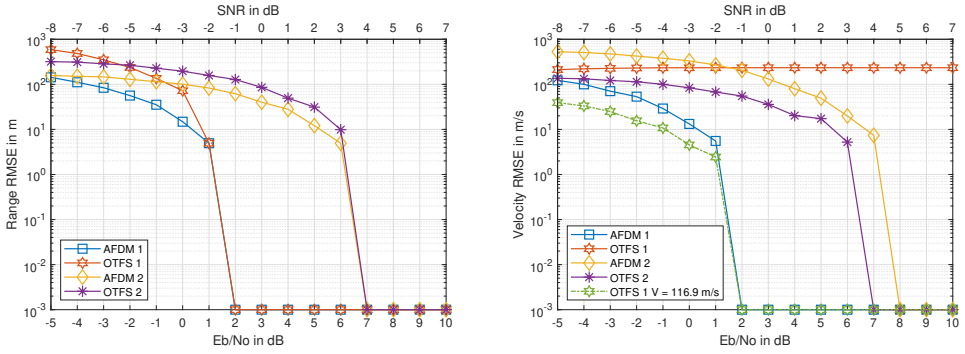

(A) Range (B) Range

FIGURE 5.14: RMSE of Set 3 RSC-coded BPSK AFDM 1 and 2 and OTFS 1 and 2 for $R_c = 0.5$

The range and velocity RMSEs of Set 3 RSC-coded BPSK AFDM 1 and 2 and OTFS 1 and 2 for $R_c = 0.5$ and no decoding are shown in Figure 5.14. Both AFDM 1 and OTFS 1 reach the range RMSE floor at the same $\mathrm{E_b/N_0}$. AFDM 2 and OTFS 2 reach the range RMSE error floor at the same $\mathrm{E_b/N_0}$, but AFDM 2 reaches the velocity RMSE floor at 8 dB $\mathrm{E_b/N_0}$, compared to the 7 dB for OTFS 2. However, further research work is required to identify whether the velocity estimation performance of AFDM 2 is consistently worse than that of OTFS 2 in diverse scenarios.

OTFS 1 maintains a high velocity RMSE for a target velocity of $\approx$ 233.8 m/s. This velocity is equivalent to a Doppler index of 4, but because OTFS 1 has $N = 4$ possible Doppler indices, the maximum Doppler index is 3. As AFDM is a single dimensional waveform, it does not impose individual limitations on delay and Doppler indices, but

rather on their combination. Hence, AFDM 1 can estimate this velocity, which demonstrates its enhanced flexibility relative to OTFS 1. The velocity RMSE performance of OTFS 1 is comparable to that of AFDM 1 when a lower target velocity is simulated, denoted as "OTFS 1 V = 116.9 m/s".

The RMSE at lower E_b/N_0 is different for AFDM and OTFS, which illustrates the effect of the difference in the number of dimensions between the two waveforms. For Set 3 OTFS 1, $M = 8$ and $N = 4$, hence there is a higher number of possible range estimates than velocity estimates, which leads to a larger range RMSE at lower E_b/N_0 values. By contrast, AFDM 1 only has a single dimension of $\ddot{N} = 32$, hence the range and velocity RMSEs are closer to each other at lower E_b/N_0 values. A similar relative RMSE trend is present for OTFS 2 and AFDM 2. In both cases, the RMSE at low E_b/N_0 values is excessive, hence this RMSE difference has no significant impact on the integer index estimation performance of these systems.

5.7 Conclusions

TABLE 5.7: E_b/N_0 in dB at which a BER of 10^{-4} is achieved for RSC-URC coding, $R_c = 0.9$, $It_{inner} = 2$, and $It_{outer} = 8$ iterations

Set index	AFDM 1	OTFS 1	AFDM 2	OTFS 2	OTFS 3	OFDM MMSE
Set 1	**6.6**	6.9	6.7	6.85	6.8	10.2
Set 2	**6.7**	6.8	7	7	7.2	10.8
Set 3	**6.8**	6.9	10.2	10	7	11.4
Set 4	10.2	**10**	11.4	N/A	**10**	N/A

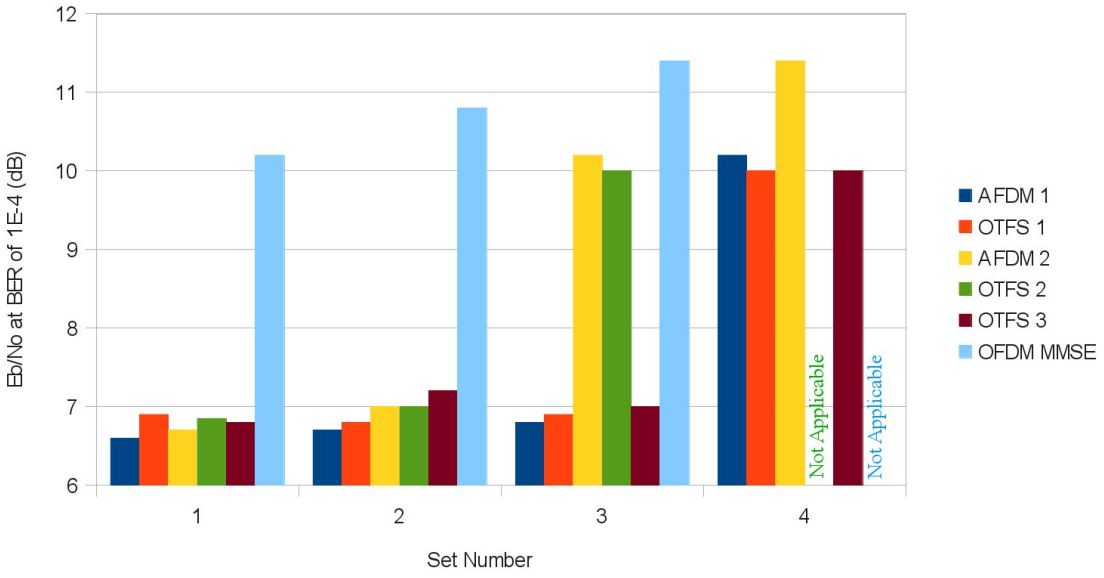

FIGURE 5.15: E_b/N_0 in dB at which a BER of 10^{-4} is achieved for RSC-URC coding, $R_c = 0.9$, $It_{inner} = 2$, and $It_{outer} = 8$ iterations

Iterative soft-MMSE equalisation in conjunction with both RSC and RSC-URC coding has been conceived for AFDM, and both the BER and EXIT chart performance have been compared to that of OFDM and different OTFS configurations. The results recorded for $R_c = 0.9$ and different variable Sets are summarised in Table 5.7 and Figure 5.15. The AFDM configurations are shown to exhibit a lower BER at high E_b/N_0 than their equivalent OTFS counterparts, at lower matrix dimension, at high coding rates, and at low iteration number. This is because AFDM possesses higher degrees of freedom than OTFS, since AFDM is a one-dimensional waveform, whereas OTFS is two-dimensional. When the number of iterations is increased, the BER performance of the AFDM configurations and their equivalent OTFS configurations are shown to be similar. At the communication receiver velocity considered (150 m/s), both AFDM and OTFS tend to outperform OFDM, for both coded and uncoded transmission. Given that the RSC BER performance fails to improve beyond two iterations, this solution is recommended for low-complexity transceivers. By contrast, if the extra complexity of the RSC-URC aided transceiver is affordable, an extra E_b/N_0 gain of 1.8 dB may be attained at a BER of 10^{-5} and a code rate of 0.5.

The sensing results show that AFDM has a comparable integer index estimation RMSE performance to that of OTFS, with a greater sensing flexibility. Scoring the estimates by decoding the reflected data does not impact the integer index estimation, likely due to the poor resolution of the systems considered. Further work is required to test whether the scoring methods may improve the performance of fractional index estimation. As shown in (5.13) and (5.14), the fractional Doppler index imposes a cumulative phase shift on the fading gain as the block index ξ is increased. A fractional index estimation method may utilise an estimated fading gain to curve fit the phase change over the received blocks, to determine the average phase change per block, and therefore the fractional Doppler index.

Chapter 6

Conclusions and Further Work

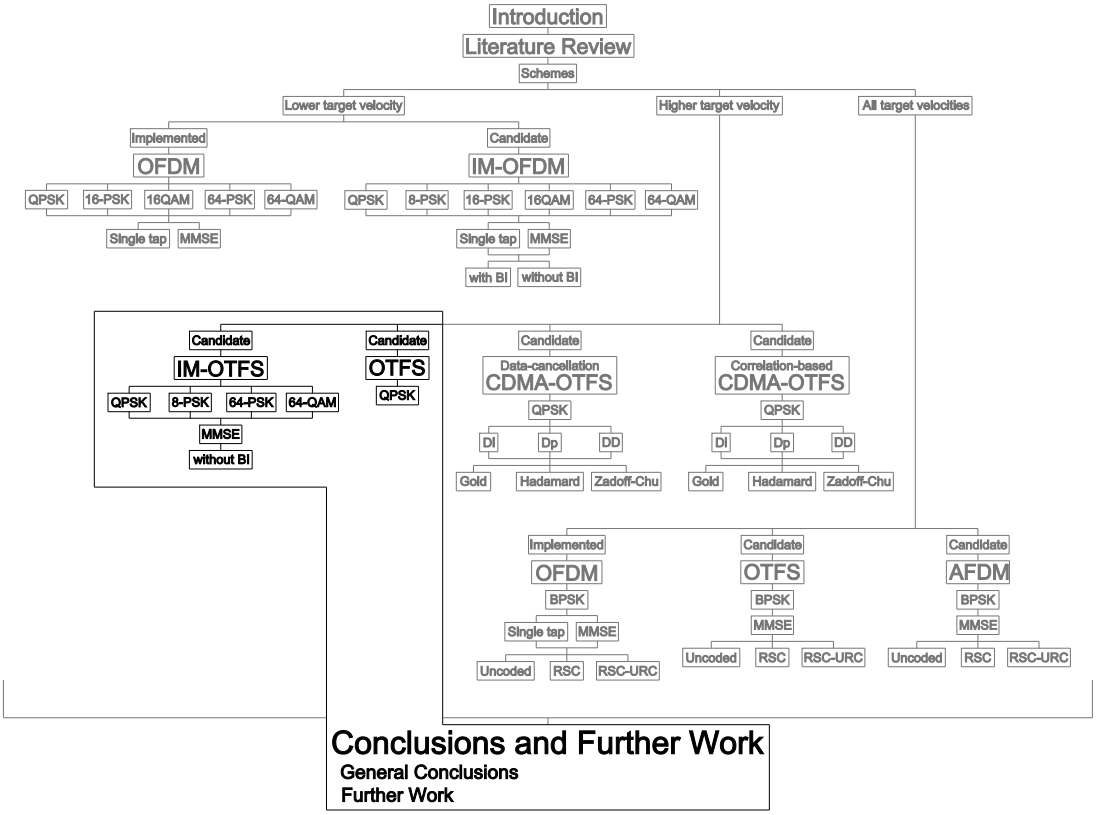

6.1 General Conclusions

The modern understanding of ISAC, using digital signal processing, dates back to the 1960s. The requirement for ISAC has become more apparent in recent years as the spectrum has become more congested due to the increase in wireless devices and the data they produce. The number of connected devices is expected to increase from 19

billion in 2019 to 30 billion in 2030 [12]. In addition, the capabilities of each device will continue to expand, which will in turn increase the volume of data transmitted and received by each device. A large proportion of these devices will also be required to sense the locations of other devices, and objects both animate and inanimate. This expanding demand has been recognised by the introduction of specific policies to promote this integration, and the applications for this technology are anticipated to be wide ranging [13], with many applications being critical for the maintenance of social and environmental standards. Conveniently, this has also become more viable due to improvements in technology, and similarities brought about by the convergence of the sensing and communication protocols.

The motivation of the work described in this Thesis is to investigate different communication waveforms, and characterise their performance when used for both communication and sensing. This then enables the identification of the relevant trade-offs between communication and sensing performance, which in turn aids in determining the conditions in which these different waveforms could be utilised. Since each application will have a different balance of requirements between communication and sensing, it is anticipated that no one single waveform will be optimal for all applications.

The waveform scheme that has been implemented for current 5G wireless communication is OFDM. The first component of the work was to quantify the communication and sensing performance of the existing implementation as a baseline, and then to consider the relative performance of IM-OFDM. FD IM reduces the TD PAPR of the OFDM signal, and increases the transmit power on the activated subcarriers through power redistribution. The communication performance of IM-OFDM has been previously characterised, but little published work has investigated its use for sensing. The sensing methods previously utilised function either by inserting a separate sensing signal, or by accepting a sensing performance equal to or lower than that of OFDM. A novel IM-OFDM ISAC solution was conceived, which outperforms OFDM ISAC by collecting multiple sensing observations. The delay caused by the collection of multiple observations has no impact on the sensing performance, as the error floors remain constant when the number of collected observations is varied. For four collected observations, the IM-OFDM(4,3) scheme is shown to outperform OFDM both in terms of sensing and communication.

A range of trade-offs was characterised in terms of the subcarrier grouping, communication throughput, and the number of sensing observation collected. If a modest sensing and communication performance improvement is deemed sufficient, the IM-OFDM(4,3) configuration may be recommended. If a higher sensing performance is desired at the cost of communication performance erosion, the IM-OFDM(2,1) or IM-OFDM(4,1) schemes may be employed, depending on the target velocity and the required throughput. It has also been shown that the IM-OFDM(4,1) scheme using PSK modulation has a better sensing performance than the other systems. As noted in the

complexity analysis, the demodulation complexity is proportional to the number of subcarriers in a group, with IM-OFDM(2,1) having the lowest demodulation complexity amongst the IM-OFDM systems. Increasing the interpolation factor leads to a similar improvement in sensing performance in all systems, albeit at the cost of increased complexity. Increasing the number of subcarriers and the number of symbol slots will also increase the sensing resolution, but would require a substantial system modification.

The OTFS waveform was chosen for investigation next as it is designed to be less affected by the Doppler shift induced by large velocities compared to OFDM. As sensing will inevitably involve the detection of moving objects, this robustness will be beneficial for ISAC in applications where relative velocities are high. There are many publications that investigate the communication performance of multi-user OTFS, but few consider their sensing capabilities. Hence, CDMA was employed to provide multi-user communication capabilities, whilst also allowing for monostatic sensing. CDMA was chosen due to its simplicity and its ability to reduce the variability in the transmit signal characteristics relative to OTFS, thereby aiding sensing. This is in contrast to the other multi-user methodologies, such as the newer SCMA multi-user method, which increases the variability in the transmit signal characteristics.

Three different configurations of CDMA-OTFS were introduced. The multi-user communication performance of Zadoff-Chu CDMA-OTFS is similar to that of single user OTFS at an equal throughput. When fewer users are present, the multi-user throughput is diminished, and Zadoff-Chu CDMA-OTFS has a lower BER than single user OTFS. The communication performance of Zadoff-Chu sequences is similar for all three CDMA-OTFS spreading configurations. Gold and Hadamard sequences do not consistently outperform single user OTFS communication. The three CDMA-OTFS spreading configurations outperform pure OTFS sensing for all the velocities considered. Hadamard sequences lead to a superior sensing performance for Dl-CDMA-OTFS at high velocities, but the three sequences have a similar performance at lower velocities. Gold sequences increase the sensing performance of Dp-CDMA-OTFS at high velocities, whereas Zadoff-Chu sequences lead to the similar sensing performance as pure OTFS at lower velocities. The sensing performance of DD-CDMA-OTFS is similar for all three sequence types at high velocities, but Gold sequences lead to an inferior sensing performance at low velocities. Following these results, Zadoff-Chu Dl-CDMA-OTFS and DD-CDMA-OTFS are the configurations that consistently outperform pure OTFS sensing, whilst maintaining a similar communication performance at the same throughput.

The added modulation complexity of CDMA-OTFS is similar to other OTFS multi-user methodologies, but the demodulation complexity of CDMA-OTFS is lower than that of some other OTFS multi-user methodologies. CDMA-OTFS sensing can also consistently outperform OTFS sensing whilst not requiring any additional complexity for

target parameter estimation. Hence, CDMA-OTFS is a computationally more attractive multi-user approach for OTFS ISAC than the alternatives in the literature.

A correlation-based method for CDMA-OTFS sensing was also implemented. In contrast to the data cancellation method, the correlation-based method leads to CDMA-OTFS sensing having an inferior performance compared to OTFS sensing. Having identified this shortcoming, further work on correlation-based CDMA-OTFS has been deferred to permit the prioritising of more promising schemes.

The next scheme investigated was iterative soft-MMSE and channel decoding aided AFDM. AFDM is a generalised form of OFDM, which can be tuned to exhibit similar characteristics to OTFS. These similarities to OTFS allow AFDM to mitigate the effects of large Doppler shifts, and to separate propagation paths by their associated delays and Doppler shifts. Hence, AFDM is an attractive alternative to OTFS, especially for ISAC. As AFDM is a novel waveform, there is a paucity of publications considering iterative equalisation and decoding methods. This turbo architecture allows for improved communication performance, and may be leveraged to improve the sensing capabilities of the system. Hence, a study of such an architecture for AFDM was performed, with comparisons to OFDM and multiple OTFS configurations. Multiple OTFS configurations were investigated as OTFS is a two dimensional waveform, whereas AFDM is a single dimension waveform, thus there was no consensus on the best OTFS and AFDM configurations to implement for a fair comparison.

Iterative soft-MMSE equalisation in conjunction with both RSC and RSC-URC coding has been utilised for AFDM, and both the BER and EXIT chart performance have been compared to that of OFDM and different OTFS configurations. The results recorded for $R_c = 0.9$ and different variable Sets are summarised in Table 5.7 and Figure 5.15. The AFDM configurations are shown to exhibit a lower BER at high E_b/N_0 than their equivalent OTFS counterparts, at lower matrix dimension, at high coding rates, and at low iteration number. This is because AFDM possesses higher degrees of freedom than OTFS, since AFDM is a one-dimensional waveform, whereas OTFS is two-dimensional. When the number of iterations is increased, the BER performance of the AFDM configurations and their equivalent OTFS configurations are shown to be similar. At the communication receiver velocity considered (150 m/s), both AFDM and OTFS tend to outperform OFDM, for both coded and uncoded transmission. Given that the RSC BER performance fails to improve beyond two iterations, this solution is recommended for low-complexity transceivers. By contrast, if the extra complexity of the RSC-URC aided transceiver is affordable, an extra E_b/N_0 gain of 1.8 dB may be attained at a BER of 10^{-5} and a code rate of 0.5.

The sensing results show that AFDM has a comparable integer index estimation RMSE performance to OTFS, with a greater sensing flexibility. Scoring the estimates by decoding the reflected data does not impact the integer index estimation, likely due to the

poor resolution of the simulated systems.

6.2 Further Work

The section introduces the further work that may be undertaken. Some preliminary results are shown for IM-OTFS communication in Section 6.2.1, and future directions for IM-OTFS ISAC are discussed. Future research ideas for the systems presented in Chapters 3-5 are proposed in Section 6.2.2. Finally, suggestions for experiments and experimental validations are presented in Section 6.2.3.

6.2.1 Index Modulation-OTFS

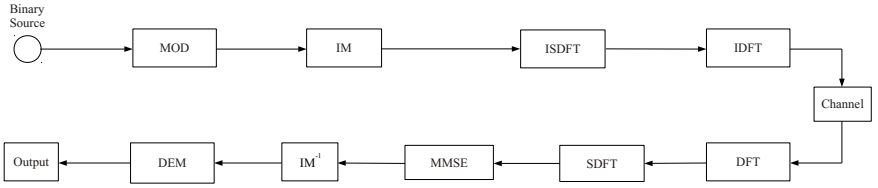

FIGURE 6.1: Block diagram of the IM-OTFS communication model

IM is applied to OTFS in the DD in a similar manner to IM-OFDM, but without block interleaving. As OTFS is a two-dimensional waveform, IM can be applied along either the delay or Doppler domains, or both. This is in contrast to the IM-OFDM system in Chapter 3, where IM is only applied along the subcarriers. A block diagram of the system is shown in Figure 6.1. The communication channel model from Chapter 4 is adopted, with similar MMSE equalisation, whilst the IM demodulation algorithms are those presented in Chapter 3.

TABLE 6.1: Communication simulation parameters for IM-OTFS

Variable	Value
Carrier frequency f_c	40 GHz
Subcarrier spacing Δf	120 kHz
Number of communication delay taps L_{com}	3
Number of communication propagation paths P_{com}	3
Rician K factor κ_{com}	0 dB
Number of subcarriers M	16
Number of symbols sent per frame N	16
Communication receiver velocity	≈ 168.634 m/s
Minimum number of bit errors	600
Maximum number of bits simulated	1×10^8

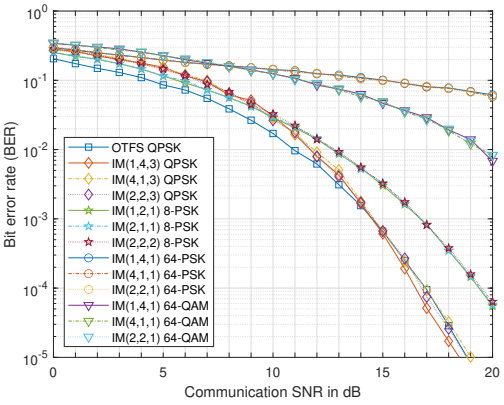

FIGURE 6.2: BER of QPSK IM-OTFS with $\frac{3}{4}$, $\frac{1}{2}$, and $\frac{1}{4}$ DD index activation.

The simulation parameter are shown in Table 6.2. IM(a, b, c) refers to IM with each DD group containing a delay indices, b Doppler indices, and activating c indices at a time in the group. As can be seen, IM does not offer any significant communication performance improvement over OTFS. Further work is required to improve the performance of IM-OTFS, for example through the addition of interleaving in the delay and/or Doppler domains.

In Chapter 3, the collection algorithm could be implemented with minimal complexity thanks to the subcarrier orthogonality of OFDM. As there is no orthogonality between DD elements in OTFS, it would be more difficult and complex to implement an equivalent collection algorithm for OTFS sensing, to harness the additional power on the activated subcarriers. Hence, a novel algorithm needs to be developed.

6.2.2 Further Development of the Presented Systems

Further work will include investigating how the communication performance of all the systems may be improved by the inclusion of error correction codes, as noted in Section 3.5.1.2. The use of error correction codes, such as LDPC in [216,221,224,230–237] and RSC in [238, 239] and Chapter 5, has been shown to improve the performance of OFDM, OTFS, and AFDM. A full analysis of the relative performance of the systems presented, considering the complexity of the coding and decoding methods, would quantify the trade-offs between the different coding methods.

The combination of channel coding and spreading [230], such as CDMA, and the related trade-offs, could also be investigated. The optimal channel coding to spreading ratio is likely to change depending on the conditions, and the waveform. The relative performance of channel coded CDMA-aided OFDM, AFDM, and OTFS should be investigated. The effect of varying the ratio of channel coding to spreading on the transmit signal characteristics for sensing is also of interest. As shown in Section 4.8, correlation-based CDMA-OTFS sensing does not outperform OTFS sensing, but this is

likely due to the multiplexing of many different spreading sequences masking the good correlation properties of the individual sequences. If fewer sequences are multiplexed, and channel coding is harnessed, the good autocorrelation properties may be exploited to improve the sensing performance utilising a correlation approach.

Future work could also be extended to the combination of channel coding and spreading for IM-OFDM. As IM only activates a subset of the subcarriers, which is dependent on the input data, this would render detection and demodulation more complex than standard channel coding and spreading. It would be of interest to observe whether channel coding would mitigate the communication benefits of IM-OFDM, or accentuate them. As the IM introduces an additional variable, a more in-depth analysis is required to find the optimal set of parameters for sensing and communication. IM for the spreading sequences could also be utilised [219]. This would compromise the potential multi-user capabilities introduced by spreading, but could improve the communication performance.

Decision-directed detection should also be investigated, utilising iterative exchange of information between the communication and sensing algorithms. This would allow the communication and sensing algorithms to share information with each other, in order to improve their respective performances. For example, embedded pilot symbols [113, 160] in conjunction with decision-direction methods can be utilised for bistatic sensing. The pilot is first used to estimate the channel/environment, then the communication data is estimated. The system iterates between these two operations, exchanging soft-information between them, until it converges to an output. Hence, the estimated data is also utilised to refine the channel/environment estimate, thereby possibly improving the achievable sensing resolution.

Additional work could consider SCMA-OTFS ISAC, as there is much interest in the employment of sparse codes for multi-user systems [199–202, 240–243]. The sparsity of these codes is expected to reduce the sensing performance. At full load, the transmit signal from a BS will not be sparse, due to the addition of the many different sparse code. The sparsity will reduce the sensing performance when the system is not at full load, and this variable sparsity will need to be mitigated. As the DD elements of OTFS are not orthogonal to each other, the collection algorithm from Chapter 3 cannot be directly applied. A more sophisticated method will therefore need to be developed.

Target tracking could also be considered. In practical systems, the targets and objects in the environment do not appear and disappear at random, but move gradually. Hence, the computational overhead can be reduced by introducing tracking methods, instead of repeating the target parameter estimation at small intervals. Kalman filters, and their extended versions, can be used for tracking [244–247], but they assume an estimation error centered around the true target parameter value. This is not the case for the systems presented in this thesis, where the estimators only output estimates from

a discrete set, based on the system resolution. Hence, other tracking methods may be more appropriate for these systems, such as track-after-scan [248, 249], or particle filters [250, 251].

Further work is required on AFDM sensing to test whether the scoring methods may improve the performance of fractional index estimation. The fractional Doppler index imposes a cumulative phase shift on the fading gain as the block index ξ is increased. A fractional index estimation method may utilise an estimated fading gain to curve fit the phase change over the received blocks, to determine the average phase change per block, and therefore the fractional Doppler index.

LEO satellite ISAC [114, 133, 134, 174–176, 208] is another promising research area that has gained traction, due to the proliferation of LEO satellite constellation in recent years. Satellite communication is likely to service the last populated areas where conventional coverage is too expensive to implement. As with many other areas, the combination of sensing and communication is also of interest, as satellites have a bird's eye view of the environment, which a ground vehicle could never replicate. This different point of view could supplement the environment information from other sources, as long as there is no obstruction between the satellite and the surface.

Harnessing RIS for ISAC is another popular research direction [41, 104, 129–132, 170–173, 179, 252, 253]. RIS has the capability to increase the coverage area of a system, and also to allow for NLoS sensing, which is of particular interest in dense environments, e.g. cities and inside large open buildings. The coverage is increased by the RIS acting as relays, which in more complex devices, can also correct distortions in the transmit signal. Due to the unpredictable nature of NLoS echoes, sophisticated algorithms need to be developed to leverage the increased sensing capability afforded by RIS. A direct connection between the RIS and the transmitter, e.g. a BS, can mitigate some of the complexity, by providing the BS with information pertaining to the RIS.

6.2.3 Experimental Validation

The theoretical studies presented and referenced above are routinely used to quantify comparative performance between different ISAC schemes. However, the usefulness of a given scheme can only be fully quantified in a commercial application by suitable experimentation in a realistic manner. Wireless communication networks had relied heavily on in-field testing both for development and validation, particularly in the early years, with specialised institutional facilities developed in countries hosting most of the early developers. This reliance has diminished in significance as improvements in simulation have combined with larger available reference data sets, with testing of new systems moving to community testbeds, but the widening gap between theoretical studies and experimental validation is considered a cause for concern ([254]).

Communication performance predicted by these studies have been shown to correlate reasonably well with experimental results, provided simulation assumptions are realistic. However, sensing is not so easily correlated, since sensing simulation assumptions are necessarily simplistic and limited compared to the complex and varied real environment. Thus, experimental studies are still routinely used for sensing validation, ranging from simple arrangements that seek to mimic the simulation assumptions, to more complex systems embedded in urban environments (e.g. [91, 114, 255, 256]. In a similar manner, the work described in Chapters 3 and 4 have shown improvements in sensing performance for the novel implementations, and these are thus valid candidates for inclusion in future testing programmes.

An example of a simplifying assumption is modeling targets as points. In practice, targets have a variety of sizes, shapes, and materials, which all affect how the reflected signal is distorted. For example, a large non-uniform object may introduce distortions that seem similar to delay and/or Doppler spreads. This may lead some sensing algorithms astray, especially those that aim to determine fractional delay and/or Doppler indices. Fractional index estimation methods rely on smaller variations in the signal, which in a theoretical model are exact, but are blurred in practice. Quantifying this sensitivity in real-world environment will be necessary before such methods can be widely implemented.

References

[1] H. Hawkins, C. Xu, L.-L. Yang, and L. Hanzo, "IM-OFDM ISAC Outperforms OFDM ISAC by Combining Multiple Sensing Observations," *IEEE Open Journal of Vehicular Technology*, vol. 5, pp. 312–329, 2024.

[2] ——, "CDMA/OTFS Sensing Outperforms Pure OTFS at the Same Communication Throughput," *IEEE Open Journal of Vehicular Technology*, vol. 6, pp. 502–519, 2025.

[3] ——, "Iterative Soft-MMSE detection aided AFDM and OTFS," *IEEE Open Journal of Vehicular Technology*, vol. 6, pp. 2944–2959, 2025.

[4] J. Henry, *Scientific Writings of Joseph Henry*, 1st ed. Washington: Smithsonian Institution, 1886.

[5] J. J. Fahie, *A History of Wireless Telegraphy 1838-1899*, 1st ed. Edinburgh and London: William Blackwood and Sons, 1899.

[6] H. G. Schantz, "On the origins of RF-based location," in *2011 IEEE Topical Conference on Wireless Sensors and Sensor Networks*, 2011, pp. 21–24.

[7] R. N. Vyvyan, *Wireless Over Thirty Years*, 1st ed. London: George Routledge and Sons Ltd., 1933.

[8] H. Hertz, "Ueber electrodynamische Wellen im Luftraume und deren Reflexion," *Annalen der Physik*, vol. 270, no. 8A, pp. 609–623, 1888. [Online]. Available: https://onlinelibrary.wiley.com/doi/abs/10.1002/andp.18882700802

[9] A. O. Bauer, "Christian Hülsmeyer and about the early days of radar inventions - a survey," 2005. [Online]. Available: http://aobauer.home.xs4all.nl/Huelspart1def.pdf

[10] P. Judkins, "Making Vision into Power: Power Struggles and Personality Clashes in British Radar, 1935–1941," *The International Journal for the History of Engineering & Technology*, vol. 82, pp. 93–124, 01 2012.

[11] D. Zhang, Y. Cui, X. Cao, N. Su, F. Liu, X. Jing, J. A. Zhang, J. Xu, C. Masouros, D. Niyato, and M. D. Renzo, "Integrated Sensing and Communications Over the Years: An Evolution Perspective," 2025. [Online]. Available: https://arxiv.org/abs/2504.06830

[12] X. Chen, Z. Feng, Z. Wei, P. Zhang, and X. Yuan, "Code-Division OFDM Joint Communication and Sensing System for 6G Machine-Type Communication," *IEEE Internet of Things Journal*, vol. 8, no. 15, pp. 12 093–12 105, 2021.

[13] C. Ciochina-Duchesne, "Integrated Sensing and Communications (ISAC); Use Cases and Deployment Scenarios," European Telecommunications Standards Institute, 650 Rte des Lucioles, Sophia Antipolis, 06921 France, Tech. Rep. ETSI GR ISC 001 V1.1.1 (2025-03), 03 2025.

[14] S. Pande, A. Yadav, and D. Dubey, "The Impact of Environmental Regulations on Agriculture," *International Journal of Advanced Research in Science, Communication and Technology (IJARSCT)*, vol. 3, pp. 2581–9429, 04 2023.

[15] R. Divanbeigi and F. Saliola, "Regulation and the Transformation of Agriculture," *Food and Agriculture Organization of the United Nations*, pp. 1–22, 2016/2018. [Online]. Available: http://www.fao.org/3/a-bp140e.pdf

[16] H. Bhandari and A. K. Mishra, "Impact of demographic transformation on future rice farming in Asia," *Outlook on Agriculture*, vol. 47, no. 2, pp. 125–132, 2018. [Online]. Available: https://doi.org/10.1177/0030727018769676

[17] Chen, Janyang, Begicheva, Svetlana, and Nazarov, Dmitry, "The role of big data in advancing precision agriculture and ensuring food security," *BIO Web of Conferences*, vol. 121, p. "02013", 2024. [Online]. Available: "https://doi.org/10.1051/bioconf/202412102013"

[18] M. Javaregowda and M. Indiramma, "Role of Big Data in Agriculture," *International Journal of Innovative Technology and Exploring Engineering*, vol. 9, pp. 3811–3821, 12 2019.

[19] S. A. Osinga, D. Paudel, S. A. Mouzakitis, and I. N. Athanasiadis, "Big data in agriculture: Between opportunity and solution," *Agricultural Systems*, vol. 195, p. 103298, 2022. [Online]. Available: https://www.sciencedirect.com/science/article/pii/S0308521X21002511

[20] Y. Nandini and A. Shrivastava, "A review on different types of autonomous agriculture machines," 01 2021.

[21] M. I. Mim, F. Sultana, and M. R. Hasan, "AI-Powered Autonomous Farming: The Future of Sustainable Agriculture," *European Journal of Theoretical and Applied Sciences*, vol. 3, no. 1, pp. 11–31, Jan. 2025. [Online]. Available: https://ejtas.com/index.php/journal/article/view/1381

[22] A. Yilmaz and S. Soysal, *The Necessity of Autonomous Systems in Agriculture*, 10 2021, pp. 301–322.

[23] Yilmaz, Abdurrahim and Yilmaz, Hilal and Soysal, Sipan and Çiftçi, Vahdettin, "Use of Nano Fertilizer in Agricultural Fields," in *International Conference on Global Practise of Multidisciplinary Scientific Studies-III*, 12 2022, pp. 284–294.

[24] P. Pramanik, P. Krishnan, A. Maity, N. Mridha, A. Mukherjee, and V. Rai, *Application of Nanotechnology in Agriculture*, 01 2020, pp. 317–348.

[25] D. Gackstetter, M. von Bloh, V. Hannus, S. T. Meyer, W. Weisser, C. Luksch, and S. Asseng, "Autonomous field management – An enabler of sustainable future in agriculture," *Agricultural Systems*, vol. 206, p. 103607, 2023. [Online]. Available: https://www.sciencedirect.com/science/article/pii/S0308521X23000124

[26] A. Salsbury, "Safeguarding Vessels by Radio," *Popular Science Monthly*, vol. 88, pp. 451–453, 1916. [Online]. Available: https://books.google.fr/books?id=giYDAAAAMBAJ&printsec=frontcover&hl=fr&source=gbs_ge_summary_r&cad=0#v=onepage&q&f=false

[27] A. O. Bauer, "Some Historical and Technical Aspects of Radio Navigation in Germany, Over the Period 1907 to 1945," 2004. [Online]. Available: https://www.cdvandt.org/Navigati.pdf

[28] H. G. Schantz, "On the Origins of RF-Based Location," in *2011 IEEE Topical Conference on Wireless Sensors and Sensor Networks*, 2011, pp. 21–24.

[29] D. S. Ilčev, "New Aspects of Progress in the Modernization of the Maritime Radio Direction Finders (RDF)," *Transactions on Maritime Science*, vol. 10, no. 1, p. 68–83, Apr. 2021. [Online]. Available: https://www.toms.com.hr/index.php/toms/article/view/359

[30] R. M. Mealey, "A Method for Calculating Error Probabilities in a Radar Communication System," *IEEE Transactions on Space Electronics and Telemetry*, vol. 9, no. 2, pp. 37–42, 1963.

[31] D. Ma, N. Shlezinger, T. Huang, Y. Liu, and Y. C. Eldar, "Joint Radar-Communication Strategies for Autonomous Vehicles: Combining Two Key Automotive Technologies," *IEEE Signal Processing Magazine*, vol. 37, no. 4, pp. 85–97, 2020.

[32] Z. Feng, Z. Fang, Z. Wei, X. Chen, Z. Quan, and D. Ji, "Joint radar and communication: A survey," *China Communications*, vol. 17, no. 1, pp. 1–27, 2020.

[33] Y. Cui, F. Liu, X. Jing, and J. Mu, "Integrating Sensing and Communications for Ubiquitous IoT: Applications, Trends, and Challenges," *IEEE Network*, vol. 35, no. 5, pp. 158–167, 2021.

[34] Y. Liu, G. Liao, J. Xu, Z. Yang, and Y. Zhang, "Adaptive OFDM Integrated Radar and Communications Waveform Design Based on Information Theory," *IEEE Communications Letters*, vol. 21, no. 10, pp. 2174–2177, 2017.

[35] G. V. Trunk, "Advanced Multifunction RF System (AMRFS) Preliminary Design Considerations," National Research Laboratory, Washington, DC, Tech. Rep. 5300-01-9914, 2001.

[36] C. Sturm and W. Wiesbeck, "Waveform Design and Signal Processing Aspects for Fusion of Wireless Communications and Radar Sensing," *Proceedings of the IEEE*, vol. 99, no. 7, pp. 1236–1259, 2011.

[37] V. Giannini, M. Goldenberg, A. Eshraghi, J. Maligeorgos, L. Lim, R. Lobo, D. Welland, C.-K. Chow, A. Dornbusch, T. Dupuis, S. Vaz, F. Rush, P. Bassett, H. Kim, M. Maher, O. Schmid, C. Davis, and M. Hegde, "9.2 A 192-Virtual-Receiver 77/79GHz GMSK Code-Domain MIMO Radar System-on-Chip," in *2019 IEEE International Solid-State Circuits Conference - (ISSCC)*, 2019, pp. 164–166.

[38] A. Hassanien, M. G. Amin, Y. D. Zhang, and F. Ahmad, "Signaling strategies for dual-function radar communications: an overview," *IEEE Aerospace and Electronic Systems Magazine*, vol. 31, no. 10, pp. 36–45, 2016.

[39] F. Liu, C. Masouros, A. P. Petropulu, H. Griffiths, and L. Hanzo, "Joint Radar and Communication Design: Applications, State-of-the-Art, and the Road Ahead," *IEEE Transactions on Communications*, vol. 68, no. 6, pp. 3834–3862, 2020.

[40] P. Kumari, J. Choi, N. González-Prelcic, and R. W. Heath, "IEEE 802.11ad-Based Radar: An Approach to Joint Vehicular Communication-Radar System," *IEEE Transactions on Vehicular Technology*, vol. 67, no. 4, pp. 3012–3027, 2018.

[41] X. Fang, W. Feng, Y. Chen, N. Ge, and Y. Zhang, "Joint Communication and Sensing Toward 6G: Models and Potential of Using MIMO," *IEEE Internet of Things Journal*, vol. 10, no. 5, pp. 4093–4116, 2023.

[42] L. Zheng and D. Tse, "Diversity and multiplexing: a fundamental tradeoff in multiple-antenna channels," *IEEE Transactions on Information Theory*, vol. 49, no. 5, pp. 1073–1096, 2003.

[43] J. Li and P. Stoica, "MIMO Radar with Colocated Antennas," *IEEE Signal Processing Magazine*, vol. 24, no. 5, pp. 106–114, 2007.

[44] L. Godara, "Application of Antenna Arrays to Mobile Communications Part II. Beam-Forming and Direction-of-Arrival Considerations," *Proceedings of the IEEE*, vol. 85, no. 8, pp. 1195–1245, 1997.

[45] M. Labib, V. Marojevic, A. F. Martone, J. H. Reed, and A. I. Zaghloui, "Coexistence between communications and radar systems: A survey," *URSI Radio Science Bulletin*, vol. 2017, no. 362, pp. 74–82, 2017.

[46] A. R. Chiriyath, B. Paul, and D. W. Bliss, "Radar-Communications Convergence: Coexistence, Cooperation, and Co-Design," *IEEE Transactions on Cognitive Communications and Networking*, vol. 3, no. 1, pp. 1–12, 2017.

[47] J. Han, B. Wang, W. Wang, Y. Zhang, and W. Xia, "Analysis for the BER of LTE system with the interference from radar," in *IET International Conference on Communication Technology and Application (ICCTA 2011)*, 2011, pp. 452–456.

[48] N. Nartasilpa, D. Tuninetti, N. Devroye, and D. Erricolo, "Let's share CommRad: Effect of radar interference on an uncoded data communication system," in *2016 IEEE Radar Conference (RadarConf)*, 2016, pp. 1–5.

[49] M. Ghorbanzadeh, E. Visotsky, P. Moorut, W. Yang, and C. Clancy, "Radar in-band and out-of-band interference into LTE macro and small cell uplinks in the 3.5 GHz band," in *2015 IEEE Wireless Communications and Networking Conference (WCNC)*, 2015, pp. 1829–1834.

[50] J. H. Reed, A. W. Clegg, A. V. Padaki, T. Yang, R. Nealy, C. Dietrich, C. R. Anderson, and D. M. Mearns, "On the Co-Existence of TD-LTE and Radar Over 3.5 GHz Band: An Experimental Study," *IEEE Wireless Communications Letters*, vol. 5, no. 4, pp. 368–371, 2016.

[51] M. R. Bell, N. Devroye, D. Erricolo, T. Koduri, S. Rao, and D. Tuninetti, "Results on spectrum sharing between a radar and a communications system," in *2014 International Conference on Electromagnetics in Advanced Applications (ICEAA)*, 2014, pp. 826–829.

[52] B. D. Cordill, S. A. Seguin, and L. Cohen, "Electromagnetic interference to radar receivers due to in-band OFDM communications systems," in *2013 IEEE International Symposium on Electromagnetic Compatibility*, 2013, pp. 72–75.

[53] W. Liu, J. Fang, H. Tan, B. Huang, and W. Wang, "Coexistence studies for TD-LTE with radar system in the band 2300–2400 MHz," in *2010 International Conference on Communications, Circuits and Systems (ICCCAS)*, 2010, pp. 49–53.

[54] A. Khawar, A. Abdel-Hadi, and C. Clancy, "A Mathematical Analysis of LTE Interference on the Performance of S-band Military Radar Systems," 04 2014.

[55] L. Zheng, M. Lops, X. Wang, E. Grossi, and J. Qian, "Joint design of co-existing communication system and pulsed radar," in *2017 IEEE 7th International Workshop on Computational Advances in Multi-Sensor Adaptive Processing (CAMSAP)*, 2017, pp. 1–5.

[56] A. R. Chiriyath, B. Paul, G. M. Jacyna, and D. W. Bliss, "Inner Bounds on Performance of Radar and Communications Co-Existence," *IEEE Transactions on Signal Processing*, vol. 64, no. 2, pp. 464–474, 2016.

[57] Y. Cui, V. Koivunen, and X. Jing, "Interference alignment based precoder-decoder design for radar-communication co-existence," in *2017 51st Asilomar Conference on Signals, Systems, and Computers*, 2017, pp. 1290–1295.

[58] L. Zheng, M. Lops, and X. Wang, "Adaptive Interference Removal for Uncoordinated Radar/Communication Coexistence," *IEEE Journal of Selected Topics in Signal Processing*, vol. 12, no. 1, pp. 45–60, 2018.

[59] F. Liu, C. Masouros, A. Li, H. Sun, and L. Hanzo, "MU-MIMO Communications With MIMO Radar: From Co-Existence to Joint Transmission," *IEEE Transactions on Wireless Communications*, vol. 17, no. 4, pp. 2755–2770, 2018.

[60] A. D. Harper, J. T. Reed, J. L. Odom, A. D. Lanterman, and X. Ma, "Performance of a Linear-Detector Joint Radar-Communication System in Doubly Selective Channels," *IEEE Transactions on Aerospace and Electronic Systems*, vol. 53, no. 2, pp. 703–715, 2017.

[61] Q. He, Z. Wang, J. Hu, and R. S. Blum, "Performance Gains From Cooperative MIMO Radar and MIMO Communication Systems," *IEEE Signal Processing Letters*, vol. 26, no. 1, pp. 194–198, 2019.

[62] A. Ahmed, Y. D. Zhang, and Y. Gu, "Dual-function radar-communications using QAM-based sidelobe modulation," *Digital Signal Processing*, vol. 82, pp. 166–174, 2018. [Online]. Available: https://www.sciencedirect.com/science/article/pii/S1051200418305487

[63] S. D. Blunt, M. R. Cook, and J. Stiles, "Embedding information into radar emissions via waveform implementation," in *2010 International Waveform Diversity and Design Conference*, 2010, pp. 000 195–000 199.

[64] J. Euzière, R. Guinvarc'h, M. Lesturgie, B. Uguen, and R. Gillard, "Dual function radar communication Time-modulated array," in *2014 International Radar Conference*, 2014, pp. 1–4.

[65] A. Hassanien, M. G. Amin, Y. D. Zhang, and F. Ahmad, "Dual-Function Radar-Communications: Information Embedding Using Sidelobe Control and Waveform Diversity," *IEEE Transactions on Signal Processing*, vol. 64, no. 8, pp. 2168–2181, 2016.

[66] ——, "Dual-function radar-communications using phase-rotational invariance," in *2015 23rd European Signal Processing Conference (EUSIPCO)*, 2015, pp. 1346–1350.

[67] ——, "A dual function radar-communications system using sidelobe control and waveform diversity," in *2015 IEEE Radar Conference (RadarCon)*, 2015, pp. 1260–1263.

[68] Z. Zhang, M. J. Nowak, M. Wicks, and Z. Wu, "Bio-inspired RF steganography via linear chirp radar signals," *IEEE Communications Magazine*, vol. 54, no. 6, pp. 82–86, 2016.

[69] W. Baxter, E. Aboutanios, and A. Hassanien, "Dual-Function MIMO Radar-Communications Via Frequency-Hopping Code Selection," in *2018 52nd Asilomar Conference on Signals, Systems, and Computers*, 2018, pp. 1126–1130.

[70] ——, "Joint Radar and Communications for Frequency-Hopped MIMO Systems," *IEEE Transactions on Signal Processing*, vol. 70, pp. 729–742, 2022.

[71] A. Hassanien, B. Himed, and B. D. Rigling, "A dual-function MIMO radar-communications system using frequency-hopping waveforms," in *2017 IEEE Radar Conference (RadarConf)*, 2017, pp. 1721–1725.

[72] I. P. Eedara, M. G. Amin, and G. A. Fabrizio, "Target Detection in Frequency Hopping MIMO Dual-Function Radar-Communication Systems," in *ICASSP 2021 - 2021 IEEE International Conference on Acoustics, Speech and Signal Processing (ICASSP)*, 2021, pp. 8458–8462.

[73] I. P. Eedara, M. G. Amin, and A. Hassanien, "Analysis of Communication Symbol Embedding in FH MIMO Radar Platforms," in *2019 IEEE Radar Conference (RadarConf)*, 2019, pp. 1–6.

[74] ——, "Controlling Clutter Modulation in Frequency Hopping MIMO Dual-Function Radar Communication Systems," in *2020 IEEE International Radar Conference (RADAR)*, 2020, pp. 466–471.

[75] J. A. Zhang, F. Liu, C. Masouros, R. W. Heath, Z. Feng, L. Zheng, and A. Petropulu, "An Overview of Signal Processing Techniques for Joint Communication and Radar Sensing," *IEEE Journal of Selected Topics in Signal Processing*, vol. 15, no. 6, pp. 1295–1315, 2021.

[76] Y. Zhang, Q. Li, L. Huang, K. Dai, and J. Song, "Waveform Design for Joint Radar-Communication with Nonideal Power Amplifier and Outband Interference," 03 2017, pp. 1–6.

[77] X. Shaojian, C. Bing, and Z. Ping, "Radar-Communication Integration Based on DSSS Techniques," in *2006 8th international Conference on Signal Processing*, vol. 4, 2006.

[78] Y. Xie, R. Tao, and T. Wang, "Method of Waveform Design for Radar and Communication Integrated System Based on CSS," in *2011 First International Conference on Instrumentation, Measurement, Computer, Communication and Control*, 2011, pp. 737–739.

[79] Y. L. Sit, C. Sturm, and T. Zwick, "Interference cancellation for dynamic range Improvement in an OFDM joint radar and communication system," in *2011 8th European Radar Conference*, 2011, pp. 333–336.

[80] ——, "One-stage selective interference cancellation for the OFDM joint radar-communication system," in *2012 The 7th German Microwave Conference*, 2012, pp. 1–4.

[81] Y. Zhang, Q. Li, L. Huang, and J. Song, "Waveform design for joint radar-communication system with multi-user based on MIMO radar," in *2017 IEEE Radar Conference (RadarConf)*, 2017, pp. 0415–0418.

[82] L. Pucci, E. Paolini, and A. Giorgetti, "System-Level Analysis of Joint Sensing and Communication Based on 5G New Radio," *IEEE Journal on Selected Areas in Communications*, vol. 40, no. 7, pp. 2043–2055, 2022.

[83] J. A. Zhang, X. Huang, Y. J. Guo, J. Yuan, and R. W. Heath, "Multibeam for Joint Communication and Radar Sensing Using Steerable Analog Antenna Arrays," *IEEE Transactions on Vehicular Technology*, vol. 68, no. 1, pp. 671–685, 2019.

[84] Y. Luo, J. A. Zhang, X. Huang, W. Ni, and J. Pan, "Optimization and Quantization of Multibeam Beamforming Vector for Joint Communication and Radio Sensing," *IEEE Transactions on Communications*, vol. 67, no. 9, pp. 6468–6482, 2019.

[85] ——, "Multibeam Optimization for Joint Communication and Radio Sensing Using Analog Antenna Arrays," *IEEE Transactions on Vehicular Technology*, vol. 69, no. 10, pp. 11 000–11 013, 2020.

[86] M. Temiz, E. Alsusa, and M. W. Baidas, "A Dual-Functional Massive MIMO OFDM Communication and Radar Transmitter Architecture," *IEEE Transactions on Vehicular Technology*, vol. 69, no. 12, pp. 14 974–14 988, 2020.

[87] ——, "Optimized Precoders for Massive MIMO OFDM Dual Radar-Communication Systems," *IEEE Transactions on Communications*, vol. 69, no. 7, pp. 4781–4794, 2021.

[88] ——, "A Dual-Function Massive MIMO Uplink OFDM Communication and Radar Architecture," *IEEE Transactions on Cognitive Communications and Networking*, vol. 8, no. 2, pp. 750–762, 2022.

[89] F. Dong, W. Wang, Z. Hu, and T. Hui, "Low-Complexity Beamformer Design for Joint Radar and Communications Systems," *IEEE Communications Letters*, vol. 25, no. 1, pp. 259–263, 2021.

[90] P. M. McCormick, S. D. Blunt, and J. G. Metcalf, "Simultaneous radar and communications emissions from a common aperture, Part I: Theory," in *2017 IEEE Radar Conference (RadarConf)*, 2017, pp. 1685–1690.

[91] P. M. McCormick, B. Ravenscroft, S. D. Blunt, A. J. Duly, and J. G. Metcalf, "Simultaneous radar and communication emissions from a common aperture, Part II: Experimentation," in *2017 IEEE Radar Conference (RadarConf)*, 2017, pp. 1697–1702.

[92] C. Qi, W. Ci, J. Zhang, and X. You, "Hybrid Beamforming for Millimeter Wave MIMO Integrated Sensing and Communications," *IEEE Communications Letters*, vol. 26, no. 5, pp. 1136–1140, 2022.

[93] B. K. Chalise, M. G. Amin, and B. Himed, "Performance Tradeoff in a Unified Passive Radar and Communications System," *IEEE Signal Processing Letters*, vol. 24, no. 9, pp. 1275–1279, 2017.

[94] C. Ding, J.-B. Wang, H. Zhang, M. Lin, and G. Y. Li, "Joint MIMO Precoding and Computation Resource Allocation for Dual-Function Radar and Communication Systems With Mobile Edge Computing," *IEEE Journal on Selected Areas in Communications*, vol. 40, no. 7, pp. 2085–2102, 2022.

[95] F. Liu, L. Zhou, C. Masouros, A. Li, W. Luo, and A. Petropulu, "Toward Dual-functional Radar-Communication Systems: Optimal Waveform Design," *IEEE Transactions on Signal Processing*, vol. 66, no. 16, pp. 4264–4279, 2018.

[96] F. Liu, C. Masouros, T. Ratnarajah, and A. Petropulu, "On Range Sidelobe Reduction for Dual-Functional Radar-Communication Waveforms," *IEEE Wireless Communications Letters*, vol. 9, no. 9, pp. 1572–1576, 2020.

[97] J. Johnston, L. Venturino, E. Grossi, M. Lops, and X. Wang, "MIMO OFDM Dual-Function Radar-Communication Under Error Rate and Beampattern Constraints," *IEEE Journal on Selected Areas in Communications*, vol. 40, no. 6, pp. 1951–1964, 2022.

[98] Z. Wang, Y. Liu, X. Mu, Z. Ding, and O. A. Dobre, "NOMA Empowered Integrated Sensing and Communication," *IEEE Communications Letters*, vol. 26, no. 3, pp. 677–681, 2022.

[99] A. Deligiannis, A. Daniyan, S. Lambotharan, and J. A. Chambers, "Secrecy Rate Optimizations for MIMO Communication Radar," *IEEE Transactions on Aerospace and Electronic Systems*, vol. 54, no. 5, pp. 2481–2492, 2018.

[100] N. Su, F. Liu, and C. Masouros, "Secure Radar-Communication Systems With Malicious Targets: Integrating Radar, Communications and Jamming Functionalities," *IEEE Transactions on Wireless Communications*, vol. 20, no. 1, pp. 83–95, 2021.

[101] T. W. Tedesso and R. Romero, "Code shift keying based joint radar and communications for EMCON applications," *Digital Signal Processing*, vol. 80,

pp. 48–56, 2018. [Online]. Available: https://www.sciencedirect.com/science/article/pii/S1051200418303233

[102] Y. Xiong, F. Liu, Y. Cui, W. Yuan, T. X. Han, and G. Caire, "On the Fundamental Tradeoff of Integrated Sensing and Communications Under Gaussian Channels," *IEEE Transactions on Information Theory*, vol. 69, no. 9, pp. 5723–5751, 2023.

[103] K. Meng, Q. Wu, S. Ma, W. Chen, and T. Q. S. Quek, "UAV Trajectory and Beamforming Optimization for Integrated Periodic Sensing and Communication," *IEEE Wireless Communications Letters*, vol. 11, no. 6, pp. 1211–1215, 2022.

[104] H. Peng, C. He, Z. Zhang, C. Han, and L. Wang, "Robust Secure Beamforming for Integrated Sensing and Communication Systems With the Active RIS," *IEEE Transactions on Vehicular Technology*, vol. 74, no. 3, pp. 5158–5163, 2025.

[105] S. Singh, A. Nakkeeran, P. Singh, E. Sharma, and J. Bapat, "Target Detection for OTFS-Aided Cell-Free MIMO ISAC System," *IEEE Transactions on Vehicular Technology*, vol. 74, no. 7, pp. 11 568–11 573, 2025.

[106] G. Mylonopoulos, L. Venturino, E. Grossi, S. Buzzi, and C. D'Elia, "Integrated Communication and RIS-Aided Track-Before-Detect Radar Sensing," *IEEE Open Journal of the Communications Society*, vol. 6, pp. 4519–4532, 2025.

[107] M. Hua, Q. Wu, W. Chen, A. Jamalipour, C. Wu, and O. A. Dobre, "Integrated Sensing and Communication: Joint Pilot and Transmission Design," *IEEE Transactions on Wireless Communications*, vol. 23, no. 11, pp. 16 017–16 032, 2024.

[108] X. Chen, Z. Feng, Z. Wei, F. Gao, and X. Yuan, "Performance of Joint Sensing-Communication Cooperative Sensing UAV Network," *IEEE Transactions on Vehicular Technology*, vol. 69, no. 12, pp. 15 545–15 556, 2020.

[109] D. Zhou, M. Yang, X. Wu, M. S. Greco, and F. Gini, "Signal-Level Fusion Detection for Moving Target in ISAC System With Uplink–Downlink Cooperation," *IEEE Communications Letters*, vol. 29, no. 9, pp. 2173–2177, 2025.

[110] M. Yin, M. Huang, R. Hu, and H. Xu, "Deep Learning-Assisted ISAC for UAV Detection in Multipath Environments With Micro-Doppler," *IEEE Wireless Communications Letters*, vol. 14, no. 9, pp. 2862–2866, 2025.

[111] A. R. Chiriyath and D. W. Bliss, "Joint radar-communications performance bounds: Data versus estimation information rates," in *MILCOM 2015 - 2015 IEEE Military Communications Conference*, 2015, pp. 1491–1496.

[112] F. Dong, F. Liu, S. Lu, and Y. Xiong, "Rethinking Estimation Rate for Wireless Sensing: A Rate-Distortion Perspective," *IEEE Transactions on Vehicular Technology*, vol. 72, no. 12, pp. 16 876–16 881, 2023.

[113] H. Zhang, T. Zhang, and Y. Shen, "Modulation Symbol Cancellation for OTFS-Based Joint Radar and Communication," in *2021 IEEE International Conference on Communications Workshops (ICC Workshops)*, 2021, pp. 1–6.

[114] Y. Xu, X. Chen, M. Ying, and Z. Zhang, "Integrated Communication and Remote Sensing in LEO Satellite Systems: Protocol, Architecture and Prototype," *IEEE Transactions on Wireless Communications*, pp. 1–1, 2025.

[115] K. Wu, J. A. Zhang, X. Huang, and Y. J. Guo, "OTFS-Based Joint Communication and Sensing for Future Industrial IoT," *IEEE Internet of Things Journal*, pp. 1–1, 2021.

[116] M. M. Şahin, I. E. Gurol, E. Arslan, E. Basar, and H. Arslan, "OFDM-IM for Joint Communication and Radar-Sensing: A Promising Waveform for Dual Functionality," *Frontiers in Communications and Networks*, vol. 2, p. 34, 2021. [Online]. Available: https://www.frontiersin.org/article/10.3389/frcmn.2021.715944

[117] Q. Wang, X. Chen, Q. Qi, M. Li, and W. Gerstacker, "Multiple-Satellite Cooperative Information Communication and Location Sensing in LEO Satellite Constellations," *IEEE Transactions on Wireless Communications*, vol. 24, no. 4, pp. 3346–3361, 2025.

[118] X. Liu, T. Huang, N. Shlezinger, Y. Liu, J. Zhou, and Y. C. Eldar, "Joint Transmit Beamforming for Multiuser MIMO Communications and MIMO Radar," *IEEE Transactions on Signal Processing*, vol. 68, pp. 3929–3944, 2020.

[119] Z. Ni, J. Andrew Zhang, K. Yang, X. Huang, and T. A. Tsiftsis, "Multi-Metric Waveform Optimization for Multiple-Input Single-Output Joint Communication and Radar Sensing," *IEEE Transactions on Communications*, pp. 1–1, 2021.

[120] Y. Luo, Y. L. Guan, Y. Ge, D. González G, and C. Yuen, "A Novel Angle-Delay-Doppler Estimation Scheme for AFDM-ISAC System in Mixed Near-Field and Far-Field Scenarios," *IEEE Internet of Things Journal*, vol. 12, no. 13, pp. 22 669–22 682, 2025.

[121] H. Bao, H. Zhuang, Z. Wang, and G. Pang, "Performance Trade-off between Communication and Sensing Based on AFDM Parameter Adjustment," in *2024 IEEE 35th International Symposium on Personal, Indoor and Mobile Radio Communications (PIMRC)*, 2024, pp. 1–6.

[122] L. Gaudio, M. Kobayashi, B. Bissinger, and G. Caire, "Performance Analysis of Joint Radar and Communication using OFDM and OTFS," in *2019 IEEE International Conference on Communications Workshops (ICC Workshops)*, 2019, pp. 1–6.

[123] L. Gaudio, M. Kobayashi, G. Caire, and G. Colavolpe, "On the Effectiveness of OTFS for Joint Radar Parameter Estimation and Communication," *IEEE Transactions on Wireless Communications*, vol. 19, no. 9, pp. 5951–5965, 2020.

[124] Y. Ni, Z. Wang, P. Yuan, and Q. Huang, "An AFDM-Based Integrated Sensing and Communications," in *2022 International Symposium on Wireless Communication Systems (ISWCS)*, 2022, pp. 1–6.

[125] A. Hassanien, M. Amin, Y. Zhang, and F. Ahmad, "Efficient sidelobe ASK based dual-function radar-communications," 05 2016, p. 98290K.

[126] A. Ahmed, Y. D. Zhang, and B. Himed, "Distributed Dual-Function Radar-Communication MIMO System with Optimized Resource Allocation," in *2019 IEEE Radar Conference (RadarConf)*, 2019, pp. 1–5.

[127] J. B. Sanson, D. Castanheira, A. Gameiro, and P. P. Monteiro, "Cooperative Method for Distributed Target Tracking for OFDM Radar With Fusion of Radar and Communication Information," *IEEE Sensors Journal*, vol. 21, no. 14, pp. 15 584–15 597, 2021.

[128] Z. Lyu, G. Zhu, and J. Xu, "Joint Maneuver and Beamforming Design for UAV-Enabled Integrated Sensing and Communication," *IEEE Transactions on Wireless Communications*, vol. 22, no. 4, pp. 2424–2440, 2023.

[129] X. Wang, Z. Fei, Z. Zheng, and J. Guo, "Joint Waveform Design and Passive Beamforming for RIS-Assisted Dual-Functional Radar-Communication System," *IEEE Transactions on Vehicular Technology*, vol. 70, no. 5, pp. 5131–5136, 2021.

[130] X. Wang, Z. Fei, J. Huang, and H. Yu, "Joint Waveform and Discrete Phase Shift Design for RIS-Assisted Integrated Sensing and Communication System Under Cramer-Rao Bound Constraint," *IEEE Transactions on Vehicular Technology*, vol. 71, no. 1, pp. 1004–1009, 2022.

[131] R. P. Sankar and S. P. Chepuri, "Beamforming in Hybrid RIS assisted Integrated Sensing and Communication Systems," in *2022 30th European Signal Processing Conference (EUSIPCO)*, 2022, pp. 1082–1086.

[132] K. V. Mishra, A. Chattopadhyay, S. S. Acharjee, and A. P. Petropulu, "Optm3sec: Optimizing Multicast Irs-Aided Multiantenna Dfrc Secrecy Channel With Multiple Eavesdroppers," in *ICASSP 2022 - 2022 IEEE International Conference on Acoustics, Speech and Signal Processing (ICASSP)*, 2022, pp. 9037–9041.

[133] X. Qiang, L. You, C. G. Tsinos, W. Wang, X. Gao, and B. Ottersten, "Joint Communications and Sensing for Hybrid Massive MIMO LEO Satellite Systems With Beam Squint," in *2022 IEEE International Conference on Communications Workshops (ICC Workshops)*, 2022, pp. 963–968.

[134] S. Aliaga, A. J. Alqaraghuli, and J. M. Jornet, "Joint Terahertz Communication and Atmospheric Sensing in Low Earth Orbit Satellite Networks: Physical Layer Design," in *2022 IEEE 23rd International Symposium on a World of Wireless, Mobile and Multimedia Networks (WoWMoM)*, 2022, pp. 457–463.

[135] K. Wu, J. A. Zhang, X. Huang, R. W. Heath, and Y. J. Guo, "Green Joint Communications and Sensing Employing Analog Multi-Beam Antenna Arrays," *IEEE Communications Magazine*, pp. 1–7, 2023.

[136] Y. Zeng, Y. Ma, and S. Sun, "Joint Radar-Communication: Low Complexity Algorithm and Self-Interference Cancellation," in *2018 IEEE Global Communications Conference (GLOBECOM)*, 2018, pp. 1–7.

[137] A. Hassanien, S. Vorobyov, and A. Khabbazibasmenj, "Transmit Radiation Pattern Invariance in MIMO Radar With Application to DOA Estimation," *IEEE Signal Processing Letters*, vol. 22, 09 2015.

[138] M. Arik and O. B. Akan, "Utilizing sidelobe ASK based joint radar-communication system under fading," in *MILCOM 2017 - 2017 IEEE Military Communications Conference (MILCOM)*, 2017, pp. 623–628.

[139] A. Hassanien, M. G. Amin, Y. D. Zhang, and F. Ahmad, "Phase-modulation based dual-function radar-communications," *IET Radar, Sonar & Navigation*, vol. 10, no. 8, pp. 1411–1421, 2016. [Online]. Available: https://ietresearch.onlinelibrary.wiley.com/doi/abs/10.1049/iet-rsn.2015.0484

[140] P. Kumari, S. A. Vorobyov, and R. W. Heath, "Adaptive Virtual Waveform Design for Millimeter-Wave Joint Communication–Radar," *IEEE Transactions on Signal Processing*, vol. 68, pp. 715–730, 2020.

[141] R. Hadani, S. Rakib, M. Tsatsanis, A. Monk, A. J. Goldsmith, A. F. Molisch, and R. Calderbank, "Orthogonal Time Frequency Space Modulation," in *2017 IEEE Wireless Communications and Networking Conference (WCNC)*, 2017, pp. 1–6.

[142] R. Hadani and A. Monk, "OTFS: A New Generation of Modulation Addressing the Challenges of 5G," 2018. [Online]. Available: https://arxiv.org/abs/1802.02623

[143] Z. Wei, W. Yuan, S. Li, J. Yuan, G. Bharatula, R. Hadani, and L. Hanzo, "Orthogonal Time-Frequency Space Modulation: A Promising Next-Generation Waveform," *IEEE Wireless Communications*, vol. 28, no. 4, pp. 136–144, 08 2021.

[144] P. Raviteja, K. T. Phan, Y. Hong, and E. Viterbo, "Orthogonal Time Frequency Space (OTFS) Modulation Based Radar System," in *2019 IEEE Radar Conference (RadarConf)*, 2019, pp. 1–6.

[145] K. Zhang, Z. Li, W. Yuan, Y. Cai, and F. Gao, "Radar sensing via OTFS signaling," *China Communications*, vol. 20, no. 9, pp. 34–45, 2023.

[146] J. Zhang, L. Cai, and H. Liu, "Integrated Sensing and Communication via Orthogonal Time Frequency Space Signaling with Hybrid Message Passing Detection and Fractional Parameter Estimation," *Sensors*, vol. 23, no. 24, 2023. [Online]. Available: https://www.mdpi.com/1424-8220/23/24/9874

[147] Z. Tang, Z. Jiang, W. Pan, and L. Zeng, "The Estimation Method of Sensing Parameters Based on OTFS," *IEEE Access*, vol. 11, pp. 66 035–66 049, 2023.

[148] S. P. Muppaneni, S. R. Mattu, and A. Chockalingam, "Channel and Radar Parameter Estimation With Fractional Delay-Doppler Using OTFS," *IEEE Communications Letters*, vol. 27, no. 5, pp. 1392–1396, 2023.

[149] A. Bemani, N. Ksairi, and M. Kountouris, "AFDM: A Full Diversity Next Generation Waveform for High Mobility Communications," in *2021 IEEE International Conference on Communications Workshops (ICC Workshops)*, 2021, pp. 1–6.

[150] T. Erseghe, N. Laurenti, and V. Cellini, "A multicarrier architecture based upon the affine Fourier transform," *IEEE Transactions on Communications*, vol. 53, no. 5, pp. 853–862, 2005.

[151] X. Ouyang and J. Zhao, "Orthogonal Chirp Division Multiplexing," *IEEE Transactions on Communications*, vol. 64, no. 9, pp. 3946–3957, 2016.

[152] M. S. Omar and X. Ma, "Performance Analysis of OCDM for Wireless Communications," *IEEE Transactions on Wireless Communications*, vol. 20, no. 7, pp. 4032–4043, 2021.

[153] H. S. Rou, G. T. F. de Abreu, J. Choi, D. González G., M. Kountouris, Y. L. Guan, and O. Gonsa, "From Orthogonal Time–Frequency Space to Affine Frequency-Division Multiplexing: A comparative study of next-generation waveforms for integrated sensing and communications in doubly dispersive channels," *IEEE Signal Processing Magazine*, vol. 41, no. 5, pp. 71–86, 2024.

[154] A. Bemani, N. Ksairi, and M. Kountouris, "Integrated Sensing and Communications With Affine Frequency Division Multiplexing," *IEEE Wireless Communications Letters*, vol. 13, no. 5, pp. 1255–1259, 2024.

[155] A. Bemani, G. Cuozzo, N. Ksairi, and M. Kountouris, "Affine Frequency Division Multiplexing for Next-Generation Wireless Networks," in *2021 17th International Symposium on Wireless Communication Systems (ISWCS)*, 2021, pp. 1–6.

[156] A. Bemani, N. Ksairi, and M. Kountouris, "Affine Frequency Division Multiplexing for Next Generation Wireless Communications," *IEEE Transactions on Wireless Communications*, vol. 22, no. 11, pp. 8214–8229, 2023.

[157] J. Zhu, Y. Tang, F. Liu, X. Zhang, H. Yin, and Y. Zhou, "AFDM-Based Bistatic Integrated Sensing and Communication in Static Scatterer Environments," *IEEE Wireless Communications Letters*, vol. 13, no. 8, pp. 2245–2249, 2024.

[158] K. R. R. Ranasinghe, H. Seok Rou, G. Thadeu Freitas de Abreu, T. Takahashi, and K. Ito, "Joint Channel, Data, and Radar Parameter Estimation for AFDM Systems in Doubly-Dispersive Channels," *IEEE Transactions on Wireless Communications*, vol. 24, no. 2, pp. 1602–1619, 2025.

[159] F. Xiao, Z. Li, and D. Slock, "Multipath Component Power Delay Profile Based Joint Range and Doppler Estimation for AFDM-ISAC Systems," 2025. [Online]. Available: https://arxiv.org/abs/2503.10833

[160] F. Zhang, Z. Wang, T. Mao, T. Jiao, Y. Zhuo, M. Wen, W. Xiang, S. Chen, and G. K. Karagiannidis, "AFDM-Enabled Integrated Sensing and Communication: Theoretical Framework and Pilot Design," 2025. [Online]. Available: https://arxiv.org/abs/2502.14203

[161] K. Zheng, M. Wen, T. Mao, L. Xiao, and Z. Wang, "Channel Estimation for AFDM With Superimposed Pilots," *IEEE Transactions on Vehicular Technology*, vol. 74, no. 2, pp. 3389–3394, 2025.

[162] W. Benzine, A. Bemani, N. Ksairi, and D. Slock, "Affine Frequency Division Multiplexing for Compressed Sensing of Time-Varying Channels," in *2024 IEEE 25th International Workshop on Signal Processing Advances in Wireless Communications (SPAWC)*, 2024, pp. 916–920.

[163] I. Roth, M. Kliesch, A. Flinth, G. Wunder, and J. Eisert, "Reliable Recovery of Hierarchically Sparse Signals for Gaussian and Kronecker Product Measurements," *IEEE Transactions on Signal Processing*, vol. 68, pp. 4002–4016, 2020.

[164] G. Huang, Y. Ding, S. Ouyang, and V. Fusco, "Index modulation for OFDM RadCom systems," *The Journal of Engineering*, vol. 2021, no. 2, pp. 61–72, 2021. [Online]. Available: https://ietresearch.onlinelibrary.wiley.com/doi/abs/10.1049/tje2.12003

[165] A. Şahin, S. S. M. Hoque, and C.-Y. Chen, "Index Modulation With Circularly-Shifted Chirps for Dual-Function Radar and Communications," *IEEE Transactions on Wireless Communications*, vol. 21, no. 5, pp. 2938–2952, 2022.

[166] T. Huang, N. Shlezinger, X. Xu, Y. Liu, and Y. C. Eldar, "MAJoRCom: A Dual-Function Radar Communication System Using Index Modulation," *IEEE Transactions on Signal Processing*, vol. 68, pp. 3423–3438, 2020.

[167] T. Huang, N. Shlezinger, X. Xu, D. Ma, Y. Liu, and Y. C. Eldar, "Multi-Carrier Agile Phased Array Radar," *IEEE Transactions on Signal Processing*, vol. 68, pp. 5706–5721, 2020.

[168] M. Li and W.-Q. Wang, "Joint Radar-Communication System Design Based on FDA-MIMO via Frequency Index Modulation," *IEEE Access*, vol. 11, pp. 67 722–67 736, 2023.

[169] X. Mu, Y. Liu, L. Guo, J. Lin, and L. Hanzo, "NOMA-Aided Joint Radar and Multicast-Unicast Communication Systems," *IEEE Journal on Selected Areas in Communications*, vol. 40, no. 6, pp. 1978–1992, 2022.

[170] A. Magbool, V. Kumar, A. Bazzi, M. F. Flanagan, and M. Chafii, "Multi-Functional RIS for a Multi-Functional System: Integrating Sensing, Communication, and Wireless Power Transfer," *IEEE Network*, vol. 39, no. 1, pp. 71–79, 2025.

[171] T. Esmaeilbeig, K. V. Mishra, and M. Soltanalian, "Beyond Diagonal RIS: Key to Next-Generation Integrated Sensing and Communications?" *IEEE Signal Processing Letters*, vol. 32, pp. 216–220, 2025.

[172] A. Hakimi, S. Zargari, and C. Tellambura, "Integrated Sensing and Communication With Symbiotic Radio and RIS-Assisted Backscatter," *IEEE Wireless Communications Letters*, vol. 14, no. 1, pp. 38–42, 2025.

[173] C. Yu, C. Feng, W. Xie, P. Zhu, X. Peng, and L. Yang, "RIS-NOMA Assisted Covert Transmission for Integrated Sensing and Communication With Statistical CSI," *IEEE Wireless Communications Letters*, vol. 14, no. 1, pp. 13–17, 2025.

[174] M. Hui, S. Zhai, D. Wang, T. Hui, W. Wang, P. Du, and F. Gong, "A Review of LEO-Satellite Communication Payloads for Integrated Communication, Navigation, and Remote Sensing: Opportunities, Challenges, Future Directions," *IEEE Internet of Things Journal*, vol. 12, no. 12, pp. 18 954–18 992, 2025.

[175] X. Lv, R. Liu, R. Hou, Q. Liu, Q. Zhu, Y. Zang, and J. S. Thompson, "Enhanced Sensing in 6G NTN: Imaging with LEO Satellite and UAV Communication Network," *IEEE Sensors Journal*, pp. 1–1, 2025.

[176] M. Sheng, C. Guo, and L. Huang, "Integrated Communication, Navigation, and Remote Sensing in Leo Networks with Vehicular Applications," *IEEE Wireless Communications*, vol. 32, no. 3, pp. 140–147, 2025.

[177] H. Lin and J. Yuan, "Orthogonal Delay-Doppler Division Multiplexing Modulation," *IEEE Transactions on Wireless Communications*, vol. 21, no. 12, pp. 11 024–11 037, 2022.

[178] H. Xv, Y. Sun, and M. Peng, "Predictive Beamforming for Joint Radar and Communication Transmission in LEO Satellite Aeronautical Systems," *IEEE Transactions on Vehicular Technology*, vol. 74, no. 8, pp. 12 206–12 221, 2025.

[179] C. Xu, L. Xiang, J. An, C. Dong, S. Sugiura, R. G. Maunder, L.-L. Yang, and L. Hanzo, "OTFS-Aided RIS-Assisted SAGIN Systems Outperform Their OFDM

Counterparts in Doubly Selective High-Doppler Scenarios," *IEEE Internet of Things Journal*, vol. 10, no. 1, pp. 682–703, 2023.

[180] C. Xu, Y. Xiong, N. Ishikawa, R. Rajashekar, S. Sugiura, Z. Wang, S.-X. Ng, L.-L. Yang, and L. Hanzo, "Space-, Time- and Frequency-Domain Index Modulation for Next-Generation Wireless: A Unified Single-/Multi-Carrier and Single-/Multi-RF MIMO Framework," *IEEE Transactions on Wireless Communications*, vol. 20, no. 6, pp. 3847–3864, 2021.

[181] G. Golub and C. Loan, *Matrix Computations*, 3rd ed. Baltimore and London: The Johns Hopkins University Press, 1996.

[182] B. Gaede, A. Bereyhi, S. Asaad, and R. R. Mueller, "A Fair Comparison Between Spatial Modulation and Antenna Selection in Massive MIMO Systems," in *WSA 2019; 23rd International ITG Workshop on Smart Antennas*, 2019, pp. 1–6.

[183] X. Li, Y. Cui, J. A. Zhang, F. Liu, D. Zhang, and L. Hanzo, "Integrated Human Activity Sensing and Communications," *IEEE Communications Magazine*, vol. 61, no. 5, pp. 90–96, 2023.

[184] S. Lu, F. Liu, Y. Li, K. Zhang, H. Huang, J. Zou, X. Li, Y. Dong, F. Dong, J. Zhu, Y. Xiong, W. Yuan, Y. Cui, and L. Hanzo, "Integrated Sensing and Communications: Recent Advances and Ten Open Challenges," *IEEE Internet of Things Journal*, vol. 11, no. 11, pp. 19 094–19 120, 2024.

[185] T. Thaj, E. Viterbo, and Y. Hong, "Orthogonal Time Sequency Multiplexing Modulation: Analysis and Low-Complexity Receiver Design," *IEEE Transactions on Wireless Communications*, vol. 20, no. 12, pp. 7842–7855, 2021.

[186] S. G. Neelam and P. R. Sahu, "Iterative Channel Estimation and Data Detection of OTSM With Superimposed Pilot Scheme and PAPR Analysis," *IEEE Communications Letters*, vol. 27, no. 8, pp. 2147–2151, 2023.

[187] Z. Sui, S. Yan, H. Zhang, S. Sun, Y. Zeng, L.-L. Yang, and L. Hanzo, "Performance Analysis and Approximate Message Passing Detection of Orthogonal Time Sequency Multiplexing Modulation," *IEEE Transactions on Wireless Communications*, vol. 23, no. 3, pp. 1913–1928, 2024.

[188] A. Doosti-Aref, E. Basar, and H. Arslan, "Sequency Index Modulation: A Novel Index Modulation for Delay-Sequency Domain Waveforms," *IEEE Wireless Communications Letters*, vol. 12, no. 11, pp. 1911–1915, 2023.

[189] A. Doosti-Aref, C. Masouros, E. Basar, and H. Arslan, "Pairwise Sequency Index Modulation With OTSM for Green and Robust Single-Carrier Communications," *IEEE Wireless Communications Letters*, vol. 13, no. 4, pp. 1083–1087, 2024.

[190] S. G. Neelam and P. R. Sahu, "Estimation and Compensation of IQ Imbalance for OTSM Systems," *IEEE Wireless Communications Letters*, vol. 11, no. 9, pp. 1885–1889, 2022.

[191] ——, "Joint Estimation and Compensation of CFO, IQ Imbalance and Channel Parameters for Zero Padded OTSM Systems," *IEEE Wireless Communications Letters*, vol. 12, no. 11, pp. 1871–1875, 2023.

[192] ——, "Joint Compensation of TX/RX IQ Imbalance and Channel Parameters for OTSM Systems," *IEEE Communications Letters*, vol. 27, no. 3, pp. 976–980, 2023.

[193] A. Singh, S. Sharma, M. Sharma, and K. Deka, "Low Complexity Deep-Decoder for OTSM With Hardware Impairments," *IEEE Communications Letters*, vol. 27, no. 12, pp. 3240–3244, 2023.

[194] B. V. S. Reddy, C. Velampalli, and S. S. Das, "Performance Analysis of Multi-User OTFS, OTSM, and Single Carrier in Uplink," *IEEE Transactions on Communications*, vol. 72, no. 3, pp. 1428–1443, 2024.

[195] N. V. Kalpage, P. Priya, and Y. Hong, "DCT-Based OTFS With Reduced PAPR," *IEEE Communications Letters*, vol. 28, no. 1, pp. 158–162, 2024.

[196] G. D. Surabhi, R. M. Augustine, and A. Chockalingam, "Multiple Access in the Delay-Doppler Domain using OTFS modulation," 2019. [Online]. Available: https://arxiv.org/abs/1902.03415

[197] V. Khammammetti and S. K. Mohammed, "OTFS-Based Multiple-Access in High Doppler and Delay Spread Wireless Channels," *IEEE Wireless Communications Letters*, vol. 8, no. 2, pp. 528–531, 2019.

[198] Y. Ge, Q. Deng, P. C. Ching, and Z. Ding, "OTFS Signaling for Uplink NOMA of Heterogeneous Mobility Users," *IEEE Transactions on Communications*, vol. 69, no. 5, pp. 3147–3161, 2021.

[199] A. Thomas, K. Deka, P. Raviteja, and S. Sharma, "Convolutional Sparse Coding Based Channel Estimation for OTFS-SCMA in Uplink," *IEEE Transactions on Communications*, vol. 70, no. 8, pp. 5241–5257, 2022.

[200] H. Wen, W. Yuan, and S. Li, "Downlink OTFS Non-Orthogonal Multiple Access Receiver Design based on Cross-Domain Detection," in *2022 IEEE International Conference on Communications Workshops (ICC Workshops)*, 2022, pp. 928–933.

[201] H. Wen, W. Yuan, Z. Liu, and S. Li, "OTFS-SCMA: A Downlink NOMA Scheme for Massive Connectivity in High Mobility Channels," *IEEE Transactions on Wireless Communications*, vol. 22, no. 9, pp. 5770–5784, 2023.

[202] K. Deka, A. Thomas, and S. Sharma, "OTFS-SCMA: A Code-Domain NOMA Approach for Orthogonal Time Frequency Space Modulation," *IEEE Transactions on Communications*, vol. 69, no. 8, pp. 5043–5058, 2021.

[203] J. Sun, Z. Wang, and Q. Huang, "An Orthogonal Time Frequency Space Direct Sequence Modulation Scheme," in *2021 IEEE International Conference on Communications Workshops (ICC Workshops)*, 2021, pp. 1–6.

[204] Y. Cao, Z. Qiu, and H. Long, "A Sequence Spread Modulation Scheme Based on Orthogonal Time Frequency Space," in *2023 IEEE 97th Vehicular Technology Conference (VTC2023-Spring)*, 2023, pp. 1–5.

[205] Y. Ma, G. Ma, N. Wang, Z. Zhong, and B. Ai, "OTFS-TSMA for Massive Internet of Things in High-Speed Railway," *IEEE Transactions on Wireless Communications*, vol. 21, no. 1, pp. 519–531, 2022.

[206] J. Shi, X. Hu, Z. Tie, X. Chen, W. Liang, and Z. Li, "Reliability performance analysis for OTFS modulation based integrated sensing and communication," *Digital Signal Processing*, vol. 144, p. 104280, 2024. [Online]. Available: https://www.sciencedirect.com/science/article/pii/S1051200423003755

[207] Q. Li, J. Li, M. Wen, X. Dang, H. Arslan, and N. Al-Dhahir, "Affine Frequency Division Multiplexing for 6G Networks: Fundamentals, Opportunities, and Challenges," *IEEE Network*, pp. 1–1, 2025.

[208] Y. Wang, Y. He, L. Zhao, and Y. Jiang, "AFDM Based Preamble Sequence Transmission for 6G Mobile Satellite Communication Systems," *IEEE Transactions on Wireless Communications*, pp. 1–1, 2025.

[209] H. S. Rou and G. T. F. de Abreu, "Chirp-Permuted AFDM for Quantum-Resilient Physical-Layer Secure Communications," *IEEE Wireless Communications Letters*, pp. 1–1, 2025.

[210] Y. I. Tek and E. Basar, "A Novel and Secure AFDM System for High Mobility Environments," *IEEE Transactions on Vehicular Technology*, pp. 1–6, 2025.

[211] V. Savaux, "Special Cases of DFT-Based Modulation and Demodulation for Affine Frequency Division Multiplexing," *IEEE Transactions on Communications*, vol. 72, no. 12, pp. 7627–7638, 2024.

[212] H. Yin, X. Wei, Y. Tang, and K. Yang, "Diagonally Reconstructed Channel Estimation for MIMO-AFDM With Inter-Doppler Interference in Doubly Selective Channels," *IEEE Transactions on Wireless Communications*, vol. 23, no. 10, pp. 14 066–14 079, 2024.

[213] H. Xia, A. Zhang, D. Guo, D. Tian, and S. Wang, "A Single-Pilot-Aided Channel Estimation Scheme Based on Interference Position Indices for AFDM in Delay-Doppler Channels," *IEEE Wireless Communications Letters*, pp. 1–1, 2025.

[214] H. Yuan, Y. Xu, X. Guo, Y. Ge, T. Ma, H. Li, D. He, and W. Zhang, "PAPR Reduction With Pre-Chirp Selection for Affine Frequency Division Multiplexing," *IEEE Wireless Communications Letters*, vol. 14, no. 3, pp. 736–740, 2025.

[215] V. M. Reddy and H. Bitra, "Papr in AFDM: Upper Bound and Reduction with Normalized mu-Law Companding," *IEEE Access*, pp. 1–1, 2025.

[216] J. Zhu, Q. Luo, G. Chen, P. Xiao, and L. Xiao, "Design and Performance Analysis of Index Modulation Empowered AFDM System," *IEEE Wireless Communications Letters*, vol. 13, no. 3, pp. 686–690, 2024.

[217] Y. Tao, M. Wen, Y. Ge, J. Li, E. Basar, and N. Al-Dhahir, "Affine Frequency Division Multiplexing With Index Modulation: Full Diversity Condition, Performance Analysis, and Low-Complexity Detection," *IEEE Journal on Selected Areas in Communications*, vol. 43, no. 4, pp. 1041–1055, 2025.

[218] G. Liu, T. Mao, Z. Xiao, M. Wen, R. Liu, J. Zhao, E. Basar, Z. Wang, and S. Chen, "Pre-Chirp-Domain Index Modulation for Full-Diversity Affine Frequency Division Multiplexing towards 6G," *IEEE Transactions on Wireless Communications*, pp. 1–1, 2025.

[219] M. Qian, F. Ji, Y. Ge, M. Wen, and Y. L. Guan, "Index Modulated Affine Frequency Division Multiplexing With Spread Spectrum," 2025. [Online]. Available: https://arxiv.org/abs/2505.09394

[220] X. Wang, L. Xiao, Q. Luo, J. Zhou, M. Wen, and T. Jiang, "Low-complexity Vector-by-Vector Detector for AFDM-IM Systems by Reconstructing Sparse Channel Matrix," *IEEE Communications Letters*, pp. 1–1, 2025.

[221] Q. Luo, P. Xiao, Z. Liu, Z. Wan, N. Thomos, Z. Gao, and Z. He, "AFDM-SCMA: A Promising Waveform for Massive Connectivity Over High Mobility Channels," *IEEE Transactions on Wireless Communications*, vol. 23, no. 10, pp. 14 421–14 436, 2024.

[222] Z. Li, C. Zhang, G. Song, X. Fang, X. Sha, and D. Slock, "Chirp Parameter Selection for Affine Frequency Division Multiplexing with MMSE Equalization," *IEEE Transactions on Communications*, pp. 1–1, 2024.

[223] X. Li, H. Wang, Y. Ge, X. Shen, Y. L. Guan, M. Wen, and C. Yuen, "Affine Frequency Division Multiplexing Over Wideband Doubly-Dispersive Channels With Time-Scaling Effects," *IEEE Transactions on Wireless Communications*, pp. 1–1, 2025.

[224] J. Xu, Z. Liang, and K. Niu, "Multi-Block UAMP Detection for AFDM Under Fractional Delay-Doppler Channel," in *2025 IEEE Wireless Communications and Networking Conference (WCNC)*, 2025, pp. 1–6.

[225] Y. Ni, P. Yuan, Q. Huang, F. Liu, and Z. Wang, "An Integrated Sensing and Communications System Based on Affine Frequency Division Multiplexing," *IEEE Transactions on Wireless Communications*, vol. 24, no. 5, pp. 3763–3779, 2025.

[226] C. Xu, S. Sugiura, S. X. Ng, P. Zhang, L. Wang, and L. Hanzo, "Two Decades of MIMO Design Tradeoffs and Reduced-Complexity MIMO Detection in Near-Capacity Systems," *IEEE Access*, vol. 5, pp. 18 564–18 632, 2017.

[227] C. Xu, D. Liang, S. Sugiura, S. X. Ng, and L. Hanzo, "Reduced-Complexity Approx-Log-MAP and Max-Log-MAP Soft PSK/QAM Detection Algorithms," *IEEE Transactions on Communications*, vol. 61, no. 4, pp. 1415–1425, 2013.

[228] P. Robertson, E. Villebrun, and P. Hoeher, "A comparison of optimal and sub-optimal MAP decoding algorithms operating in the log domain," in *Proceedings IEEE International Conference on Communications ICC '95*, vol. 2, 1995, pp. 1009–1013 vol.2.

[229] L. Hanzo, T. H. Liew, B. L. Yeap, R. Y. S. Tee, and S. X. Ng, *Turbo Equalisation for Partialresponse Systems*, 2011, pp. 289–323.

[230] A. Serener, B. Natarajan, and D. M. Gruenbacher, "Lowering the Error Floor of Optimized Short-Block-Length LDPC-Coded OFDM via Spreading," *IEEE Transactions on Vehicular Technology*, vol. 57, no. 3, pp. 1646–1656, 2008.

[231] C.-Y. Yang and M.-K. Ku, "LDPC coded OFDM modulation for high spectral efficiency transmission," in *2008 4th European Conference on Circuits and Systems for Communications*, 2008, pp. 280–284.

[232] Y. Gong, Z. Li, L. Yang, L. Tian, J. Miao, D. Zhang, and Z. Xu, "LDPC-Hadamard Code-Assisted OTFS in High-Mobility Scenarios," *IEEE Open Journal of Vehicular Technology*, vol. 6, pp. 1849–1860, 2025.

[233] S. Li, J. Yuan, W. Yuan, Z. Wei, B. Bai, and D. W. K. Ng, "Performance Analysis of Coded OTFS Systems Over High-Mobility Channels," *IEEE Transactions on Wireless Communications*, vol. 20, no. 9, pp. 6033–6048, 2021.

[234] Q. Luo, J. Zhu, Z. Liu, Y. Tang, P. Xiao, G. Chen, and J. Shi, "Joint Sparse Graph for Enhanced MIMO-AFDM Receiver Design," *IEEE Transactions on Wireless Communications*, pp. 1–1, 2025.

[235] S. Huang, Y. Xu, T. Ma, H. Ju, X. Guo, Q. Luo, P. Xiao, and D. He, "A Sub-block Interleaving Algorithm to Mitigate Pilot Interference in LDPC-coded AFDM Systems," in *2025 IEEE/CIC International Conference on Communications in China (ICCC)*, 2025, pp. 1–6.

[236] Y. Qi, H. Yin, Y. Tang, X. Y. Fu, and L. Liu, "MAMP Detector for AFDM under Doubly Dispersive Channels," in *2025 IEEE/CIC International Conference on Communications in China (ICCC Workshops)*, 2025, pp. 1–6.

[237] Y. Chi, J. Liang, L. Liu, Y. Ge, and J. Guo, "IFDMA for Massive Connectivity Over High Mobility Channels," in *2025 IEEE 26th International Workshop on Signal Processing and Artificial Intelligence for Wireless Communications (SPAWC)*, 2025, pp. 1–5.

[238] N. Ahmad, S. K. S-Yusof, and N. Fisal, "Analysis of recursive systematic convolutional turbo codes in MB-OFDM UWB with channel estimation," in *2010 International Conference on Computer Applications and Industrial Electronics*, 2010, pp. 137–141.

[239] I. B. Oluwafemi and S. H. Mneney, "Error Performance of Concatenated Super-orthogonal Space-Time-Frequency Trellis Coded MIMO-OFDM System," *SAIEE Africa Research Journal*, vol. 103, no. 3, pp. 116–126, 2012.

[240] L. Xiang, Y. Liu, C. Xu, R. G. Maunder, L.-L. Yang, and L. Hanzo, "Iterative Receiver Design for Polar-Coded SCMA Systems," *IEEE Transactions on Communications*, vol. 69, no. 7, pp. 4235–4246, 2021.

[241] L. Li, Z. Ma, P. Z. Fan, and L. Hanzo, "High-Dimensional Codebook Design for the SCMA Down Link," *IEEE Transactions on Vehicular Technology*, vol. 67, no. 10, pp. 10 118–10 122, 2018.

[242] W. Yuan, N. Wu, C. Yan, Y. Li, X. Huang, and L. Hanzo, "A Low-Complexity Energy-Minimization-Based SCMA Detector and Its Convergence Analysis," *IEEE Transactions on Vehicular Technology*, vol. 67, no. 12, pp. 12 398–12 403, 2018.

[243] Y. Liu, L. Xiang, R. G. Maunder, L.-L. Yang, and L. Hanzo, "Hybrid Iterative Detection and Decoding of Near-Instantaneously Adaptive Turbo-Coded Sparse Code Multiple Access," *IEEE Transactions on Vehicular Technology*, vol. 70, no. 5, pp. 4682–4692, 2021.

[244] S. Aghashahi, Z. Zeinalpour-Yazdi, A. Tadaion, M. B. Mashhadi, and A. Elzanaty, "Single Antenna Tracking and Localization of RIS-Enabled Vehicular Users," *IEEE Transactions on Vehicular Technology*, vol. 74, no. 3, pp. 4362–4375, 2025.

[245] Q. Yuan, S. Zhuge, Z. Lin, Y. Ma, and Y. Zeng, "Kalman Filtering based Target Tracking for Multistatic Sensing in ISAC Systems," in *2025 IEEE International Symposium on Circuits and Systems (ISCAS)*, 2025, pp. 1–5.

[246] Y. Fu, Z. Li, R. Sun, C. Li, F. Richard Yu, and N. Cheng, "A Predictive Integrated Sensing, Communication and Computation Over-the-Air Approach for IoV: Optimization and Trade-off Analysis," *IEEE Journal on Selected Areas in Communications*, pp. 1–1, 2025.

[247] D. Hu, J. Nakazato, J. Ehsan, K. Maruta, R. Dinis, and M. Tsukada, "DoA Estimation and Kalman Filter based Multi-Antenna System for Vehicle Position in mmWave Network," *IEEE Open Journal of Vehicular Technology*, pp. 1–15, 2025.

[248] J. Yan, W. Pu, J. Dai, H. Liu, and Z. Bao, "Resource Allocation for Search and Track Application in Phased Array Radar Based on Pareto Bi-Objective Optimization," *IEEE Transactions on Vehicular Technology*, vol. 68, no. 4, pp. 3487–3499, 2019.

[249] J. Zhang, Q. Liang, L. Du, and M. Hua, "Track-After-Scan Based ISAC System with Detection, Tracking, and Communications," in *2025 IEEE/CIC International Conference on Communications in China (ICCC Workshops)*, 2025, pp. 1–6.

[250] Z. Ying, Y. Cui, J. Mu, and X. Jing, "Particle Filter based Predictive Beamforming for Integrated Vehicle Sensing and Communication," in *2021 IEEE 94th Vehicular Technology Conference (VTC2021-Fall)*, 2021, pp. 1–5.

[251] W.-X. Long, W. Song, Y. Liu, Y. Liu, M. Moretti, and R. Chen, "GPS-Denied ISAC Vehicle Localization Based on mmWave Radar and Identification," *IEEE Open Journal of Vehicular Technology*, vol. 6, pp. 2343–2357, 2025.

[252] C. Xu, J. An, T. Bai, L. Xiang, S. Sugiura, R. G. Maunder, L.-L. Yang, and L. Hanzo, "Reconfigurable Intelligent Surface Assisted Multi-Carrier Wireless Systems for Doubly Selective High-Mobility Ricean Channels," *IEEE Transactions on Vehicular Technology*, vol. 71, no. 4, pp. 4023–4041, 2022.

[253] C. Pan, H. Ren, K. Wang, J. F. Kolb, M. Elkashlan, M. Chen, M. Di Renzo, Y. Hao, J. Wang, A. L. Swindlehurst, X. You, and L. Hanzo, "Reconfigurable Intelligent Surfaces for 6G Systems: Principles, Applications, and Research Directions," *IEEE Communications Magazine*, vol. 59, no. 6, pp. 14–20, 2021.

[254] I. Guvenc, K. Chowdhury, S. Fdida, and M. Masuda, "Guest Editorial: Experimentation in Large-Scale Wireless Community Testbeds," *IEEE Communications Magazine*, vol. 63, no. 2, pp. 44–45, 2025.

[255] "Integrated Sensing and Communications (ISAC); Channel Modelling, Measurements and Evaluation Methodology," European Telecommunications Standards Institute, 650 Rte des Lucioles, Sophia Antipolis, 06921 France, Tech. Rep. ETSI GR ISC 002 V1.1.1 (2025-08), 08 2025.

[256] G. Liu, L. Han, R. Xi, L. Ma, Z. Han, Y. Xue, H. Zhao, J. Jin, Q. Wang, and F. Xu, "Cooperative Sensing for 6G ISAC: Concept, Key Technologies, Performance Evaluation, and Field Trial," *Engineering*, 2025. [Online]. Available: https://www.sciencedirect.com/science/article/pii/S209580992500551X